Ultrafast Metrology in the Quantum Domain

by

Jean-Philippe MacLean

A thesis
presented to the University of Waterloo
in fulfillment of the
thesis requirement for the degree of
Doctor of Physics
in
Physics

Waterloo, Ontario, Canada, 2019

Examining Committee Membership

The following served on the Examining Committee for this thesis. The decision of the Examining Committee is by majority vote.

External Examiner:	James Franson Professor, Dept. of Physics, University of Maryland Baltimore County
Supervisor(s):	Kevin Resch Professor, Dept. of Physics & Astronomy, University of Waterloo
Internal Member:	Donna Strickland Professor, Dept. of Physics & Astronomy, University of Waterloo
Internal-External Member:	Michal Bajcsy Professor, Dept. of Electrical and Computer Engineering, University of Waterloo
Other Member(s):	Rob Spekkens Professor, Dept. of Physics & Astronomy, University of Waterloo

Author's Declaration

I hereby declare that I am the sole author of this thesis. This is a true copy of the thesis, including any required final revisions, as accepted by my examiners.

I understand that my thesis may be made electronically available to the public.

Abstract

Single photons are a natural platform for quantum technologies as they support entanglement in many degrees of freedom and are inherently well protected from a detrimental type of noise called decoherence. In order to fully exploit photons for quantum technologies, it will be necessary to be able to shape, control, and measure their properties in all degrees of freedom: space, time, frequency, and polarization.

The time-frequency degree of freedom of light is of particular interest for quantum information tasks as it supports various encodings, including frequency bins and time bins, and is intrinsically robust for propagation through long-distance fibre links. Applications which harness quantum correlations in this degree of freedom, referred to as energy-time entanglement, include dispersion cancellation and high-dimensional quantum key distribution. However, detection of this entanglement and observation of these effects requires time resolution beyond the capabilities of current photon detectors. Thus, for operations on ultrafast time scales, more powerful and complex methods are required.

In this thesis, we use a nonlinear technique known as optical gating to surpass the limitations in current detectors and measure single photon pairs, improving the time resolution by two orders of magnitude. When a single photon enters a nonlinear medium at the same time as a strong laser pulse, it may upconvert to a higher energy photon. The strong laser pulse effectively acts as an ultrafast shutter or gate and this creates a high resolution snapshot of the photon in time. Optical gating in conjunction with single photon spectrometers then allow us to measure both the spectral and temporal features of photons on subpicosecond time scales.

These high resolution measurements enable us to explore a host of quantum effects which remained previously inaccessible. First, we directly observe energy-time entanglement, analogous to Einstein-Rosen-Podolsky correlations but *in frequency and time*. Then, with full control over the dispersion of each photon, we observe nonlocal dispersion cancellation on femtosecond time scales. We also explore ultrafast interferometry in the quantum domain by temporally resolving two-photon interference from a Franson interferometer and observe a violation of the CHSH-Bell inequality. Finally, we show that, using these measurements, it is possible to reconstruct a two-photon energy-time entangled state. Such measurement capabilities will be essential to precisely control both the spectral and temporal shape of entangled photons and to develop new applications in quantum state engineering.

Acknowledgements

My graduate school experience has been challenging, fascinating, and fun. It has been a real privilege to work with and meet so many remarkable and passionate individuals at the Institute for Quantum Computing, the University of Waterloo, and around the world. At times, it can be demanding and frustrating to complete such a long personal endeavour, but these difficulties are made surmountable with the support, guidance, and help of all the people whom I have met along this journey.

First, I'd like to thank my supervisor, Kevin Resch, for taking me on fresh out of my bachelor's degree in my early twenties and mentoring me throughout graduate school. I am very grateful for your insights into quantum optics, physics, and finance, for sharing your scientific vision and helping me anytime issues in the lab came up. I respect and admire your work ethic, and devotion to both your family and the institution. Thank you to my committee members, Michal Bajcsy, Rob Spekkens, and Roger Melko for keeping me in check throughout the years, to Donna Strickland for teaching me nonlinear optics, and to James Franson whose ideas inspired much of this work. Thanks to NSERC, IQC, and the University of Waterloo for generously providing the funding to support my research throughout this degree.

When I arrived in Waterloo, I had the privilege to walk into a wonderful group which has made this experience all the more enjoyable. Thanks to Denis Hamel for setting the standard on how to work hard at physics and keep a balanced personal life. I will always admire "l'infatigable" trio composed of Kent Fisher, Mike Mazurek, and John Donohue. These three musketeers of the QOQI group are real role models on how one should go about to do good science and have some fun along the way. Kent Fisher deserves thanks for sharing the road trips to Ottawa, with mandatory stops for milkshakes, the ice-cold winter walks to and from NRC with occasional discussions bordering on physics and philosophy, and splitting large cappuccinos in two, because, well, we're both partly Scottish. Thanks to John Donohue for bringing me up to speed with the world of ultrafast quantum optics, for your contagious positive attitude, and being enthusiastic about almost everything. Thanks to Mike Mazurek for your patience in explaining things and putting up with my occasional outbursts of singing in the lab.

Thanks to all the other members that have been a big part of the ride, to Morgan Mastrovich, Patrick Daley, Ruoxun Xu, Matt Brown, Jeff Salvail, Megan Agnew, Klaudia Golos, and Lydia Vermeyden. Thanks to Connor Paddock and Andrew Cameron for simply being awesome office mates. Thanks to Sacha Schwarz for jumping on board the ultrafast quantum experiments with enduring joy and cheerfulness, and for sharing your European

tastes for all the good things in life. Thanks to the many other friends I have made at IQC and in Waterloo, including Filippo Miatto, Electra Eleftheriadou, Olivia Di Matteo, Gary Oak, Corey Rae McRae, Jérémy Béjanin, Bohdan Kulchytskyy, Arnaud Carignan-Dugas, Hammam Qassim, and Anirudh Krishna.

Special thanks also go to the Quantum Technologies crew at the National Research Council in Ottawa. Duncan England, Philip Bustard, and Ben Sussman hosted Kent and I for half a year while we bravely attempted to keep up with their puns and love of smoke meat and sushi. I am deeply indebted to Duncan England for making us feel welcome in Ottawa, sharing my love of x-country skiing, and continually being a good sport in work and in life. Thanks to Rob Spekkens and Katja Ried for all those discussions at the Perimeter Institute. It was a real pleasure to have the opportunity to test some of your ideas on quantum causality in the lab.

Thanks to the members of the UW OSA student chapter, Aimee Gunther, Ian Andrews, Kent Fisher, Mike Mazurek, and Sarah Kaiser for taking part in what started out as a crazy idea and, after a year and a half of work, turned into a full-fledged museum exhibit on the science of light. Thanks to Donna Strickland for encouraging us, IQC for supporting us, and to Angela Olano for guiding us through the entire process.

Et puis, merci à ma famille pour toute l'aide et tout l'encouragement que vous m'avez donnés et qui m'ont permis de devenir qui je suis aujourd'hui. Merci à mes parents, Nadine et Steve. Vous êtes et avez toujours été des modèles pour moi tant au niveau personnel que professionnel. Merci à mes soeurs, Catherine et Michèle, pour l'humanité que vous m'apportez. Finalement, merci, Katryn, pour toute la joie et tout l'amour que tu me donnes. Merci pour ton appui inconditionnel tout au long de cette entreprise. Tu gardes un équilibre sain dans ma vie, qui me permet de décrocher quand c'est nécessaire et de vivre dans le moment présent. C'est un vrai plaisir de partager cette aventure au quotidien avec toi.

À ma famille.

"The strongest arguments prove nothing so long as the conclusions are not verified by experience. Experimental science is the queen of sciences and the goal of all speculation."

Roger Bacon

"Quantum phenomena do not occur in a Hilbert space. They occur in the laboratory."

Asher Peres

Table of Contents

List of Tables

List of Figures

Chapter 1

Quantum optics

1.1 Introduction

Quantum computing

The exotic features of quantum mechanics have the potential to revolutionize information technologies in computing, communication, and precision measurement. Quantum computers could tackle problems exponentially faster than conventional computers while entanglement could provide intrinsically secure communications across the globe. Finding suitable physical systems that will allow the development of quantum information and quantum communication technologies is a long-standing grand challenge of experimental science.

Since my introduction to the field of quantum information and quantum computing in the fall of 2013, this venture has grown far beyond solely an academic endeavour and into a multi-billion dollar enterprise involving massive companies like Google, IBM, and Intel, as well as multiple startups racing towards finding the best platform for quantum computing. Research teams have demonstrated 50-qubit quantum simulators using trapped ions [1, 2], IBM has placed a 20-qubit quantum computer based on a superconducting architecture "in the cloud" and is working towards a 50-qubit one [3, 4], and Google has a blueprint to go beyond 50 [5]. Such machines are by no means sufficient for traditional applications of quantum computing such as running Shor's algorithm to factor large numbers or running Grover's search algorithm on large configuration spaces [6]. Nonetheless, these devices have reached a new frontier referred to as Noisy Intermediate-Scale Quantum (NISQ)

technologies [7], and may be sufficient to run small simulations of, for example, the Dirac equation [8].

Other physical implementations for computing and information technologies are also actively being explored using nuclear magnetic resonance, atom, cavity quantum electrodynamics, and solid state systems. One approach which has been pursued since the beginning is photonics. In classical computing, the dream of an optical computer has been around since at least the invention of the transistor and has resurfaced time and time again as new optical and optoelectronic technologies became available [9]. Today, the dominant physical quantity limiting current classical computation is energy. Power dissipation limits the performance of silicon chips and battery life is a constant issue for mobile devices. Optical interconnects on-chip or between chips could significantly reduce the energy loss and increase the transmission speed of signals compared with current metallic wires used in classical computing [10]. For quantum computing, an optical transistor at the single-photon level could allow truly quantum operations required for quantum logic and information processing.

In order to perform logic and computation, any physical object, such as a photon, requires the ability to interact or change state based on the state of another such object. Unfortunately with light, since Maxwell's equations are linear in vacuum, photons don't interact, or at least very weakly. A medium is needed to mediate interactions between photons. One example of where such interactions can occur is in nonlinear optics. A strong laser field can displace bound electrons in a crystal. The response of these bound electrons can be nonlinear in the applied field [11] and is extremely fast, on the order of 1 to 2 fs [12]. However, the induced nonlinearities are weak and, at single-photon levels, almost negligible. Proposals for quantum computing with Kerr nonlinearties have nonetheless been considered [13], but it was found that the non-instantaneous response of the Kerr nonlinearity prevents high-fidelity operations required for quantum computing [14]. Many other methods to mediate photon-photon interactions are actively being explored in strongly interacting systems which have very high nonlinearities at the single photon level. Examples of these include electromagnetically induced transparency (EIT) in hollow-core fibres [15], cavity-QED systems [16, 17], and strongly interacting Rydberg atoms [18, 19, 20].

In 2001, the quantum computing scheme proposed by Knill, Laflamme, and Milburn changed the rules of the game [21]. Quantum interference at beam splitters, linear optics, and single-photon detectors became sufficient to produce effective photon-photon interactions. Shortly afterwards, entangling gates required for quantum computation with light were demonstrated [22]. Experimental one-way computing [23] shifted the problem from obtaining two-photon interactions to producing large cluster states which were experimentally demonstrated with frequency combs [24] and temporal multiplexing [25]. Using such

techniques, the field of integrated silicon photonics has recently attracted lots of attention for quantum computing with light due to the ability to employ CMOS compatible technologies perfected by the silicon industry to scale photonic qubits on a chip [26, 27, 28]. It's even been argued that photonic-based quantum computing may in fact be the platform of choice to achieve fault tolerance [26].

Quantum communication

Regardless of which physical platform succeeds in the computing race, photons remain natural carriers of information, and have emerged as the only viable platform for quantum communication applications. They travel at nature's speed limit, their polarization modes are robust to decoherence, and they are well isolated from their environment, with some estimates on their lifetime from the cosmic microwave background radiation going as far back as the Big Bang [29, 30]. The possibility to encode information in light's different degrees of freedom also makes it a versatile platform. Polarization, space, time, and frequency are each suited for different types of applications. Time and frequency are of particular interest as they are robust to long distance propagation in both fibre and free space, and are used by the telecommunication industry as a multiplexing degree of freedom.

Quantum communication with light requires precise control over three basic tools: single- or entangled-photon sources, transmission channels, and detectors. Since the first demonstration of quantum teleportation in a lab in 1997 [31], much of the effort in quantum optics over the last two decades has been in building, designing and improving these three aspects of quantum communication. Developments in these areas has enabled recent demonstrations of long-distance quantum key distribution on Earth [32] and in space [33]. Moreover, photonic states with one to two qubits can be controlled with high precision, and for this reason, they have been an ideal platform for foundational tests of quantum mechanics. From the first violation of Bell's inequality [34] to the more recent loophole free violations [35, 36, 37], photons have also been employed to test noncontextuality [38] and to explore the role of quantum mechanics in understanding causality [39, 40, 41].

The most well-controlled source of entangled photons is spontaneous parametric downconversion (SPDC), which produces two lower-energy photons from a higher-energy pump photon. Parametric downconversion has been the workhorse of quantum optics, with the first experimental observations dating back to just over 50 years ago [42, 43, 44]. Its use as a photon source remains so far unchallenged with the ability to produce heralded single photons [45, 46], as well as entangled photons in many degrees of freedom including polarization [47], orbital angular momentum [48], and energy-time degrees of freedom [49, 50].

Parametric downconversion, while extremely useful for many proof-of-principle demonstrations, remains an inherently probabilistic process, rendering large scale on-demand multi-photon states infeasible. Overcoming this limitation will require either developing high-efficiency and high-purity on-demand single-photon sources [51], using multiplexing schemes [52], or using quantum memories.

A quantum memory is a device that acts as a buffer for photonic states. It can be used to synchronize quantum optical states of light [53] or to distribute of entanglement between remote locations [54]. Many different platforms for quantum memories exist, ranging from EIT [55], atomic frequency combs [56], to Raman memories [57]. Within the Raman memories, different implementations exist including caesium vapour [57], bulk diamond [58], and molecular hydrogen [59].

As an example, in the diamond quantum memory, photons are stored as optical phonons, or vibrations of the diamond lattice. The memory works at room temperature and we showed that it can store high-bandwidth photons directly from downconversion [58], as well as one half of an entangled Bell state [60]. The Raman transition in diamond can be used to change the frequency and bandwidth of photons [61] and interfere photons and phonons [62]. However, the short 3.5 ps lifetime of the diamond memory circumvents applications requiring long storage times. Nonetheless, it remains a proof of principle demonstration for other Raman-type memories which promise longer storage times [53, 63].

Transmission channels are primarily based on fibre-optic networks which work in the telecommunication band. However, propagation in fibre is limited to 300–400 km due to loss [64, 65]. Whereas classical telecommunication signals can be reamplified with erbium-doped fibre amplifiers, the no-cloning theorem prevents the amplification of quantum states of light. As a result, extending communication links to a global quantum network will likely require a combination of fibre optics, quantum repeaters, and space-based communication [66].

Single-photon detector technology has significantly improved in the past decade. Avalanche photodiodes (APDs) can achieve 65% efficiency and 40 ps timing resolution in the near-infrared (NIR) and at room temperature [67]. However, their efficiency drops to 10% for telecommunication wavelengths, which limits their use to the NIR. With the advent of superconducting nanowire single photon detectors (SNSPDs), the landscape of possibilities has changed drastically. SNSPDs can achieve over 90% efficiency in the NIR [68] and close to 60% efficiency at telecom wavelengths [69], opening up a vast array of experiments not previously possible. Moreover, the timing jitter for SNPDs is continually being reduced, and current state of the art detectors have a timing jitter below 5 ps [70], approaching the coveted subpicosecond regime in ultrafast optics. The work in this thesis is related to this

third tool: that of state detection on ultrafast time scales.

The need for speed

Quantum correlations in time and frequency, referred to as energy-time entanglement, can be produced with parametric downconversion. These types of correlations can be advantageous for applications requiring high-dimensional and high-capacity communication [71, 72] or for multiplexing schemes [73]. However, the photons required for such applications have features on subpicosecond time scales. Thus, universal control and characterization in time and frequency requires fast manipulation and fast detection. Manipulating quantum correlations on ultrafast time scales has been achieved using nonlinear optical techniques [74]. However, certifying the presence of energy-time entanglement remains a challenge as, on these time scales, photon counting detectors are simply too slow [67, 75]. Consequently, a different approach is required.

How do you measure a short event in time? You need a shorter event in time. This idea, which has been around for centuries, was elegantly demonstrated by Edward Muybridge and Harold Edgerton, both pioneers in imaging short events in time in the 19th and 20th centuries [76, 77]. To build a fast detector from a slow detector, you need a fast shutter to gate the detector. In ultrafast optics, the fastest shutter available is the light pulse itself, and this has led to the adoption of nonlinear processes to gate one light pulse with another pulse, or with the pulse itself.

Nonlinear optical techniques will also be required for fast manipulation and characterization of single photons. However, the low power levels of single photons and the weak nonlinearities in crystals, coupled with the fact that the photons may be entangled, creates new challenges for the field of ultrafast quantum optics. Nonetheless, the development of optimized single photon sources [78, 79, 80] and the continual improvement of waveguide technologies [81] are rapidly opening the door to exploring and exploiting nonlinear effects at the single-photon level, important for applications such as quantum frequency conversion and waveform conversion [82, 83, 84].

In this thesis, I present our work on developing fast detectors by combining a nonlinear optical technique called optical gating with a slow detector. I first discuss the classical and quantum theory of optical gating in Chapter 2, followed by the different experimental techniques used to manipulate and measure ultrafast pulses in Chapter 3, many of which can be used with ultrafast quantum states of light. Fast detectors in the quantum regime enable us to directly characterize energy-time entanglement in Chapter 4, explore ultrafast

quantum interferometry in Chapter 5, and reconstruct an energy-time entangled state in Chapter 6.

1.2 Chapter Overview

For the remainder of this chapter, I present some of the important concepts and tools in quantum optics used in the remainder of the thesis. I start with the quantum description of light in order to discuss different ways in which it's possible to encode information into light's degrees of freedom. Both the polarization and the time-frequency degree of freedom are considered in Sec. 1.4. This leads to a comparison of two forms of entanglement in these two degrees of freedom in Sec. 1.5. Finally, I address the different ways to distinguish quantum and classical light which are used in this thesis in Sec. 1.6. In particular, I look at second-order coherence functions, time-bandwidth inequalities, and fringe visibilities in interference phenomena.

1.3 A quantum description of light

Light is a propagating of electromagnetic waves. For a quantum description of light, the field must be quantized. The canonical quantization of the electromagnetic field can be obtained inside a cavity, where the allowed electromagnetic modes are the solutions to Maxwell's equations which satisfy the boundary conditions of the cavity [85, 86, 87]. In the quantum description, each mode is converted into a quantum harmonic oscillator. This leads to an operator for the quantized electric field, which is,

$$\hat{E}(r,t) = i\sum_k \left(\frac{\hbar\omega_k}{2\epsilon_0 V}\right)^{1/2} \hat{\epsilon}_k \left[a_k e^{-i\omega_k t + i\vec{k}\cdot\vec{r}} - a_k^\dagger e^{i\omega_k t - i\vec{k}\cdot\vec{r}}\right]. \tag{1.1}$$

The field operator is a sum of optical modes, which are solutions to Maxwell's equations, with wave vector $\vec{k}$, frequency ω_k, and polarization indicated by $\hat{\epsilon}_k$, inside a cavity of volume V. Each mode k has a creation, $a_k^\dagger$, and annihilation, a_k, ladder operator associated with it, which creates or destroys an excitation of the mode. These operators obey the commutation relation $[a_k^\dagger, a_{k'}] = \delta_{k,k'}$ of the quantum harmonic oscillator. We can therefore think of a photon as a single excitation of an optical mode. The spatial and temporal properties of these modes are the same for the quantized and non-quantized field, since they obey the same differential equations. As a result, many phenomena in quantum optics are

identical to their classical counterparts, especially with regards to first-order interference or propagation effects such as dispersion and diffraction. However, stark distinctions arise due to the operator structure of the ladder operators.

Most experiments, and all the ones in this thesis, have no identifiable cavity. Instead, the intensity of light flows from the source to the detector. For experiments of this type, the electric field can be quantized in free space with a set of electromagnetic modes characterized by a continuous wave vector [88, 85]. The quantized electric field operator for a single spatial mode, with finite cross-sectional area A, but a continuum of spectral modes in the z direction is then,

$$\hat{E}(z,t) = i\int d\omega \left(\frac{\hbar\omega}{4\pi\epsilon_0 cA}\right)^{1/2}\left[a(\omega)e^{-i\omega t+ikz} - a^\dagger(\omega)e^{i\omega t-ikz}\right] \tag{1.2}$$

$$= E^{(+)}(z,t) + E^{(-)}(z,t), \tag{1.3}$$

where the $a^\dagger(\omega)$ and $a(\omega)$ are, respectively, the continuous-mode creation and annihilation operators, obeying the commutation relation $[a^\dagger(\omega), a(\omega')] = \delta(\omega-\omega')$. In Eq. 1.3, the electric field is separated into two parts, which are referred to as the (quite unintuitively) positive $E^{(+)}$ and negative $E^{(-)}$ frequency components, and take the role of photon annihilation and creation operators.

In order to have finite energy, a continuous mode state with a finite number of photons must take the form of a pulse. The photon wave packet,

$$|\psi\rangle = \int d\omega\ F(\omega)a^\dagger(\omega)\,|0\rangle\,, \tag{1.4}$$

describes a superposition of frequency modes $a^\dagger(\omega)$ weighted by the spectral amplitude $F(\omega)$. For a normalized quantum state of light, $\int d\omega|F(\omega)|^2 = 1$. The probability of finding the photon in a specific frequency ω is then,

$$\begin{aligned}
\langle\hat{n}_\omega\rangle &= \langle\psi|\,a^\dagger(\omega)a(\omega)\,|\psi\rangle = |\langle 0|\,a(\omega)\,|\psi\rangle|^2 \\
&= \left|\langle 0|\,a(\omega)\int d\omega' F(\omega')a^\dagger(\omega')\,|0\rangle\right|^2 \\
&= \left|\int d\omega' F(\omega')\,\langle 0|\,a(\omega)a^\dagger(\omega')\,|0\rangle\right|^2 \\
&= \left|\int d\omega' F(\omega')\delta(\omega-\omega')\right|^2 \\
&= |F(\omega)|^2\,.
\end{aligned} \tag{1.5}$$

If we define the Fourier-transformed ladder operators,

$$a(t) = \frac{1}{\sqrt{2\pi}} \int d\omega a(\omega) \exp(i\omega t) \tag{1.6}$$

$$a^\dagger(t) = \frac{1}{\sqrt{2\pi}} \int d\omega a^\dagger(\omega) \exp(-i\omega t), \tag{1.7}$$

then we can also calculate the probability of finding the photon at a specific time t,

$$\begin{aligned} \langle \hat{n}_t \rangle &= \langle \psi | \, a^\dagger(t) a(t) \, | \psi \rangle = |\langle 0 | \, a(t) \, | \psi \rangle|^2 \\ &= \left| \langle 0 | \frac{1}{\sqrt{2\pi}} \int d\omega a(\omega) e^{i\omega t} \int d\omega' F(\omega') a^\dagger(\omega') \, |0\rangle \right|^2 \\ &= \left| \frac{1}{\sqrt{2\pi}} \int d\omega F(\omega) e^{i\omega t} \right|^2 \\ &= |f(t)|^2 \end{aligned} \tag{1.8}$$

where $f(t)$ is the temporal amplitude function which is defined as the Fourier transform of $F(\omega)$. This is the same relationship that relates the spectral and temporal profiles of a classical pulse, and as a result, this formalism is very convenient for capturing many of the essential features of ultrafast quantum states of light. We will use these continuous-mode states when discussing nonlinear optical processes with quantum states of light.

Of course, in quantum mechanics and in the lab, we often work with mixed states. The density operator formalism of quantum mechanics is useful for characterizing mixed states. An operator $\hat{\rho}$ acting on the Hilbert Space $\mathcal{H}$ is a state or density operator if it has trace 1, is Hermitian and is positive semidefinite. Geometrically, these density operators form a convex set. Given two states $\hat{\rho}_1$ and $\hat{\rho}_2$, this implies the convex combination $\hat{\rho} = p\hat{\rho}_1 + (1-p)\hat{\rho}_2$ is also a state.

One notable example is heralded single photons produced in downconversion. If there are any time-frequency correlations between the two photons, then ignoring one photon will leave the photon on the other side in a mixed state. In such a scenario, the probability of detecting the photon at a specific frequency $\langle \hat{n}_\omega \rangle$ and at a specific time $\langle \hat{n}_t \rangle$, which for the pure state were given by $|F(\omega)|^2$ and $|f(t)|^2$, respectively, will not be related by Fourier transforms. For a general mixed state $\hat{\rho}$ which is a convex combination of pure states $|\psi_i\rangle$,

$$\hat{\rho} = \sum_i p_i \, |\psi_i\rangle \langle \psi_i| \, , \tag{1.9}$$

we can calculate the expectation value of the frequency with respect to the state ρ,

$$\begin{aligned}\langle \hat{n}_\omega \rangle_\rho &= \mathrm{Tr}\left[\sum_i p_i \hat{n}_\omega \left|\psi_i\right\rangle \left\langle\psi_i\right|\right] = \sum_i p_i \mathrm{Tr}\left[\hat{n}_\omega \left|\psi_i\right\rangle \left\langle\psi_i\right|\right] \\ &= \sum_i p_i \langle \hat{n}_\omega \rangle_i = \sum_i p_i |F_i(\omega)|^2\end{aligned} \tag{1.10}$$

where $\langle \cdots \rangle_i$ is the expectation value with respect to the pure state $|\psi_i\rangle$. The expectation value of the frequency for the state $\hat{\rho}$ is simply the convex sum of the expectation values of the frequencies for the pure state $|\psi_i\rangle$ which make up $\hat{\rho}$. And likewise, we find an analogous form for t,

$$\langle \hat{n}_t \rangle_\rho = \sum_i p_i |f_i(t)^2|. \tag{1.11}$$

1.4 Encoding quantum information into light

Classical computation is built around the concept of the bit, a unit of information commonly represented as a 0 or 1. Any physical system that can be in two possible distinct states, for example, an electrical switch or two distinct voltage levels, can represent a bit of information. By extension, quantum computation and quantum communication are built upon quantum bits, or "qubits". In the computational basis, the state of a qubit can be either $|0\rangle$ or $|1\rangle$, or any coherent superposition of the two, $\alpha|0\rangle + \beta|1\rangle$, with $|\alpha|^2 + |\beta|^2 = 1$ to enforce normalization. To represent a qubit, a physical system must also be able to realize all these possible superpositions.

To encode qubits or qudits, their higher-dimensional counterparts, into a photon, we use the different physical states of light's degrees of freedom. These can be the horizontal and vertical polarization modes, the different frequencies of electromagnetic waves, or the different spatial distributions a photon can take such as the orbital angular momentum of light [89]. The work in this thesis primarily uses the frequency and time degrees of freedom of light, which we compare to the polarization degree of freedom below.

1.4.1 Polarization

Polarization is convenient to work with due to the wide availability of high-efficiency polarization control elements and the relatively low changes in birefringence induced by thermal

drifts. The horizontal, $|H\rangle = a_H^\dagger |0\rangle$, and vertical, $|V\rangle = a_V^\dagger |0\rangle$, polarizations, where $|0\rangle$ here is the vacuum state, are defined as the directions of oscillations of the electromagnetic field in the horizontal or vertical direction with respect to a reference, such as an optical table. To encode a qubit into the polarization degree of freedom, it's often convenient to associate these two polarization modes of a light to the computational basis,

$$|H\rangle = \begin{pmatrix} 1 \\ 0 \end{pmatrix} \quad |V\rangle = \begin{pmatrix} 0 \\ 1 \end{pmatrix}. \tag{1.12}$$

The other polarization states which we commonly use are the diagonal and anti-diagonal states,

$$|D\rangle = \frac{1}{\sqrt{2}} \left(|H\rangle + |V\rangle \right) \quad |A\rangle = \frac{1}{\sqrt{2}} \left(|H\rangle - |V\rangle \right) \tag{1.13}$$

as well as the right- and left-circular polarization states,

$$|R\rangle = \frac{1}{\sqrt{2}} \left(|H\rangle + i\,|V\rangle \right) \quad |L\rangle = \frac{1}{\sqrt{2}} \left(|H\rangle - i\,|V\rangle \right). \tag{1.14}$$

The H/V states are eigenstates of the Pauli-Z operator, whereas the D/A and R/L states are eigenstates of the Pauli-X and Pauli-Y operators, respectively, where,

$$X = \begin{pmatrix} 0 & 1 \\ 1 & 0 \end{pmatrix} \quad Y = \begin{pmatrix} 0 & -i \\ i & 0 \end{pmatrix} \quad Z = \begin{pmatrix} 1 & 0 \\ 0 & -1 \end{pmatrix}. \tag{1.15}$$

The polarization state of a photon is straightforward to control and measure using combinations of wave plates and polarizing beam splitters. A quarter-wave plate and a half-wave plate can rotate the horizontal polarization, $|H\rangle$ to an arbitrary polarization, $|H\rangle + e^{i\phi} |V\rangle$, or vice-versa, and a polarizing beam splitter acts as a projective measurement transmitting the horizontal polarization and reflecting the vertical polarization. A polarization qubit can be characterized using these optical elements and quantum state tomography by means of maximum likelihood reconstruction [90, 91].

1.4.2 Time-frequency degree of freedom

Polarization is extremely useful as a degree of freedom since it's easy to control and measure. However, polarization states are inherently limited to a two-dimensional Hilbert

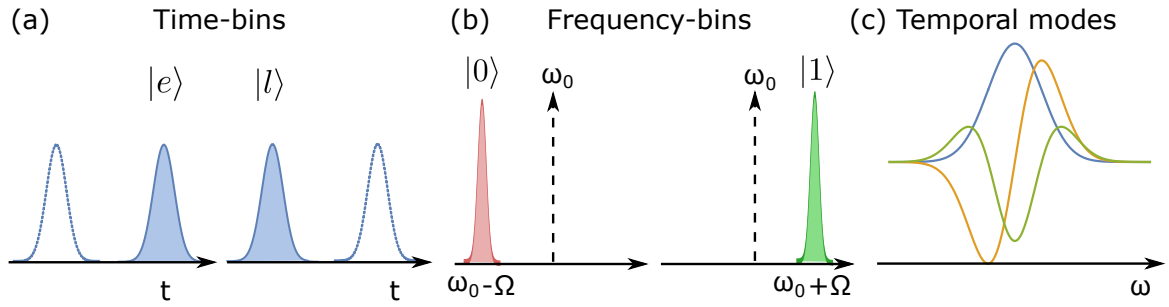

Figure 1.1: **Time-frequency degree of freedom.** Three different possible ways of encoding information into photons using the time-frequency degree of freedom. (a) Information in time-bin states is encoded in the time of arrival of the photon, either early $|e\rangle$ or late $|l\rangle$. (b) With frequency bins, the different frequencies of light represent the different computational states, $|0\rangle$ or $|1\rangle$. (c) Temporal modes are broadband overlapping states in frequency and time which are orthogonal to each other. Example temporal modes represented by the first three Hermite-Gauss states.

space. For long distance high capacity communication, other degrees of freedom must be used. The time-frequency degree of freedom offers different types of encoding, such as time bins, frequency bins, and temporal modes. It is extremely robust for propagation through long-distance fibre links, and is already being used extensively by the telecommunication industry as a multiplexing degree of freedom [92, 93].

Time-bin states can be prepared by an unbalanced interferometer, where the photons that take the short path and arrive early are denoted $|e\rangle$ and the photons that take the long path and arrive late are denoted $|l\rangle$ [94]. By controlling the beam splitter reflectivity and phase, a coherent superposition of the two, $\alpha|e\rangle + \beta|l\rangle$, is created. They can also be measured with an unbalanced interferometer. The separation between time-bins must be larger than the coherence time of the photons to avoid crosstalk between bins. Separations on the order of nanoseconds can be distinguished with fast electronics [95], and nonlinear optical transformations can reduce the separation to picosecond time scales near the coherence time of the photons [96]. Time-bin states are robust against mode distortions, and polarization effects from optical elements [97], and they can be used for differential-phase-shift keying [98], an encoding scheme used in classical telecommunications [99]. They can be converted to frequency bins using sum-frequency generation with chirped pulses [100].

Frequency bins use the different frequencies of light as their basis states [101]. They have been produced using four-wave mixing in ring resonators with 200 GHz frequency separation [102, 103]. Phase modulators are used to interfere different bins and electro-optic beam

splitters and tritters have been demonstrated in this way [104]. The use of monochromatic frequency bins as a basis for communication and computation has a number of advantages including the availability of straightforward high-resolution measurements, reduced constraints on timing jitter from detectors, and the possibility to simultaneously process multiple modes with telecommunication components. Linear optics quantum computing schemes have been explored with both frequency bin [105] and time bin [106] qubits.

Temporal modes provide another flexible and high-dimensional basis for the time-frequency degree of freedom that can be used for linear optics quantum computing and cluster state quantum computing [107]. These are field-orthogonal broadband wave-packet states which are superpositions of time and frequency, such as the Hermite-Gauss modes. They are analogous to the Hermite-Gauss spatial modes in that they overlap in time and frequency but each mode is mutually orthogonal. Temporal modes can be generated in parametric downconversion and manipulated and measured using a quantum pulse gate [108, 109, 110, 110].

1.5 Photonic Entanglement

Entanglement is the hallmark of quantum information. Since the first convincing experiment in favour of Bell's theorem by Aspect, Grangier, and Roger in 1981 [34] and the first demonstration of quantum teleportation by the Zeilinger group in 1997 [31], much of the efforts in quantum information and quantum optics have been towards trying to find novel ways to generate, characterize, and utilize this resource.

Entanglement is related to strong correlations between different parties. These correlations will be made explicit with polarization entanglement in Sec. 1.5.1. For now, we abstract away the physical degree of freedom and describe the correlations with a density operator $\hat{\rho}$ in a Hilbert space $\mathcal{H}$. Let's start with the correlations between two parties, labelled as A and B. The joint Hilbert space of two subsystems, with Hilbert spaces $\mathcal{H}_\mathcal{A}$ and $\mathcal{H}_\mathcal{B}$, is represented with a tensor product, $\mathcal{H} = \mathcal{H}_A \otimes \mathcal{H}_B$. For a bipartite system, with $\rho^A \in \mathcal{H}_A$, $\rho^B \in \mathcal{H}_B$, a state is called separable if it can be written as a convex sum with probability p_i [111],

$$\sum_i p_i \rho_i^A \otimes \rho_i^B. \tag{1.16}$$

Formally, a state is entangled if it is not separable[1]. The definition distinguishes between three scenarios: completely uncorrelated, separable, and entangled states. Separable states

[1]While it's usually bad practice to define something by what it isn't, here, this seems to be fine.

are classically correlated states that can be produced using only local operations and classical communication (LOCC) [112]. Inseparable or entangled states cannot be produced locally and cannot be written as a convex sum of product states as in Eq. 1.16.

For systems involving multiple parties, describing entanglement becomes notoriously tricky. For example, in a three qubit state, the qubits can be fully separable, have bipartite entanglement between any two qubits, or exhibit genuine tripartite entanglement between all three qubits. The work in this thesis concerns itself with bipartite entanglement that is potentially high-dimensional. In such a case, one tool of great value is the Schmidt decomposition. The Schmidt decomposition says that if we have a pure state $|\psi\rangle$ for a composite system AB, then there exists an orthonormal basis of states $|u_k\rangle$ for system A and $|v_k\rangle$ for system B such that,

$$|\psi\rangle = \sum_k^N \lambda_k |u_k\rangle |v_k\rangle , \tag{1.17}$$

where λ_k are non-negative real numbers satisfying $\sum_k \lambda_k^2 = 1$. The number N of non-negative eigenvalues λ_k is the Schmidt rank of the state, and it is preserved under unitary operations [111].

One way to characterize entanglement is by looking at one subsystem when the other is ignored. We keep one system and trace the other one out using the partial trace. If we calculate the purity of the partial trace, P, of the Schmidt decomposition, we obtain,

$$\begin{aligned} P = Tr\left[Tr_A\left(|\psi\rangle\langle\psi|\right)^2\right] &= Tr\left[Tr_A\left(\sum_{j,k}\lambda_j\lambda_k |u_j\rangle\langle u_k| |v_j\rangle\langle u_k|\right)^2\right] \\ &= Tr\left[\left(\sum_k \lambda_k^2 |u_k\rangle\langle u_k|\right)^2\right] = \sum_k \lambda_k^4. \end{aligned} \tag{1.18}$$

We find that when the state is factorizable, or separable, then $N = 1, \lambda_k = 1$ and the purity of the partial trace is 1, whereas if $N > 1$, then the purity of the partial trace will be less than one. For systems with dimensions greater than or equal to two, a useful quantity to consider is the inverse of P,

$$K = \frac{1}{P} = \frac{1}{\sum_k^N \lambda_k^4}, \tag{1.19}$$

as this will be "roughly speaking" related to the number of orthonormal modes in the system; if $N = 1$ then $K = 1$, and if $N > 1$ then $K > 1$. Since $\lambda_k^2 = p(k)$ is the

probability of obtaining each mode, then, $\sum \lambda_k^2 \lambda_k^2 = \sum_k p(k) \lambda_k^2$ is the probability of mode k being occupied, average over k. If there are more modes this number will necessarily be lower, and consequently, the inverse will be larger. For example, suppose each mode had the same probability, then $\lambda_k^2 = 1/N$. In this case, the purity of the partial trace would be $\sum \lambda_k^2 \lambda_k^2 = 1/N$, and as a result, the inverse would be exactly the number of modes contributing to the entangled state. This quantity will be especially useful when working with continuous-variable systems such as energy and time.

1.5.1 Polarization entanglement

Conceptually, the simplest forms of entanglement produced with light are the polarization-entangled Bell states.

$$\left|\Phi^{\pm}\right\rangle = \frac{1}{\sqrt{2}} \left(|HH\rangle \pm |VV\rangle\right), \quad \left|\Psi^{\pm}\right\rangle = \frac{1}{\sqrt{2}} \left(|HV\rangle \pm |VH\rangle\right). \tag{1.20}$$

These are superpositions of two polarization states. For example, in the $|\Phi^+\rangle$ state, both photons are horizontally polarized *and* both photons are vertically polarized. If we measure the first photon in the horizontal (vertical) polarization, the second photon will also be in the horizontal (vertical) polarization; the two photons are perfectly correlated in the horizontal/vertical basis. However, strong correlations in one basis aren't sufficient to signal the presence of entanglement. A mixed state, such as, $|HH\rangle\langle HH| + |VV\rangle\langle VV|$, will produce these same correlations. Instead, one feature of entanglement is the ability to produce strong correlations in different bases. Using the example of the $|\Phi^+\rangle$ state, it can be expressed in three different ways,

$$\left|\Phi^{+}\right\rangle = \frac{1}{\sqrt{2}} \left(|HH\rangle + |VV\rangle\right) = \frac{1}{\sqrt{2}} \left(|DD\rangle + |AA\rangle\right) = \frac{i}{\sqrt{2}} \left(|RL\rangle + |LR\rangle\right), \tag{1.21}$$

and we see that it exhibits strong correlations in the H/V basis, the D/A basis, and strong anti-correlations in the L/R basis.

Extensions of the Bell states to multiple photons are called GHZ states. For example, the maximally entangled three-qubit state is,

$$\left|GHZ^{\pm}\right\rangle = \frac{1}{\sqrt{2}} \left(|HHH\rangle \pm |VVV\rangle\right). \tag{1.22}$$

GHZ states can be used to herald Bell states [113], an important characteristic when working with probabilistic sources. Optical quantum computing architectures with GHZ states have also been proposed [114].

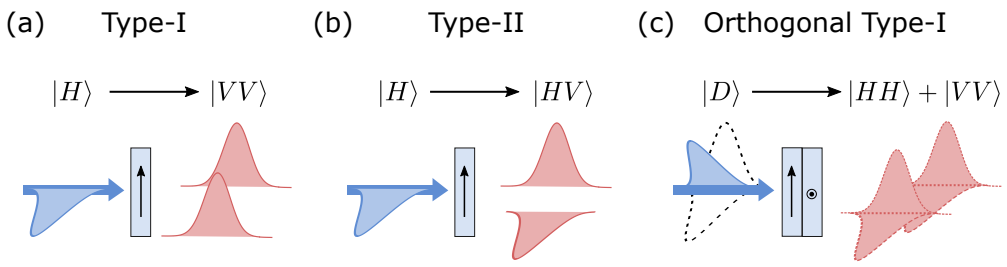

Figure 1.2: **Types of downconverison.** (a) In type-I downconversion both photons are produced in the opposite polarization of the pump. (b) In type-II downconverison, one photon will have the same polarization and the other photon will have the opposite polarization of the pump. For type-II downconverion, photons can always be separated via their polarization. For type-I downconversion, other degrees of freedom such as frequency or space must be used. When the pairs are nondegenerate, they can be separated with a dichroic mirror, whereas when they are degenerate, they must be produced in different spatial modes [117]. Polarization entanglement can be produced with a (b) type-II configuration or (c) with two orthogonally oriented crystals in a type-I configuration.

Sources of polarization-entangled photons

There exist a few standard ways to produce polarization entanglement, and historically, these were achieved later than in other degrees of freedom [115, 47]. The first source of polarization-entangled photons was constructed using a continuous wave (CW) pump and type-II parametric downconverison (see Fig. 1.2). Here, photons are created in two cones of orthogonal polarization [47]. At the intersections of the two cones, correlated photons are produced in the $|\Psi^+\rangle$ state. However, since only a small fraction of the photons produced is collected, the number of entangled pairs collected per input pump power, or brightness, is low. A second method to produce polarization entanglement uses two crystals with type-I parametric downconversion. There, the two crystals are oriented with their optic axis aligned perpendicularly. The downconversion can occur in either crystal: one crystal can produce two horizontally polarized photons, $|HH\rangle$, and the other two vertically polarized photons, $|VV\rangle$. By using a pump along the diagonal axis, the two possible downconversions can be made coherent and can't be distinguished. The state $|HH\rangle + e^{i\phi}|VV\rangle$ is created [see Fig. 1.2(c)]. The phase ϕ can be adjusted with another birefringent crystal. This type of photon source allows the collection of all pairs of a given colour that are entangled, thereby increasing the brightness compared to type-II [116].

The two examples above employed a continuous-wave laser to pump the downconversion. Parametric downconversion sources pumped by pulsed lasers are also particularly useful because the times of emission of the photons occur at well-defined intervals given by the repetition rate of the pulsed laser. In entanglement-based quantum key distribution, this allows both receivers to synchronize their detection events to a common clock pulse [118]. They are crucial in quantum teleportation [31], entanglement distillation [119], and the generation of multiphoton GHZ states [120, 121], where time-synchronized entangled photons must be available.

Following the development of CW sources, pulsed entangled photon sources were initially tried with type-II downconversion. However, the entangled states produced were shown to have low visibility quantum interference [122, 123]. Type-II downconversion has more stringent phase matching constraints, and for the larger bandwidths of a pulsed laser, this creates correlations between polarization and the frequencies of the photons. As a result, the photon pairs produced can be to some degree spectrally distinguishable, reducing the visibility of two-photon polarization interference. Inteferometric schemes were proposed to overcome this limitation [124]. Nevertheless, for pulsed sources, type-I configurations are preferable since the phase-matching restrictions for type-I downconversion are less restrictive. Highly entangled polarization states with a large flux can be achieved with a pulsed pump using two type-I crystals in orthogonal orientations [125, 126]. In this case, compensation crystals are required to make the downconversion in the first and second crystal indistinguishable [118].

Interferometric techniques also exist to produce polarization entangled photons, the most successful being the Sagnac interferometer as it provides a phase stable configuration without the need for active stabilization. There, the downconversion crystal is placed inside a Sagnac interferometer. Pump light is sent through both the clockwise and counterclockwise paths of the interferometer and downconverted pairs are produced in both directions and collected at the output of the interferometer. Sagnac sources work best with CW type-II downconversion [127] but have also been demonstrated with pulsed type-I [128] downconversion. They can achieve very high fidelity with the Bell states in Eq. 1.20 [129].

Methods to produce multipartite entanglement in polarization are particularly challenging. The first methods to produce GHZ states combined photons from different sources and required outcome post-selection, where only a subset of the measured outcomes are considered to compose the final state [120]. This was used to produce four- [121], eight- [130], and ten- [131] photon GHZ states. Such techniques can be used for linear optics quantum computing, but cannot be used to herald the presence of Bell states, as observing the GHZ state requires detecting the photons which simultaneously destroys it. The first direct generation of GHZ states to demonstrate heralded Bell states was performed using

cascaded downconversion [132], i.e. downconverting a downconverted photon.

1.5.2 Energy-time entanglement

Polarization entanglement is conceptually intuitive and easy to measure, but entanglement in polarization cannot be extended to higher dimensional qudits and it is difficult to scale to multiple particles. On the other hand, entanglement in the frequency and time degree of freedom of light can be potentially high-dimensional, and one particular form, energy-time entanglement is produced naturally in parametric downconversion. Since the measurement of energy-time entangled two-photon states is central to this thesis, we introduce it briefly here.

Energy-time entanglement was initially proposed by Franson via the cascaded decay of an atom [49], and was very quickly adapted to parametric downconversion [133, 134, 115]. In parametric downconversion, by energy conservation, the energies of the two photons must sum up to the energy of the pump, $\omega_p = \omega_1 + \omega_2$. Moreover, the process is spontaneous and therefore the photons are typically produced in a small time window, such that $t_2 - t_1 \approx 0$. The state is analogous to the original Einstein-Podoslky-Rosen (EPR) correlations introduced for position and momentum, where in this case, $x_2 - x_1 = 0$ and $p_1 + p_2 = 0$ [135].

One way to represent energy-time entanglement, to which we will refer often in this thesis, is with the following state,

$$|\psi\rangle = \int d\omega_1 d\omega_2 F(\omega_1, \omega_2) a_1^\dagger(\omega_1) a_2^\dagger(\omega_2) |0\rangle . \tag{1.23}$$

Here, instead of having a superposition of two polarization modes as in the case of the polarization entangled states in Eq. 1.20, the energy-time entangled state in Eq. 1.23 is a superposition of the continuous frequency creation operators, $a_1^\dagger(\omega_1)$ and $a_2^\dagger(\omega_2)$, acting on the vacuum and weighted by the distribution $F(\omega_1, \omega_2)$. The properties of the function $F(\omega_1, \omega_2)$, referred to as the joint spectral amplitude, will determine whether the state $|\psi\rangle$ is entangled or not. If the photons exhibit strong correlations in both frequency and time, as in Fig. 1.3, the spectral distribution $F(\omega_1, \omega_2)$ will not be factorizable into a product of states, $F(\omega_1, \omega_2) \neq F_1(\omega_1) F_2(\omega_2)$, and will be entangled. The joint spectral amplitude $F(\omega_1, \omega_2)$ is fundamental to this thesis, as most of the important spectral and temporal properties of the photons pairs can be derived from it. We explore these experimentally in subsequent chapters.

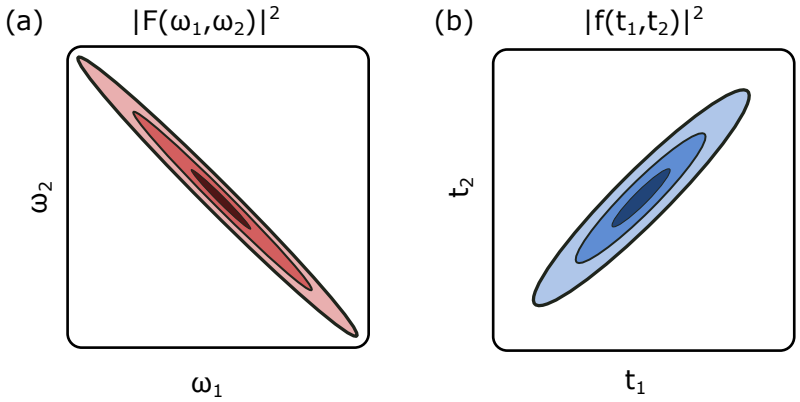

Figure 1.3: **An example energy-time entangled state.** The probability of measuring both photons (a) with frequency ω_1 and ω_2 and (b) at time t_1 and t_2. The strong anti-correlations between the frequencies of the two photons and the strong positive correlations between the time of arrival of the two photons is an indication of energy-time entanglement. Both the joint spectral amplitude function $F(\omega_1, \omega_2)$ and its analogue, the joint temporal amplitude function $f(t_1, t_2)$, in the example are not separable.

There exists an equivalent description using discrete variables which highlights the high dimensionality of the energy-time entangled state in Eq. 1.23. Using the Schmidt decomposition, we can write the joint-spectral amplitude as [136, 137, 138],

$$F(\omega_1, \omega_2) = \sum_k \lambda_k \varphi_k(\omega_1) \phi_k(\omega_2), \tag{1.24}$$

which is a sum of two orthonormal bases of spectral amplitude functions $\{\varphi_k(\omega_s)\}$ and $\{\phi_k(\omega_i)\}$, with weighting coefficients λ_k. The energy-time entangled state in Eq. 1.23 becomes,

$$\begin{aligned} |\psi\rangle &= \sum_k \lambda_k \int d\omega_1 \varphi_k(\omega_1) a_1^\dagger(\omega_1) \left|0\right\rangle_1 \int d\omega_2 \phi_k(\omega_2) a_2^\dagger(\omega_2) \left|0\right\rangle_2 \\ &= \sum_k \lambda_k \left|\varphi_k\right\rangle \left|\phi_k\right\rangle \end{aligned} \tag{1.25}$$

where $|\varphi_k\rangle = \int d\omega_1 \varphi_k(\omega_1) a_1^\dagger(\omega_1) \left|0\right\rangle_1$ and $|\phi_k\rangle = \int d\omega_2 \phi_k(\omega_2) a_2^\dagger(\omega_2) \left|0\right\rangle_2$ are the Schmidt modes of the two photons. We see that the photons appear only in pairs of Schmidt modes. The decomposition identifies exactly which modes are produced in pairs: if one photon is found in the state $|\varphi_k\rangle$, then the other must be in the state $|\phi_k\rangle$. Moreover,

although there are infinitely many modes k, it usually happens that only a few λ_k's are significant, in which case Eq. 1.25 tells us the effective dimensionality of the Hilbert space. The Schmidt modes of a model of downconversion are illustrated in Sec. 2.3.5.

The most common way of detecting energy-time entanglement is by projecting the continuous-variable entanglement into a two-valued projector [139] using two unbalanced interferometers as originally proposed by Franson [49]. This method is described in detail in Sec. 5.3. Using this method, high-visibility quantum interference and Bell inequality violations can be observed [50], and it is robust over long distance fibre propagation [95]. While it has been extended to qutrits [140], it remains an indirect way of detecting the potentially higher dimensional entanglement present in Eq. 1.23. The challenge is in directly detecting energy-time entanglement from the correlations in Fig. 1.3. Depending on the photonic system being explored, measuring either the frequency distribution in Fig. 1.3(a) or the temporal distribution in Fig. 1.3(b) will be difficult. We address this challenge with SPDC photons in Chap. 4.

While the work in this thesis focuses on energy-time entanglement as presented in Eq. 1.23, other forms of entanglement are possible with the time and frequency degrees of freedom. Time-bin entanglement [94, 141], which involves superpositions of photon pairs at early and late times, has been demonstrated using pulsed sources and unbalanced interferometers. These have also been found to be robust to decoherence in fibre [142, 64] and have been used for long-distance teleportation at telecommunication wavelengths [143]. High dimensional frequency-bin entanglement has been realized by downconverting frequency combs in bulk [144] and using four-wave mixing in a chip-based ring resonator [145].

1.6 Signatures of classical and quantum states of light

In an experimental setting, it is not possible to create a perfectly pure state due to imperfections in the physical system and decoherence with the environment. If the amount of decoherence with the environment becomes too large, quantum correlations and entanglement can be lost. As a result, if we wish to take advantage of the quantum properties of light, it is important to find ways in which we can distinguish quantum and classical light or certify the presence of entanglement. The methods presented below are all used in subsequent chapters to distinguish classical and quantum states of light.

1.6.1 Second-order coherence function

The first question to ask[2] when assessing the quantum properties of a light source is "what's the second-order coherence function at zero time delay?" or, for short, "what's the g2?" Quantum and classical states of light have different statistical properties, and if we measure these statistics, we obtain information on the types of states we've produced in the lab. In fact, the first conclusive demonstration that single photons existed was done using the $g^{(2)}(0)$ [146]. So what is it? The *second order temporal coherence function* for a classical field is defined as follows,

$$g^{(2)}(\tau) = \frac{\langle I(t)I(t+\tau)\rangle}{\langle I(t)\rangle^2} \tag{1.26}$$

$$= \frac{\langle E^*(t)E^*(t+\tau)E(t+\tau)E(t)\rangle}{\langle E^*(t)E(t)\rangle^2}. \tag{1.27}$$

Equation 1.27 measures the average correlation between the intensity of a field at two-different times. The second order coherence function has a special restriction for classical light which doesn't hold for quantum states of light. Two measurements of the intensity at times t_1 and t_2 must satisfy, $[I(t_1) - I(t_2)]^2 \geq 0$, and this implies by Cauchy's inequality that the numerator in Eq. 1.27 is always greater than or equal to the denominator,

$$\langle I(t)\rangle^2 \leq \left\langle I(t)^2\right\rangle. \tag{1.28}$$

Therefore, the degree of second order coherence for zero time delay must be greater than or equal to one,

$$g^{(2)}(0) \geq 1. \tag{1.29}$$

With quantum states of light, the second-order coherence function takes the same form as in Eq. 1.27, but with electric field operators from Eq. 1.3,

$$g^{(2)}(\tau) = \frac{\left\langle \hat{E}^{(-)}(t)\hat{E}^{(-)}(t+\tau)\hat{E}^{(+)}(t+\tau)\hat{E}^{(+)}(t)\right\rangle}{\left\langle \hat{E}^{(-)}(t)\hat{E}^{(+)}(t)\right\rangle^2}. \tag{1.30}$$

[2] Assuming you're an experimentalist working in quantum optics

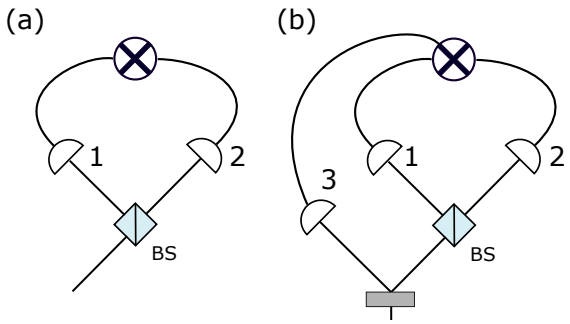

Figure 1.4: **Measuring the second-order coherence.** Two different measurements of the second-order coherence function. (a) The (unheralded) $g^{(2)}(0)$ is obtained by measuring the ratio of the probability of getting coincidences between detectors 1 and 2, and the probability of getting a single click at each detector. (b) The heralded $g^{(2)}(0)$ is obtained by only collecting data when detector 3 also fires. It is obtained by taking the ratio of the probability of getting threefold coincidences between detectors 1,2, and 3 to two-fold coincidences between detectors 1 and 2, and, 2 and 3.

The normal ordering, $E^{(+)}$ to the right of $E^{(-)}$, ensures that light is not created out of the vacuum. With quantum states of light there is no restriction as in Eq. 1.29 and all we can say is $g^{(2)} \geq 0$. As a result, if we find a state that has a $g^{(2)}(0) < 1$, then this is a signature of a non-classical state.

For example, the second-order coherence of a single-mode state, obtained by inserting the field operators Eq. 1.3 into Eq. 1.27, is found to be [87],

$$g^{(2)}(0) = \frac{\left\langle a_k^\dagger a_k^\dagger a_k a_k \right\rangle}{\left\langle a_k^\dagger a_k \right\rangle^2}. \tag{1.31}$$

A genuine single photon, which is a single excitation of an electromagnetic field mode, represented by the Fock state $|1\rangle_k = a_k^\dagger |0\rangle$ will have a $g^{(2)}(0) = 0$, as the numerator in Eq. 1.31 destroys two excitation of the field. Other quantum states will exhibit different statistics. Coherent states $|\alpha\rangle$, which are eigenstates of the lowering operator, $\hat{a}_k |\alpha\rangle_k = \alpha_k |\alpha\rangle_k$, have a $g^{(2)}(0) = 1$ and thermal states have a $g^{(2)}(0) = 2$. I refer the reader to Refs. [85, 87] for an in-depth overview of the statistics of quantum states of light.

How can we measure these statistics? Eq. 1.31 can give us some insight. We need to measure the probability that there exists two excitations, or photons, at the same

instant in time, normalized by the probability of finding one excitation at that time. This can be measured using a non-polarizing beam splitter and two detectors. This is known as a Hanbury-Brown Twiss interferometer, shown in Fig. 1.4. Interestingly, this type of interferometer was initially invented to estimate the diameter of a star [147]. In Fig. 1.4(a), the second order coherence is given by the probability of measuring a coincidence between detectors 1 and 2, divided by the probability of measuring single clicks at each detector. The probability is given by the number of measured counts N divided by the number of trials performed. For pulsed lasers, the number of trials is given by the repetition rate of the laser, R, and we obtain,

$$g^{(2)}(0) = \frac{P(1\&2)}{P(1)P(2)} = \frac{N_{12}R}{N_1 N_2}. \tag{1.32}$$

Many experiments are performed in a heralded manner, i.e., a photon is only measured heralded on the presence of the other. The number of trials is then given by the number of measured heralds. In this scenario, as in Fig. 1.4(b), the heralded $g^{(2)}(0)$ is,

$$g^{(2)}(0) = \frac{P(1\&2\&3)}{P(1\&3)P(2\&3)} = \frac{N_{123}N_3}{N_{13}N_{23}}. \tag{1.33}$$

Experimentally, the bottom line is that a single photon cannot be separated into two parts by a beam splitter. As a result, for a single photon state, detectors 1 and 2 will never fire at the same time resulting in a $g^{(2)}(0) = 0$.

1.6.2 Inseparability criterion for continuous variable states

How can we certify the presence of entanglement? In discrete variable systems, if the quantum state is known, the positive partial transpose (PPT) criteria provides a sufficient condition for detecting entanglement [148] and a necessary and sufficient condition for quantum states with dimensions, 2x2 and 2x3. The PPT requires the density matrix of the state which, in an experimental context, must be first reconstructed using quantum state tomography. Since the number of measurement settings required to completely reconstruct a state increases exponentially with the number of qubits, this becomes challenging for multipartite states. Entanglement witnesses have been shown to be exponentially more efficient at detecting multipartite entanglement. For example, there exists an entanglement witness that can detect genuine multipartite entanglement of GHZ states with only two measurement settings, independently of the number of qubits [112].

With continuous variable states, Duan *et al.* found that, for all separable states, there is a lower bound to the total variance of a pair of EPR type operators [149]. These types of

inequalities based on variances can be generalized for multipartite entanglement [150, 151]. Following these ideas, an uncertainty relation is derived in this section which places a bound on the product of correlations in the frequency and in the time of arrival of photon pairs. This will be used to detect energy-time entanglement. Note that there also exists entanglement witnesses involving only two measurements for certifying continuous-variable entanglement [152].

Time-bandwidth product for classical pulses

For a classical pulse of light $E(t)$, it is well known that the product of the spectral bandwidth and the duration of the pulse, referred to as the time-bandwidth product, cannot be less than a certain value. There is a limit to how sharp a distribution in time and frequency can simultaneously be. One can, for example, specify an arbitrary pulse shape in frequency or an arbitrary shape in time, but not in both. To characterize the time-bandwidth product, we'll define the width of the pulse in frequency and in time using the standard deviation or the root mean square,

$$\Delta(\omega) = \sqrt{\left\langle (\omega - \langle\omega\rangle)^2 \right\rangle} = \sqrt{\int d\omega \, (\omega - \omega_0)^2 \, |E(\omega)|^2} \tag{1.34}$$

$$\Delta(t) = \sqrt{\left\langle (t - \langle t\rangle)^2 \right\rangle} = \sqrt{\int dt \, (t - t_0)^2 \, |E(t)|^2}, \tag{1.35}$$

where $\langle \cdots \rangle$ denotes the average over the electric field, $\omega_0 = \langle\omega\rangle$, and $t_0 = \langle t\rangle$. Using these definitions, we can calculate the time-bandwidth product for a Gaussian pulse with no spectral phase, $E(\omega) = \exp\left[-(\omega - \omega_0)^2/(4\sigma_\omega^2)\right]$. In this case, the standard deviation in frequency is $\Delta(\omega) = \sigma_\omega$ and the corresponding standard deviation in time is $\Delta(t) = 1/(2\sigma_\omega)$. As a result, the time-bandwidth product is $\Delta(\omega)\Delta(t) = 1/2$. Had we used another definition, the time-bandwidth product would be different. For example, another common way to define the width of a pulse is to use the full width at half maximum (FWHM), which is related to the standard deviation via,

$$\mathrm{FWHM}(x) = 2\sqrt{2\ln(2)}\Delta(x). \tag{1.36}$$

Using the FWHM for the same Gaussian pulse, we'd find a time-bandwidth product of $\mathrm{FWHM}(\omega) \times \mathrm{FWHM}(t) = 4\ln(2)$.

Different pulse shapes can have a different time-bandwidth product, however, it's possible to place a lower bound on the time-bandwidth product independently of the pulse

shape. This interdependence between time and frequency is often referred to as an uncertainty relation or time-bandwidth inequality,

$$\Delta(\omega)\Delta(t) \geq 1/2. \tag{1.37}$$

Similar to other uncertainty relations, it places a bound on the product of the variance of two conjugate variables. Importantly, it is derived simply from the fact that the frequency and temporal representations of the pulse are Fourier transforms of each other [153]. It is thus an inherent property of all conjugate variables in wavelike systems. A pulse that satisfies the equality in Eq. 1.37, is referred to as "transform-limited", since its standard deviation in frequency and in time is limited by the Fourier transform.

The time-bandwidth inequality can also be cast into an uncertainty relation based on sums of uncertainties rather than products [149]. Since this will become very useful to derive an inseparability criterion for continuous variable entanglement, I mention it here. If we introduce a constant a with units $[t]^2$, then we can obtain the inequality,

$$\begin{aligned} a\Delta(\omega)^2 + \frac{1}{a}\Delta(t)^2 &\geq a\Delta(\omega)^2 + \frac{1}{a}\left(\frac{1}{4\Delta(\omega)^2}\right) \\ &\geq 1, \end{aligned} \tag{1.38}$$

where the second line is obtained by minimizing the RHS with respect to a, achieved by setting $a = 1/(2\Delta\omega^2)$. A similar uncertainty relation can be derived in an analogous way for the Heisenberg uncertainty relation. For example, using the position $\hat{x}$ and momentum $\hat{p}$ operators, and a constant a which has units of [length]^2, we find,

$$a\Delta(\hat{x})^2 + \frac{1}{a}\Delta(\hat{p})^2 \geq |[\hat{x}, \hat{p}]|. \tag{1.39}$$

Time-bandwidth product of a mixed state

In the previous section, we found a time-bandwidth inequality, Eq. 1.38, that holds for classical coherent pulses. As mentioned already, in quantum optics, we work with pure and mixed states. For pure states, the spectral and temporal amplitude functions, $F(\omega)$ in Eq. 1.5 and $f(t)$ in Eq. 1.8 are related by the Fourier transform. We therefore expect them to also obey the same time-bandwidth product, $\Delta(\hat{n}_\omega)\Delta(\hat{n}_t) \geq 1/2$. As will be shown, the time-bandwidth product also holds for mixed states.

The variance in frequency $\Delta(\omega)^2_\rho$ with respect to a mixed state ρ is,

$$\begin{aligned}
\Delta(\omega)^2_\rho &= \left\langle \omega^2 \right\rangle_\rho - \langle\omega\rangle^2_\rho \\
&= \sum_i p_i \left\langle \omega^2 \right\rangle_i - \left(\sum_i p_i \langle\omega\rangle_i \right)^2 \\
&= \sum_i p_i \left(\left\langle \omega^2 \right\rangle_i - \langle\omega\rangle^2_i \right) + \sum_i p_i \langle\omega\rangle^2_i - \left(\sum_i p_i \langle\omega\rangle_i \right)^2 \\
&= \sum_i p_i \Delta\left(\omega\right)^2_i + \sum_i p_i \langle\omega\rangle^2_i - \left(\sum_i p_i \langle\omega\rangle_i \right)^2 ,
\end{aligned} \tag{1.40}$$

where $\Delta(\omega)^2_i$ is the variance with respect to the pure state $|\psi_i\rangle$. Using the Cauchy-Schwarz inequality, $\langle X^2\rangle \langle Y^2\rangle \geq |\langle XY\rangle|^2$, letting $X = \langle\omega_i\rangle$ and $Y = 1$, we find $(\sum_i p_i \times 1^2) \sum_i p_i \langle\omega\rangle^2_i \geq (\sum_i p_i 1 \times \langle\omega\rangle_i)^2$. The last two terms in the last line of Eq. 1.40 are thus bounded from below by zero, and consequently,

$$\Delta(\omega)^2_\rho \geq \sum_i p_i \ \Delta\left(\omega\right)^2_i . \tag{1.41}$$

The variance of the state ρ has to be at least as large as the convex combination of the variances of the pure states $|\psi_i\rangle$. We can find a similar expression for the variance in time,

$$\Delta(t)^2_\rho = \left\langle t^2 \right\rangle_\rho - \langle t\rangle^2_\rho \geq \sum_i p_i \ \Delta\left(t\right)^2_i . \tag{1.42}$$

Using the results of Eq. 1.41 and Eq. 1.42, we find,

$$\begin{aligned}
a\Delta(\omega)^2_\rho + \frac{1}{a}\Delta(t)^2_\rho &\geq a \sum_i p_i \ \Delta\left(\omega\right)^2_i + \frac{1}{a} \sum_i p_i \ \Delta\left(t\right)^2_i \\
&= \sum_i p_i \ \left(a\Delta\left(\omega\right)^2_i + \frac{1}{a}\Delta\left(t\right)^2_i \right),
\end{aligned} \tag{1.43}$$

and by the result of Eq. 1.38, each term in the sum of the second line must be greater than or equal to 1, and therefore,

$$a\Delta(\omega)^2_\rho + \frac{1}{a}\Delta(t)^2_\rho \geq 1. \tag{1.44}$$

Thus, the result of Eq. 1.38 also holds for mixed states. It relies only on the fact that each pure state is coherent, and since mixed states are convex combination of pure states, we expect the total variance to be at least as large.

Time-bandwidth inequality for a separable state

We'll consider a general separable state, which is a convex combination of density matrices ρ_{i1} and ρ_{i2} on modes 1 and 2, respectively,

$$\rho = \sum_i p_i \rho_{i_1} \otimes \rho_{i2}, \tag{1.45}$$

where we assume ρ_{i1} and ρ_{i2} to be normalized states, $p_i \geq 0$ and $\sum_i p_i = 1$. We can calculate the variance of the sum of the frequencies for the state ρ,

$$\begin{aligned}
\Delta(\omega_1+\omega_2)_\rho^2 &= \left\langle (\omega_1+\omega_2)^2 \right\rangle_\rho - \left\langle (\omega_1+\omega_2) \right\rangle_\rho^2 \\
&= \sum_i p_i \left\langle (\omega_1+\omega_2)^2 \right\rangle_i - \left(\sum_i p_i \left\langle \omega_1+\omega_2 \right\rangle_i \right)^2 \\
&= \sum_i p_i \left(\left\langle \omega_1^2 \right\rangle_i + \left\langle \omega_2^2 \right\rangle_i + 2 \left\langle \omega_1 \right\rangle_i \left\langle \omega_2 \right\rangle_i \right) - \left(\sum_i p_i \left\langle \omega_1+\omega_2 \right\rangle_i \right)^2 \\
&= \sum_i p_i \ \left(\Delta(\omega_1)_i^2 + \Delta(\omega_2)_i^2 \right) \\
&+ \sum_i p_i \left\langle \omega_1+\omega_2 \right\rangle_i^2 - \left(\sum_i p_i \left\langle \omega_1+\omega_2 \right\rangle_i \right)^2 ,
\end{aligned} \tag{1.46}$$

where here, $\langle \cdots \rangle_i$ denotes the average of the product of density operators $\rho_{i1} \otimes \rho_{i2}$, and we used the fact that the state was separable to write $\langle \omega_1 \omega_2 \rangle_i = \langle \omega_1 \rangle_i \langle \omega_2 \rangle_i$. Now, as before, by the Cauchy-Schwarz inequality, the last line is bounded from below by zero, and

$$\Delta(\omega_1+\omega_2)_\rho^2 \geq \sum_i p_i \ \left(\Delta(\omega_1)_i^2 + \Delta(\omega_2)_i^2 \right), \tag{1.47}$$

and likewise,

$$\Delta(t_1+t_2)_\rho^2 \geq \sum_i p_i \ \left(\Delta(t_1)_i^2 + \Delta(t_2)_i^2 \right). \tag{1.48}$$

Using Eq. 1.47 and Eq. 1.48, we can calculate the total variance,

$$\begin{aligned}
a\Delta(\omega_1+\omega_2)_\rho^2 + \frac{1}{a}\Delta(t_2-t_1)_\rho^2 &\geq a \sum_i p_i \ \left(\Delta(\omega_1)_i^2 + \Delta(\omega_2)_i^2 \right) + \frac{1}{a} \sum_i p_i \ \left(\Delta(t_1)_i^2 + \Delta(t_2)_i^2 \right) \\
&= \sum_i p_i \ \left(a\Delta(\omega_1)_i^2 + \frac{1}{a}\Delta(t_1)_i^2 + a\Delta(\omega_2)_i^2 + \frac{1}{a}\Delta(t_2)_i^2 \right) \\
&\geq 2
\end{aligned} \tag{1.49}$$

The inequality holds for any value of a and places a bound on the total variance of a separable state. It is more practical to turn this inequality into a product inequality, which removes the arbitrary constant a. To do so, we find the value of a that minimizes the left-hand side. We do this in the usual way by setting the derivative with respect to a to 0 and solving for a, for which we find $a = \Delta(t_2 - t_1)_\rho / \Delta(\omega_1 + \omega_2)_\rho$. By substituting this value of a into Eq. 1.49, we find,

$$\frac{\Delta(t_2 - t_1)_\rho}{\Delta(\omega_1 + \omega_2)_\rho} \Delta(\omega_1 + \omega_2)_\rho^2 + \frac{\Delta(\omega_1 + \omega_2)_\rho}{\Delta(t_2 - t_1)_\rho} \Delta(t_2 - t_1)_\rho^2 \geq 2 \tag{1.50}$$

which simplifies to

$$\Delta(\omega_1 + \omega_2)_\rho \; \Delta(t_2 - t_1)_\rho \geq 1. \tag{1.51}$$

This is the product form of Eq. 1.49. It provides a sufficient condition for the inseparability of a continuous variable two-mode state; a state which violates the inequality is not separable. For all Gaussian continuous variable states, Eq. 1.51 provides a necessary and sufficient inseparability criterion [149].

1.6.3 Visibility in stochastic and quantum descriptions of light

Nonclassical interference between photon pairs in parametric downconversion is often used to witness the presence of entanglement. This occurs when the visibility of interference in the coincidences between two detectors is above some threshold that is not possible to achieve with a classical description of light. While the interference visibility required to claim nonclassicality has been largely discussed [154, 155, 50], there exists an inequality which bounds the visibility of interference of experiments with classical fields [156]. Furthermore, and importantly, if it is known that the light is coincident within a small time interval, then this inequality limits the interference visibility of classical light to 50%. Quantum light can violate the inequality allowing for high-visibility interference. Since a great deal of struggle occurs in experimental quantum optics to overcome this 50% bound, its origins are discussed in this section.

Consider a classical electric field that passes through an unbalanced interferometer. The field that travels through the short arm is not delayed whereas the field that travels through the long arm acquires a time delay τ and a phase ϕ. The total field after going through the interferometer is,

$$E_T(t) = E(t) + E(t - \tau)e^{i\phi}, \tag{1.52}$$

where $E(t)$ and $E(t-\tau)$ describe the fields that have taken the short or long path in the interferometer, respectively. The instantaneous intensity for the total field is,

$$\begin{aligned} I_T(t) &= E_T(t)E_T(t)^* \\ &= I(t) + I(t-\tau) + E(t)^*E(t-\tau)e^{i\phi} + E(t)E(t-\tau)^*e^{-i\phi}, \end{aligned} \tag{1.53}$$

where $I(t) = E(t)E(t)^*$. In a stochastic description of light, $E(t)$ and $E(t-\tau)$ are random variables described by a classical distribution. The output of the detector is averaged over the different statistical realizations of the field, which is approximated as a time average over the field,

$$\langle I_T(t)\rangle = \langle I(t)\rangle + \langle I(t-\tau)\rangle + \left\langle E(t)^*E(t-\tau)e^{i\phi} + c.c.\right\rangle, \tag{1.54}$$

where the brackets $\langle\cdots\rangle$ denote an average over a long time interval. As the phase ϕ is changed, interference between the fields from the two paths can occur and the measured intensity will vary with a fringe visibility given by,

$$V_{\text{singles}} = \frac{2\text{Re}[\langle \text{E(t)E(t}-\tau)^*\rangle]}{\langle I(t)\rangle + \langle I(t-\tau)\rangle}. \tag{1.55}$$

The visibility is proportional to the overlap, $\langle E(t)E(t-\tau)^*\rangle$, of the field at different times. In order to observe a difference between a classical and quantum descriptions of light, we measure the intensity correlations between the output of two unbalanced interferometers. This can be observed with the coincidence rate, which will be given by,

$$\begin{aligned} C(\phi_1,\phi_2) =& \langle I_{T1}(t)I_{T2}(t)\rangle \\ =& \Big\langle \left[I_1(t) + I_1(t-\tau) + E_1(t)^*E_1(t-\tau)e^{i\phi_1} + E_1(t)E_1(t-\tau)^*e^{-i\phi_1}\right] \\ &\times \left[I_2(t) + I_2(t-\tau) + E_2(t)^*E_2(t-\tau)e^{i\phi_2} + E_2(t)E_2(t-\tau)^*e^{-i\phi_2}\right]\Big\rangle. \end{aligned} \tag{1.56}$$

Equation 1.56 has 16 terms. If the experiment is performed to measure the average coincidence rate as a function of the phase sum $\phi_+ = \phi_1 + \phi_2$, any terms which oscillate as ϕ_1, ϕ_2, or $\phi_1 - \phi_2$ will be averaged out. As a result, any interference in the coincidences that could arise from interference in the singles rates will be removed. The resulting phase averaged coincidence rate is given by,

$$\begin{aligned} \bar{C}(\phi_+) =& \int d\phi_1 d\phi_2 C(\phi_1,\phi_2)\delta(\phi_+ - \phi_1 - \phi_2) \\ =& \langle I_1(t)I_2(t)\rangle + \langle I_1(t-\tau)I_2(t-\tau)\rangle + \langle I_1(t)I_2(t-\tau)\rangle + \langle I_1(t-\tau)I_2(t)\rangle \\ &+ \langle E_1(t)^*E_1(t-\tau)E_2(t)^*E_2(t-\tau)\rangle\, e^{i\phi_+} + c.c. \end{aligned} \tag{1.57}$$

The visibility of the interference in the coincidences will be given by,

$$V_{cc} = \frac{\bar{C}_{\max} - \bar{C}_{\min}}{\bar{C}_{\max} + \bar{C}_{\min}} \tag{1.58}$$

$$= \frac{2\left\langle \mathrm{Re}[E_1(t)^* E_1(t-\tau) E_2(t)^* E_2(t-\tau)] \right\rangle}{\langle I_1(t) I_2(t)\rangle + \langle I_1(t-\tau) I_2(t-\tau)\rangle + \langle I_1(t) I_2(t-\tau)\rangle + \langle I_1(t-\tau) I_2(t)\rangle}. \tag{1.59}$$

The numerator in Eq. 1.59 can be bounded, first by its absolute value, $\mathrm{Re}[\cdot] \leq |\cdot|$, then, by using a generalization of the Cauchy Schwarz inequality, $|ab| \leq \frac{1}{2}(|a|^2 + |b|^2)$. If we set $a = E_1(t)^* E_2(t-\tau)$ and $b = E_1(t-\tau) E_2(t)^*$, we obtain the inequality [156],

$$\left\langle |E_1(t)^* E_1(t-\tau) E_2(t)^* E_2(t-\tau)| \right\rangle \leq \frac{1}{2}\left\langle I_1(t) I_2(t-\tau)\right\rangle + \frac{1}{2}\left\langle I_1(t-\tau) I_2(t)\right\rangle. \tag{1.60}$$

The interference modulation on the left-hand side must be less than or equal to the right-hand side, which is the average intensity correlation between a field on one side and the time-delayed field on the other. The inequality in Eq. 1.60 must hold for all classical fields, and can therefore be used to limit the amount of modulation that can be observed between classical fields. Inserting Eq. 1.60 into Eq. 1.59, we obtain a bound which limits the interference visibility in the coincident measurement,

$$V_{cc} \leq \left(1 + \frac{\langle I_1(t) I_2(t)\rangle + \langle I_1(t-\tau) I_2(t-\tau)\rangle}{\langle I_1(t) I_2(t-\tau)\rangle + \langle I_1(t-\tau) I_2(t)\rangle}\right)^{-1}. \tag{1.61}$$

In order to observe interference in the coincidences in Eq. 1.61, the correlations, $\langle I_1(t) I_2(t-\tau)\rangle$, between $I_1(t)$ and the time-delayed $I_2(t-\tau)$ (or vice versa) must be larger than the correlations, $\langle I_1(t) I_2(t)\rangle$, between $I_1(t)$ and $I_2(t)$.

It's possible to simplify Eq. 1.61 further with a few assumptions. For sufficiently long time intervals, a constant offset can't affect the intensity cross-correlation, and

$$\langle I_1(t) I_2(t)\rangle = \langle I_1(t-\tau) I_2(t-\tau)\rangle. \tag{1.62}$$

Furthermore, if we assume the two beams are symmetric, we can set,

$$\langle I_1(t) I_2(t-\tau)\rangle = \langle I_1(t-\tau) I_2(t)\rangle. \tag{1.63}$$

In downconversion, the photons pairs produced are coincident within a small time window, which can be made smaller than τ. These timing correlations will be measured explicitly in Chap. 4. As a result, we are much more likely to measure two coincident detector clicks

at the same time than two coincident detector clicks separated by a time interval τ, and therefore,

$$\langle I_1(t) I_2(t-\tau) \rangle \leq \langle I_1(t) I_2(t) \rangle \,. \tag{1.64}$$

A valid classical model of the experiment should then also exhibit tight timing correlations and be consistent with Eq. 1.64. Inserting the assumptions of Eq. 1.62, Eq. 1.63, and the requirement on the timing correlations from Eq. 1.64 into Eq. 1.61, we obtain,

$$V_{cc} \leq \left(1 + \frac{\langle I_1(t) I_2(t) \rangle}{\langle I_1(t) I_2(t-\tau) \rangle}\right)^{-1} \leq (1+1)^{-1} = \frac{1}{2}. \tag{1.65}$$

We find the interference visibility cannot be greater than 50%. In other words, a classical stochastic model of light cannot exhibit tight timing correlations satisfying the inequality of Eq. 1.64, and have interference visibilities which are greater than 50%. As will be shown in Sec. 5.3, and as one by now expects, this is not the case for quantum models.

Chapter 2

Ultrafast nonlinear optics

2.1 Chapter Overview

In this chapter I introduce, both from a classical and quantum perspective, one of the primary tools used in this thesis to produce and measure photons: three-wave mixing. I develop the classical model and intuition in Sec. 2.2, by first discussing how a strong laser field changes the polarization of a material and how the polarization response modifies the original field. This leads to the nonlinear process of sum-frequency generation (SFG) in Sec. 2.2.3 which we use in optical gating. The "classical" intuition developed for sum-frequency generation carries over naturally to single photons as they also support the same electromagnetic modes. The classical picture is followed by the quantum picture in Sec. 2.3, where I introduce the three-wave mixing Hamiltonian, discuss spontaneous parametric downconversion starting in Sec. 2.3.3, and quantum sum-frequency generation in Sec. 2.3.8.

2.2 Classical nonlinear optics

The goal of this section is to arrive at an equation that describes the propagation of electromagnetic fields in a material with a nonlinear response. In particular, I want to arrive at a differential equation that captures the important behaviour and evolution of the frequency modes involved in sum-frequency generation. This will be useful for understanding the optical techniques employed in the experiments presented in Chap. 4, Chap. 5, and Chap. 6.

2.2.1 The linear and nonlinear polarization: how light changes matter

In general, to describe the interactions between the electric field E and magnetic field H inside a medium, we must consider the charge density ρ, current density J, polarization density P and magnetic density M of the medium as well as the electric and magnetic flux densities D and B. These considerations lead to Maxwell's equations in matter,

$$\begin{aligned} \nabla \cdot D &= \rho & \nabla \times E &= \frac{-\partial B}{\partial t} \\ \nabla \cdot B &= 0 & \nabla \times H &= \frac{\partial D}{\partial t} + J. \end{aligned} \tag{2.1}$$

For our purposes, and following the standard treatment in nonlinear optics, we are interested in solutions to these equations in a dielectric material where there are no free charges, $\rho = 0$, no free currents $J = 0$, and the material is non-magnetic, $M = 0$, such that the magnetic field and magnetic flux density are proportional, $B = \mu_0 H$, where μ_0 is the vacuum permeability. The material response to the electric field E *is* taken into account by the polarization P. The electric field causes the displacement of bound charges in the dielectric which creates a dipole moment. The induced dipole moment per unit volume is the polarization of the material,

$$P(\vec{r}, t) = P^{(1)}(\vec{r}, t) + P_{NL}(\vec{r}, t), \tag{2.2}$$

which can be both linear $P^{(1)}(\vec{r}, t)$ and nonlinear $P_{NL}(\vec{r}, t)$ in the electric field $E(\vec{r}, t)$. The contributions from the electric field and the polarization will modify the displacement field in Maxwell's Eq. 2.1,

$$\begin{aligned} D(\vec{r}, t) &= \epsilon_0 E(\vec{r}, t) + P(\vec{r}, t) \\ &= \epsilon_0 E(\vec{r}, t) + P^{(1)}(\vec{r}, t) + P_{NL}(\vec{r}, t), \end{aligned} \tag{2.3}$$

which accounts for the effects of both the field and the induced polarization. Both the linear and nonlinear polarization have important effects on the propagation of pulses in material and much of this thesis is about exploring ways in which these can be exploited for controlling quantum effects with light.

The optical susceptibility

We like to work with electric fields. As such, rather than keep the polarization term around, it's much more convenient to describe the effect of the polarization in terms of

how it *couples* to the electric field. A fairly general way to relate the polarization to the electric field is via a response function. For the linear polarization, this is given by,

$$P_i^{(1)}(\vec{r},t) = \epsilon_0 \int_0^\infty d\tau R_{ij}^{(1)}(\vec{r},\tau) E_j(\vec{r},t-\tau), \tag{2.4}$$

where the permittivity, ϵ_0, which has units Farads per metre, is the measure of capacitance that is encountered when forming an electric field in vacuum, and R_{ij} is the response function of the material. The Roman indices are for labelling different spatial directions which are summed over according to the Einstein summation notation. The integration limits ensure that the polarization can only depend on the electric field in the past. It's often more convenient to work in the frequency domain, in which case Eq. 2.4 becomes,

$$\begin{aligned} P_i^{(1)}(\vec{r},\omega) &= \frac{1}{\sqrt{2\pi}} \int dt P_i^{(1)}(\vec{r},t) e^{-i\omega t} \\ &= \frac{1}{\sqrt{2\pi}} \int dt\ \epsilon_0 \int_0^\infty d\tau R_{ij}^{(1)}(\vec{r},\tau) E_j(\vec{r},t-\tau) e^{-i\omega t} \\ &= \frac{1}{\sqrt{2\pi}} \int dt\ \epsilon_0 \int_0^\infty d\tau R_{ij}^{(1)}(\vec{r},\tau) \frac{1}{\sqrt{2\pi}} \int d\omega' E(\vec{r},\omega') e^{i\omega'(t-\tau)} e^{-i\omega t} \\ &= \epsilon_0 \left[\int_0^\infty d\tau R_{ij}^{(1)}(\vec{r},\tau) e^{-i\omega\tau} \right] E_j(\vec{r},\omega). \end{aligned} \tag{2.5}$$

The third line is obtained from the second by inserting the Fourier transform of $E_j(\vec{r},t)$ and the fourth line is obtained by performing the integral over t. The term in brackets,

$$\chi_{ij}^{(1)}(\omega) = \int_0^\infty d\tau R_{ij}^{(1)}(\vec{r},\tau) e^{-i\omega\tau}, \tag{2.6}$$

is the linear susceptibility that describes how the electric field drives the frequency component ω of the polarization, such that,

$$P_i^{(1)}(\vec{r},\omega) = \epsilon_0 \chi_{ij}^{(1)}(\omega) E_j(\vec{r},\omega). \tag{2.7}$$

Here, the linear susceptibility, $\chi_{ij}^{(1)}(\omega)$, is a frequency dependent tensor that determines the strength of the coupling for each frequency and spatial direction. For the nonlinear polarization, an analogous treatment yields higher order nonlinear susceptibilities. In particular, the second order nonlinear polarization is related to the electric field via the second-order nonlinear susceptibility by,

$$P_i^{(2)}(\vec{r},\omega_1+\omega_2) = \epsilon_0 \chi_{ijk}^{(2)}(\omega_1+\omega_2,\omega_1,\omega_2) E_j(\vec{r},\omega_1) E_k(\vec{r},\omega_2). \tag{2.8}$$

The polarization $P_i^{(2)}$ at frequency $\omega_1 + \omega_2$ depends on how both fields E_j at frequency ω_1 and E_k at frequency ω_2 combine in the crystal or medium.

A full treatment of nonlinear optics must consider both the fields and polarization as vectors and the susceptibilities as tensors. As a result, the expressions for the susceptibility in Eq. 2.8 can become rather complicated. Luckily, these can be greatly simplified by considering the symmetries of the susceptibility [11]. A quantum mechanical derivation of the susceptibility can justify these simplifications. Moreover, it relates the susceptibilities to the material dipole transition moments and atomic energy levels allowing predictions of the numerical values of the susceptibilities [11]. In this work, we will approximate the susceptibility as a scalar quantity. We will employ *Kleinman's* symmetry condition, which is valid when the material is lossless and transparent. In this limit, the nonlinear susceptibility in Eq. 2.8 has no frequency dependence [87]. The frequency dependence of the linear susceptibility in Eq. 2.7 will nonetheless be retained as it has important implications in ultrafast optics.

The induced polarization of the material will modify the propagating electromagnetic field. However, to observe this, we must solve Maxwell's equations. As we will see in Sec. 2.2.2, the effect of the linear susceptibility $\chi^{(1)}$ is to modify the propagation of light caused by the presence of the medium, whereas the effect of the nonlinear susceptibility $\chi^{(2)}$, is to introduce new frequency components to the field. As a simple example, in a linear medium which is lossless, and dispersionless, the linear susceptibility will be a frequency-independent constant, such that,

$$P_i^{(1)}(\vec{r},t) = \epsilon_0 \chi_{ij}^{(1)} E_j(\vec{r},t). \tag{2.9}$$

In Eq. 2.9, the material polarization responds instantaneously to the electric field. If the strength of the driving field is increased, we have to consider the additional nonlinear terms,

$$P_i(\vec{r},t)_{NL} = \epsilon_o \left(\chi_{ijk}^{(2)} E_j(\vec{r},t) E_k(\vec{r},t) + \chi_{ijkl}^{(3)} E_j(\vec{r},t) E_k(\vec{r},t) E_l(\vec{r},t) + \cdots \right). \tag{2.10}$$

In the case where all fields are identical, they are proportional to E^2 and E^3 and so on. If the field E has a frequency component at ω_0, then the nonlinear polarization will introduce frequencies at $2\omega_0$ and $3\omega_0$, leading to a rich set of nonlinear phenomena such as three- and four-wave mixing, respectively. All the materials used in this thesis exhibit $\chi^{(2)}$ nonlinearities where the dominant nonlinear susceptibility is second-order in the electric field. Its effect on a propagating electric field will be discussed in the next section, Sec. 2.2.2.

2.2.2 The forced wave equation: how matter changes light

The evolution of the electromagnetic field as a result of its coupling to the polarization is obtained by solving Maxwell's equations. For a uniform, source free, and non-magnetic material, Maxwell's equations in Eq. 2.1 can be simplified,

$$\frac{-\partial(\nabla \times B)}{\partial t} = \nabla \times (\nabla \times E) = \nabla(\nabla \cdot E) - \nabla^2 E = -\mu_0 \frac{\partial^2 D}{\partial t^2}, \tag{2.11}$$

and with the further assumption that $\nabla \cdot E \approx 0$, which is a good approximation when the nonlinear polarization is weak [11], we arrive at the forced wave equation in the time domain,

$$\nabla^2 E(\vec{r}, t) - \frac{1}{\epsilon_0 c^2} \frac{\partial^2 D^{(1)}(\vec{r}, t)}{\partial t^2} = \frac{1}{\epsilon_0 c^2} \frac{\partial^2 P_{NL}(\vec{r}, t)}{\partial t^2}, \tag{2.12}$$

where $D^{(1)}(\vec{r}, t) = \epsilon_0 E(\vec{r}, t) + P^{(1)}(\vec{r}, t)$ is the linear part of the displacement field. Inserting Eq. 2.9 into Eq. 2.12 leads to a driven inhomogeneous wave equation where the nonlinear polarization of the medium, which appears on the right-hand side of the equation, responds instantaneously to the field and acts as a source term for the wave equation.

The instantaneous response of the polarization to the electric field, however, remains unphysical for any material. Instead, the dielectric material that we work with are dispersive and, as a result, the polarization of the material induced by the electric field depends on the frequency. Therefore, it is the polarization induced at each frequency that is directly related to the electric field via the frequency-dependent susceptibility, $P^{(1)}(\vec{r}, \omega) = \epsilon_0 \chi^{(1)}(\omega) E(\vec{r}, \omega)$. We must therefore consider the coupling between fields for each frequency component separately. This is obtained by expressing the field quantities with their Fourier Transform,

$$E(\vec{r}, t) = \frac{1}{\sqrt{2\pi}} \int d\omega E(\vec{r}, \omega) e^{i\omega t} \tag{2.13}$$

$$D^{(1)}(\vec{r}, t) = \frac{1}{\sqrt{2\pi}} \int d\omega D^{(1)}(\vec{r}, \omega) e^{i\omega t} \tag{2.14}$$

$$P_{NL}(\vec{r}, t) = \frac{1}{\sqrt{2\pi}} \int d\omega P_{NL}(\vec{r}, \omega) e^{i\omega t}. \tag{2.15}$$

If the material is transparent, then dissipation in the material can be neglected. In such cases, the relationship between $D^{(1)}(\vec{r}, \omega)$ and $E(\vec{r}, \omega)$ can be expressed via a real frequency-

dependent linear susceptibility,

$$\begin{aligned} D^{(1)}(\vec{r},\omega) &= \epsilon_0 E(\vec{r},\omega) + P^{(1)}(\vec{r},\omega) \\ &= \epsilon_0[1+\chi^{(1)}(\omega)]E(\vec{r},\omega) \\ &= \epsilon_0 n^2(\omega)E(\vec{r},\omega), \end{aligned} \tag{2.16}$$

where $n(\omega) = \sqrt{1+\chi^{(1)}(\omega)}$ is the index of refraction. This usually remains a good approximation since most dielectric material we work with are transparent at the frequencies of interest. Inserting Eqs. 2.13 – 2.15, into Eq. 2.12, we obtain the forced nonlinear wave equation in the frequency domain,

$$\nabla^2 E(\vec{r},\omega) + \frac{n^2(\omega)\omega^2}{c^2}E(\vec{r},\omega) = -\frac{\omega^2}{\epsilon_0 c^2}P_{NL}(\vec{r},\omega). \tag{2.17}$$

The nonlinear polarization $P_{NL}(\vec{r},\omega)$ can oscillate at many different frequencies, and Eq. 2.17 must hold for each frequency. The frequency component ω of the nonlinear polarization will drive the linear wave equation on the left-hand side at the same frequency ω.

The nonlinear wave equation therefore captures the evolution of a forward travelling laser pulse through a nonlinear material. Our physical picture at this stage is the following. An oscillating electromagnetic wave creates an oscillating dipole moment or polarization in the material. The linear part of the oscillating polarization creates a lag on the electric field and this is manifested via the index of refraction. On the other hand, the nonlinear part of the polarization can cause new frequencies to develop in the dielectric material not initially present in the incident field. These new frequency components act as a source term which drives the propagation of new electromagnetic fields in the wave equation.

2.2.3 Weak coupling regime

Without the nonlinear polarization driving the field, $P_{NL} = 0$, one solution to the wave equation (Eq. 2.17) is given in terms of the spectral amplitude function,

$$E(\omega,z) = A(\omega-\omega_0)e^{-ik(\omega)z} + A^*(-\omega-\omega_0)e^{ik(\omega)z}, \tag{2.18}$$

where,

$$k(\omega) = n(\omega)\omega/c, \tag{2.19}$$

is the propagation constant or wave vector in the absence of a nonlinearity, and the spectral amplitude $A(\omega)$ is constant in z. The solution describes plane waves with a carrier frequency ω_0 travelling in the z direction. The spectral amplitude of the field $|A(\omega)|$ is unmodified as it travels forward, but the field picks up a phase $\phi(\omega) = k(\omega)z$, leading to the propagation of ultrafast pulses in a linear regime. The effect of the frequency dependent wave vector $k(\omega)$ has important consequences on the propagation of ultrafast pulses and broadband quantum states of light and these effects will be discussed Sec. 3.2.

In the presence of a weak nonlinearity, we assume the nonlinear polarization can only slowly modify the envelope of the forward-travelling pulse on the length scale of one wavelength. We thus look for solutions to the wave equation in terms of the slowly varying complex spectral field amplitude, $A(\vec{r},\omega)$, as it travels through the material along the z direction,

$$E(\vec{r},\omega) = A(\vec{r},\omega-\omega_0)e^{-ik(\omega)z} + A^*(\vec{r},-\omega-\omega_0)e^{ik(\omega)z} \tag{2.20}$$

$$\approx A(\vec{r},\omega-\omega_0)e^{-ik(\omega)z}. \tag{2.21}$$

The approximation in the second line is made by noting that for a slowly varying field, $A(\vec{r},\omega)$, should not have significant component at $2\omega_0$. Inserting this into 2.17, and separating $\nabla^2 = \nabla_\perp^2 + \frac{\partial^2}{\partial z^2}$ into its propagating and transverse directions we obtain,

$$\left[\nabla_\perp^2 A + \frac{\partial^2 A}{\partial z^2} - 2ik(\omega)\frac{\partial A}{\partial z} + \left(\frac{n^2(\omega)\omega^2}{c^2} - k(\omega)^2\right)A\right]e^{ik(\omega)z} = -\frac{\omega^2}{\epsilon_0 c^2}P_{NL}(\vec{r},\omega). \tag{2.22}$$

The fourth term in the square brackets can be directly eliminated using Eq. 2.19. In addition, under the slowly varying envelope approximation, the fractional change of the amplitude during a period of one wavelength should be small, $\frac{1}{|A|}\frac{\partial|A|}{\partial z}\lambda \ll 1$. The relation can also be expressed in the form, $\frac{\partial^2|A|}{\partial z^2} \ll k\frac{\partial|A|}{\partial z}$, and therefore we neglect the second derivative $\frac{\partial^2|A|}{\partial z^2}$ in Eq. 2.22. As a result, we find that the Fourier components of the electric field and the nonlinear polarization are related by,

$$\frac{\partial A(\vec{r},\omega-\omega_0)}{\partial z} = -\frac{i}{2k(\omega)}\nabla_\perp^2 A(\vec{r},\omega-\omega_0) - \frac{i\omega}{2\epsilon_0 cn(\omega)}P_{NL}(\vec{r},\omega)e^{-ik(\omega)z}. \tag{2.23}$$

This is the frequency-domain forced wave equation in the slowly varying field approximation used widely in nonlinear optics. Equation 2.23 has three components: $\nabla_\perp^2 A(\vec{r},\omega)$ in the first term accounts for spatial diffraction, the nonlinear polarization $P_{NL}(\vec{r},\omega)$ acts as a source term that modifies the spectral amplitude of the electric field, and the full effect of chromatic dispersion is included in the propagation term, $\exp[-ik(\omega)z]$.

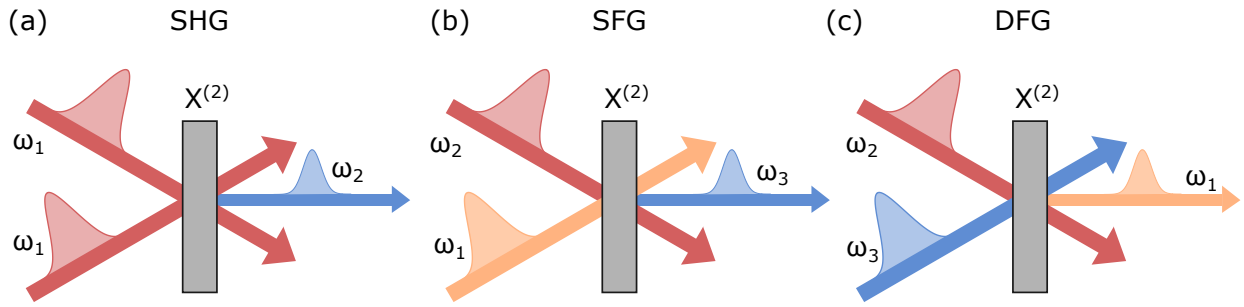

Figure 2.1: **Three-wave mixing.** Different ways in which three-fields can couple in a $\chi^{(2)}$ material. (a) In second-harmonic generation (SHG), one low-frequency field centred at ω_1 drives the second harmonic frequency, $\omega_2 = \omega_1 + \omega_1$, (b) in sum-frequency generation (SFG), two low-frequency fields at ω_1 and ω_2 drive a third sum frequency at $\omega_3 = \omega_1 + \omega_2$, and (c) in difference frequency generation (DFG), two frequencies at ω_3 and ω_1 drive the difference frequency $\omega_1 = \omega_3 - \omega_2$.

2.2.4 Sum-Frequency Generation

The relation for nonlinear wave propagation in Eq. 2.23 is valid in the slowly varying envelope approximation, which holds for almost all nonlinear processes including three- and four-wave mixing. Here, I will consider three-wave mixing, which includes, second-harmonic generation (SHG), sum-frequency generation (SFG), and difference-frequency generation (DFG) as illustrated in Fig. 2.1. These processes can be used for many applications including frequency conversion, parametric amplification, and bandwidth compression. I'll focus on sum-frequency generation as this is the process we use for optical gating.

Three wave-mixing is a nonlinear process which can occur in a $\chi^{(2)}$ material. The process describes the interaction of three travelling fields with components at three distinct frequencies. The total field is,

$$\begin{aligned} E(z,t) &= \frac{1}{2}\left[E_1(z,t) + E_2(z,t) + E_3(z,t) + c.c.\right] \\ &= \frac{1}{2}\left[|E_1(z,t)|e^{i\omega_{10}t} + |E_2(z,t)|e^{i\omega_{20}t} + |E_3(z,t)|e^{i\omega_{30}t} + c.c.\right], \end{aligned} \tag{2.24}$$

where E_1, E_2, and E_3 are the fields with central carrier frequencies at ω_{10}, ω_{20}, and ω_{30}, respectively, and $c.c.$ is the complex conjugate. If we assume an effective frequency independent nonlinear susceptibility, $\chi^{(2)}_{\text{eff}}$, then the nonlinear polarization induced by these

fields is,

$$P_{NL}(z,t) = 2\epsilon_0 \chi^{(2)}_{\text{eff}} E(z,t)^2. \tag{2.25}$$

E^2 has 12 distinct frequency components and can therefore induce an oscillating polarization field P_{NL} at all 12 frequencies. Inserting the total field Eq. 2.24 into Eq. 2.25, we could calculate the nonlinear polarization for each frequency component, however, typically one nonlinear process will be dominant. What leads to only certain processes occurring? Microscopically, all non-zero tensor elements of the nonlinear susceptibility in Eq. 2.8 will create an oscillating dipole moment. However, as we will see, macroscopically, only those that add up in phase or coherently across the length of the crystal will build up significant power to be observed. In sum-frequency generation, for example, two incident fields ω_1 and ω_2 drive a third polarization field $\omega_3 = \omega_1 + \omega_2$, which then acts as a source of electromagnetic waves at this higher frequency. It is therefore sufficient to calculate the nonlinear polarization for the three frequencies of interest, ω_1, ω_2, and ω_3. The nonlinear polarization at the third frequency $\omega_3 = \omega_1 + \omega_2$ will be,

$$\begin{aligned}
P_{NL}(z,\omega_3) &= \epsilon_0 \chi^{(2)}_{\text{eff}} \tfrac{1}{\sqrt{2\pi}} \int dt E_1(z,t) E_2(z,t) e^{-i\omega_3 t} \\
&= 2\epsilon_0 \chi^{(2)}_{\text{eff}} \tfrac{1}{\sqrt{2\pi}} \int dt \tfrac{1}{\sqrt{2\pi}} \int d\omega_1 E_1(z,\omega_1) e^{i\omega_1 t} \tfrac{1}{\sqrt{2\pi}} \int d\omega_2 E_2(z,\omega_2) e^{i\omega_2 t} e^{-i\omega_3 t} \\
&= 2\frac{\epsilon_0 \chi^{(2)}_{\text{eff}}}{\sqrt{2\pi}} \int d\omega_1 E_1(z,\omega_1) \int d\omega_2 E_2(z,\omega_2) \tfrac{1}{2\pi} \int dt e^{-i(\omega_3-\omega_2-\omega_1)t} \\
&= 2\epsilon_0 \chi^{(2)}_{\text{eff}} \frac{1}{\sqrt{2\pi}} \int d\omega_1 E_1(z,\omega_1) E_2(z,\omega_3-\omega_1),
\end{aligned} \tag{2.26}$$

and we find, as expected, that the input frequencies ω_1 and $\omega_2 = \omega_3 - \omega_1$ combine in various pairs to drive the frequency component ω_3 of the nonlinear polarization. Energy conservation is thus satisfied automatically. Inserting the slowly varying fields of Eq. 2.21 into Eq. 2.26, and defining the translated frequencies, $\tilde{\omega}_i = \omega_i - \omega_{i0}$, we obtain,

$$P_{NL}(z,\omega_3) = 2\epsilon_0 \chi^{(2)}_{\text{eff}} \frac{1}{\sqrt{2\pi}} \int d\omega_1 A_1(z,\tilde{\omega}_1) A_2(z,\tilde{\omega}_3 - \tilde{\omega}_1) e^{-ik_1(\omega_1)z - ik_2(\omega_3-\omega_1)z}, \tag{2.27}$$

where k_1 and k_2 are the wave vectors of the two incident fields A_1 and A_2, respectively. Repeating a similar process, we can find the component of the nonlinear polarization at ω_1 and ω_2,

$$P_{NL}(z,\omega_1) = 2\epsilon_0 \chi^{(2)}_{\text{eff}} \frac{1}{\sqrt{2\pi}} \int d\omega_3 A_3(z,\tilde{\omega}_3) A_2^*(z,\tilde{\omega}_3 - \tilde{\omega}_1) e^{-ik_3(\omega_3)z + ik_2(\omega_3-\omega_1)z} \tag{2.28}$$

$$P_{NL}(z,\omega_2) = 2\epsilon_0 \chi^{(2)}_{\text{eff}} \frac{1}{\sqrt{2\pi}} \int d\omega_3 A_3(z,\tilde{\omega}_3) A_1^*(z,\tilde{\omega}_3 - \tilde{\omega}_2) e^{-ik_3(\omega_3)z + ik_1(\omega_3-\omega_2)z}. \tag{2.29}$$

The component of the nonlinear polarization at each frequency will drive the linear wave equation at the corresponding frequency. We can insert Eq. 2.27, Eq. 2.28, and Eq. 2.29 into the nonlinear wave equation, Eq. 2.23, to determine the evolution of the three fields. In order to obtain an intuitive picture of sum-frequency generation, we assume plane-wave inputs and neglect the effects of diffraction by setting $\nabla_{\perp}^2 A = 0$. We obtain a set of three coupled field equations which describe the propagation of the three spectral amplitude functions through the crystal,

$$\frac{\partial A_3(z,\tilde{\omega}_3)}{\partial z} = -\frac{i\omega_3 \chi_{\text{eff}}^{(2)}}{\sqrt{2\pi}cn(\omega_3)} \int d\omega_1 A_1(z,\tilde{\omega}_1) A_2(z,\tilde{\omega}_3 - \tilde{\omega}_1) e^{i(k_3(\omega_3)z - k_1(\omega_1)z - k_2(\omega_3-\omega_1)z)} \tag{2.30}$$

$$\frac{\partial A_2(z,\tilde{\omega}_2)}{\partial z} = -\frac{i\omega_2 \chi_{\text{eff}}^{(2)}}{\sqrt{2\pi}cn(\omega_2)} \int d\omega_3 A_3(z,\tilde{\omega}_3) A_1(z,\tilde{\omega}_3 - \tilde{\omega}_1) e^{-i(k_3(\omega_3)z - k_1(\omega_3-\omega_2)z - k_2(\omega_2)z)} \tag{2.31}$$

$$\frac{\partial A_1(z,\tilde{\omega}_1)}{\partial z} = -\frac{i\omega_1 \chi_{\text{eff}}^{(2)}}{\sqrt{2\pi}cn(\omega_1)} \int d\omega_3 A_3(z,\tilde{\omega}_3) A_2^*(z,\tilde{\omega}_3 - \tilde{\omega}_1) e^{-i(k_3(\omega_3)z - k_1(\omega_3-\omega_2)z - k_2(\omega_2)z)}. \tag{2.32}$$

Low-efficiency sum frequency generation

In general, a complete solution to the sum-frequency generation process requires solving all three coupled field equations simultaneously. Luckily for us, our experiments operate in the low efficiency regime, which simplifies the problem considerably. In optical gating, a strong gate pulse A_2 interacts with a weak input pulse A_1 to produce a third field A_3. We can assume the strong gate pulse A_2 is undepleted during the process and remains unchanged during the interaction and, moreover, that the initial field A_3 is empty. As a result, the three coupled field equations reduce to only one differential equation, Eq. 2.30, and we can solve for the Fourier component of the upconverted field, A_3, directly.

The interaction medium has length L, and therefore we can integrate Eq. 2.30 over the length of the crystal along z, from 0 to L,

$$A_3(\tilde{\omega}_3) = -\frac{i\omega_3 \chi^{(2)}}{\sqrt{2\pi}cn(\omega_3)} \int d\omega_1 A_1(\tilde{\omega}_1) A_2(\tilde{\omega}_3 - \tilde{\omega}_1) \int_0^L dz e^{i[k_3(\omega_3) - k_1(\omega_1) - k_2(\omega_3-\omega_1)]z}. \tag{2.33}$$

The terms in the argument of the exponential are the phases of the upconverted frequency ω_3 and the two incident fields, ω_1 and ω_2, at a point z in the crystal. The integral over

the length of the crystal is the accumulated phase difference between the fields. It can be evaluated directly and this leads to the *phase-matching function*,

$$\begin{aligned}\Phi(\omega_1, \omega_3 - \omega_1, \omega_3) &= \frac{1}{L}\int_0^L dz e^{i[k_3(\omega_3) - k_1(\omega_1) - k_2(\omega_3 - \omega_1)]z} \\ &= \exp\left(\frac{i\Delta k(\omega_1, \omega_3 - \omega_1, \omega_3)L}{2}\right)\mathrm{sinc}\left(\frac{\Delta k(\omega_1, \omega_3 - \omega_1, \omega_3)L}{2}\right),\end{aligned} \tag{2.34}$$

where the *phase mismatch* is a function of all three frequencies,

$$\Delta k(\omega_1, \omega_3 - \omega_1, \omega_3) = k_3(\omega_3) - k_2(\omega_3 - \omega_1) - k_1(\omega_1). \tag{2.35}$$

The phase-matching function in Eq. 2.34 effectively captures the interaction between the material polarization and the propagating fields. As the two incident fields A_1 and A_2 propagate through the material, they create oscillating dipoles at each instant in the crystal which radiate at the sum frequency of the fields. For efficient conversion, the radiation from the dipoles at each length of the crystal must add up coherently or in phase, and this occurs when there is no mismatch between the momentum wave vectors of the three travelling fields, $\Delta k = 0$. When this condition is fulfilled, the generated wave maintains a fixed phase relation with respect to the nonlinear polarization and is able to extract energy from the medium. Reducing the phase mismatch between the fields is therefore crucial to efficiently realize any nonlinear process in the lab, and we will revisit it in Section 2.2.5.

The spectral amplitude of the upconverted field after propagation through length L of the medium is thus,

$$A_3(\tilde{\omega}_3) = -\frac{i\omega_3\chi^{(2)}L}{\sqrt{2\pi}cn(\omega_3)}\int d\omega_1 A_1(\tilde{\omega}_1)A_2(\tilde{\omega}_3 - \tilde{\omega}_1)\Phi(\omega_1, \omega_3 - \omega_1, \omega_3). \tag{2.36}$$

We find that the upconverted spectral field A_3 is a convolution of the two input fields A_1 and A_2 with a transfer function given by the phase-matching function Φ. Equation 2.36 is the equation of interest in this section and it will be used to determine many of the important features related to sum-frequency generation. Moreover, it accounts for the effects of dispersion as the phase-matching function and phase mismatch in Eq. 2.34 and Eq. 2.35 are valid for arbitrary variations of $k(\omega)$.

The spectral intensity of the upconverted field is given by,

$$\begin{aligned}I_3(\omega_3) =& 2n(\omega_3)\epsilon_0 c|A_3(z, \tilde{\omega}_2)|^2 \\ =& \frac{2\epsilon_0\left(\omega_3\chi^{(2)}L\right)^2}{n(\omega_3)c}\left|\frac{1}{\sqrt{2\pi}}\int d\omega_1 A_1(\tilde{\omega}_1)A_2(\tilde{\omega}_3 - \tilde{\omega}_1)\Phi(\omega_1, \omega_3 - \omega_1, \omega_3)\right|^2.\end{aligned} \tag{2.37}$$

In the limit where the phase-matching function is broad, $\Phi(\omega_1, \omega_3 - \omega_1, \omega_3) \approx 1$, Eq. 2.36 becomes a convolution of the spectra of the two input fields, corresponding to a medium which is dispersionless over the bandwidths of interest. The upconversion efficiency is proportional to L^2 and thus scales quadratically in the length of the interaction. In the time domain, the upconverted intensity for the broad phase-matching limit is simply a multiplication of the two fields,

$$I_3(t) \propto \left(\chi^{(2)} L\right)^2 |A_1(t)|^2 |A_2(t)|^2, \tag{2.38}$$

corresponding to the idealized scenario where the polarization of the medium responds instantaneously to the propagating electric field.

2.2.5 Phase matching in sum-frequency generation

Phase-matching bandwidth

Phase mismatch in sum-frequency generation arises from the variations of the refractive index with frequency. If the refractive index were constant for all frequencies, perfect momentum conservation would be possible with no phase mismatch. The phase-matching function tells us how far from perfect momentum conservation we can be before the upconversion efficiency is significantly reduced. As we will see in Sec. 3.3.5, it also plays an important role in the measurement of pulses using sum-frequency generation. We can gain some intuition about the effects of phase-matching on sum-frequency generation by calculating the effective acceptance bandwidth for sum-frequency generation from the phase-matching function.

The full phase-matching function for type-I SHG in BiBO is shown in Fig. 2.2(a). We perform the first-order Taylor expansion of the phase mismatch Δk in Eq. 2.35, and assume the zero order is phase-matched such that $k_3(\omega_{30}) = k_2(\omega_{20}) + k_1(\omega_{10})$. The phase mismatch Δk is then given by,

$$\begin{aligned}
\Delta k(\omega_1, \omega_2, \omega_3) &= k_3(\omega_{30}) - k_2(\omega_{20}) - k_1(\omega_{10}) \\
&\quad + \frac{dk_3}{d\omega}(\omega_3 - \omega_{30}) - \frac{dk_2}{d\omega}(\omega_2 - \omega_{20}) - \frac{dk_1}{d\omega}(\omega_1 - \omega_{10}) \\
&= \left(\frac{dk_3}{d\omega} - \frac{dk_2}{d\omega}\right)(\omega_3 - \omega_{30}) + \left(\frac{dk_2}{d\omega} - \frac{dk_1}{d\omega}\right)(\omega_1 - \omega_{10}) \\
&= \eta_{32}(\omega_3 - \omega_{30}) + \eta_{21}(\omega_1 - \omega_{10}),
\end{aligned} \tag{2.39}$$

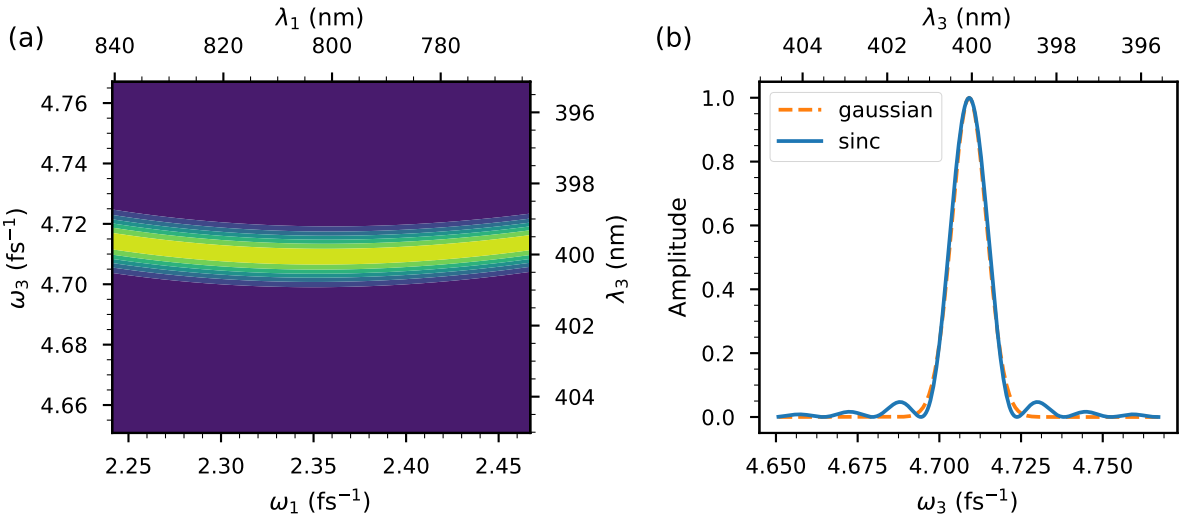

Figure 2.2: **Example sum-frequency generation phase-matching function.** (a) Phase-matching function for type-I sum-frequency generation of NIR 800 nm light in 1 mm of bismuth borate (BiBO) calculated from the Sellmeier equations with a crystal angle of 151.24 degrees. We observe the phase-matching function depends only on the upconverted wavelength λ_3 over approximately a 20 nm range from 790 nm to 810 nm. (b) Comparaison of the full phase-matching function with λ_1=800 nm and centred at λ_3=400 nm with the first-order Gaussian approximation in Eq. 2.41 of the same bandwidth. We find an acceptance bandwidth of 1 nm (12.5 ps^{-1}) FWHM .

where $\eta_{ij} = dk_i/d\omega - dk_j/d\omega = v_i^{-1} - v_j^{-1}$ is the difference in the inverse group velocities $v_i = (dk_i/d\omega)^{-1}$ (see Eq. 3.12 in Sec. 3.2.1). In type-I sum-frequency generation, the wave vectors k_1 and k_2 for the two incident fields are the same. If in addition the frequencies of these fields are similar, $\omega_1 \approx \omega_2$, then the group velocities will also be similar, $v_1 \approx v_2$, and $\eta_{21} \approx 0$. Within the limits of the first-order expansion, the second term Eq. 2.39 drops out and the phase-matching function only depends on the upconverted frequency, $\Phi(\omega_1, \omega_2, \omega_3) = \Phi(\omega_3)$. As a result, the intensity of the upconverted field in the low-

efficiency limit becomes,

$$\begin{aligned} I_3(\omega_3) =& \frac{2\epsilon_0 \left(\omega_{30}\chi^{(2)}L\right)^2}{n(\omega_3)c} \left| \frac{1}{\sqrt{2\pi}} \int d\omega_1 A_1(\tilde{\omega}_1) A_2(\tilde{\omega}_3 - \tilde{\omega}_1) \Phi(\omega_3) \right|^2 \\ \propto& \left(\chi^{(2)}L\right)^2 |\Phi(\omega_3)|^2 \left| \frac{1}{\sqrt{2\pi}} \int d\omega_1 A_1(\tilde{\omega}_1) A_2(\tilde{\omega}_3 - \tilde{\omega}_1) \right|^2 . \end{aligned} \tag{2.40}$$

The phase-matching function, $|\Phi(\omega_3)|$, acts as a spectral filter on the upconverted frequencies ω_3. Frequencies that lie outside the phase-matching bandwidth will be significantly suppressed. We can calculate the acceptance bandwidth of the filter by approximating the phase-matching function with a Gaussian, $\mathrm{sinc}(\mathrm{x}/2) = \exp(-\gamma x^2)$ with $\gamma = 0.0482$, such that both functions have the same FWHM [157],

$$|\phi(\omega_3)|^2 = \mathrm{sinc}(\Delta k L/2)^2 \approx \exp(-2\gamma \Delta k^2 L^2) = \exp(-2\gamma \eta_{31}^2 L^2 (\omega_3 - \omega_{30})^2). \tag{2.41}$$

The approximation is illustrated in Fig. 2.2(b). We find a filter bandwidth, $\sigma_{PM} = 1/\sqrt{4\gamma\eta_{31}^2 L^2}$, that is inversely proportional to the group-velocity mismatch and the length of the crystal. This can tell us how large the input bandwidths can be before the upconverted field is affected by the phase-matching. For example, if the two-input fields are bandwidth limited Gaussian pulses with bandwidth σ_{ω_1} and σ_{ω_2}, then the upconverted field, which is the convolution of the two input fields, will also be a Gaussian function. Its bandwidth will be the quadrature sum of the two input bandwidths, $\sqrt{\sigma_{\omega_1}^2 + \sigma_{\omega_2}^2}$. The effects of phase-matching in the upconversion will become significant when $\sqrt{\sigma_{\omega_1}^2 + \sigma_{\omega_2}^2} > \sigma_{PM} = 1/\sqrt{4\gamma\eta_{31}^2 L^2}$.

When working with ultrafast pulses, the input pulse bandwidths can be large, requiring large phase-matching acceptance bandwidths. One way to achieve this is to use short crystals. Fig. 2.3(a) shows the phase-matching acceptance bandwidth for two crystals, BiBO and BBO as a function of the crystal length. For example, the upconversion bandwidth of two transform-limited 40 fs laser pulses is about 18 ps^{-1}, which corresponds to about 1.5 nm at a wavelength of 400 nm. Matching the phase-matching bandwidth to the upconversion bandwidth, based on Fig. 2.3(a), would require less than 700 μm of BBO or 300 μm of BiBO.

Efficiency scaling of low-efficiency regime

Thin crystals reduce the upconversion efficiency, which is generally not a problem for high-power applications but must be taken into consideration for quantum applications. As

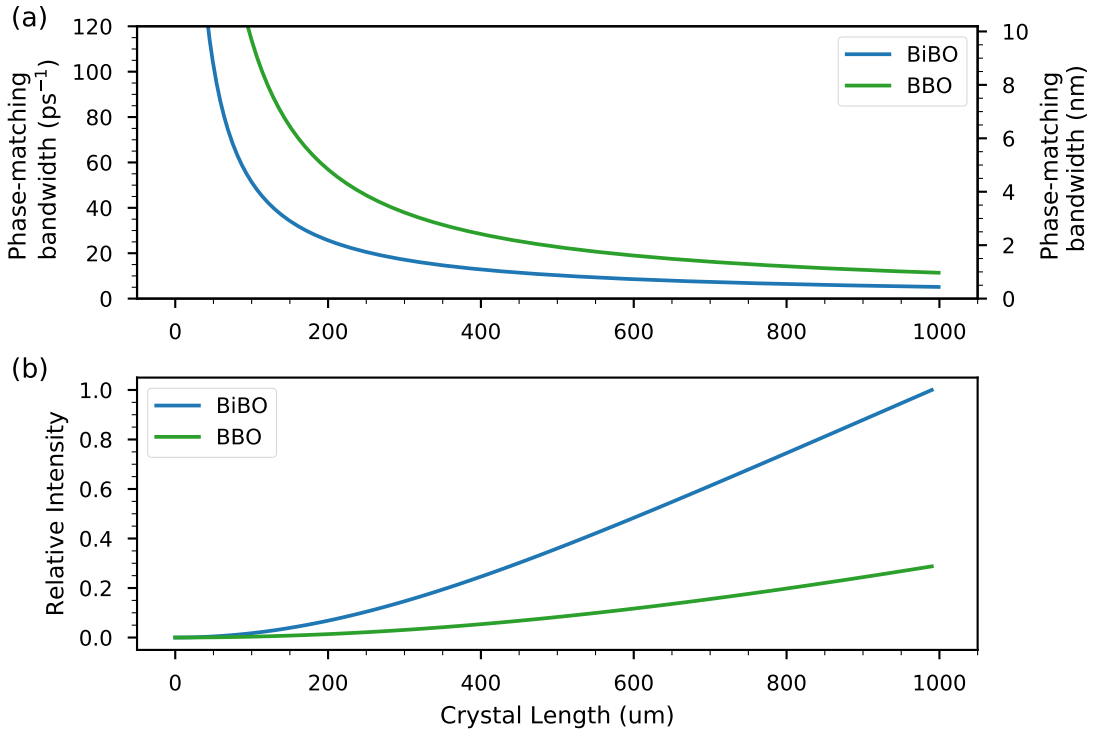

Figure 2.3: **Phase-matching bandwidth and relative upconversion intensity for sum-frequency generation.** (a) In type-I sum-frequency generation, the acceptance bandwidth of the crystal is inversely proportional to the length of the crystal and the group-velocity mismatch between the incident and upconverted fields. In the NIR, BBO has a lower group-velocity mismatch then BiBO and will therefore have a larger acceptance bandwidth for the same crystal length. (b) Relative strength of the upconversion intensity as a function of crystal length normalized to 1 mm of BiBO. The strength of the nonlinearity $\chi^{(2)}$ is about twice as large in BiBO then in BBO. We observe a quadratic to linear change in the intensity as the crystal length increases and the phase-matching bandwidth decreases.

a result, we would like to get an idea of how the upconversion efficiency scales with the crystal length. In the low efficiency regime for which Eq. 2.37 is valid, we can obtain the upconversion efficiency scaling by integrating over the upconverted frequencies ω_3. From Eq. 2.37, we naively expect the efficiency to scale as L^2. However, this is only true when phase-matching is broad or flat, $|\phi(\omega_3)| \approx 1$, such that we can ignore its contribution to the integral. The situation is slightly more interesting when this is not the case. For simplicity,

we'll assume the incident fields A_1 and A_2 are normalized transform-limited Gaussian pulses, and that the central frequency ω_{30} is much larger than the bandwidth, such that we can ignore the ω_3 in front of the integral. We find the total intensity proportional to,

$$\begin{aligned} I_3 &= \int d\omega_3 I_3(\omega_3) = \frac{2\epsilon_0 \left(\omega_{30}\chi^{(2)}L\right)^2}{n(\omega_3)c} \\ &\times \int d\omega_3 e^{-2\gamma\eta_{31}^2 L^2(\omega_3-\omega_{30})^2} \left| \frac{1}{\sqrt{2\pi}} \int d\omega_1 \frac{1}{2\pi\sqrt{\sigma_{\omega_1}\sigma_{\omega_2}}} e^{-\frac{(\omega_1-\omega_{10})^2}{4\sigma_{\omega_1}^2}} e^{-\frac{(\omega_3-\omega_1-(\omega_{30}-\omega_{10}))^2}{4\sigma_{\omega_2}^2}} \right|^2 \\ &\propto \left(\chi^{(2)}\right)^2 \frac{\sigma_{\omega_1}\sigma_{\omega_2}}{\sigma_{\omega_1}^2+\sigma_{\omega_2}^2} \frac{L^2}{\sqrt{\frac{1}{\sigma_{\omega_1}^2+\sigma_{\omega_2}^2}+4\gamma\eta_{31}^2L^2}}. \end{aligned} \tag{2.42}$$

The scaling with L depends on the ratio between the upconversion bandwidth $\sqrt{\sigma_{\omega_1}^2+\sigma_{\omega_2}^2}$ and the phase-matching bandwidth $\sigma_{PM} = 1/(2\gamma^{1/2}\eta_{31}L)$. When the phase-matching bandwidth is much larger than the upconversion bandwidth, $\sigma_{PM} \gg \sqrt{\sigma_{\omega_1}^2+\sigma_{\omega_2}^2}$, the intensity does indeed scale as the length squared, $I_3 \propto L^2$. On the other hand, when $\sigma_{PM} \ll \sqrt{\sigma_{\omega_1}^2+\sigma_{\omega_2}^2}$, the factor of L in the denominator remains and $I_3 \propto L$. As the crystal becomes shorter, the upconversion intensity is reduced but the phase-matching bandwidth also increases. This allows more frequencies to be upconverted, and partially compensates for the reduction in crystal length. A comparison of these benchmarks for two different crystals is shown in Fig. 2.3(b). The phase-matching bandwidth and the upconversion efficiency are important to consider when deciding on the types and lengths of crystals to use for sum-frequency generation.

2.3 Quantum nonlinear optics

As we've seen in the previous section, three-wave mixing is a nonlinear process whereby energy is exchanged between the modes of three electromagnetic fields. It is used extensively as a source of single photons, via the process of spontaneous parametric downconversion, but also to optically gate photons via sum-frequency generation. In this section, I'll treat it from a quantum perspective.

2.3.1 Three-wave mixing Hamiltonian

For a quantum mechanical approach to three-wave mixing, we need a Hamiltonian. This can be achieved via a lengthy derivation which requires first writing down the Langragian

whose equations yield Maxwell's equations, obtaining the Hamiltonian, and then quantizing the electric field in the medium [158, 87]. The result in the interaction picture for the Hamiltonian describing the three-wave mixing interaction is,

$$\hat{H}_{3WM}(t) = -\frac{\epsilon_0}{3}\int d^3\vec{r}\chi^{(2)}_{ijk}\hat{E}_i(\vec{r},t)\hat{E}_j(\vec{r},t)\hat{E}_k(\vec{r},t), \tag{2.43}$$

which is a product of three fields coupled by the nonlinear susceptibility $\chi^{(2)}_{ijk}$. Some intuition for the form of the Hamiltonian in Eq. 2.43 can be obtained from the classical energy density of the field. In Sec. 2.2.1, we found that light induces a polarization in the medium creating a displacement field D. The displacement field modifies the classical energy density of the field according to,

$$\begin{aligned} u &= D(\vec{r},t)\cdot E(\vec{r},t)/2 \\ &= \left(\epsilon_0 E(\vec{r},t) + P^{(1)}(\vec{r},t) + P^{(2)}(\vec{r},t)\right)\cdot E(\vec{r},t)/2, \end{aligned} \tag{2.44}$$

where the displacement field from Eq. 2.3 has the linear and second order contributions to the polarization included. The second-order nonlinear polarization in Eq. 2.44, adds a second order correction to the energy density, which is found to be [159, 11],

$$u^{(2)} = -\frac{\epsilon_0}{3}\chi^{(2)}_{ijk}E^*_i(\vec{r},t)E_j(\vec{r},t)E_k(\vec{r},t). \tag{2.45}$$

Working in the interaction picture, the classical Hamiltonian is the total energy of the interaction of interest. This is obtained by integrating Eq. 2.45 over space,

$$H(t) = -\frac{\epsilon_0}{3}\int d^3\vec{r}\chi^{(2)}_{ijk}E^*_i(\vec{r},t)E_j(\vec{r},t)E_k(\vec{r},t). \tag{2.46}$$

The Hamiltonian in Eq. 2.46 captures the energy correction of the three fields due to the presence of the medium. Comparing Eq. 2.46 with Eq. 2.43, we find a very similar form.

Returning to Eq. 2.43, if we substitute each field with its positive and negative frequency contributions $\hat{E} \to \hat{E}^{(+)} + \hat{E}^{(-)}$, this leads to 8 different combinations of lowering and raising operators, consisting of the 8 ways to add and subtract photons from the different modes. For a given process, only two of these terms will conserve energy. As a result, we only keep those energy conserving terms as the others will drop out naturally. Furthermore, we assume there is only a single $\chi^{(2)}$ tensor component. The two normal-ordered energy conserving terms are,

$$\hat{H}_{3WM}(t) = -\frac{\epsilon_0}{3}\chi^{(2)}\int d^3\vec{r}\ \hat{E}^{(-)}_1\hat{E}^{(-)}_2\hat{E}^{(+)}_3 + \hat{E}^{(-)}_3\hat{E}^{(+)}_2\hat{E}^{(+)}_1, \tag{2.47}$$

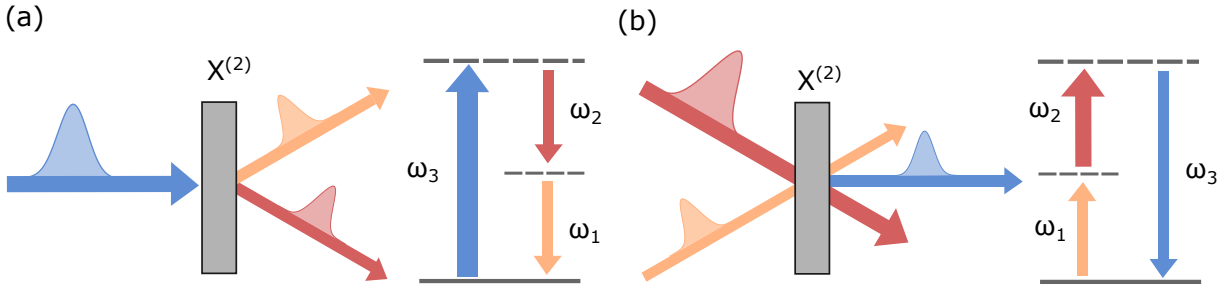

Figure 2.4: **Three-wave mixing Hamiltonian.** Two terms in the three-wave mixing Hamiltonian corresponding to (a) spontaneous parametric downconversion (SPDC) and (b) sum-frequency generation (SFG). Energy-level diagram for the semi-classical picture of SPDC and SFG are shown. In SPDC, one higher energy photon ω_3 is destroyed and two lower energy photons are simultaneously produced at $\omega_1 + \omega_2 = \omega_3$. In SFG, two photons at frequencies ω_1 and ω_2 are destroyed and a photon of frequency $\omega_3 = \omega_1 + \omega_2$ is simultaneously created. The solid and dashed lines represent the ground state and virtual excited states of the atom, respectively.

where we have chosen mode 3 to be the higher energy mode. The first term corresponds to SPDC, where a high-energy photon is destroyed and two-lower energy photons are produced, whereas the second term corresponds to sum-frequency generation, where two low-energy photons are combined to produce a higher energy one. These two processes are illustrated in Fig. 2.4.

When working only with time-frequency degree of freedom, we can directly insert the electric field operators of Eq. 1.3, setting ϵ to $n(\omega)^2\epsilon_0$, into the three-wave mixing Hamiltonian in Eq. 2.47,

$$\hat{H}_{3WM}(t) = -\frac{\epsilon_0}{3}\chi^{(2)}\left(\frac{\hbar}{4\pi\epsilon_0 cA}\right)^{3/2} \tag{2.48}$$
$$\int dz \int d\omega_1 \sqrt{\tfrac{\omega_1}{n(\omega_1)}} a_1^\dagger(\omega_1) e^{i\omega_1 t - ik_1 z} \int d\omega_2 \sqrt{\tfrac{\omega_2}{n(\omega_2)}} a_2^\dagger(\omega_2) e^{i\omega_2 t - ik_2 z} \int d\omega_3 \sqrt{\tfrac{\omega_3}{n(\omega_3)}} a_3(\omega_3) e^{-i\omega_3 t + ik_3 z} + h.c.$$

We can immediately perform the integral in space,

$$\Phi(\omega_1, \omega_2, \omega_3) = \frac{1}{L}\int_0^L dz e^{i(k_3 - k_2 - k_1)z} = \exp\left(i\frac{\Delta kL}{2}\right)\mathrm{sinc}\left(\frac{\Delta \mathrm{kL}}{2}\right) \tag{2.49}$$

where we have defined $\Phi(\omega_1, \omega_2, \omega_3)$ as the phase-matching function with the phase mismatch, $\Delta k = k_3 - k_2 - k_1$, and where k is implicitly frequency dependent, $k_i = n(\omega_i)\omega_i/c$.

The phase-matching function is of considerable importance for both SPDC and SFG with broadband fields. Its effect on SPDC will be considered in Sec. 2.3.3.

If we assume the photon bandwidths are small compared to their central frequency, then we can replace the frequency variables in the square root with constants, $\omega_k \to \omega_{k0}$, and rearranging the integrals, we get,

$$\begin{aligned}\hat{H}_{3WM}(t) = i\frac{\epsilon_0}{3}\chi^{(2)}L\left(\frac{\hbar}{4\pi\epsilon_0 cA}\right)^{3/2}\sqrt{\frac{\omega_{10}\omega_{20}\omega_{30}}{n_{10}n_{20}n_{30}}} \\ \times\int d\omega_1 d\omega_2 d\omega_3 a_1^\dagger(\omega_1)a_2^\dagger(\omega_2)a_3(\omega_3)\Phi(\omega_1,\omega_2,\omega_3)e^{-i(\omega_3-\omega_2-\omega_1)t}+h.c.\end{aligned} \tag{2.50}$$

2.3.2 Three-wave mixing unitary

The evolution of a state under this Hamiltonian will depend on the nature of the Hamiltonian. For a time dependent Hamiltonian that commutes with itself at different times, the unitary evolution will be (Sec. 2.1 of [160]),

$$U = \exp\left[-\frac{i}{\hbar}\int dt\hat{H}(t)\right], \tag{2.51}$$

which is calculated by a Taylor expansion. Unfortunately, the Hamiltonian in Eq. 2.50 does not generally commute with itself [161], and therefore a general solution requires consideration of time-ordering using a Dyson series. However, it was shown that if the phase-matching function is flat, $\Phi \approx 1$, then a Taylor series expansion of Eq. 2.51 remains valid [162, 163]. Furthermore, the experimental work in this thesis takes place in a low-efficiency regime where the probability of two conversions is very low and, consequently, the first-order expansion is sufficient. At this order, the series expansions are the same with or without time-ordering. As a result, the unitary operator for three-wave mixing in the low-efficiency regime becomes,

$$\begin{aligned}U_{3WM} &\approx 1-\frac{i}{\hbar}\int dt\hat{H}_{3WM}(t) \\ &= 1+\frac{\epsilon_0}{3}\chi^{(2)}L\left(\frac{1}{4\pi\epsilon_0 cA}\right)^{3/2}\sqrt{\frac{\omega_{10}\omega_{20}\omega_{30}\hbar}{n_{10}n_{20}n_{30}}}\times \\ &\quad\int dt\int d\omega_1 d\omega_2 d\omega_3 a_1^\dagger(\omega_1)a_2^\dagger(\omega_2)a_3(\omega_3)\Phi(\omega_1,\omega_2,\omega_3)e^{-i(\omega_3-\omega_2-\omega_1)t}+h.c.\end{aligned} \tag{2.52}$$

We can perform the integral in time which enforces energy conservation,

$$\int dt e^{-i(\omega_3-\omega_2-\omega_1)t} = 2\pi\delta(\omega_3-\omega_2-\omega_1), \tag{2.53}$$

and we see that any process where $\omega_3 \neq \omega_1+\omega_2$ would be eliminated. Finally, collecting all constants, the unitary for three-wave mixing to first order is,

$$\begin{aligned} U^{(1)}_{3WM} = 1 + \frac{\chi^{(2)}L}{12}\sqrt{\frac{\omega_{10}\omega_{20}\omega_{30}\hbar}{n_{10}n_{20}n_{30}\pi\epsilon_0 c^3 A^3}} \times \\ \int d\omega_1 d\omega_2 a_1^\dagger(\omega_1)a_2^\dagger(\omega_2)a_3(\omega_1+\omega_2)\Phi(\omega_1,\omega_2,\omega_1+\omega_2) + h.c. \end{aligned} \tag{2.54}$$

2.3.3 Spontaneous parametric downconversion

This section provides the foundations to understand the spectral correlations [164, 157, 165] of the photons produced in parametric downconversion, whereby a high energy-pump photon is converted into pairs of lower energy photons. I will show that energy-time entanglement is naturally produced in the process. In general, an analysis of parametric downconversion must take into consideration both the spatial and the spectral correlations of the three modes involved. Entanglement between the space and frequency degrees of freedom is important to consider for source design and otherwise can lead to low heralding efficiencies [166]. In experiments in this thesis, light is collected in a small cone by coupling into single-mode fibre, thereby removing any transversal correlations.

We can model the downconversion interaction as a strong pump downconverting into two lower energy photons, which are referred to as the signal and the idler, such that $\omega_p = \omega_s + \omega_i$, where s, i, and p label the signal, idler, and pump, respectively. The initial state is,

$$|\psi_0\rangle = |0\rangle_s |0\rangle_i |\psi\rangle_p , \tag{2.55}$$

where the pump is modelled by a coherent state, which is an eigenstate of the lowering operator, $\hat{a}(\omega)|\alpha(\omega)\rangle = \alpha(\omega)|\alpha(\omega)\rangle$, with a spectral shape given by $\alpha(\omega_p)$,

$$|\psi\rangle_p = \int d\omega_p |\alpha(\omega_p)\rangle . \tag{2.56}$$

It's assumed that no signal or idler fields are initially present. To first order, the evolution of the initial state $|\psi_0\rangle$ will be $|\psi^{(1)}\rangle = U^{(1)}_{3WM}|\psi_0\rangle$. Since the signal and idler are initially

in a vacuum state, the *h.c.* term in Eq. 2.54 corresponding to sum-frequency generation, is immediately eliminated as it has a lowering operator on both those modes. Furthermore, if we post-select on the final two-photon state, this removes the constant term in Eq. 2.54. As a result, the remaining state of interest for SPDC is proportional to,

$$\left|\psi^{(1)}\right\rangle \propto \frac{\chi^{(2)}L}{12}\int d\omega_s d\omega_i \alpha(\omega_s+\omega_i)\Phi(\omega_s,\omega_i,\omega_s+\omega_i)a_s^\dagger(\omega_s)a_i^\dagger(\omega_i)\left|0\right\rangle_s\left|0\right\rangle_i. \tag{2.57}$$

The SPDC wavefunction in Eq. 2.57 describes a state which is a superposition of signal and idler frequency modes, $a_s^\dagger(\omega_s)$ and $a_i^\dagger(\omega_i)$, with amplitudes weighted by the product of the pump amplitude, $\alpha(\omega_s+\omega_i)$, and the phase-matching function $\Phi(\omega_s,\omega_i,\omega_s+\omega_i)$. We refer to this weighting function as the joint spectral amplitude (JSA),

$$F(\omega_s,\omega_i) = \alpha(\omega_s+\omega_i)\Phi(\omega_s,\omega_i,\omega_s+\omega_i), \tag{2.58}$$

and it characterizes the spectral correlations of the photons produced in SPDC. In general, the joint spectral amplitude function in Eq. 2.58 will not be separable, $F(\omega_s,\omega_i) \neq F_s(\omega_s)F_i(\omega_i)$. As a result, the photons produced in downconversion will be energy-time entangled.

An example joint-spectral amplitude function for SPDC is shown in Fig. 2.5. The contribution from the pump in Fig. 2.5(a) is always at 45 degrees. Due to energy conservation, if the signal photon has a higher energy, then the idler photon must have a lower energy such that they both add up to the same pump energy. The contribution from the phase-matching function, which is related to momentum conservation, will depend on the particular wavelengths and crystals being used. Typical crystals and wavelengths will also produce anti-correlations in the phase-matching (see Sec. 2.3.4), as in Fig. 2.5(b) [164]. As a result, the photons from downconversion are typically anti-correlated in frequency, as illustrated in Fig. 2.5(c). Nonetheless, it is possible to tailor the phase-matching function by choosing the appropriate crystals and wavelengths to manipulate the joint spectral amplitude in order to create both uncorrelated and correlated states [157, 167, 168, 169, 170].

Spectral filters are often used on each photon with two main roles: to define spectral properties and remove noise or background light from the pump. Spectral filtering can also be used to improve the purity of single photon state, at the cost of a reduced heralding efficiency [171]. If spectral filters are included, then the JSA in Eq. 2.58 becomes,

$$F(\omega_s,\omega_i) = \alpha(\omega_s+\omega_i)\Phi(\omega_s,\omega_i,\omega_s+\omega_i)H_s(\omega_s)H_i(\omega_i), \tag{2.59}$$

where H_s and H_i are the spectral filters applied to the signal and idler, respectively.

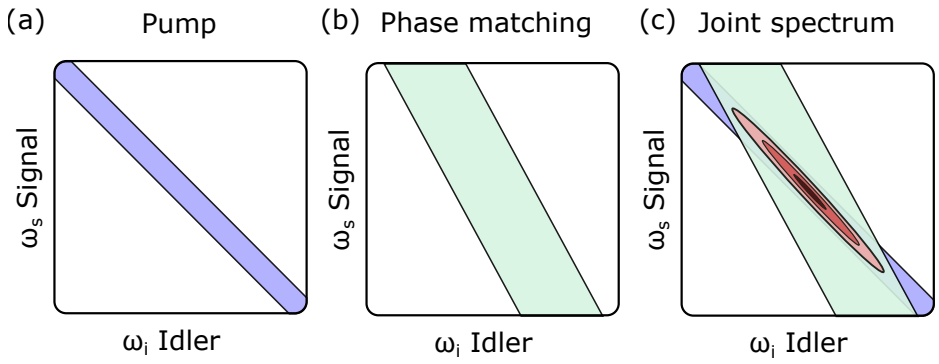

Figure 2.5: **Joint spectrum of parametric downconversion.** The spectral correlations of the photons produced in downconversion are a product of the (a) pump shape and the (b) phase-matching function. Energy conservation enforces the pump contribution to the joint spectral amplitude to always be at 45 degrees. The phase-matching function, however, depends on the wavelengths of the photons involved and the specific crystals being used. For the BiBO crystals and wavelengths used in this thesis, the phase-matching function is slightly off the 45 degree axis, giving a (c) joint spectral amplitude function, $F(\omega_s, \omega_i)$, with strong frequency anti-correlations. Different phase-matching conditions will lead to a different joint spectral amplitude function.

2.3.4 A Gaussian model of downconversion

To first order, in order to capture the spectral correlations of downconversion, and in particular energy-time entanglement, we can use the following wavefunction,

$$|\psi\rangle = \int d\omega_s \omega_i F(\omega_s, \omega_i) a_s^\dagger(\omega_s) a_i^\dagger(\omega_i) \, |0\rangle \, . \tag{2.60}$$

We can obtain intuition on the form of the JSA and the spectral correlations in downconversion by modelling the functions in Eq. 2.59 as Gaussian functions. Since the product of two Gaussian functions is also a Gaussian function, then the JSA will also be Gaussian. This model is used extensively in subsequent chapters, and as a result we mention its origins here. Note that it will not account for higher-order terms in the downconversion Hamiltonian, in particular related to double-pair emission.

We take the pump spectral amplitude function, $\alpha(\omega_p)$, to be a Gaussian with central frequency ω_p and an RMS bandwidth σ_p, and assume there is no spectral phase,

$$\alpha(\omega_p) = \frac{1}{\sqrt{2\pi\sigma_p}} \exp\left(\frac{\omega_p - \omega_{p0}}{4\sigma_p^2}\right) . \tag{2.61}$$

As before, we Taylor expand the phase mismatch Δk to first order assuming the 0th order is phase-matched,

$$\begin{aligned}\Delta k(\omega_s,\omega_i,\omega_p) &= \frac{dk_p}{d\omega}(\omega_p-\omega_{p0}) - \frac{dk_s}{d\omega}(\omega_s-\omega_{s0}) - \frac{dk_i}{d\omega}(\omega_i-\omega_{i0}) \\ &= \left(\frac{dk_p}{d\omega}-\frac{dk_i}{d\omega}\right)(\omega_i-\omega_{i0}) + \left(\frac{dk_p}{d\omega}-\frac{dk_s}{d\omega}\right)(\omega_s-\omega_{s0}) \\ &= \eta_{pi}(\omega_i-\omega_{i0}) + \eta_{ps}(\omega_s-\omega_{s0}),\end{aligned} \tag{2.62}$$

where $\eta_{ij} = dk_i/d\omega - dk_j/d\omega$ is the difference in the inverse group velocities of photons in mode i and mode j, as they travel through the downconversion crystal. We approximate the phase-matching function as a Gaussian, such that,

$$\phi(\omega_1,\omega_2,\omega_1+\omega_2) = \exp(-i\Delta kL/2)\mathrm{sinc}(\Delta kL/2) \approx \exp(-i\Delta kL/2)\exp(-\gamma\Delta k^2L^2), \tag{2.63}$$

and we model the filters as Gaussian functions,

$$H_j(\omega_j) = \exp\left(\frac{\omega_j-\omega_{j0}}{4\Pi_j^2}\right). \tag{2.64}$$

Combining the approximations for the pump bandwidth and the phase-matching function, we have a JSA approximated to first order by,

$$\begin{aligned}F(\omega_s,\omega_i) \approx \exp\Bigg[&\left(-\frac{1}{4\sigma_p^2}-\frac{1}{4\Pi_s^2}-\gamma\eta_{ps}^2L^2\right)(\omega_s-\omega_{s0})^2 \\ &+\left(-\frac{1}{4\sigma_p^2}-\frac{1}{4\Pi_i^2}-\gamma\eta_{pi}^2L^2\right)(\omega_i-\omega_{i0})^2 \\ &+\left(-\frac{1}{2\sigma_p^2}-2\gamma\eta_{pi}\eta_{ps}L^2\right)(\omega_s-\omega_{s0})(\omega_i-\omega_{i0})\Bigg].\end{aligned} \tag{2.65}$$

The exponent in Eq. 2.65 consists of three terms: the first two are applied to only the signal and only the idler, respectively, and the third term is related to the correlations between the signal and idler photons.

Rather than keep track of all the parameters in Eq. 2.65, a convenient way of expressing two-dimensional correlated Gaussian functions is in the form [172],

$$\begin{aligned}F(\omega_s,\omega_i) = &\frac{1}{\sqrt{2\pi\sigma_{\omega_s}\sigma_{\omega_i}}(1-\rho_\omega^2)^{1/4}} \\ \times\exp&\left(-\frac{1}{2(1-\rho_\omega^2)}\left[\frac{(\omega_s-\omega_{s0})^2}{2\sigma_{\omega_s}^2}+\frac{(\omega_i-\omega_{i0})^2}{2\sigma_{\omega_i}^2}-\frac{\rho_\omega(\omega_s-\omega_{s0})(\omega_i-\omega_{i0})}{\sigma_{\omega_s}\sigma_{\omega_i}}\right]\right).\end{aligned} \tag{2.66}$$

where σ_s, and σ_i, are the standard deviations of the marginals for the signal and idler, respectively, and ρ_ω is the statistical correlations. A list of properties and a visual representation of 2D Gaussian functions such as in Eq. 2.66 are detailed in Appendix B. These parameters can be measured experimentally (see Table 4.1), and can be subsequently used to predict properties of the state.

In this representation, we can explicitly write out the marginal bandwidths, σ_s, σ_i, and the statistical correlation, ρ_ω, which are,

$$\begin{aligned}
\sigma_s &= \Pi_s \sqrt{\frac{\left[{\sigma_p}^2 + {\Pi_i}^2\left(1 + 4L^2\gamma{\eta_{pi}}^2{\sigma_p}^2\right)\right]}{{\sigma_p}^2 + {\Pi_s}^2\left(1 + 4L^2\gamma{\eta_{ps}}^2{\sigma_p}^2\right) + \Pi_i^2\left(1 + 4L^2\gamma\eta_{pi}^2\sigma_p^2\right) + 4L^2\gamma{\Pi_i}^2\Pi_s^2(\eta_{pi} - \eta_{ps})^2}} \\
\sigma_i &= \Pi_i \sqrt{\frac{\left[{\sigma_p}^2 + {\Pi_s}^2\left(1 + 4L^2\gamma{\eta_{ps}}^2{\sigma_p}^2\right)\right]}{{\sigma_p}^2 + {\Pi_s}^2\left(1 + 4L^2\gamma{\eta_{ps}}^2{\sigma_p}^2\right) + \Pi_i^2\left(1 + 4L^2\gamma\eta_{pi}^2\sigma_p^2\right) + 4L^2\gamma{\Pi_i}^2\Pi_s^2(\eta_{pi} - \eta_{ps})^2}} \\
\rho_\omega &= \frac{-\frac{1}{{\sigma_p}^2} - 4L^2\gamma\eta_{pi}\eta_{ps}}{\sqrt{4L^2\gamma{\eta_{pi}}^2 + \frac{1}{{\Pi_i}^2} + \frac{1}{{\sigma_p}^2}}\sqrt{4L^2\gamma{\eta_{ps}}^2 + \frac{1}{{\Pi_s}^2} + \frac{1}{{\sigma_p}^2}}}.
\end{aligned} \tag{2.67}$$

We consider the statistical correlation ρ. We can see that the numerator consists of two terms, one which contains the pump bandwidth, σ_p, and the other which contains $\eta_{pi}\eta_{ps}$, the product of the difference in group delays of the pump and the downconverted photons. For most materials, the pump travels slower than the downconverted photons, and as a result, $\eta_{ps} = \tau_p - \tau_s > 0$ and $\eta_{pi} = \tau_p - \tau_i > 0$, are both positive. This makes ρ_ω negative, and the photons anti-correlated in frequency as in Fig. 2.5. To change the sign of the correlation directly from the source, the phase-matching function must be engineered such that either the signal travels slower than the pump, $\eta_{ps} < 0$, or the idler travels slower than the pump, $\eta_{pi} < 0$, but not both such that $\eta_{ps}\eta_{pi} < 0$.

In the limit of flat phase-matching, which we approximate with $L \to 0$, the parameters from Eq. 2.66 which characterize the distribution are,

$$\sigma_s = \Pi_s \sqrt{1 - \frac{\Pi s^2}{\Pi i^2 + \Pi s^2 + \sigma p^2}} \tag{2.68}$$

$$\sigma_i = \Pi_i \sqrt{1 - \frac{\Pi i^2}{\Pi i^2 + \Pi s^2 + \sigma p^2}} \tag{2.69}$$

$$\rho_\omega = -\frac{1}{\sqrt{1 + \frac{\sigma_p^2}{{\Pi_i}^2}}\sqrt{1 + \frac{\sigma_p^2}{{\Pi_s}^2}}}. \tag{2.70}$$

The spectral marginals, σ_s (Eq. 2.68) and σ_i (Eq. 2.69), are heavily influenced by the bandwidth of spectral filters, Π_s and Π_i, respectively. The spectral correlations, ρ_ω (Eq 2.70), between the photons are always negative, as one would expect with no phase matching, and depend on the ratio of the pump bandwidth to the filters.

2.3.5 Schmidt modes of downconversion

The spectral amplitude function provides a complete description of the two-photon state in a continuous time-frequency space, and the work in Chapter 6 consists in developing techniques to reconstruct it. If the JSA is known, then a Schmidt decomposition from Eq. 1.25, $|\psi\rangle = \sum_k \lambda_k |\varphi_k\rangle |\phi_k\rangle$, can be applied directly. The resulting Schmidt modes of downconversion ($|\varphi_k\rangle$ and $|\phi_k\rangle$), have been studied both theoretically [173, 174, 175, 176, 177, 178] and experimentally [109, 179].

We can calculate the Schmidt modes of the Gaussian model above using a singular value decomposition. The transform-limited Gaussian state $F(\omega_s, \omega_i)$ in Eq. 2.66 is first discretized into a 2-d array, and the singular value decomposition is then applied directly to the array. The decomposition gives a series of orthogonal states, $|\varphi_k\rangle$ and $|\phi_k\rangle$ (see Eq. 1.24 and Eq. 1.25), which are shown in Fig. 2.6 for a frequency anti-correlated state with $\rho = -0.995$. These can be shown to be exactly the Hermite-Gauss modes [180]. We observe by comparing Fig. 2.6(b) and Fig. 2.6(c), that the odd signal and idler Schmidt modes are anti-correlated in frequency. In Fig. 2.6(d), the joint spectral intensity is illustrated for the Schmidt decomposition when the first $k = \{0, 1, 2, 3\}$ terms in the series are included. These will constructively or destructively interfere depending on the value of the weighting coefficient λ_k. We observe, from left to right, that the JSA becomes more anti-correlated as successive terms in the series are added.

The number of Schmidt modes, in the sense of Eq. 1.19 is given by,

$$K = \frac{1}{P} = \frac{1}{\sum_k^N \lambda_k^4} = \frac{1}{\sqrt{1-\rho_\omega^2}}. \tag{2.71}$$

The larger the spectral correlations, the larger the entanglement, and the larger the number of Schmidt modes which are required to describe the state. A straightforward way to experimentally assess the effective number of spectral modes produced in downconversion is with a measurement of the unheralded $g^{(2)}(0)$. In the low-gain regime, the unheralded $g^{(2)}(0)$ can be related to the effective number of modes K [173, 181],

$$g^{(2)}(0) = \frac{\langle \hat{n}_a \hat{n}_b \rangle}{\langle \hat{n}_a \rangle \langle \hat{n}_b \rangle} \approx 1 + \frac{1}{K}, \tag{2.72}$$

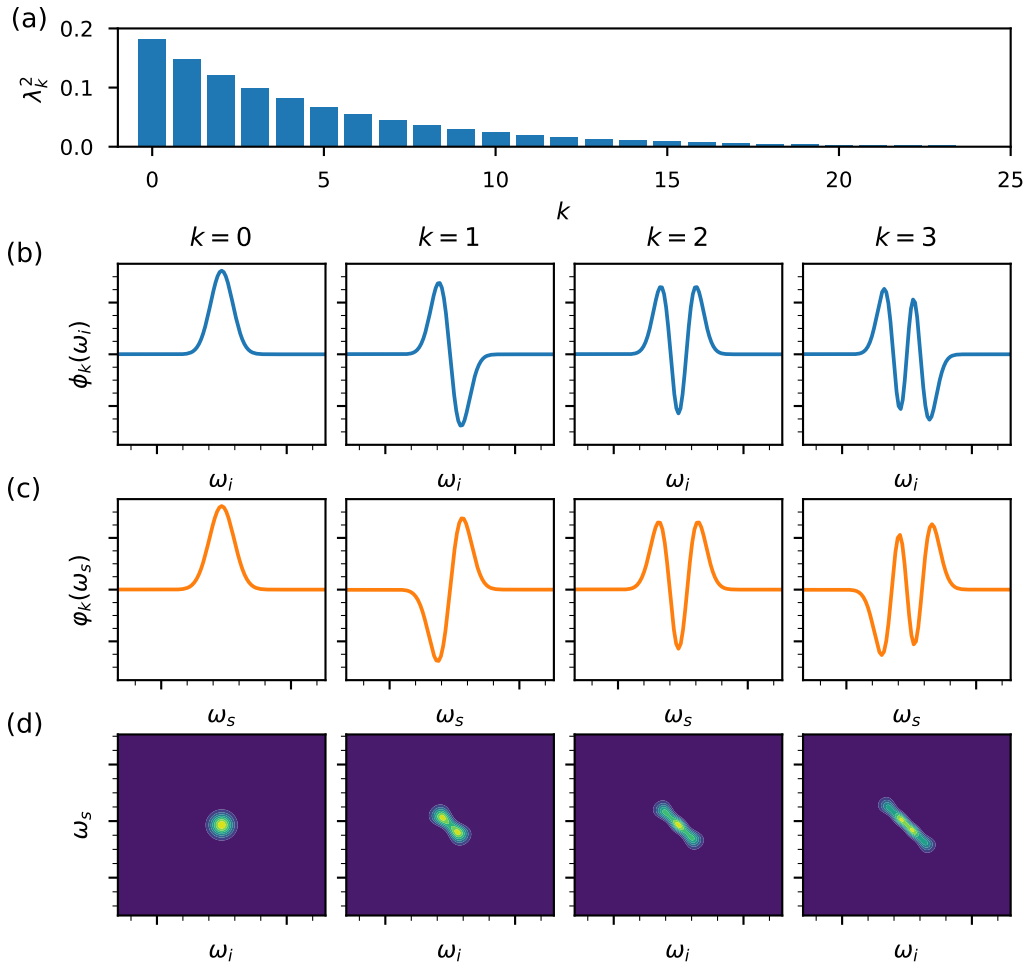

Figure 2.6: **Schmidt modes of the SPDC state.** A singular value decomposition is applied to the joint spectral amplitude of the SPDC state in the downconversion, $|\psi\rangle = \sum_k \lambda_k |\varphi_k\rangle |\phi_k\rangle$. (a) The probability λ_k^2 of each mode is illustrated along with the first few eigenmodes of the decomposition for the (b) idler and (c) signal. The state has an effective mode number of $K \approx 10$. (d) The downconversion state when the first k terms are included in the series expansion. As successive terms in the series are added, the JSA becoming more and more anti-correlated.

which can be calculated explicitly by applying the Schmidt decomposition directly to the Hamiltonian in Eq. 2.50 and considering each spectral mode k in the sum as a two-mode squeezed state. When one mode of a two-mode squeezed state is traced out, the reduced

state is a thermal state, which has a $g^{(2)}(0) = 2$. However, when the two-mode state is composed of multiple two-mode squeezers, this reduces the $g^{(2)}(0)$. In the limit of an infinite number of modes ($K \to \infty$), the reduced state has the same statistics as a coherent state, which has a $g^{(2)}(0) = 1$. Therefore, the unheralded $g^{(2)}(0)$ will have a value between 1 and 2 depending on the number of spectral modes composing the state.

2.3.6 Heralded single photons

As was discussed in Chap. 1, heralded sources of single photons are important for quantum communication and linear optics quantum computing. Using our model of photon pairs in Eq. 2.60, we can predict the spectral properties of these heralded photons. A heralded signal photon is obtained by triggering on a detection of the idler photon. Mathematically, we take the partial trace of the idler in Eq. 2.60, leaving the reduced density matrix of the signal,

$$\hat{\rho}_s = \mathrm{Tr_i}\left[|\psi\rangle\langle\psi|\right] = \int \mathrm{d}\omega_\mathrm{s}\omega'_\mathrm{s}\mathrm{F_s}(\omega_\mathrm{s},\omega'_\mathrm{s})\mathrm{a}^\dagger(\omega_\mathrm{s})\,|0\rangle\,\langle 0|_\mathrm{s}\,\mathrm{a}(\omega'_\mathrm{s}). \tag{2.73}$$

Equation 2.73 is the mixed state describing a heralded single photon composed of a mixture of frequency modes weighted by the spectral amplitude function,

$$F_s(\omega_s,\omega'_s) = \int d\omega_i F(\omega_s,\omega_i)F^*(\omega'_s,\omega_i). \tag{2.74}$$

Applying the Schmidt decomposition to the joint-spectral amplitude functions in Eq. 2.74, we find,

$$F_s(\omega_s,\omega'_s) = \sum_k \lambda_k^2\phi_k(\omega_s)\phi_k^*(\omega'_s), \tag{2.75}$$

where $\phi_k(\omega_s)$ are orthonormal spectral amplitude functions and λ_k are weighting coefficients as in Eq. 1.24. We see that Eq. 2.75 is just the two-time correlation function of the mixed state in Eq. 2.73, $C(\omega_s,\omega'_s) \equiv \langle\phi(\omega_s)\phi^*(\omega'_s)\rangle = \sum_k \lambda_k^2\phi_k(\omega_s)\phi_k^*(\omega'_s)$, where the weighted average is over all modes k [182]. For the Gaussian model above, Eq. 2.74 is,

$$\begin{aligned} F_s\left(\omega_s,\omega'_s\right) &= \sqrt{2\pi\left(1-\rho_\omega^2\right)\sigma_s^2} \\ &\times \exp\left(-\frac{1}{4\left(1-\rho_\omega^2\right)\sigma_s^2}\left[\left(\omega_s-\omega_{s0}\right)^2+\left(\omega'_s-\omega_{s0}\right)^2-\frac{\rho_\omega^2\left(\omega_s+\omega'_s-2\omega_{s0}\right)^2}{2}\right]\right). \end{aligned} \tag{2.76}$$

If $\rho_\omega = 0$, then Eq. 2.76 is factorizable and $\hat{\rho}_s = |\psi_s\rangle \langle\psi_s|$ in Eq. 2.73 is pure, whereas, if $\rho_\omega \neq 0$, $\hat{\rho}$ is not pure and the heralded single-photon will be in a mixed state.

For a more quantitative analysis, we can calculate the purity of the heralded photon state, which is equivalent to the purity of the partial trace over the idler photon. For the two-photon wavefunction in Eq. 2.60, this is [183],

$$\begin{aligned} P &= Tr\left[Tr_i\left(|\psi\rangle\langle\psi|\right)^2\right] \\ &= \int d\omega_i d\omega_s d\omega_i' d\omega_s' F\left(\omega_i, \omega_s\right) F^*\left(\omega'_i, \omega_s\right) F\left(\omega_i', \omega_s'\right) F^*\left(\omega_i, \omega_s'\right), \end{aligned} \tag{2.77}$$

and for the correlated two-photon Gaussian state in Eq. 2.66, this is,

$$P = \sqrt{1 - \rho_\omega^2}. \tag{2.78}$$

The purity of the partial trace can also be used to indicate the presence of entanglement [111]. When $\rho_\omega = 0$, the purity of the partial trace is $P = 1$, indicating a pure single photon state and a factorizable two-photon state. On the other hand, as the magnitude of ρ_ω gets larger, the purity decreases and the entanglement in the two-photon state increases. Therefore, from Eq. 2.78, we see that the statistical correlation ρ_ω between the two photons is directly related to whether entanglement is present in the system or not. Consequently, photon pairs which would be useful for applications requiring high-dimensional energy-time entanglement, and therefore strong spectral correlations, would not be useful for linear optics quantum computing, which requires spectrally pure states [21].

2.3.7 Coherence times of downconversion

Coherence is an extremely important to both classical and quantum optics as it sets the important length scales or time scales of any interference phenomena. It is the subject of entire textbooks [184] and central to the development of quantum optics [185, 186]. In Sec. 5.3.1, we will experimentally revisit the concepts of single-photon and two-photon coherence times in the context of Franson interferometry. For now we simply distinguish the one-photon and two-photon coherence times in parametric downconversion.

Classical light sources are often characterized by their coherence time. In parametric downconversion, photons are created in pairs and can be entangled. As a result, there are two time scales of interest: the time scales over which the photons on either side can interfere with themselves, for example as in the case of heralded single photons, and the time scales over which interference in the coincidences can occur. These are important to

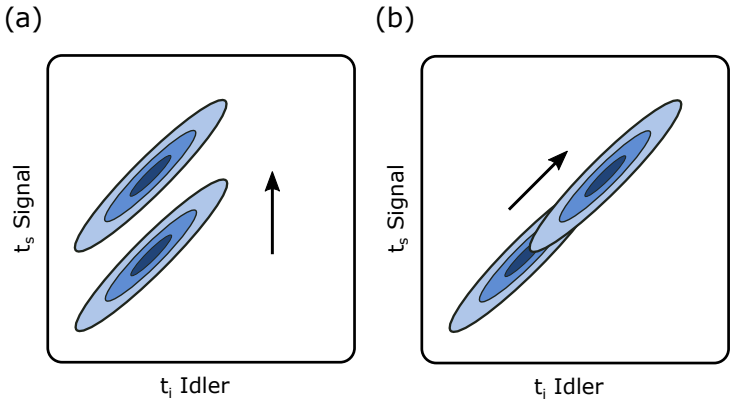

Figure 2.7: **Coherence times in downconversion.** We distinguish the (a) single-photon coherence time and the (b) two-photon coherence time as the time scales over which interference in the singles rates and the coincidence rate can occur. This is represented with the joint-temporal intensity for an example two-photon state produced in parametric downconversion (a) which is shifted in one direction, corresponding to a time delay applied to only one photon and (b) which is shifted along both directions, corresponding to a time delay applied to both photons. Interference will be observed when there is overlap between the two distributions.

track down in any experiment involving SPDC sources as they set the size of interferometers that we can use in the lab. They can be quickly estimated by considering the following quantity [156],

$$Q \equiv \left| \left\langle \hat{E}_1^{(-)}(t)\, \hat{E}_2^{(-)}(t)\, \hat{E}_2^{(+)}(t-\tau_2)\, \hat{E}_1^{(+)}(t-\tau_1) \right\rangle \right|, \tag{2.79}$$

which was seen previously in Sec. 1.6.3 when considering the interference visibility of stochastic fields. Equation 2.79 describes the average overlap between two electric field modes, $E_1^{(+)}(t-\tau_1)$ and $E_2^{(+)}(t-\tau_2)$ displaced by a time delay τ_1 and τ_2, with two undisplaced electric field modes, $E_1^{(-)}(t)$ and $E_2^{(-)}(t)$.

For the two-photon wavefunction in Eq. 2.60, with the modes 1 and 2 replaced by the signal and idler modes, Eq. 2.79 is,

$$Q = \left| \int d\omega_s d\omega_i F(\omega_s, \omega_i) F^*(\omega_s, \omega_i) e^{i\omega_s \tau_s} e^{i\omega_i \tau_i} \right| \tag{2.80}$$

and for the Gaussian model in Eq. 2.66, this becomes,

$$Q = \exp\left[-\frac{1}{2}(\sigma_s\tau_s - \sigma_i\tau_i)^2 - (1+\rho)\sigma_s\sigma_i\tau_s\tau_i\right] \tag{2.81}$$

We learn two things from Eq. 2.81. First, if one of the delays is set to zero, $\tau_i = 0$, then Q is the average overlap between a heralded single photon and its delayed copy, as in Fig. 2.7(a), and $Q = \exp\left[-\frac{1}{2}\sigma_s^2\tau_s^2\right]$. There is a characteristic time scale, $1/\sigma_s = 1/\Delta\omega_s$, which is the inverse marginal bandwidth (see Appendix B). When the applied delay is much greater than this time scale, $\tau_s \gg 1/\sigma_s$, $Q = 0$ and interference of a heralded single photon is no longer visible. This is the single-photon coherence time, and is identical to the classical coherence time. Second, when $\tau_i = \tau_s$ and $\sigma_i = \sigma_s$, then equal time delays are applied to both copies, as in Fig. 2.7(b), and $Q = \exp\left[-(1+\rho)\sigma^2\tau^2\right]$. We find a second characteristic time scale $1/\sqrt{2(1+\rho)\sigma} = 1/\Delta(\omega_s + \omega_i)$, which is related to the two-photon bandwidth (see Appendix B). When the delays are larger than this time scale, $\tau \gg 1/\sqrt{2(1+\rho)\sigma}$, interference in the coincidences no longer occurs. This is the two-photon coherence time. Both time scales are important in interferometry experiments with photons produced in downconversion as will be seen in Chap. 5.

2.3.8 Quantum sum-frequency generation

We briefly revisit sum-frequency generation but from a quantum point of view. Since sum-frequency generation is a completely classical process, we expect its quantum analogue to be similar. In this section, we calculate the sum-frequency generation unitary and show that this is indeed the case for the low-efficiency regime. With the quantum description, however, it is straightforward to calculate the evolution of a mixed state or a partially entangled state under sum-frequency generation, something not possible with the classical model of sum-frequency generation. We calculate the state after upconverting both photons from a downconversion pair.

Starting with the three-wave mixing Hamiltonian in Eq. 2.52, making the substitution, $\omega_2 = \omega_3 - \omega_1$, and emphasizing the *h.c.* term in Eq. 2.52 instead, the unitary for sum-frequency generation in the low-efficiency regime is,

$$\begin{aligned} U_{SFG}^{(1)} = 1 + \frac{\chi^{(2)}L}{12}\sqrt{\frac{\omega_{10}\omega_{20}\omega_{30}\hbar}{n_{10}n_{20}n_{30}\pi\epsilon_0 c^3 A^3}} \times \\ \int d\omega_1 d\omega_3 a_3^\dagger(\omega_3) a_2(\omega_3 - \omega_1) a_1(\omega_1) \Phi(\omega_1, \omega_3 - \omega_1, \omega_3) + h.c. \end{aligned} \tag{2.82}$$

The term in the unitary describes the destruction of two low-energy modes 1 and 2 and the creation of a higher energy mode 3. We label the signal, s, and the gate, g, as the two low energy modes and the upconverted signal mode u_s, such that $\omega_s + \omega_g = \omega_{u_s}$. The initial state is,

$$|\psi_0\rangle = |0\rangle_{u_s} |\alpha\rangle_g |\psi\rangle_s \,, \tag{2.83}$$

where the strong gate pulse, $|\alpha\rangle_g = \int d\omega_g \, |\alpha(\omega_g)\rangle$, is modelled as a coherent state with spectral amplitudes $\alpha(\omega_g)$ and the input signal photon $|\psi_s\rangle = \int d\omega_s F(\omega_s) a^\dagger(\omega_s) \, |0\rangle_s$ is modelled as a pure state with spectral amplitude $F(\omega_s)$. Applying the sum-frequency generation unitary to the initial state, $U^{(1)}_{SFG} \, |\psi_0\rangle$, the *h.c.* term in Eq. 2.82 drops out as the initial upconverted mode is the vacuum. Keeping the term of interest, we find the final state to be,

$$\left|\psi^{(1)}\right\rangle \propto \frac{\chi^{(2)} L}{12} \int d\omega_s d\omega_{u_s} \alpha(\omega_{u_s} - \omega_s) \Phi(\omega_s, \omega_{u_s} - \omega_s, \omega_{u_s}) F(\omega_s) a^\dagger_{u_s}(\omega_{u_s}) \, |0\rangle_{u_s} \,, \tag{2.84}$$

which is a convolution of the spectral amplitude of the gate pulse $\alpha(\omega_{u_s} - \omega_s)$ and the spectral amplitude of the input signal photon $F(\omega_s)$ with the phase-matching function $\Phi(\omega_s, \omega_{u_s} - \omega_s, \omega_{u_s})$ of the process. The upconverted state in Eq. 2.84 has exactly the structure as the classical upconverted field found in Eq. 2.36. This is expected since the starting signal mode is in a spectrally pure state.

Now, however, it's possible to extend the calculation to upconverted photon pairs from an entangled state. Figure 2.8 provides an example of such a scenario. We start with a signal and idler pair in a potentially entangled state $|\psi_{si}\rangle$ of the form of Eq. 2.60. Both photons are individually upconverted by strong gate pulses $|\alpha\rangle_{g_i}$ and $|\alpha\rangle_{g_s}$ to upconverted modes u_s and u_i. The initial state is thus,

$$|\psi_0\rangle = |0\rangle_{u_s} |\alpha\rangle_{g_s} |0\rangle_{u_i} |\alpha\rangle_{g_i} |\psi\rangle_{si} \,. \tag{2.85}$$

Assuming the same crystal configurations and upconversion efficiencies, the final state after upconversion on both sides is,

$$\begin{aligned} \left|\psi^{(1)}\right\rangle &= U^{(1)}_{SFG_s} \otimes U^{(1)}_{SFG_i} \, |\psi_0\rangle \\ &\propto \left(\frac{\chi^{(2)} L}{12}\right)^2 \int d\omega_s d\omega_i d\omega_{u_i} d\omega_{u_s} \alpha(\omega_{u_s} - \omega_s) \Phi(\omega_s, \omega_{u_s} - \omega_s, \omega_{u_s}) \\ &\qquad \times \alpha(\omega_{u_i} - \omega_i) \Phi(\omega_i, \omega_{u_i} - \omega_i, \omega_{u_i}) \\ &\qquad \times F(\omega_s, \omega_i) a^\dagger_{u_s}(\omega_{u_s}) a^\dagger_{u_i}(\omega_{u_i}) \, |0\rangle_{u_s} |0\rangle_{u_i} \end{aligned} \tag{2.86}$$

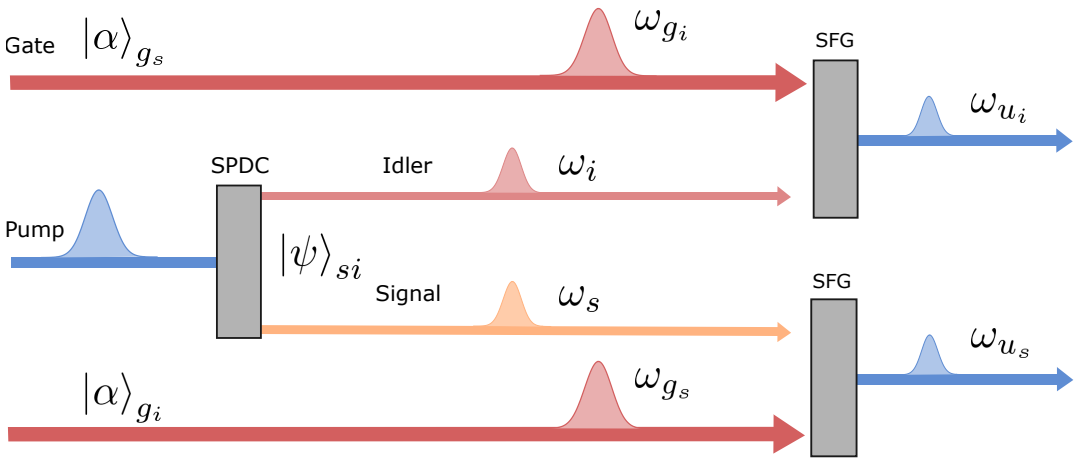

Figure 2.8: **Model for double upconversion.** Photon pairs produced in parametric downconversion are upconverted with two strong gate pulses.

The resulting wavefunction describes an energy-time entangled state in which both photons are upconverted. It holds in the low-efficiency regime. High-efficiency and high-fidelity conversion may also be achieved in principle with Gaussian waveforms on both single and energy-time entangled photons [163, 161]. In Chap. 6, the result obtained in Eq. 2.86 will be used to numerically model the expected measured intensity correlations when upconverting two photons with realistic nonlinear crystals.

Chapter 3

Ultrafast pulse manipulation and measurement

3.1 Chapter Overview

Femtosecond lasers provide excellent tools for pulse generation. Such pulses can be used as a measurement tools for physical [187], chemical [188], and biological processes [189], but others require precise control over the waveform of light [190] which can be achieved with pulse-shaping [191]. With the development and increased control over ultrafast pulses of light comes the problem of pulse measurement [192, 182]. Pulses in the several picoseconds or longer can be measured with standard photodetectors. With knowledge of the spectrum, this can provide a reasonable characterization of the laser pulse. However, many phenomena require the ability to measure events with subpicosecond resolution.

In this chapter, I focus on the techniques used to manipulate and measure ultrafast classical pulses of light. Since both classical and quantum states of light support the same electromagnetic time-frequency modes, the models for describing the manipulation and measurement of classical light extend naturally to ultrafast quantum states of light. Many can thus be tailored for quantum applications with light. The concepts of dispersion and chirp are first established in Sec. 3.2. Then, a few standard techniques used to measure ultrafast pulses are presented in Sec. 3.3. These employ the fast nonlinearities of $\chi^{(2)}$ materials to make a fast detector out of a fast gate and a slow detector. In particular, I describe optical gating in Sec. 3.3.1 and frequency resolved optical gating (FROG) in Sec. 3.3.4. These discussions bring us to the topic of phase retrieval and its connection to the full reconstruction of the electric field in Sec. 3.4.

3.2 Ultrafast pulse manipulation

When a light pulse travels through a medium, different electromagnetic modes will interact differently with the dipoles in the medium, and as a result these modes will travel at different speeds. The power will be dispersed and the pulse is stretched out in time. This can be due to a variety of effects, including modal dispersion, polarization dispersion, nonlinear dispersion, and chromatic dispersion, and each will have important consequences on optical communications. In this work, chromatic dispersion plays an important role in manipulating the temporal shape of entangled photons. Chromatic dispersion occurs when the group velocity changes as a function of the frequency. For short pulses composed of many frequencies, a small amount of chromatic dispersion can very rapidly distort the pulse. This can be a problem for long-distance communication through passive optical systems such as fibres but can also be exploited for controlling, manipulating, and measuring light pulses [182]. In this section, the concepts of chirp and chromatic dispersion are introduced via the pulse propagation equation.

3.2.1 Pulse propagation through dispersive media

In the absence of a nonlinearity, pulses propagate according to Eq. 2.18 and the spectral amplitude is constant. The spectrum in Eq. 2.18 contains both positive and negative frequency components. However, since the field in time is real, the two regions contain the same information. Therefore, we'll ignore the negative-frequency region [192, 11] and just work with the complex amplitude of the wave. The frequency components of the propagating *complex* field are thus given by,

$$\tilde{E}(\omega, z) = |\tilde{E}(\omega, z)|e^{-i\phi(\omega,z)}. \tag{3.1}$$

If a pulse is composed of many frequencies, each frequency component in the pulse will pick up a *spectral phase*,

$$\phi(\omega, z) = k(\omega)z. \tag{3.2}$$

The relative phase of each frequency will change as the pulse propagates and this will modify the temporal profile $\tilde{E}(t, z)$ of the pulse. The resulting complex field in time will be,

$$\tilde{E}(t, z) = \frac{1}{\sqrt{2\pi}} \int d\omega |\tilde{E}(\omega, z)|e^{-i\phi(\omega,z)}e^{i\omega t} \tag{3.3}$$

$$= |\tilde{E}(t, z)|e^{-i\psi(t,z)}, \tag{3.4}$$

where $\psi(t,z)$ is the *temporal phase* of the pulse. Since we are typically concerned with signals centred around a central frequency ω_0, the wave vector can be expanded around ω_0,

$$\begin{aligned} k(\omega) &= k(\omega_0) + \frac{dk}{d\omega}(\omega-\omega_0) + \frac{1}{2}\frac{d^2k}{d\omega^2}(\omega-\omega_0)^2\frac{1}{6}\frac{d^3k}{d\omega^2}(\omega-\omega_0)^3 + \cdots \\ &= k_0 + k_1(\omega-\omega_0) + \frac{1}{2}k_2(\omega-\omega_0)^2 + \frac{1}{6}k_3(\omega-\omega_0)^3 + \cdots, \end{aligned} \tag{3.5}$$

where k_n is the nth derivative of $k(\omega)$ evaluated at ω_0. Inserting the expansion of Eq. 3.5 into Eq. 3.2, we see that the derivatives of the propagation constant, k_0, k_1, k_2, k_3 also correspond to the constant, linear, quadratic, and cubic terms of the spectral phase. The nice thing about this expansion is that up to the quadratic spectral phase, each of these terms has a very physical meaning in terms of the pulse propagation. For example, a Gaussian wave packet travelling through a medium will evolve as,

$$\begin{aligned} \tilde{E}(t,z) &= \frac{1}{\sqrt{2\pi}}\int d\omega \tilde{E}(\omega,z)e^{i\omega t} \\ &= \frac{1}{\sqrt{2\pi}}\int d\omega e^{-\frac{(\omega-\omega_0)^2}{4\sigma_\omega^2} - (k_0 + k_1(\omega-\omega_0) + \frac{1}{2}k_2(\omega-\omega_0)^2)z + i\omega t} \\ &\propto \exp\left[i\omega_0\left(t - \frac{k_0}{\omega_0}z\right)\right]\exp\left[-(1-i2k_2z\sigma_\omega^2)\frac{(t-k_1z)^2}{\frac{1}{\sigma_\omega^2}+4k_2^2z^2\sigma_\omega^2}\right]. \end{aligned} \tag{3.6}$$

By inspecting Eq. 3.6, we see that the pulse remains Gaussian with modified parameters. The first coefficient k_0 in the expansion shows up in the first term of Eq. 3.6 and is related to the phase velocity $v_\phi = \omega_0/k_0$. The first derivative k_1 appears in the second term, and is the inverse group velocity $v_g = 1/k_1$ of the pulse. The decreased velocity in the medium makes the wave packet arrive with a group delay $\tau_g = z/v_g$.

Higher order derivatives will modify the shape of the pulse. In particular, chromatic dispersion occurs when the quadratic spectral phase is nonzero, $k_2 z \neq 0$. This can be observed by evaluating frequency-dependent time delay, which is the derivative of the spectral phase and has units of time,

$$\begin{aligned} \tau(\omega) = \frac{d\phi}{d\omega} &= k_1 z + k_2(\omega-\omega_0)z \\ &= \tau_g + 2A\times(\omega-\omega_0). \end{aligned} \tag{3.7}$$

The relative time delay of each frequency depends on the chirp parameter, $A = k_2 z/2$, and the separation to the centre frequency ω_0. Different frequencies travelling at different

velocities walk off from each other in time, and as a result, the pulse is stretched in time as seen in Fig. 3.1. The pulse duration at z is obtained from Eq. 3.6,

$$\begin{aligned}\sigma_t(z) &= \sqrt{\frac{1}{4\sigma_\omega^2} + 16k_2^2 z^2 \sigma_\omega^2} \\ &= \sqrt{\frac{1}{4\sigma_\omega^2} + 4A^2\sigma_\omega^2} = \sqrt{\sigma_{t_0}^2 + \frac{A^2}{\sigma_{t_0}^2}}.\end{aligned} \tag{3.8}$$

where $\sigma_{t_0} = 1/(2\sigma_\omega)$ is the transform limited pulse duration. When $A = \sigma_{t_0}^2$, the pulse duration will be a factor $\sqrt{2}$ larger than the transform limited pulse duration. The presence of a spectral or temporal phase will increase the time-bandwidth product from Eq. 1.37. A spectral phase will not modify the spectral content of the pulse, and therefore the spectral bandwidth $\Delta(\omega) = \sigma_\omega$ remains the same. From Eq. 3.8, it will increase the time duration of the pulse, $\Delta(t) = \sigma_t$, and therefore for any value $|A| > 0$, the time-bandwidth product $\Delta(\omega)\Delta(t)$ will increase. It is therefore also a useful metric to characterize the degree of chirp [12].

In the time domain, Eq. 3.6 has a temporal phase,

$$\psi(t) = \omega_0\left(t - \frac{k_0}{\omega_0}z\right) + \left[2k_2 z\sigma^2 \frac{(t-k_1 z)^2}{\frac{1}{\sigma^2} + 4k_2^2 z^2\sigma^2}\right], \tag{3.9}$$

with both linear and quadratic terms in time. The quadratic term in the temporal phase leads to an instantaneous frequency that changes with time t. The instantaneous frequency is obtained from the derivative of the temporal phase in Eq. 3.9,

$$\begin{aligned}\omega_{inst}(t) = \frac{d\psi}{dt} &= \omega_0 + \frac{4k_2 z\sigma_\omega^2(t-k_1 z)}{\frac{1}{\sigma_\omega^2} + 4k_2^2 z^2\sigma_\omega^2} \\ &= \omega_0 + \frac{2A\sigma_\omega^2(t-\tau)}{\sigma_t^2},\end{aligned} \tag{3.10}$$

and it changes linearly with time t, i.e., the pulse is chirped. In addition, the frequency ω_{inst} will increase or decrease as a function of time depending on the sign of the chirp parameter, A.

In summary, a quadratic spectral phase $\phi(\omega)$ shifts the different frequency components in time. The successive coefficients of the Taylor series expansion modify the pulse as it

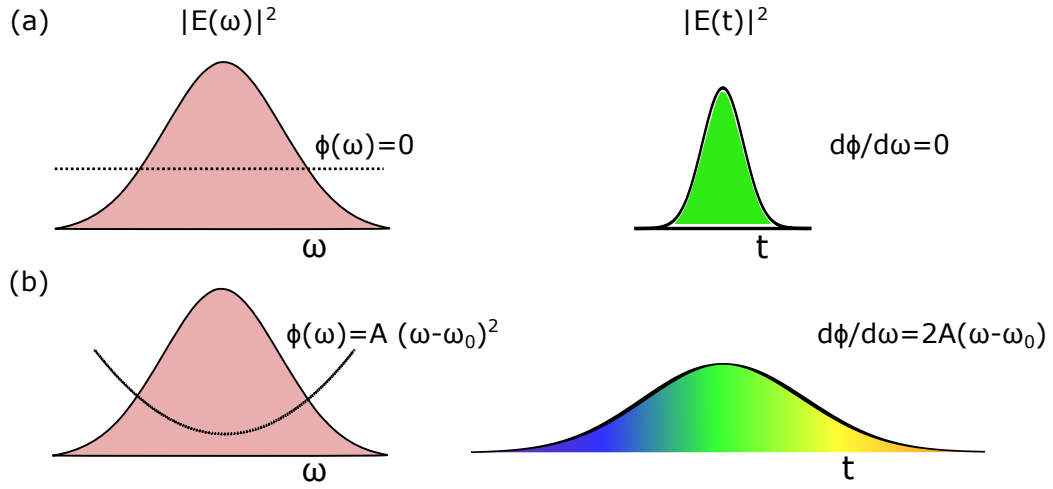

Figure 3.1: **The effect of spectral chirp on temporal profile of a pulse.** (a) A transform limited Gaussian pulse has no spectral phase, $\phi(\omega) = 0$, and all frequency components arrive at the same time. (b) A light pulse with chirp A has a frequency that changes with time. The derivative of the spectral phase $d\phi/d\omega$ has units of time and corresponds to the time delay of each frequency, which depends on the distance to the centre frequency. Lower frequencies arrive before or after higher frequencies depending on the sign of A.

travels, and this can be summarized as follows:

$$\text{Phase velocity}: \quad v_\phi = \frac{\omega_0}{k_0} \tag{3.11}$$

$$\text{Group velocity}: \quad v_g = \left(\frac{dk}{d\omega}\right)^{-1} = \frac{1}{k_1} \tag{3.12}$$

$$\text{Group velocity dispersion}: \quad \frac{d}{d\omega}\left(\frac{1}{v_g}\right) = k_2 \tag{3.13}$$

A quadratic temporal phase $\psi(t)$ shifts the instantaneous frequency at a specific time. Control over both quadratic spectral and temporal phases enable the shaping and measurement of pulses in frequency and in time [182].

3.2.2 Controlling and manipulating chirp

The three main sources of dispersion in optics arise from material dispersion, angular dispersion from refraction and diffraction, and interferometric effects. A variety of methods exist in each of these categories to control the spectral phase of light using tools and optical components readily available in most ultrafast labs. In this work, we distinguish two different types of dispersion. The first is normal dispersion, which corresponds to a positive chirp, $A > 0$, where low frequencies travel faster than high frequencies. Normal dispersion occurs when light travels through most material including nonlinear crystals and fibres, due to the variation of the refractive index with frequency. The second is negative or anomalous dispersion, which corresponds to negative chirp, $A < 0$, when high frequency components travel faster than low frequencies. Negative dispersion can be engineered in dispersion-compensating fibre in the telecom using waveguide dispersion [193]. In the NIR, geometric techniques using angular dispersion are widely used to implement negative dispersion [194]. The idea is to use the frequency dependent deflection angle of light at certain optical interfaces to create different path lengths for different wavelengths through an optical system. This has provided powerful methods to engineer negative dispersion using prism compressors [195] and diffraction gratings [196]. Pulse shapers with spatial light modulators [197, 198] can also be used to provide more control over the spectral phase.

Prism compressors provide low-loss negative dispersion making them advantageous for applications in mode-locked lasers or near single-photon level [199]. Prism compressors can provide fine tuned dispersion compensation, however, for large amounts of dispersion they require large inter-prism distances which can introduce spatio-temporal distortions [200, 201]. Folded geometries have been employed to overcome these effects [201, 199] with the ability to introduce on the order of -50 fs^2/mm. Grating compressors use the diffraction of light between two gratings to provide angular dispersion. They can introduce larger amounts of dispersion but also come with higher loss. However, with the correct geometry, the energy scattered into the first-order diffracted beam can be 90% of the incident beam [202], making them still amenable for single-photon applications [161]. Diffraction gratings cannot however easily provide dispersion control through a zero value [195]. In this work, we overcome this limitation using a dispersion control system consisting of material dispersion in fibre and grating compressors, providing large tunable control of the quadratic spectral phase of photons. Both components of the dispersion control system are detailed below. Such a technique, however, is not practical for high-intensity pulses due to the possibility of self-phase modulation in fibre [11].

Material dispersion

The dispersive properties of material arise from the frequency dependent index of refraction $n(\omega)$. In fibre, both the material dispersion and waveguide dispersion need to be considered. Only the effect of material dispersion is considered here. Using Eq. 2.19, the group velocity and group velocity dispersion is:

$$k_1 = \frac{dk}{d\omega} = \frac{\omega}{c}\left(\frac{n\left(\omega\right)}{\omega} + \frac{dn\left(\omega\right)}{d\omega}\right) \tag{3.14}$$

$$k_2 = \frac{d^2k}{d\omega^2} = \frac{\omega}{c}\left(\frac{d^2n\left(\omega\right)}{d\omega^2} + \frac{2}{\omega}\frac{dn\left(\omega\right)}{d\omega}\right) \tag{3.15}$$

$$k_3 = \frac{d^3k}{d\omega^3} = \frac{\omega}{c}\left(\frac{d^3n(\omega)}{d\omega^3} + \frac{3}{\omega}\frac{d^2n(\omega)}{d\omega^3}\right), \tag{3.16}$$

Therefore, if we know $n(\omega)$ then we can predict how a pulse will propagate through the material. For optically transparent materials and wavelengths far from resonance, the susceptibility, and therefore the wavelength dependent index of refraction, is well described by the Sellmeier equation [202, 11],

$$\chi^{(1)}(\lambda) = n^2(\lambda) - 1 = \sum_k \frac{c_k\lambda^2}{\lambda^2 - \lambda_k^2}, \tag{3.17}$$

which has the form of the Lorentz model of the atom but for multiple resonances [202]. The different terms in the expansion account for different resonances at λ_k with coefficient c_k, which can be found in tables [193].

Since the Sellmeier equations are usually given in terms of wavelength, we express Eq. 3.14 and Eq. 3.15 in terms of the wavelength. By the chain rule, we find,

$$k_1 = \frac{dk}{d\omega} = \frac{dk}{d\lambda}\frac{d\lambda}{d\omega} = \frac{\lambda}{c}\left(\frac{n\left(\lambda\right)}{\lambda} - \frac{dn\left(\lambda\right)}{d\lambda}\right) \tag{3.18}$$

$$k_2 = \frac{d^2k}{d\omega^2} = \frac{d}{d\omega}\left(\frac{dk}{d\lambda}\frac{d\lambda}{d\omega}\right) = \frac{\lambda^3}{2\pi c^2}\frac{d^2n\left(\lambda\right)}{d\lambda^2} \tag{3.19}$$

$$k_3 = -\frac{\lambda^4}{4\pi^2c^3}\left(\lambda\frac{d^3n(\lambda)}{d\lambda^3} + 3\frac{d^2n(\lambda)}{d\lambda^2}\right). \tag{3.20}$$

In optical and quantum communication, fibres made from silicon dioxide (SiO_2) are the channels that connect sources and detectors. In quantum optics experiments, they are

Table 3.1: **Sellmeier Equations.** Wavelength dependence of the index of refraction for fused silica (SiO_2) used in fibre optics, barium borate (BBO), and bismuth borate (BiBO), two common nonlinear crystals for ultrafast applications. BBO is uniaxial and has two axes, an ordinary axis, n_o, and extraordinary axis, n_e, whereas BiBO is a bi-axial crystal and all three axes must be specified. Values obtained from Ref. [193, 203].

Material	Sellmeier Equation (λ in μm)	Wavelength Region (μm)
SiO_2	$n^2 = 1 + \frac{0.6962\lambda^2}{\lambda^2-(0.06840)^2} + \frac{0.4079\lambda^2}{\lambda^2-(0.1162)^2} + \frac{0.8975\lambda^2}{\lambda^2-(9.8962)^2}$	0.21-3.71
BBO	$n_o^2 = 2.7359 + \frac{0.01878\lambda^2}{\lambda^2-(0.01822)^2} - 0.01354\lambda^2$ $n_e^2 = 2.3753 + \frac{0.01224\lambda^2}{\lambda^2-(0.01667)^2} - 0.01516\lambda^2$	0.22-1.06
BiBO	$n_x^2 = 3.0740 + \frac{0.0323\lambda^2}{\lambda^2-(0.0316)^2} - 0.01337\lambda^2$ $n_y^2 = 3.1685 + \frac{0.0373\lambda^2}{\lambda^2-(0.0346)^2} - 0.01750\lambda^2$ $n_z^2 = 3.6545 + \frac{0.0511\lambda^2}{\lambda^2-(0.0371)^2} - 0.02260\lambda^2$	0.286-2.50

often used to decouple the source from the experiment allowing independent optimization of each. In the NIR, fibres always produce positive chirp. For ultrafast applications, it's important to know how much chirp this will create. We can estimate the chirp produced by a fibre neglecting waveguide dispersion. Inserting the Sellmeier equation for SiO_2 from Table 3.1 into Eq. 3.18 and Eq. 3.19, we find at 800 nm a group velocity about 2/3 the speed of light, $v_g = 0.68\ c$, and a chirp parameter $A = 180$ fs^2/cm. In such a fibre, a 120 fs (rms) pulse will broaden to $\sqrt{2}$ times its size after 80 cm of fibre.

Grating based compressors

The bending of light due to diffraction leads to ways of engineering group-velocity dispersion [196]. This is achieved by using a pair of parallel gratings where the separation between the gratings determines the amount of spectral chirp applied to the input light. A schematic of a grating compressor is shown in Fig. 3.2. An input broadband beam is incident on the first grating with an incident angle θ_{in}. The diffracted angle at the first grating θ_D is a function of the wavelength λ, and is given by the grating equation [12],

$$\sin(\theta_D) = \sin(\theta_{in}) + m\lambda\Lambda \tag{3.21}$$

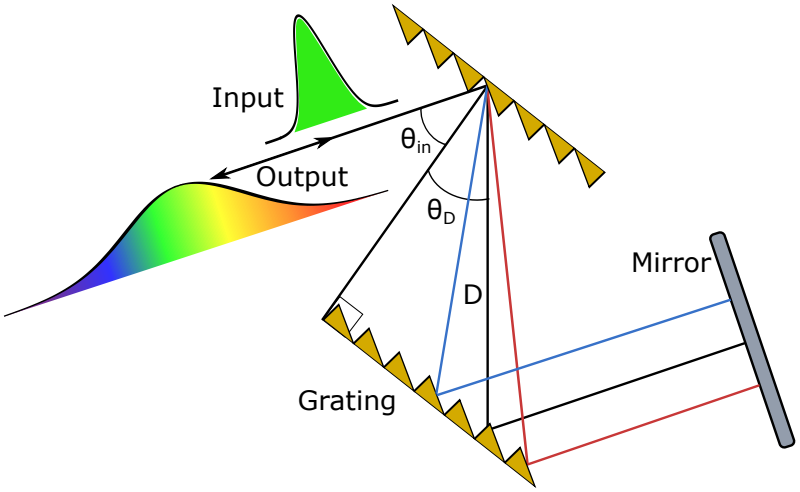

Figure 3.2: **Grating compressor.** A pair of gratings can be used to produce anomalous dispersion or negative chirp. A broadband beam is incident on the first grating at angle θ_{in}. The diffracted angle θ_D is a function of frequency, measured with respect to the grating normal.

where Λ is the period of the grating often quoted in lines per mm (l/mm) and m is the diffraction order. The longer wavelengths (red) are diffracted at a larger angle than shorter wavelengths (blue), as in Fig. 3.2.

After the second diffraction, different frequencies are parallel and separated in space. The angular dispersion created by the first grating is converted to spatial dispersion. To remove the spatial dispersion, the light can be passed through the optical system a second time. A mirror placed perpendicularly to the output rays will reflect the rays back onto themselves and back through the compressor. At the output, all frequencies end up in the same spatial mode, with higher frequencies (blue) having travelled less distance than lower frequencies (red) in the compressor, such that the higher frequencies leave the compressor ahead of the lower frequencies.

The diffraction order, $m = -1$, is the order normally used for pulse compression and spectrometers. Commercial gratings are most efficient when the light is diffracted back along the incident ray, $\sin(\theta_D) = -\sin(\theta_i)$ such that $\theta_D = \arcsin(m\lambda\Lambda/2)$. This condition is known as the Littrow configuration [202]. With this order and configuration, an efficiency above 90% at 800 nm can be achieved for a single reflection, with the total compressor efficiency after 4 grating reflections of 65%. However, the efficiency is wavelength dependent and can drop rapidly for smaller wavelength. For example, the same grating at 725 nm

will have an 80% efficiency at each reflection, corresponding to a total efficiency of 40%. As a result, the wavelength range must be kept in mind when buying gratings.

The total quadratic chirp produced by the double-pass grating compressor is given by [195, 12],

$$A = \frac{1}{2}\frac{d^2\phi}{d\omega^2} = -\frac{m^2\lambda^3\Lambda^2\ D}{2\pi c^2\cos\left(\theta_D\right)^2}. \tag{3.22}$$

Passage through the compressor always leads to negative dispersion, which is linear in the separation D between the gratings. By adjusting this separation, it is possible to control the amount of negative chirp applied. This can be used to compress a positively chirped pulse or stretch a transform-limited pulse. Since fibres in the visible apply positive dispersion and a compressor applies negative dispersion, a grating compressor can be used to compensate for the material dispersion introduced by the fibre. As a result, it's possible to control the quadratic spectral phase with a fibre and a compressor. At a wavelength of λ=800 nm, a periodicity of Λ=1200 lines/mm, and a diffraction angle close to the Littrow condition, $\theta_D \approx 29°$, a quadratic of chirp of $A \approx -1700$ fs^2/mm is attained, approximately 100 times more spectral chirp than in fibre. It is possible to make the dispersion of a grating compressor positive by inserting two convex lenses between the gratings, which effectively makes the distance D in Eq. 3.22 between the gratings negative [204].

For large bandwidths, the third-order dispersion becomes important to consider. The amount of cubic chirp introduced by the grating compressor is,

$$A^{(3)} = \frac{1}{6}\frac{d^3\phi}{d\omega^3} = -\frac{1}{6}\frac{d^2\phi}{d\omega^2}\frac{3\lambda}{2\pi c}\left[1+\frac{m\lambda\Lambda\ \sin\left(\theta_D\right)}{\cos\left(\theta_D\right)^2}\right] = -A\ \frac{\lambda}{2\pi c}\left[1+\frac{m\lambda\Lambda\ \sin\left(\theta_D\right)}{\cos\left(\theta_D\right)^2}\right]. \tag{3.23}$$

The third-order dispersion in Eq. 3.23 always has the opposite sign of the second-order dispersion in Eq. 3.22. Since gratings always apply negative second-order dispersion, the third-order dispersion will be positive. This is the same sign as the material dispersion introduced by fibres in the visible. As a result, while compressors can cancel second-order dispersion, the third-order dispersion of a fibre and compressor system will add. Using a combination of grating compressor and prism compressor can compensate for second- *and* third-order dispersion [205, 206].

3.3 Ultrafast pulse measurement techniques

In this section, I will introduce a few standard pulse measurement techniques employed in the ultrafast and nonlinear optics communities, including optical gating, the intensity

cross-correlation and auto-correlation, as well as frequency resolved optical gating (FROG). For an excellent review of ultrashort electromagnetic pulse characterization see the review by Walmsley and Dorrer [182].

3.3.1 Optical gating

In ultrafast optics, nonlinear processes are often used to provide a gate in time. The extremely fast response time of the polarization to an electric field provides the necessary interaction to create an optical gate on very short time scales. We can estimate the response time by Fourier transforming the linear susceptibility in Eq. 2.6, $R(\tau) = \mathcal{F}\left[\chi^{(1)}(\omega)\right] = \mathcal{F}\left[n^2(\omega) - 1\right]$, where the index of refraction is obtained by the Sellmeier equations in Eq. 3.17. Using the values for BBO found in Table. 3.1, this leads to a response time of about 2 fs. Thus, in principal optical gating with ultrafast pulses can resolve processes down to this time scale. In practice, however, ultrafast pulses near 2 fs are extremely challenging to produce as this time scale is close to a single-cycle of the electric field. Other techniques such as attosecond generation are used to get below one femtosecond [207].

Common approaches for optical gating use second harmonic generation of an input field or sum-frequency generation of two fields in a nonlinear crystal, as shown in Fig. 3.3. The delay between the two pulses is varied such that only when the two input fields overlap in time inside the crystal, a higher energy upconverted field will be produced which can be measured on a slow detector. From Eq. 3.24, the intensity of the upconverted field,

$$I_u(t) \propto I_s(t) I_g(t - \tau), \tag{3.24}$$

is proportional to the product of the signal intensity, $I_s(t) = |E_s(t)|^2$, and gate pulse intensity, $I_g(t) = |E_g(t)|^2$, and also depends on the time delay τ between the two fields. If the separation in time τ between the two pulses is larger than their width in time, the upconverted intensity goes to zero. As a result, one laser pulse, mediated by the interaction in the crystal, provides a fast gate in time for the other pulse. Moreover, the time resolution of the measurement is no longer limited by the response time of the detector but by the classical pulse duration of the gate, which for an ultrafast laser pulse can easily be on the order of 100 fs. Equation 3.24 remains valid in the low-efficiency regime, such that the gate power depletion can be ignored, and for broad phase-matching bandwidths. Phase matching has a considerable effect on optical gating and its effects on pulse measurement will be discussed in Section 3.3.5.

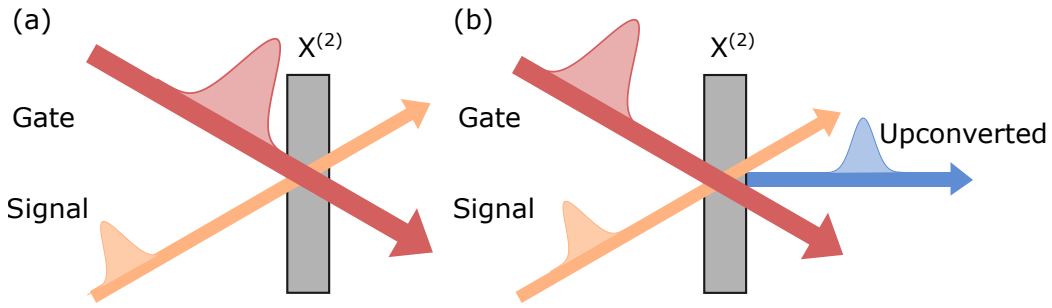

Figure 3.3: **Noncollinear sum-frequency generation for optical gating.** An ultrafast laser pulse mediated by a nonlinear crystal acts as a fast gate for another signal field. (a) When the gate pulse and input field arrive at different times in the crystal, nothing is observed. (b) However, when the gate and signal overlap in time in the crystal, an upconverted signal can be observed on a slow photodetector.

Common experimental arrangements for measurements involving optical gating include collinear and noncollinear geometries. In a noncollinear geometry as shown in Fig. 3.3, the sum frequency generated signal is emitted in a different direction than the second harmonic of the individual signal and gate pulses. This has the advantage that the constant SHG background can be spatially filtered from the SFG signal. In addition, if the signal and gate have different wavelengths, it's possible to further spectrally filter the SHG background. A combination of these techniques has proven useful for single-photon applications where noise rejection is critical [208, 84, 100, 209].

3.3.2 Intensity correlation measurements

Cross-correlation

Optical gating is used extensively in this thesis to obtain information on the temporal profile of laser pulses or photons. The simplest measurements to perform is the intensity cross-correlation of two fields or intensity auto-correlation of one input field. Here, a signal and a gate field are mixed in a nonlinear crystal and the average power of the upconverted light is measured as function of the time delays between the two pulses. The time-integrated power of the upconverted light at each time delay τ is proportional to the intensity cross-correlation, given by,

$$C^{(2)}(\tau) \propto \int dt I_s(t) I_g(t-\tau). \tag{3.25}$$

The intensity cross-correlation, by definition, is insensitive to any temporal phase, but can nonetheless be used to recover the intensity trace of the signal. When the gate pulse I_g is much shorter than the signal pulse I_s, the cross-correlation yields the intensity $I_s(t)$ of the signal pulse. Replacing $I_g(t)$ with a delta function $\delta(t)$ gives $I_s(t)$ exactly. More realistically, the signal pulse is convolved with a gate pulse of finite width and this has a tendency to make measured cross-correlation broader. For example, the intensity cross-correlation of a Gaussian signal $I_s(t) = \exp\left(-t^2/2\Delta t_s^2\right)$ with width Δt_s and a Gaussian gate $I_g(t) = \exp\left(-t^2/2\Delta t_g^2\right)$ with width Δt_g results in an RMS width of $\Delta\tau = \sqrt{\Delta t_s^2 + \Delta t_g^2}$. Inferring the width of the signal pulse from the cross-correlation thus requires deconvolving the broadening effect due to the gate. With knowledge of the spectrum of the signal, the width of the signal pulse can be used to determine the proximity of the signal to a transform limited pulse duration and estimate the amount of chirp present.

Auto-correlation

If a reference pulse is unavailable, and the same pulse is used as the signal and the gate, $I_s = I_g$, Equation 3.25 becomes the intensity auto-correlation. This can give an idea of the temporal extent, but it cannot provide details of the pulse shape. Assuming a Gaussian pulse, the intensity auto-correlation will be $\sqrt{2}$ broader than the input signal, and as a result, the signal width can be estimated from the auto-correlation. The factor will vary, however, depending on the assumed functional form, e.g., whether it is Gaussian, Lorentzian, or any other shape. Therefore, the intensity auto-correlation can only provide an estimate of the temporal width. In general however, the intensity auto-correlation cannot be used to recover the temporal intensity of the input signal. From the Wiener-Khinchin theorem [184] but applied to the intensity instead, the Fourier transform of the intensity auto-correlation functions yields the magnitude squared of the Fourier transform of the intensity,

$$\mathcal{F}\left[\int dt I_s^*(t) I_s(t-\tau)\right] = \int d\tau \int dt I_s^*(t) I_s(t-\tau) e^{-i\omega\tau} = |\tilde{I}(\omega)|^2, \tag{3.26}$$

where $\tilde{I}(\omega)$ is the Fourier transform of $I(t)$. Equation 3.26 doesn't provide the phase of $\tilde{I}(\omega)$, which is necessary in general to completely recover the temporal intensity $I(t)$. The temporal profile of the intensity auto-correlation is necessarily symmetric and in general not unique. Therefore caution must be taken when estimating the intensity pulse shape from the auto-correlation.

As in optical gating, noncollinear upconversion geometries are advantageous for intensity correlation measurements as they allow the signal to be isolated from the constant

background. In such configurations, geometrical smearing can lead to a slight temporal broadening of the measured correlation [210]. For small opening angles, the effect at 800 nm is negligible [12]. With large opening angles, the effect has been used for single-shot auto-correlation of pulses [211].

3.3.3 Spectrography

Instead of measuring only the integrated power for each time delay, resolving the spectrum of the upconverted field provides more information than the auto-correlation or cross-correlation alone. Such a measurement consists in a form of spectrography, whereby the spectral and temporal intensities are measured in series and aim at measuring simultaneously the arrival time and frequency of a pulse.

The measurement of the frequency distribution of a pulse at different temporal slices is known as a spectrogram,

$$S(\tau, \Omega) = \left| \int dt E(t) g(t-\tau) e^{-i\Omega t} \right|^2, \tag{3.27}$$

where $g(t)$ is the time gating function. The measurement of the temporal intensity profile of different spectral slices is known as a sonogram,

$$S(\Omega, \tau) = \left| \int dw E(\omega) H(\Omega-\omega) e^{-i\omega\tau} \right|^2, \tag{3.28}$$

where $H(\omega)$ is the spectral filter. The spectrogram and the sonogram in Eq. 3.27 and Eq. 3.28 are mathematically equivalent ways of representing a time-frequency map of the pulse and allow the full recovery of the instantaneous frequency. The spectrogram can be measured via frequency-resolved optical gating (FROG) whereas a sonogram can be measured with a streak camera [212]. A major breakthrough in spectrography occurred when it was realized that the knowledge of the spectrogram was sufficient to completely determine the amplitude and phase of the field $E(t)$, using methods developed in image processing. This will be discussed further in Sec. 3.4 and will lead to the FROG algorithm in Sec. 3.4.4 for phase retrieval.

3.3.4 Frequency-resolved optical gating

One of the most widely used techniques in ultrafast optics to measure a spectrogram is frequency-resolved optical gating (FROG). In FROG, one field $E_1(t)$ is gated by another

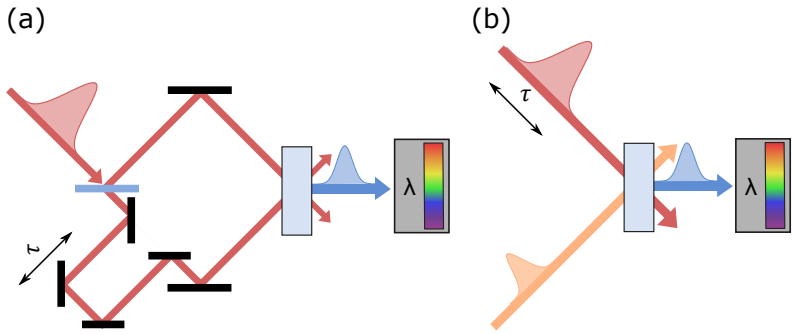

Figure 3.4: **Pulse measurement techniques.** In frequency resolved optical gating (FROG), the spectrum of the second harmonic or the sum-frequency generation is resolved at each delay τ. A spectrogram of the signal pulse can be measured for the (a) second harmonic generation FROG (SHG-FROG) or (b) cross-correlation FROG (XFROG) with a known reference gate pulse. The measured spectrogram enables the complete retrieval of the amplitude and phase of pulse using an iterative algorithm. Replacing the spectrometer with a photodetector yields the (a) intensity auto-correlation and (b) intensity cross-correlation.

field $E_2(t)$ via a nonlinear interaction and the resulting signal is spectrally resolved. In the case of $\chi^{(2)}$ nonlinearity, the two-dimensional trace is given by,

$$I_{\text{FROG}}(\tau,\omega) = \left| \int dt E_1(t) E_2(t-\tau) e^{-i\omega t} \right|^2 \tag{3.29}$$

$$= \left| \int d\omega' E_1(\omega') E_2(\omega-\omega') e^{i(\omega-\omega')\tau} \right|^2 . \tag{3.30}$$

The ultrafast gate function can be the pulse itself as in second-harmonic generation FROG (SHG-FROG) or another pulse as in cross-correlation FROG (XFROG), as shown in Fig. 3.4(c) and Fig. 3.4(d), respectively. It's possible to obtain an intuitive understanding of the spectrogram, especially in the case of XFROG, and to visualize the effect of spectral phase. Consider a signal and gate field which are chirped Gaussian pulses centred at ω_{s0} and ω_{g0},

$$E_s(\omega_s) = \exp\left[\frac{-(\omega_s-\omega_{s0})}{4\sigma_s^2} + iA_g(\omega_s-\omega_{s0})^2 \right], \tag{3.31}$$

$$E_g(\omega_g) = \exp\left[\frac{-(\omega_g-\omega_{g0})}{4\sigma_g^2} + iA_s(\omega_g-\omega_{g0})^2 \right], \tag{3.32}$$

with spectral bandwidth σ_s and σ_g and spectral chirp parameters A_s and A_g, respectively. The spectrogram can be calculated by inserting Eq. 3.31 and Eq. 3.32 into Eq. 3.30 and the result can be written as a correlated two-dimensional Gaussian (see Appendix B),

$$I_{\mathrm{FROG}}(\tau,\omega) \propto \exp\left[\frac{1}{(1-\rho)^2}\left(-\frac{(\omega-\omega_{u0})^2}{2\sigma_\omega^2}-\frac{\tau^2}{2\sigma_\tau^2}+\frac{\rho\tau(\omega-\omega_{u0})}{\sigma_\omega\sigma_\tau}\right)\right], \tag{3.33}$$

where the centre upconverted frequency $\omega_{u0}=\omega_{s0}+\omega_{g0}$ is the sum of the signal and gate centre frequencies and where the standard deviations and the statistical correlation are given by:

$$\sigma_\omega = \sqrt{\sigma_s^2+\sigma_g^2} \tag{3.34}$$

$$\sigma_\tau = \sqrt{\frac{1}{4\sigma_s^2}+4A_s^2\sigma_s^2+\frac{1}{4\sigma_g^2}+4A_g^2\sigma_g^2} \tag{3.35}$$

$$\rho = \frac{2(A_s\sigma_s^2-A_g\sigma_g^2)}{\sigma_\omega\sigma_\tau}. \tag{3.36}$$

The spectrogram takes the form of an ellipse whose inclination depends on the amount of chirp on the signal and the gate. A quadratic spectral phase on the signal A_s or the gate A_g adds a frequency dependent delay which induces correlations in the measured spectrogram as seen in Eq. 3.36. The spectral chirp on the signal or the gate also increases the length of the pulses in time, which increases the marginal in time (Eq. 3.35), but leaves the frequency marginal (Eq. 3.34) unchanged. This is visualized in Fig. 3.5 which shows the XFROG spectrogram between a Gaussian signal, with and without chirp, and a transform-limited Gaussian gate.

For a fixed time delay, the instantaneous frequency of the measured pulse,

$$\langle\omega\rangle_\tau = \frac{\int d\omega\ \omega I_{\mathrm{FROG}}(\tau,\omega)}{\int d\omega I_{\mathrm{FROG}}(\tau,\omega)} = \omega_0+\frac{\rho\sigma_\omega}{\sigma_\tau}\tau = \omega_0+\frac{2\left(A_s\sigma_s^2-A_g\sigma_g^2\right)\tau}{\frac{1}{4\sigma_s^2}+4A_s^2\sigma_s^2+\frac{1}{4\sigma_g^2}+4A_g^2\sigma_g^2}, \tag{3.37}$$

will vary as a function of the time delay between the gate and the signal in the presence of chirp. For a negative spectral phase ($A_s<0, A_g=0$) as in Fig. 3.5(b), lower frequencies arrive later and the upconverted field will have lower frequencies for larger delays, as reflected in Eq. 3.37. Similarily, for a positive spectral phase ($A_s>0, A_g=0$) as in Fig. 3.5(c), higher frequencies arrive later than lower frequencies and the upconverted field will have a higher frequency for larger delays.

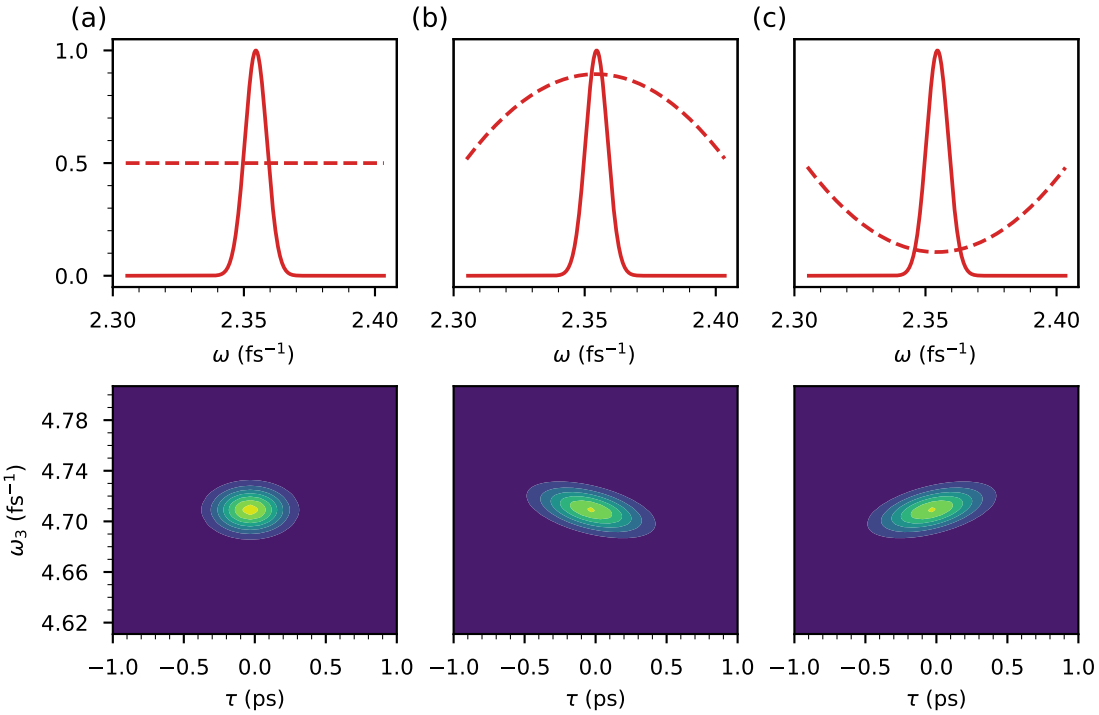

Figure 3.5: **Example spectrograms with XFROG.** (Top) Spectral intensity (solid line) and phase (dashed line) with (bottom) corresponding spectrograms for (a) transform limited, (b) negative, and (c) positive spectral chirp applied to a Gaussian pulse centred at 2.35 fs^{-1} (800 nm) with a bandwidth of 0.4 ps^{-1} (1.4 nm) and using a transform limited Gaussian gate pulse of the same bandwidth.

In SHG-FROG, as in the intensity auto-correlation, the spectrogram is necessarily symmetric. It is therefore not possible to distinguish between a positive and negative spectral phase without further information, making the SHG-FROG spectrograms less intuitive than in XFROG. Experimentally this is usually not a problem, however, as it's relatively easy to determine the sign of the spectral phase by adding dispersion on one side with a piece of glass and comparing the FROG trace with and without the added dispersion.

3.3.5 The effect of phase matching on the measurement of pulses

Nonlinear effects play an important role in ultrashort pulse measurements. As we've seen in Sec. 2.2.5, the phase mismatch in the SHG or SFG narrows the spectral bandwidth of the upconverted light and broadens it in time. These effects will also have important consequences on the measurement of ultrashort pulses.

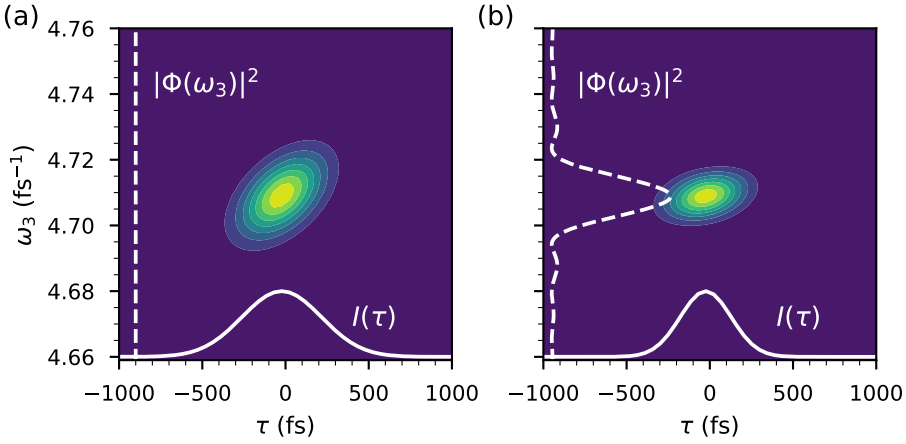

Figure 3.6: **Effect of phase-matching on XFROG Spectrogram.** Example of a XFROG spectrogram for a pulse with chirp for a phase-matching function $\Phi(\omega)$ (dashed line) which is (a) a flat and (b) a sinc function. The marginal in time $I(\tau)$ (solid line) is shown below. The phase matching function acts as a frequency filter which reduces the bandwidth of the upconverted frequencies, and also reduces the measured marginal in time $I(\tau)$.

For type-I phase matching, we include the effect of the group velocity mismatch through the effective frequency filter as in Eq. 2.40. Since the spectrogram measurements like FROG and XFROG explicitly measure the upconverted frequencies ω_3, the effect of group velocity mismatch appears directly in the spectrogram, as,

$$I_{\mathrm{FROG}}(\tau,\omega_3) = \left| \int d\omega_1 E_1(\omega_1) E_2(\omega_3-\omega_1) e^{i(\omega_3-\omega_1)\tau} \Phi(\omega_1,\omega_3) \right|^2 \tag{3.38}$$

$$\approx |\Phi(\omega_3)|^2 \left| \int d\omega_1 E_1(\omega_1) E_2(\omega_3-\omega_1) e^{i(\omega_3-\omega_1)\tau} \right|^2, \tag{3.39}$$

where we've made the assumption that $\Phi(\omega_1, \omega_3) \approx \Phi(\omega_3)$. As one would expect, the FROG trace is narrowed along the upconverted frequency axis. This is demonstrated in Fig. 3.6 which compares the XFROG spectrogram of a pulse with a flat [Fig. 3.6(a)] and a sinc [Fig. 3.6] phase matching function.

The more surprising aspect is the effect this has on the intensity cross-correlation, which is related to the FROG spectrogram delay marginal, as shown in Fig. 3.6. We can calculate the effect of group velocity mismatch on the auto-correlation by integrating the FROG spectrogram along the frequency axis, equal to,

$$\begin{aligned} I(\tau) &= \int d\omega_3 \; I_{\mathrm{FROG}}(\tau, \omega_3) \\ &= \int d\omega_3 |\Phi(\omega_3)|^2 \left| \int d\omega_1 E_1(\omega_1) E_2(\omega_3 - \omega_1) e^{i(\omega_3 - \omega_1)\tau} \right|^2 . \end{aligned} \tag{3.40}$$

The effect on the time delay marginal is also shown in Fig. 3.6. Since chirp causes different frequencies to arrive at different times, it sheers the XFROG spectrogram. If these frequencies lie outside the phase matching bandwidth, they are suppressed. This reduces the delay marginal in time, as seen by comparing Fig. 3.6(a) and Fig. 3.6(b) making the pulse appear shorter than it actually is.

As a general principle, when nonlinear effects are used to measure ultrafast pulses, the phase matching bandwidth needs to be broad for the experimental auto-correlation and FROG spectrograms to be identical to the ideal values. However, in spectrogram measurements such as FROG, it is possible to correct for the effect of phase mismatch if the cross-correlation of the spectrums of the two pulses is known, and this has been used for reconstructing ultra-broadband 10 fs pulses [210].

3.4 Phase retrieval and electric field reconstruction

The techniques to measure ultrafast pulses presented in this chapter so far attempt to extract information about a laser pulse that cannot be obtained from the spectrum alone. The additional measurements in time described above can often provide an indication as to the structure of the spectral phase of a pulse, but ideally, we would like to completely retrieve the phase information. One goal of the work in this thesis is to try and adapt these techniques to measure ultrafast quantum states of light. In particular, we initially set out to develop a quantum analogue of FROG for reconstructing two-photon states of light. In this section, I introduce the developments with respect to the phase retrieval problem that enable us to do so in Chap. 6.

The phase retrieval problem was initially posed by Pauli [213], and is related to the following question as formulated by Saxton [214], that is,"how far do the modulus of the Fourier transform of a function and the modulus of the function itself define the phase of that function?" It is fundamental in the realm of science; direct phase measurements present difficulties in wave systems in the electromagnetic spectrum, from X-rays to infrared light, but also in high-frequency sound waves and electrical circuits. Often, only the modulus of a function or the intensity of a field can be measured, but the phase is required for a full description of the signal. The value of a potential solution is therefore apparent, with ramifications in fields from astronomy to material science [215].

A few practical solutions have been proposed and developed for different formulations of the problem. In 1972, while studying electron diffraction, Gerchberg and Saxton introduced an iterative algorithm for rapidly determining the complete wave function of an electron beam from intensity recordings in the image and diffraction planes [216]. Their iterative algorithm, known as the Gerchberg-Saxton (GS) algorithm, was invented to recover the phase of a signal from two intensity measurements and could be applied to optical systems [217]. In 1978, a few years after the GS algorithm, Fienup put forward a modified GS algorithm known as the error-reduction algorithm for obtaining a two-dimensional image from one intensity measurement of its Fourier transform and weaker constraints on the image such as non-negativity or known support [218, 219, 220]. This type of phase-retrieval problem has been extensively studied in crystallography [221], astronomy [215], due to the wide availability of charged-couple devices (CCD) and the ease with which it is possible to measure the intensity of a field in space. It has also been instrumental in of X-ray imaging for developing a technique known as coherent X-ray diffraction [222, 223].

In ultrafast optics, the problem of phase retrieval has also been extensively studied. Knowing the pulse duration remains critical, both in terms of diagnostics and applications, and many different techniques have been explored involving tomography, spectrography, and interferometry [182]. A major breakthrough occurred when it was realized that it was possible to invert the spectrogram of a pulse to obtain its amplitude and phase using an iterative algorithm very similar to the error-reduction algorithm introduced by Fienup. Ultrafast pulses don't satisfy the finite support constraint in the error-reduction algorithm, and therefore the error-reduction algorithm can't be applied directly. However, in 1993, Trebino showed that if the support constraint in the error-reduction algorithm were replaced with another type of constraint, called a mathematical form constraint, it became possible to recover the amplitude and phase of the signal from its spectrogram [224, 225]. This forms the basis of one of the most popular nonlinear measurement techniques used today known as frequency-resolved optical gating (FROG) and the related FROG algorithm to recover the pulse.

3.4.1 Phase retrieval from two intensity measurements

For the problem of recovering phase from two-intensity measurements as in electron microscopy or wavefront sensing, one has access to the intensity in two domains which are related by the Fourier transform,

$$F(k_x, k_y) = |F(k_x, k_y)|e^{i\phi(k_x,k_y)} = \frac{1}{\sqrt{2\pi}} \int dk_x dk_y f(x, y) e^{-ik_x x - ik_y y}, \tag{3.41}$$

$$f(x, y) = |f(x, y)|e^{i\psi(x,y)} = \frac{1}{\sqrt{2\pi}} \int dx dy F(k_x, k_y) e^{ik_x x + ik_y y}, \tag{3.42}$$

and wishes to recover the phase $\phi(k_x, k_y)$ or $\psi(x, y)$ from measurements of the intensities $I(x, y) = |f(x, y)|^2$ and $I(k_x, k_y) = |F(k_x, k_y)|^2$. The general problem is highly non-trivial, not unique, and with no closed solution. Yet, the reliability of modern computers has enabled the growth and popularity of the iterative GS algorithm, which converges on a solution in many practical scenarios.

There are a few ambiguities in the phase solution that should be mentioned before describing the algorithm itself. If $f(x, y)$ is a solution, then the following are also solutions to the problem:

1. an absolute phase factor: $e^{i\psi_0} f(x, y)$
2. a translation: $f(x - x_0, y - y_0)$
3. inversion: $f(-x, -y)^*$.

These arise because of the modulus of the Fourier transform is insensitive to a constant phase factor, a translation, and an inversion. For most imaging problems, these typically don't pose a problem and are therefore referred to as to as "trivial" ambiguities [215].

The third ambiguity can arise if the intensity distribution in one plane is centrosymmetric. Then, the complex conjugate of any solution will also be a solution, leading to a two-fold ambiguity. To see why this is the case, consider a function $F(k_x, k_y) = \int dx dy f(x, y) e^{ik_x x + ik_y y}$. Its modulus squared is,

$$|F(k_x, k_y)|^2 = \int dx dy f(x, y) e^{ik_x x + ik_y y} \int dx' dy' f(x', y')^* e^{-ik_x x' - ik_y y'}, \tag{3.43}$$

and, by construction, we can think of $f(x, y)$ as a solution satisfying the constraint $I(k_x, k_y) = |F(k_x, k_y)|^2$. If the modulus is centrosymmetric, $|F(k_x, k_y)|^2 = |F(-k_x, -k_y)|^2$, then we can replace $(k_x, k_y) \to (-k_x, -k_y)$ in Eq. 3.43. After swapping the two terms, we obtain,

$$|F(k_x, k_y)|^2 = \int dx'dy' f(x', y')^* e^{ik_x x' + ik_y y'} \int dxdy f(x, y) e^{-ik_x x - ik_y y}, \tag{3.44}$$

and, comparing with Eq. 3.43, we see that the conjugate $f(x, y)^*$ is also a solution to $|F(k_x, k_y)|^2$. If the intensity distribution in *both* planes is centrosymmetric, then the complex conjugate in either plane will also be a solution. This ambiguity will show up in the context of two-photon state reconstruction.

3.4.2 Gerchberg-Saxton Algorithm

The GS algorithm is based on a method of alternate projections. It employs the Fast Fourier Transform (FFT) to switch between the object domain and the Fourier domain, imposing the measured intensity constraints at each step, but preserving the phase from the previous step.

The algorithm consists of the following four steps which are illustrated in Fig. 3.7:

1. Replace the magnitude of $F(k_x, k_y)$ with the measured values $F'(k_x, k_y) = \frac{F(k_x,k_y)}{|F(k_x,k_y)|}\sqrt{I(k_x, k_y)}$.
2. Inverse Fourier transform $F'(k_x, k_y)$ to obtain an estimate of $f(x, y)$.
3. Replace the magnitude of $f(x, y)$ with the measured values $f'(x, y) = \frac{f(x,y)}{|f(x,y)|}\sqrt{I(x, y)}$.
4. Fourier transform $f'(x, y)$ to obtain an estimate of $F'(k_x, k_y)$.

The algorithm can be seeded with an initial guess containing the sampled image amplitudes accompanied with a random phase. In the first iteration, we make a projection onto the constraint set that satisfies the measured intensities in the object domain. We then project onto the other set that satisfies the measured intensities in the Fourier domain. At each step, an error is calculated between the measured and reconstructed intensities. This can take many forms. For example, one could use the normalized root mean square error

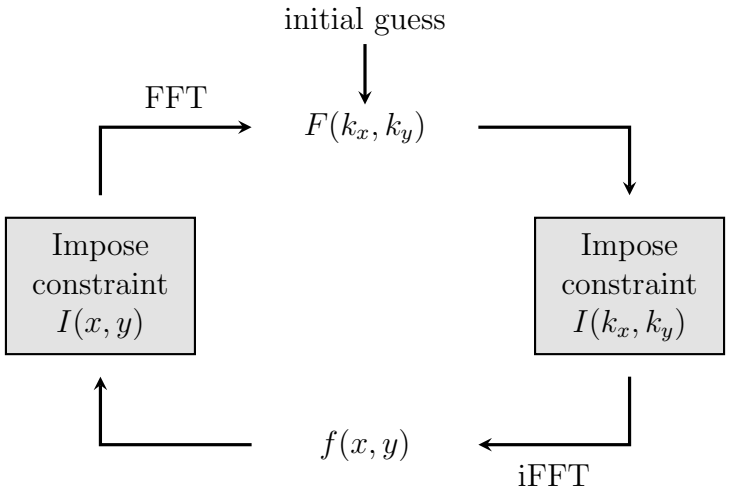

Figure 3.7: **Block diagram of the Gerchberg-Saxton algorithm.** At every iteration, the Fast Fourier Transform is applied to one axis of the state after which the magnitude of state is replaced with the measured data while the phase of the state is preserved. This is repeated until the error between the measured and recovered intensities converges.

between the measured image and the reconstructed image in either plane,

$$e_F^2 = \frac{\sum_{k_x,k_y} \left(\sqrt{I(k_x,k_y)} - |F(k_x,k_y)|\right)^2}{\sum_{k_x,k_y} I(k_x,k_y)} \tag{3.45}$$

$$e_f^2 = \frac{\sum_{x,y} \left(\sqrt{I(x,y)} - |f(x,y)|\right)^2}{\sum_{x,y} I(x,y)}, \tag{3.46}$$

where the sum is over all the pixels in the image. More sophisticated error models exist that are invariant under a linear phase term, which shouldn't be included in the error model as they correspond to translations of the image [226]. Importantly, Gerchberg and Saxton showed using Parseval's theorem that at each iteration, the measured error must decrease or remain constant [216, 214]. Thus, while the algorithm can "lock", such that the error remains the same at each iteration, the error will not diverge.

As a simple example, suppose we had an initial distribution in momentum space given by the Gaussian function shown in Fig. 3.8(a). We could ask what phase profile to use to create the spatial distribution in Fig. 3.8(d). This is the analogous synthesis problems with applications in wavefront shaping [227]. Feeding these two images into the GS algorithm,

and normalizing their intensities to satisfy Parseval's theorem, after 1000 iterations, we find the phase distribution in Fig. 3.8(c) produces the intensity pattern in Fig. 3.8(e) with an error $e_f = 0.36$. The reconstructed intensity in Fig. 3.8(e) is not a perfect reconstruction of

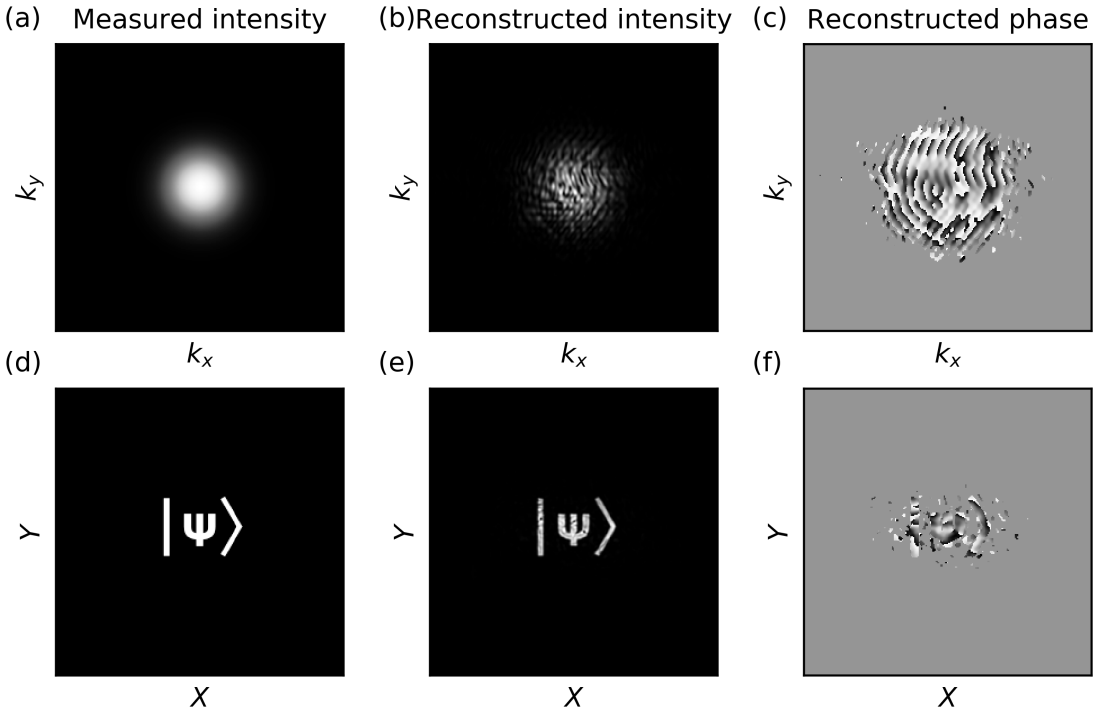

Figure 3.8: **Example GS algorithm applied to image synthesis.** The GS algorithm is applied to the measured intensity profiles in (a) momentum and in (d) space. After 1000 iterations the reconstructed intensities in (b) momentum and (e) space are found with corresponding reconstructed phase profiles (c) and (f), respectively.

the measured intensity in Fig. 3.8(d), nonetheless, it's remarkable that such a simple algorithm can return an image resembling the desired output. Due to its simplicity and ease to code on a computer, the GS algorithm remains a very popular phase-retrieval method used today [228] with applications in pulse-shaping [229], holography [227], spectroscopy [230], mode reconstruction [231], neutron tomography [232], and imaging exoplanets [233].

3.4.3 Phase retrieval from one intensity measurement

It's not always possible to obtain the intensity in both domains. In various fields of science including electron microscopy, crystallography, astronomy, optical imaging, and laser physics, sometimes only the intensity measurement or the phase in the Fourier domain is available. The problem then consists in recovering the function $f(\vec{x})$ from the magnitude of its Fourier transform $|F(\vec{k})|$ and potentially some additional constraints.

This problem has been of considerable interest for many decades. In one dimension, it was shown that there is an infinite number of functions $f(x)$ that satisfy the modulus of the Fourier transform $|F(k)|$ [234, 235]. Moreover, even if, in addition, the support of $f(x)$ were known, i.e., where $f(x)$ goes to zero, this is still insufficient to uniquely determine $f(x)$ [192]. Most interestingly, it was found that this was not the case for the two-dimensional problem. The phase retrieval problem from one intensity measurement has an essentially unique solution in two dimensions as long as additional information on where the function goes to zero is available [215]. After the success of the iterative GS algorithm, Fienup showed that if in addition to the Fourier modulus, $|F(k_x, k_y)|$, the support of $|f(x, y)|$ was known, this was enough to recover the object $f(x, y)$ [218, 220, 236]. He introduced an error-reduction algorithm that only required one intensity measurement, unlike the GS algorithm which required two.

The error-reduction algorithm is an iterative algorithm which has a very similar structure to the GS algorithm, except that the magnitude constraint in step (3) in Sec. 3.4.2 is replaced with a domain or support constraint,

$$3.\ f'(x,y) = \begin{cases} f(x,y) & \{x,y\} \notin \gamma \\ 0 & \{x,y\} \in \gamma, \end{cases}$$

where γ is the set of points where $f(x, y)$ violates the domain constraint, such that $f'(x, y)$ is set to 0 at these points. Importantly, Fienup showed that his form of the error-reduction algorithm was equivalent to a gradient-descent algorithm providing a partial intuition as to why it worked at all [220]. Since then, different versions of the original algorithm have been explored, and in particular the more successful hybrid input-output algorithm which has a higher rate of convergence [236, 223].

3.4.4 FROG Algorithm

The problem of phase retrieval is prevalent in ultrafast optics since the spectrum of a pulse can easily be measured but not the pulse temporal profile. Recovering the phase from

the spectrum alone is a phase-retrieval problem from one intensity measurement in one dimension and, as detailed earlier, it's bad news for anyone trying to solve it. Therefore, more sophisticated methods are required.

The FROG algorithm is an iterative algorithm that recovers the amplitude and phase of a pulse from the FROG spectrogram, and which is widely used in ultrafast optics as it is relatively straightforward to measure spectrograms in the lab using nonlinear techniques (see Sec. 3.3.4). The algorithm is a type of spectrogram inversion that falls into the same category as the phase retrieval problem from one intensity measurement but in *two dimensions*. In fact, the innovation of the FROG algorithm is to transform the one-dimensional phase-retrieval problem in ultrafast optics, which is a priori not solvable, into a two-dimensional phase retrieval problem that can be solved using an algorithm similar to the error-reduction algorithm [192]. A comprehensive description of the FROG technique and reconstruction algorithm can be found in Rick Trebino's book [192]. It is definitely worth picking up for anyone trying to implement FROG in the lab and apply the FROG algorithm to measured spectrograms. Note that phase retrieval can also be performed using the sonogram of an ultrafast pulse [237].

The measured spectrogram in FROG has the general form,

$$I_{\mathrm{FROG}}(\tau,\omega) = \left| \int dt \; E_{\mathrm{sig}}(\tau,t) e^{-i\omega t} \right|^2, \tag{3.47}$$

where $E_{\mathrm{sig}}(\tau,t)$ is the signal field which will depend on the particular FROG geometry being used. For the case of XFROG, the signal field is $E_{\mathrm{sig}}(\tau,t) = E_1(t)E_2(t-\tau)$, and in SHG-FROG, the signal and the gate are the same, $E_{\mathrm{sig}}(\tau,t) = E_1(t)E_1(t-\tau)$. If the Fourier transform is taken with respect to τ, then the spectrogram becomes,

$$I_{\mathrm{FROG}}(\tau,\omega) = \left| \int \int dt d\Omega \; E_{\mathrm{sig}}(\Omega,t) e^{-i\omega t - i\Omega\tau} \right|^2. \tag{3.48}$$

Expressing the FROG trace in this form may seem arbitrary at first but this is exactly the form of a two-dimensional phase-retrieval problem, i.e., find $E_{\mathrm{sig}}(\Omega,t)$ given the modulus of its Fourier transform, $I_{\mathrm{FROG}}(\tau,\omega)$. Note that knowing $E_{\mathrm{sig}}(\Omega,t)$ is sufficient to recover the original field $E(t)$ as detailed below.

Thus, one could try to apply Fienup's error-reduction algorithm directly. Unfortunately, unlike image recovery, the representation of the electric fields as a pulse doesn't have finite support. If the electric field in time is finite, the field in frequency won't be. Consequently, the typical constraint of finite support doesn't apply. There is a stronger constraint, however, that is available. We know the mathematical structure of the signal

field $E_{\text{sig}}(\tau, t)$ from the FROG geometry. For example, in SHG-FROG, the upconverted signal field is constrained to be the product of the two input fields, $E_{\text{sig}}(\tau, t) = E_1(t)E_1(t-\tau)$. Therefore, by replacing the finite support constraint in the error-reduction algorithm with the mathematical form constraint, we obtain the FROG algorithm illustrated in Fig. 3.9.

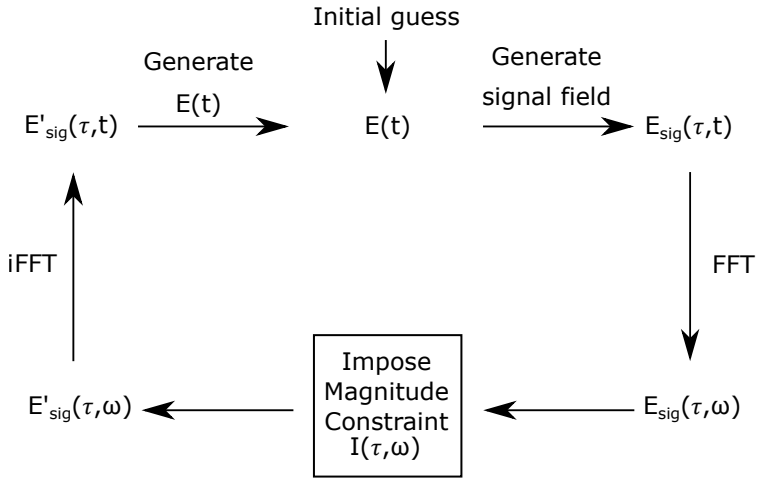

Figure 3.9: Block diagram for a generic FROG Algorithm

Its steps are the following:

1. Generate the signal field $E_{\text{sig}}(\tau, t)$ from $E(t)$ using the known FROG geometry.
2. Fourier transform $E_{\text{sig}}(\tau, t)$ to obtain an estimate of $E_{\text{sig}}(\tau, \omega)$.
3. Replace the magnitude of $E_{\text{sig}}(\tau, \omega)$ with the measured values $E'_{\text{sig}}(\tau, \omega) = \frac{E_{\text{sig}}(\tau,\omega)}{|E_{\text{sig}}(\tau,\omega)|}\sqrt{I(\tau, \omega)}$.
4. Inverse Fourier transform $E'_{\text{sig}}(\tau, \omega)$ to obtain an estimate of $E'_{\text{sig}}(\tau, t)$.
5. Generate a new estimate of $E(t)$ from $E'_{\text{sig}}(\tau, t)$.

The first step (1) is a straightforward calculation of the signal field $E_{\text{sig}}(t, \tau)$ from the current estimate of the electric field $E_1(t)$ and the gate $E_2(t)$, and based on the particular FROG geometry. The following three steps (2-4) are identical to other alternate projection algorithms, where the current estimate is projected onto the set that satisfies the measured data.

The last step (5) requires generating the next estimate of $E(t)$ from the signal field $E'_{\text{sig}}(t,\tau)$. This is the mathematical form constraint. There are a number of different ways of approaching this problem, which lead to the different versions of the FROG algorithm [192]. The initial proposal, known as the "Vanilla" FROG algorithm, calculates the next estimate by integrating the signal field [224],

$$E(t) = \int d\tau E'_{\text{sig}}(\tau, t). \tag{3.49}$$

This method is fast and works well for SHG-FROG but cannot be applied to XFROG. Improvements over the "Vanilla" FROG algorithm led to the Generalized Projections algorithm [238]. Here, the next guess is obtained by finding the field $E(t)$ that minimizes the distance to the signal field $E'_{\text{sig}}(t,\tau)$,

$$Z = \sum_{t,\tau}^{N} \left| E'_{\text{sig}}(t,\tau) - E_1(t)E_2(t-\tau) \right|^2. \tag{3.50}$$

This method works and solves certain convergence issues of the "Vanilla" FROG algorithm but can be rather slow and difficult to implement. Another approach involves representing the field $E'_{\text{sig}}(t,\tau)$ as an outer product using array manipulation and keeping only the principal component of a singular value decomposition (SVD) as the next estimate for $E(t)$. The idea being that if the spectrogram field is correct, the outer product of the signal field should only have one eigenvalue and one eigenvector. Keeping the eigenvector associated to the largest eigenvalue in the SVD is then the next best guess for the field. This version, called the Principle Component Generalized Projections Algorithm (PCGPA) [239], is very fast allowing real-time reconstructions of electric fields and also turns out to be easier to implement in software than the Generalized Projections algorithm.

In order to track the progress of the algorithm, it's common to define the FROG error,

$$E^{(k)}_{\text{FROG}} = \sqrt{\frac{1}{N^2} \sum_{i,j=1}^{N} \left(I_{\text{FROG}}(\omega_i, \tau_j) - \mu \left| E^{(k)}_{\text{sig}}(\omega_i, \tau_i) \right|^2 \right)^2} \tag{3.51}$$

where I_{FROG} is the measured spectrogram, $|E^{(k)}_{\text{sig}}(\omega_i,\tau_i)|^2$ is the intensity at the kth iteration, and μ is a real normalization constant that minimizes the error. If measured trace $I_{\text{FROG}}(\omega_i,\tau_j)$ is normalized to 1 before inserting it into Eq. 3.51, then the FROG error can be thought of as the average percentage error between the measured and recovered trace.

As in other phase-retrieval algorithms, the FROG algorithm assumes that the field in frequency and time are related by the Fourier transforms. As a result, FROG also suffers

from the usual "trivial" ambiguities: global phase, translations, and inversions. This is usually not a problem, except in the case of SHG-FROG where the field and its conjugate give the same trace. In addition, the use of the Fourier transform implies that the pulse to be retrieved is assumed to be coherent or in a pure state. Therefore, the FROG algorithm as it stands will not work for an incoherent field or by extension a mixed state. Modifications to the PCGP FROG algorithm have been explored to handle incoherent states [240].

Measurements in the lab are always noisy. Luckily, the FROG algorithm is fairly robust to noise. There is nonetheless a certain amount of post-processing that must be applied to the data prior to feeding it into the algorithm. Techniques such as background subtraction, corner suppression, and low-pass filtering are often required to make the FROG algorithm converge [241, 192]. Furthermore, the use of discrete FFT enforces a constraint on the relationship between the binning of the frequency and time axes. Since the signal field $E_{\text{sig}}(\tau, t)$ in step 1 is generated from $E(t)$, the time bins for the axes t and τ are necessarily the same. The use of the FFT in step 2 forces the bins in frequency to be related to those in time. As a result, before applying the FROG algorithm, the measured FROG spectrogram must be binned such that the frequency and time axes are scaled appropriately to that required by the discrete FFT. Other iterative techniques have been devised that forgo this need for binning, such as time-domain ptychography [242]. The FROG reconstruction technique will be revisited in Ch. 6 where it will be used as a benchmark for the algorithm we developed to reconstruct two-photon entangled states.

Chapter 4

Direct Characterization of Ultrafast Energy-Time Entangled Photon Pairs

Notes and acknowledgements

The contents of this chapter were published on January 30, 2018, as [209]:

J.P.W. MacLean, J.M. Donohue, K.J. Resch. *Direct characterization of ultrafast energy-time entangled photon pairs.* Phys. Rev. Lett. **120**, 053601 (2018).

Author Contributions

Kevin Resch and **John Donohue** conceived of the study.

John Donohue built the initial photon source and acquisition software.

Jean-Philippe MacLean and **John Donohue** carried out the experiment and analyzed the data.

Jean-Philippe MacLean wrote the first draft of the manuscript.

All authors contributed to the final version.

4.1 Chapter Overview

Energy-time entangled photons are critical in many quantum optical phenomena and have emerged as important elements in quantum information protocols. Entanglement in this degree of freedom often manifests itself on ultrafast time scales making it very difficult to detect, whether one employs direct or interferometric techniques, as photon-counting detectors have insufficient time resolution. Here, we implement ultrafast photon counters based on nonlinear interactions and strong femtosecond laser pulses to probe energy-time entanglement in this important regime. Using this technique and single-photon spectrometers, we characterize all the spectral and temporal correlations of two entangled photons with femtosecond resolution. This enables the witnessing of energy-time entanglement using uncertainty relations and the direct observation of nonlocal dispersion cancellation on ultrafast time scales. These techniques are essential to understand and control the energy-time degree of freedom of light for ultrafast quantum optics.

4.2 Context

The energy-time degree of freedom of nonclassical light is of great interest for quantum information as it supports various encodings, including frequency bins [243], time bins [141], and broadband temporal modes [107], and is intrinsically robust for propagation through long-distance fiber links [244]. Applications which harness quantum correlations in this degree of freedom, referred to as energy-time entanglement [49], include dispersion cancellation [245, 246], high-dimensional quantum key distribution [71, 72], and quantum-enhanced clock synchronization [247]. In ultrafast optics and attosecond physics, the ability to measure both frequency and temporal features has led to important innovations in electric field reconstruction techniques [225, 182] and pulse characterization on very short time scales, enabling advances in spectroscopy [188], laser physics [248], nonlinear optics [249], and imaging [189]. In order to characterize and control energy-time entangled photons and advance biphoton pulse shaping, similar measurement capabilities are essential in the quantum regime.

Experimental signatures of entanglement can arise in correlation measurements of complementary variables [250], or through nonlocal quantum effects [49, 245]. With the energy-time degree of freedom, one complementary set consists of measuring the intensity correlations as a function of the photon frequencies and as a function of their time of arrival. These have been individually realized for different photonic systems with measurements in frequency [170, 251] or in time [252, 151, 253]. Certifying the presence of entanglement with

direct measurements requires both spectral and temporal correlations, since acquiring only one remains insufficient to uniquely specify the other due to the ambiguity of the spectral phase. Depending on the platform, this can be challenging. Narrow-band photons from atomic systems can be readily measured in time but are difficult to spectrally resolve [253]. THz-bandwidth photons produced in spontaneous parametric down-conversion (SPDC) are often characterized spectrally, but they can have features on femtosecond time scales below current detector resolution [75].

Other techniques can be employed to infer the presence of energy-time entanglement. High-order interference effects with Franson interferometers have been used to illustrate entanglement between two [50] and three photons [254]. Nonlocal dispersion cancellation [245], whereby the temporal spread in coincidences remains unchanged when equal and opposite dispersion is applied to each photon, can also be used to witness entanglement [255, 256]. For either method to be effective, the detector resolution must be shorter than the time scales of the correlations. Strong energy-time entanglement can nonetheless exist when the time scales of the correlations are shorter. Certain observations have pointed to nonlocal dispersion cancellation in this regime, but they either required introducing a very large amount of dispersion such that temporal resolution could be achieved with standard detectors [257], or used sum-frequency generation (SFG) between the photon pairs [258], which, unlike measurements with fast and independent detectors, has a close classical analogue [259]. Directly measuring ultrafast quantum effects requires new methods to control and analyze single photons in the time domain.

In nonlinear optics and laser physics, optical gating is widely used to overcome limitations with detectors which are too slow to observe features on subpicosecond time scales. The gating is achieved by combining the signal with a short gate pulse in a nonlinear medium and measuring the up-conversion signal on the detector. With fast gates and slow detectors, an effective fast detector can be engineered to temporally resolve single photons [208, 260] and photon pairs [252].

In this chapter, we develop fast optical gating to achieve subpicosecond timing resolution for spatially separated pairs of single photons. We use this technique in conjunction with single-photon spectrometers to explicitly measure both the spectral and temporal correlations of broadband photons, as well as the cross-correlations between the frequency of one photon and the time of arrival of the other. Furthermore, by controlling the dispersion of each photon, our high-resolution joint temporal measurements make it possible to directly observe nonlocal dispersion cancellation on femtosecond time scales.

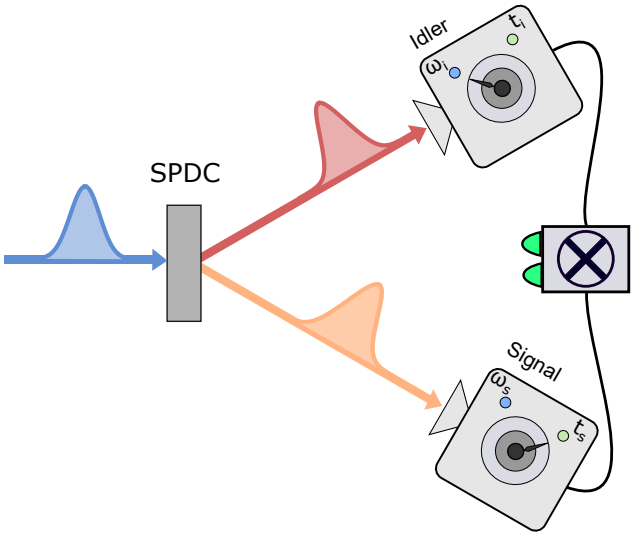

Figure 4.1: **Measuring frequency-entangled photons in frequency and time.** Frequency-entangled photon pairs are created through spontaneous parametric down-conversion of an ultrafast pump pulse. Signatures of energy-time entanglement can arise through correlation measurements in the frequency and time of arrival of the photons or by observing nonlocal dispersion cancellation. However, for THz-bandwidth SPDC photons, both methods require fast coincidence detectors.

4.3 Concept and Theory

Through spectral and temporal measurements, energy-time entanglement can be witnessed by violating uncertainty relations [261, 262]. Two separable photons or classical pulses must satisfy the following inequality [250, 151],

$$\Delta(\omega_s + \omega_i)\Delta(t_s - t_i) \geq 1, \tag{4.1}$$

where each photon, labeled signal, and idler is described by its frequency ω and its time of arrival t, and Δ represents the standard deviation in the joint spectrum or joint temporal intensity. In other words, there is a nontrivial limit to the strength of the product of correlations between the sum of the frequencies and the difference in time of arrival if the photons are separable. However, this is not the case for energy-time entangled photons where the right side of Eq. (4.1) can approach zero. Thus, the uncertainty relation is an entanglement witness.

Two-photon states produced via SPDC are usually energy-time entangled. In down-conversion, energy conservation tends to lead to entangled states with frequency anti-correlations, although dispersion engineered SPDC sources have been explored to produce photon pairs with uncorrelated [167, 263] or even positively correlated frequencies [164, 157, 138, 80, 74]. For a pure state with no spectral phase, strong frequency correlations imply strong correlations in the time of arrival of the photons. Under these conditions, Eq. (4.1) can be violated provided one has sufficient resolution in the measurements.

4.3.1 Signatures of energy-time entanglement

In this section, we calculate the joint-uncertainty product $\Delta(\omega_s + \omega_i)\Delta(t_s - t_i)$ using a model for a two-photon state with variable energy-time entanglement [259, 74]. We show that entangled quantum states can violate the inequality of Eq. 4.1 and describe the time-bandwidth products (TBP) of this state. This requires calculating both the joint spectral intensity and the joint temporal intensity.

Consider the correlated two-mode state,

$$|\psi\rangle = \int d\omega_s d\omega_i F(\omega_s, \omega_i) a^\dagger_{\omega_s} a^\dagger_{\omega_i} |0\rangle \,, \tag{4.2}$$

with the normalized joint-spectral amplitude expressed in Gaussian form as,

$$\begin{aligned} F(\omega_s, \omega_i) &= \frac{1}{\sqrt{2\pi\sigma_{\omega_s}\sigma_{\omega_i}}\left(1-\rho_\omega^2\right)^{1/4}} \\ &\times \exp\left(-\frac{1}{2\left(1-\rho_\omega^2\right)}\left[\frac{\left(\omega_s-\omega_{s0}\right)^2}{2\sigma_{\omega_s}^2} + \frac{\left(\omega_i-\omega_{i0}\right)^2}{2\sigma_{\omega_i}^2} - \frac{\rho_\omega\left(\omega_s-\omega_{s0}\right)\left(\omega_i-\omega_{i0}\right)}{\sigma_{\omega_s}\sigma_{\omega_i}}\right]\right). \end{aligned} \tag{4.3}$$

In the two-mode state of Eq. 4.3, there are two relevant length scales for the signal and idler, which we refer to as the marginal width, $\Delta\omega^{(m)}$, and the heralded or coincident width, $\Delta\omega^{(h)}$, and where, here, $\Delta x = \sqrt{\langle x^2\rangle - \langle x\rangle^2}$ refers to the intensity standard deviation or $1/\sqrt{e}$ width of the variable x. The marginal widths in the equation are obtained by taking the marginal over one photon, while the heralded widths are obtained by fixing the frequency of either the signal or idler to its central frequency ($\omega_s \to \omega_{s0}$ or $\omega_i \to \omega_{i0}$) and varying the other. Using Eq. 4.3 above, we find,

$$\Delta\omega^{(m)}_{s,i} = \sigma_{\omega_{s,i}} \tag{4.4}$$

$$\Delta\omega^{(h)}_{s,i} = \sqrt{1-\rho_\omega^2}\sigma_{\omega_{s,i}} \tag{4.5}$$

The correlation parameter $\rho_\omega = \Delta(\omega_s\omega_i)/\Delta\omega_s\Delta\omega_i$ describes the statistical correlations between the frequency of the signal and idler modes and is related to the purity of the partial trace, $P = \sqrt{1-\rho_\omega^2}$. When $\rho_\omega = 0$, the joint-spectral amplitude $F(\omega_s, \omega_i)$ factorizes and the state is separable, whereas when $\rho_\omega \to -1$, the photons are perfectly anticorrelated in frequency and when $\rho_\omega \to 1$, they are perfectly correlated.

The joint temporal amplitude is obtained by taking the Fourier transform of the joint spectral amplitude,

$$\begin{aligned} f\left(t_s, t_i\right) &= \int d\omega_i d\omega_s F\left(\omega_i, \omega_s\right) e^{i\omega_i t_i} e^{i\omega_s t_s} \\ &= \frac{1}{\pi}\sqrt{2\pi\sigma_{\omega_s}\sigma_{\omega_i}}(1-\rho_\omega^2)^{1/4} \exp\left(-t_s^2\sigma_{\omega_s}^2 - t_i^2\sigma_{\omega_i}^2 - 2t_s t_i\rho_\omega\sigma_{\omega_s}\sigma_{\omega_i} - i\left(t_s\omega_{s0} + t_i\omega_{i0}\right)\right). \end{aligned} \tag{4.6}$$

Equation 4.6 can be recast as a two-dimensional Gaussian in the form of Eq. 4.3 and in doing so, we obtain expressions for the marginal pulse width $\Delta t^{(m)}$ and the heralded pulse width $\Delta t^{(h)}$ for the signal and idler, as well as the statistical correlations ρ_t between the time of arrival of the photons,

$$\Delta t_{s,i}^{(m)} = \frac{1}{2\sqrt{1-\rho_\omega^2}\sigma_{\omega_{s,i}}} \tag{4.7}$$

$$\Delta t_{s,i}^{(h)} = \frac{1}{2\sigma_{\omega_{s,i}}} \tag{4.8}$$

$$\rho_t = -\rho_\omega. \tag{4.9}$$

We observe that the marginal pulse width $\Delta t^{(m)}$ is inversely proportional to the heralded bandwidth $\sqrt{1-\rho_\omega^2}\sigma_\omega$ and heralded pulse widths $\Delta t^{(h)}$ is inversely proportional to the marginal bandwidth σ_ω. In addition, the statistical correlations in the temporal intensity, ρ_t, are reversed from those in the spectral intensity, ρ_ω.

Joint-uncertainty product

Using both joint amplitude functions of Eq. 4.3 and Eq. 4.6, we can calculate the variance in the sum of the frequencies of the signal and idler,

$$\Delta(\omega_s + \omega_i)^2 = \sigma_{\omega_s}^2 + 2\rho_\omega\sigma_{\omega_i}\sigma_{\omega_s} + \sigma_{\omega_i}^2, \tag{4.10}$$

and variance in the difference in time of arrival,

$$\Delta(t_s - t_i)^2 = \frac{\sigma_{\omega_s}^2 + 2\rho_\omega \sigma_{\omega_i} \sigma_{\omega_s} + \sigma_{\omega_i}^2}{4\left(1 - \rho_\omega^2\right) \sigma_{\omega_i}^2 \sigma_{\omega_s}^2}, \tag{4.11}$$

in order to obtain the joint uncertainty product,

$$\Delta(\omega_s + \omega_i)\Delta(t_s - t_i) = \sqrt{\frac{\left(\sigma_{\omega_s}^2 + 2\rho_\omega \sigma_{\omega_i} \sigma_{\omega_s} + \sigma_{\omega_i}^2\right)^2}{4\left(1 - \rho_\omega^2\right) \sigma_{\omega_i}^2 \sigma_{\omega_s}^2}}. \tag{4.12}$$

If the bandwidths $\sigma_{\omega_s} = \sigma_{\omega_i}$ are equal, then for the state above, the joint uncertainty product is $\Delta(\omega_s + \omega_i)\Delta(t_s - t_i) = \sqrt{(1+\rho_\omega)/(1-\rho_\omega)}$. In this case, the joint uncertainty product for the transform limited two-photon state depends entirely on the frequency correlation parameter ρ_ω. When $\rho_\omega < 0$, the state clearly violates Eq. 4.1; the simultaneous correlations in frequency and time are stronger than those achievable with classical pulses and the state is energy-time entangled. When $\rho_\omega = 0$, the state satisfies the equality as it is separable. The presence of dispersion on either photon increases the overall product. Spectral phase stretches the temporal profile of the photons and increases the uncertainty $\Delta(t_s - t_i)$ in their arrival time without affecting the uncertainty in the bandwidth $\Delta(\omega_s + \omega_i)$. If the photons are positively correlated $\rho_\omega > 0$, a different joint-uncertainty product can be used to verify entanglement, namely $\Delta(\omega_s - \omega_i)\Delta(t_s + t_i)$ which is also always greater than or equal to one for separable states.

Time-bandwidth products

From the joint spectral and joint temporal amplitude functions, we can also obtain a set of time-bandwidth products (TBP) for the individual modes. For a classical pulse, the TBP must satisfy the uncertainty relation,

$$\Delta\omega \Delta t \geq 1/2. \tag{4.13}$$

On the other hand, for correlated photons, there are four possible time-bandwidth products. The first two time-bandwidth products of the individual photons compare the marginal (heralded) bandwidth to the heralded (marginal) temporal pulse width. For the Fourier limited two-photon state presented above, using Eqs. 4.4, 4.5, 4.7, and 4.8, they are,

$$\Delta\omega^{(m)} \Delta t^{(h)} = 1/2 \tag{4.14}$$

$$\Delta\omega^{(h)} \Delta t^{(m)} = 1/2. \tag{4.15}$$

These TBPs take place of the classical time-bandwidth products, and hold regardless of the amount of entanglement in the system. In the presence of a nonzero spectral phase, the temporal widths will increase whereas the frequency widths will remain the same, and the TBP will only get larger. The value 1/2 is thus a minimum which is attained when there is no spectral phase.

The last two TBPs compare both marginal widths and both heralded widths, and we find,

$$\Delta\omega^{(m)}\Delta t^{(m)} = \frac{1}{2}\frac{1}{\sqrt{1-\rho_\omega^2}} \tag{4.16}$$

$$\Delta\omega^{(h)}\Delta t^{(h)} = \frac{1}{2}\sqrt{1-\rho_\omega^2}. \tag{4.17}$$

These TBPs depend on the strength of the frequency correlations ρ_ω. Both reduce to 1/2 when there are no spectral correlation, $\rho_\omega = 0$, and the state is pure. The marginal TBP, $\Delta\omega^{(m)}\Delta t^{(m)}$, will increase for a correlated state $0 < |\rho_\omega| < 1$, whereas the heralded TBP, $\Delta\omega^{(h)}\Delta t^{(h)}$, will decrease. Energy-time entangled states can have a heralded TBP much smaller than 1/2 when $\rho_\omega < 0$. Since this is forbidden for classical pulses, it can also be used as a measure of entanglement, and has been shown to be directly related to the spectral purity of the state [264]. Similarly to the two previous TBPs, both the marginal TBP and the heralded TBP will increase in the presence of nonzero spectral phase.

4.3.2 Energy-time entanglement with dispersion

We next analyze the effect of dispersion on the energy-time entangled state in order to determine its effect on the joint-uncertainty product and the conditions under which nonlocal dispersion cancellation can be observed. Starting with the joint spectral amplitude in Eq. 4.3, we apply dispersion to both photons,

$$F(\omega_s, \omega_i) \rightarrow F(\omega_s, \omega_i)e^{i\phi(\omega_s,\omega_i)}, \tag{4.18}$$

and assume spectral phase has the separable form, $\phi(\omega_s, \omega_i) = A_i(\omega_i - \omega_{i0})^2 + A_s(\omega_s - \omega_{s0})^2$, with chirp parameters A_i and A_s. The presence of spectral phase will not affect any of the spectral intensity measurements. It will, however, stretch the temporal marginal of the photons, and we can witness this change in the increase of the marginal pulse widths,

$${\Delta t_{s,i}}^{(m)} = \sqrt{\frac{1}{4(1-\rho_\omega^2)\sigma_{s,i}^2} + 4{A_{s,i}}^2{\sigma_{\omega_{s,i}}}^2}. \tag{4.19}$$

The marginal width in time with dispersion has two terms. The first term is the Fourier limited marginal width found in Eq. 4.7. When the chirp parameter is nonzero, $A_{s,i} \neq 0$, for the signal or the idler, we see an increase in the corresponding marginal due to the second term $4A_{s,i}^2\sigma_{s,i}^2$, regardless of the sign of $A_{s,i}$. Moreover, the dispersion A is applied to the entire marginal frequency bandwidth σ_ω. On the other hand, the joint temporal properties of the photons do depend on the relative sign of A_i and A_s, and we can observe this in the heralded pulse width ${\Delta t_s}^{(h)}$ or in the variance of the difference in time of arrival of the signal and idler $\Delta(t_s - t_i)^2$. For example, the signal heralded pulse width under dispersion is,

$${\Delta t_s}^{(h)} = \sqrt{\frac{1}{4\sigma_s^2} + 4A_s^2(1-\rho_\omega^2)\sigma_s^2 + \frac{4\rho_\omega^2\left(A_s\sigma_s^2 + A_i\sigma_i^2\right)^2}{\sigma_s^2(1+16A_i^2(1-\rho^2)\sigma_i^4)}}, \tag{4.20}$$

the idler heralded pulse width $\Delta t_i^{(h)}$ is obtained from Eq. 4.20 by exchanging all subscripts s with subscripts i, and the variance $\Delta(t_s - t_i)^2$ is,

$$\Delta(t_s - t_i)^2 = \frac{\sigma_s^2 + 2\rho_\omega\sigma_i\sigma_s + \sigma_i^2}{4\left(1-\rho_\omega^2\right)\sigma_i^2\sigma_s^2} + 4(A_s\sigma_s + A_i\sigma_i)^2 - 8A_iA_s\left(1+\rho_\omega\right)\sigma_i\sigma_s. \tag{4.21}$$

We focus on the variance, $\Delta(t_s - t_i)^2$, in Eq. 4.21 as the other two heralded pulse widths have a similar structure. We find that it consists of three distinct terms: the first is the Fourier-limited variance when no chirp is applied as in Eq. 4.11, the second is the origin of the nonlocal dispersion cancellation as it goes to 0 when $A_s\sigma_s = -A_i\sigma_i$, and the third results from the finite correlations in the model and also goes to zero for perfect anticorrelations $\rho_\omega \to -1$. The variance in Eq. 4.21 can only increase in the presence of dispersion, and therefore, the same holds for the joint-uncertainty product of Eq. 4.1.

In order to observe complete nonlocal dispersion cancellation for frequency anticorrelated photons, two conditions must be met: the dispersion must be opposite in sign with ratios given by $A_s\sigma_s = -A_i\sigma_i$, and the photons must be perfectly anticorrelated in frequency, $\rho_\omega = -1$. In the present experiment, the first condition is satisfied by setting the signal chirp A_s and finding the idler chirp A_i that minimizes the uncertainty in arrival time. However, since we apply dispersion to photons with finite correlations, $\rho_\omega > -1$, the second condition isn't met exactly, and this contributes to increasing the spread in arrival times $\Delta(t_s - t_i)$ as observed in the imperfect cancellation of Fig. 4.5(d).

4.4 Experimental Setup

Our experimental setup is shown in Fig. 4.2. The experiment uses a titanium-sapphire (Ti:Sapph) laser with an 80 MHz repetition rate which produces femtosecond laser pulses 12.5 ns apart centred at 775 nm with a $1/\sqrt{e}$ bandwidth of 2.25 nm. These are frequency-doubled through second harmonic generation in 2 mm of type-I phasematched bismuth borate (BiBO) generating pulsed pump light centred at 387.5 nm with a $1/\sqrt{e}$ bandwidth of 0.6 nm and an average power of 900 mW. The resulting pump light is spectrally narrowed using a 0.085 nm ($1/\sqrt{e}$) bandpass filter, from which we estimate a pump coherence length of approximately 470 fs ($1/\sqrt{e}$). The remaining 300 mW of filtered pump is focussed in 5 mm of type-I BiBO for spontaneous parametric down conversion (SPDC). Signal-idler photon pairs are created with central wavelengths of 728.6 nm and 827.3 nm, respectively, and split with dichroic mirrors. These wavelengths are chosen such that the up-converted photon is spectrally far from the laser second-harmonic generation (SHG) background. The spectral bandwidths of the photons are controlled using a pair of shortpass and long-pass edge filters on each side. Each photon is then coupled into single-mode fiber, which allow for easy switching between spectral measurement, temporal measurement, and direct detection. The dispersion of the fiber links is then compensated with grating-based pulse compressors.

Spectral measurements are performed with two grating-based scanning monochromators (1200 lines/mm), one for each of the two near-infrared (NIR) SPDC photons. See Ref. [74] for further details. The resolutions of the spectrometers, obtained from the emitted spectra of a Ne-Ar calibration lamp, are 0.081 nm and 0.135 nm for the signal and idler, respectively, the difference arising from slightly different slit widths in each monochromater. Temporal measurements are performed through sum-frequency generation in 1 mm of type-I BiBO with a strong gate laser pulse with an intensity temporal width of 120 fs ($1/\sqrt{e}$), measured using an auto-correlation and assuming a Gaussian spectrum. The up-converted photons are detected after passing through spectral bandpass filters which remove the second harmonic background of the gate pulse.

For the temporal measurements, signal and idler photons are sent through 16.2 m and 21.2 m of fiber respectively. Grating-based compressors compensate for this chirp and allow variable control over the dispersion. A polarizing beam splitter separates the Ti:Sapph fundamental into two gates pulses. Due to the added propagation in fiber, the signal and idler photons originate respectively 7 and 9 pulses behind the gate pulses. Each photon then co-propagates with a gate pulse from the respective side with a spatial separation of about 8 mm and is subsequently focussed into 1 mm of type-I phasematched BiBO

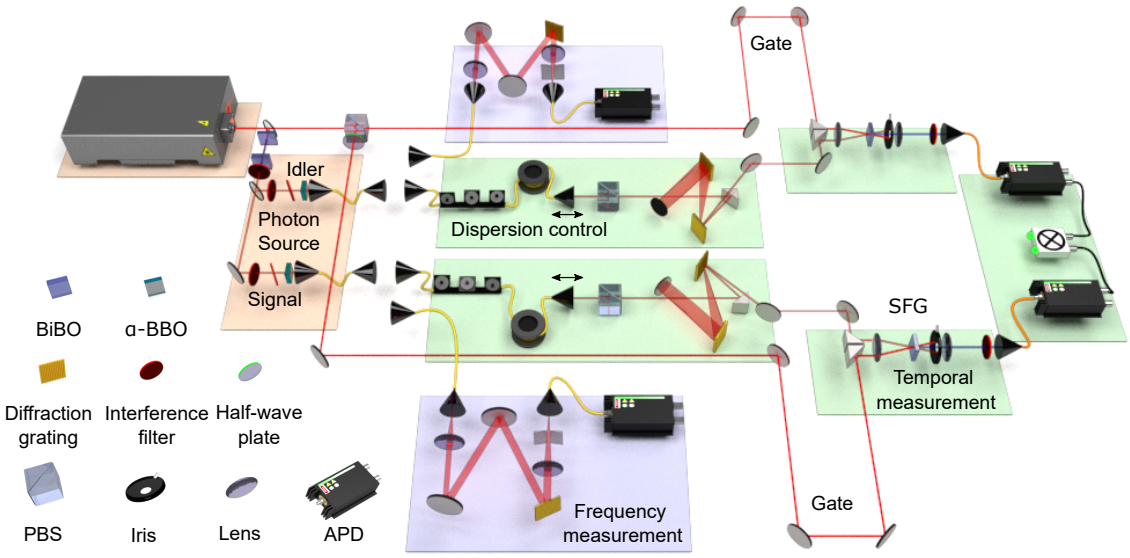

Figure 4.2: **Experimental setup.** Frequency-entangled photons are created through spontaneous parametric down-conversion of an ultrafast pulse from a frequency doubled Ti:sapphire laser. Measurements of either the frequency or the time of arrival of each photon can be performed in coincidence. Spectral measurements are made with dual single-photon monochromators. Temporal measurements are performed using optically gated single-photon detection. The gating is implemented via noncollinear sum-frequency generation between a strong gate pulse from the Ti:Sapph laser and the signal or idler. The dispersion of the signal and idler photons is controlled with a combination of single mode fibers and grating compressors before the up-conversion. The up-converted signal is filtered with bandpass filters which remove the background second harmonic generation from the gate pulse. Temporal and frequency measurements are performed in coincidence to observe the spectral and temporal features of the photons.

for sum-frequency generation (SFG). The up-converted light, with central wavelengths of 375 nm and 400 nm for the signal and idler sides, respectively, is recollimated, spectrally filtered with bandpass filters to remove second-harmonic background, and then coupled into multimode fiber. The SHG background was approximately 10 times higher for the idler SFG compared to the signal SFG and therefore, different gate powers were used to maximize the signal-to-noise ratios in each arm, with 500 mW for the signal gate pulse and 200 mW for the idler gate pulse. Both up-converted photons are detected with silicon avalanche photodiodes with quantum efficiencies of approximately 30% near 400nm. The

coincidence window for detection events was set to 3 ns.

The SFG employed in the temporal measurements can approach unit efficiency when the temporal duration of the photon is approximately the same length in time or shorter than the gate pulse [265]. However, in the present experiment, the photons are much longer than the gate, and consequently, we estimate a maximum up-conversion efficiency of approximately 30% [163]. The absolute efficiency of the temporal measurement apparatus at the cross-correlation peak, including fiber coupling, chirp compensation, and up-conversion, is found to be approximately 2% of this maximum.

The relative separation of the gratings in each compressor is initially scanned to cancel the chirp from the fibers. This is achieved by minimizing the up-conversion width as a function of the grating separation. The location of the minimum defines the centre position of the gratings in the compressor where zero dispersion is applied. The amount of dispersion provided by each compressor is then determined from the displacement of the gratings from their centre position and their angle with respect to the incident and reflected light. The compressors on the signal and idler arm are thus found to give 1315 fs^2 and 1925 fs^2 per mm of displacement, respectively, due to the cubic dependence on wavelength [196].

Photons were produced at the source at a rate of 673,000 coincidence counts per second with 3.4×10^6 and 3.5×10^6 single-detection events per second for the signal and idler, respectively. The heralded second-order coherence of the source, measured with a Hanbury Brown-Twiss interferometer [147], was $g^{(2)}(0) = 0.416 \pm 0.004$ for the signal and $g^{(2)}(0) = 0.415 \pm 0.003$ for the idler. In general, double pair emission will lead to a broad background in the joint spectrum and joint temporal intensity. However, due to the tight temporal filtering on both sides, we estimate that double pairs contribute to less than 1% of the measured up-converted signal. After the up-conversion on each side, approximately 30 coincidence counts ($10,000$ up-converted signal singles and $16,000$ up-converted idler singles per second) per second were measured at the peak, from which about 0.6 coincidence counts (360 and 3,000 singles) per second were background from the second harmonic of the gate pulse.

4.5 Experimental Results

Detection events for the signal and idler are measured in coincidence after they have passed through either both spectrometers, both temporal gates, or one of each. The corresponding measured joint spectrum, joint temporal intensity, and time-frequency plots, which measure

the frequency of one photon in coincidence with the arrival time of the other, are shown in Fig. 4.3. Background subtraction has not been employed in the data.

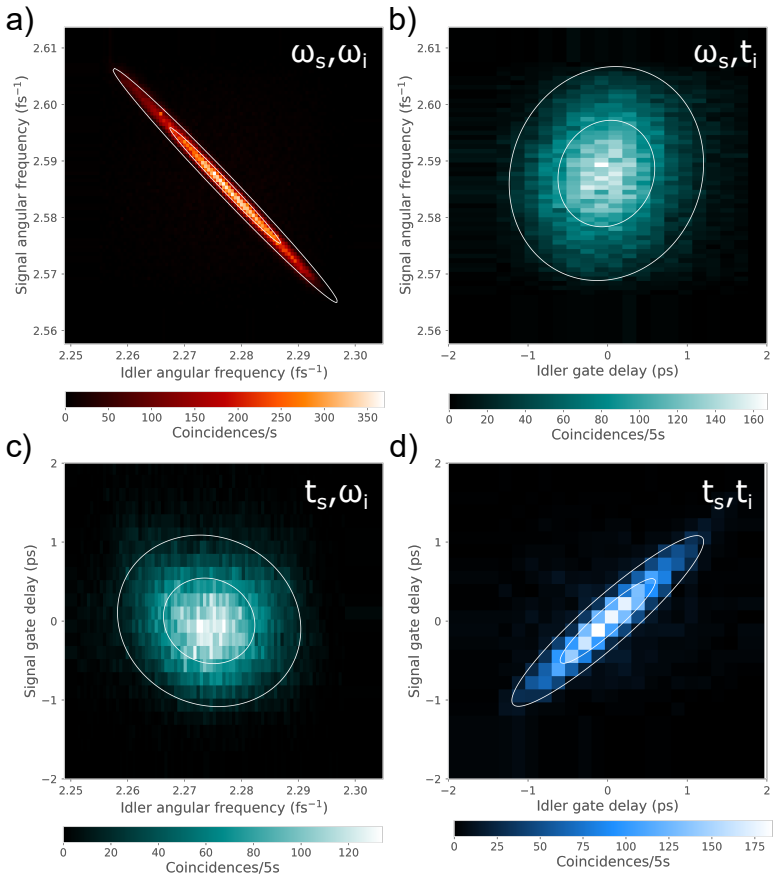

Figure 4.3: **Spectral and temporal characterization of ultrafast photons.** A combination of spectral and temporal measurements are made in coincidence in order to measure (a) the joint spectrum, (d) the joint temporal intensity, as well as the (b),(c) cross-correlations between the time (frequency) of the idler and frequency (time) of the signal. (a) Frequency anticorrelations with statistical correlation -0.9951 ± 0.0001 are accompanied with (d) positive correlations 0.987 ± 0.004 in the signal-idler arrival times. The time-frequency plots (b),(c) show little correlation — (0.111 ± 0.008) and (-0.106 ± 0.008), respectively— indicating low dispersion in the signal and idler photons. White lines on all plots correspond to 1σ and 2σ contours of two-dimensional Gaussian fits.

Table 4.1: **Ultrafast two-photon state parameters.** Measured marginals, heralded widths, and correlations of the joint spectrum and joint temporal intensity presented Figs. 4.3(a) and 4.3(d). All values are deconvolved to account for the finite resolution of the spectrometers and the temporal gate. Measured properties are widths in standard deviations and error bars are calculated from Monte Carlo simulations assuming Poissonian noise.

Property	Joint spectrum	Joint temporal intensity
Signal marginal width	(10.56 ± 0.04) ps^{-1}	(0.537 ± 0.009) ps
Signal heralded width	(1.02 ± 0.05) ps^{-1}	(0.066 ± 0.018) ps
Idler marginal width	(9.69 ± 0.03) ps^{-1}	(0.587 ± 0.015) ps
Idler heralded width	(0.94 ± 0.04) ps^{-1}	(0.070 ± 0.019) ps
Correlation ρ	-0.9951 ± 0.0001	0.987 ± 0.004

For each joint measurement of Fig. 4.3, the marginal width is obtained by fitting the marginals to a one-dimensional Gaussian, while the heralded width is obtained taking the average of several slices of the data when the frequency or time of one photon is fixed. The statistical correlation, ρ, is obtained by finding the value that best fits a two-dimensional Gaussian with the measured marginals. Since the finite resolution of both spectral and temporal measurements are of the same order of magnitude as the spectral and temporal distributions, the measured features will be broadened. To account for this, the fit parameters are deconvolved assuming a Gaussian response function [74], and these values for the joint spectrum and joint temporal distribution of Figs. 4.3(a) and 4.3(d) are presented in Table 4.1.

The measured joint spectrum shown in Fig. 4.3(a) exhibits strong anticorrelation (-0.9951 ± 0.0001) in the signal and idler frequencies, while the joint temporal intensity of Fig. 4.3(d) shows strong positive correlations (0.987 ± 0.004) in the arrival times of the photons. We can witness the effect of the spectral phase in Figs. 4.3(b) and 4.3(c), which show weak correlations between the frequency of one photon and the time of arrival of the other. Low correlations in the time-frequency plots may indicate little uncompensated dispersion in the experiment.

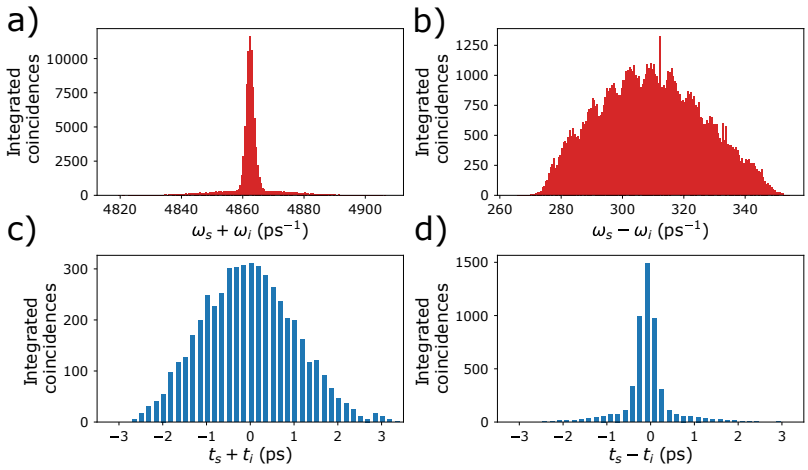

Figure 4.4: **Histograms of the frequency and time of arrival correlations between signal and idler photons.** Coincidences are confined to a small region in (a) with $\Delta(\omega_s+\omega_i) = (1.429\pm0.006)$ ps^{-1} (1.329 ± 0.007 ps^{-1} when corrected for the finite resolution of the gate) compared to (b) with $\Delta(\omega_s - \omega_i) = (18.16 \pm 0.05)$ ps^{-1} (18.16 ± 0.05 ps^{-1}) indicating strong anticorrelations in frequency. Likewise, coincidences are localized in (d) with $\Delta(t_s - t_i) = 0.203 \pm 0.005$ ps (0.110 ± 0.010 ps) compared to (c) with $\Delta(t_s + t_i) = 1.066 \pm 0.016$ ps (1.052 ± 0.016 ps) corresponding to strong correlations in the time of arrival. From these values, we find a joint uncertainty product $\Delta(\omega_s + \omega_i)\Delta(t_s - t_i) = 0.290 \pm 0.007$ (0.15 ± 0.01).

4.5.1 Energy-time uncertainty relation

The spectral and timing correlations are further analyzed by binning the data presented in Figs. 4.3(a) and 4.3(d) into histograms based on $\omega_1 + \omega_2$ and $t_s - t_i$, as well as $\omega_s - \omega_i$ and $t_s + t_i$ for comparison, as shown in Fig. 4.4. The bin size was selected to match the step size of the measurement apparatus. Gaussian fits to the histograms give a joint uncertainty product $\Delta(\omega_s + \omega_i)\Delta(t_s - t_i) = (1.429 \pm 0.006$ ps$^{-1})(0.203 \pm 0.005$ ps$) = 0.290 \pm 0.007$, which violates the inequality of Eq. (4.1) by about 100 standard deviations. Error bars are obtained via Monte Carlo simulations assuming Poissonian noise. When deconvolved, we find $\Delta(\omega_s + \omega_i)\Delta(t_s - t_i) = (1.329 \pm 0.007$ ps$^{-1})(0.110 \pm 0.010$ ps$) = 0.15 \pm 0.01$. The measured uncertainty products thus provide a clear witness of energy-time entanglement on ultrafast time scales.

The small fringes observed in the histogram in Fig. 4.4(b) could arise from photon interference in α-barium borate (α-BBO) crystals 2 mm in length which were placed in

both the signal and idler arms of the photon source, after the interference filters but before the couplers in Fig. 4.2(b). A slight angle of less than one degree between the polarization of the photons and the axis of the α-BBO crystals could result in interference between two modes causing the observed fringes.

4.5.2 Nonlocal dispersion cancellation

We now turn to the problem of measuring the impact of dispersion on our energy-time entangled state. We directly observe the effect of applied dispersion on the temporal correlations, as presented in the joint temporal intensities of Fig. 4.5. We control the spectral phase of the photons, $\phi(\omega_s, \omega_i) \approx A_s(\omega_s - \omega_{s0})^2 + A_i(\omega_i - \omega_{i0})^2$, with two grating compressors where the chirp parameters A_s and A_i are for the signal and idler fields, respectively. We estimate the magnitude of the applied dispersion from the geometry of the compressor and the relative position of the gratings [196], and measure the standard deviation $\Delta(t_s - t_i)$ of a Gaussian fit from histograms of $t_s - t_i$.

Starting from the case with no dispersion [Fig. 4.5(a)], we apply positive dispersion $A_s = (0.0373 \pm 0.0015)$ ps^2 to only the signal [Fig. 4.5(b)] and negative dispersion $A_i = -(0.0359 \pm 0.0014)$ ps^2 to only the idler [Fig. 4.5(c)]. In these two cases, we observe a large increase in the timing uncertainty $\Delta(t_s - t_i)$ and a vertical or horizontal shear of the joint-temporal intensity along the corresponding axis. We then apply the same amount of positive and negative dispersion to the signal and idler as before [Fig. 4.5(d)], where the dispersion applied to the idler is set to minimize the timing uncertainty between the two photons. Here, the timing uncertainty in arrival time $\Delta(t_s - t_i)$ is almost unchanged. This is the signature of nonlocal dispersion cancellation, limited by the finite correlations of the initial two-photon state. The temporal marginals in Fig. 4.5(d) still increase since each side remains exposed to a significant amount of dispersion.

For classical pulses, the effect of dispersion on the correlations in arrival times can be expressed as an inequality [255], $\Delta(t_s - t_i)_F^2 \geq \Delta(t_s - t_i)_0^2 + 4A^2/\Delta(t_s - t_i)_0^2$, where $\Delta(t_s - t_i)_0$ is the initial difference in detection times, and $\Delta(t_s - t_i)_F$ is the final difference with equal and opposite dispersion A applied on each side. Under the assumption that the initial state is unchirped, taking the measured initial value from Fig. 4.5(a), $\Delta(t_s - t_i)_0 = 0.235$ ps (0.162 ps when corrected for the gate resolution), and using the average magnitude of the applied dispersion $A = 0.0366$ ps^2, we calculate that the standard deviation in arrival times for classical pulses has to be at least $\Delta(t_s - t_i)_F \geq 0.390$ ps (0.480 ps). However, the measured uncertainty observed in Fig. 4.5(d), $\Delta(t_s - t_i) = (0.245 \pm 0.004)$ ps, remains

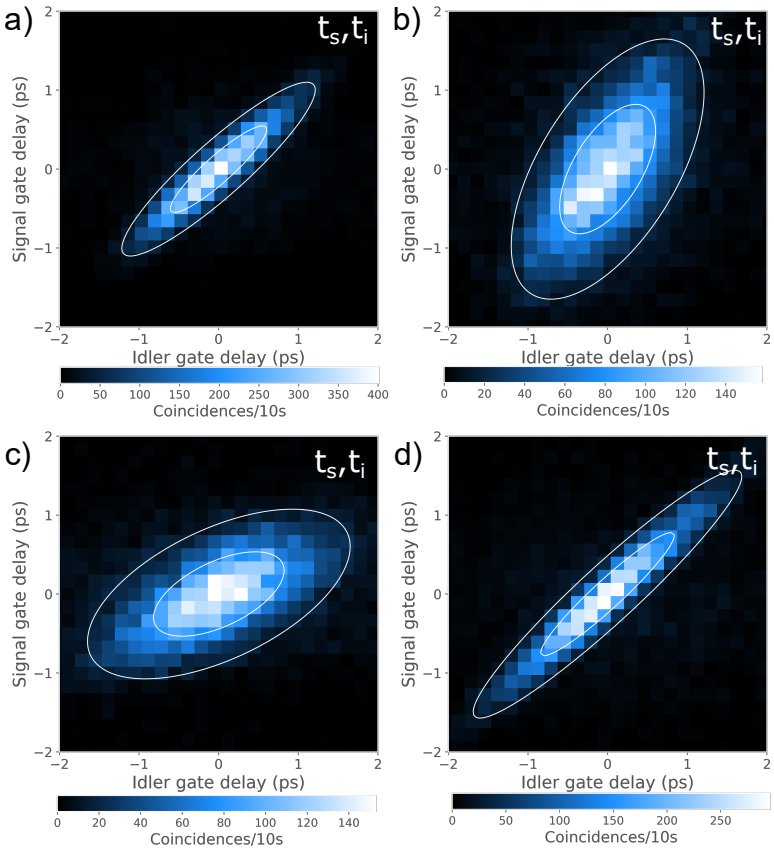

Figure 4.5: **Nonlocal dispersion cancellation.** Joint temporal intensity for the signal and idler pair: (a) without dispersion, (b) with a positive dispersion of $A_s = (0.0373 \pm 0.0015)$ ps^2 on the signal, (c) with a negative dispersion of $A_i = (-0.0359 \pm 0.0014)$ ps^2 on the idler, and (d) with both a positive dispersion of $A_s = (0.0373 \pm 0.0015)$ ps^2 on the signal and a negative dispersion of $A_i = (-0.0359 \pm 0.0014)$ ps^2 on the idler. For each, we measure the uncertainty in the difference in arrival times of the signal and idler $\Delta(t_s - t_i)$ and find: (a) 0.235 ± 0.003 ps (0.162 ± 0.005 ps when corrected for the finite resolution of the gate), (b) 0.708 ± 0.013 ps (0.688 ± 0.013 ps), (c) 0.714 ± 0.010 ps (0.693 ± 0.011 ps), (d) 0.245 ± 0.004 ps (0.175 ± 0.006 ps). We witness nonlocal dispersion cancellation in the timing uncertainty $t_s - t_i$ in (d) as the width $\Delta(t_s - t_i)$ remains almost unchanged with the one measured in (a).

significantly smaller. The experimental apparatus thus provides a direct way to detect this inherently quantum effect in a regime inaccessible to current detectors.

4.6 Additional Experimental Details

The deconvolution of each parameter is performed by assuming that the measured state can be described by a two-dimensional Gaussian function and assuming a Gaussian response function for the spectral and temporal measurements. A two-dimensional Gaussian function of variables x and y can be specified by its marginals, σ_x and σ_y, and the correlation ρ between the two variables,

$$f(x,y) = \exp\left(-\frac{1}{(1-\rho^2)}\left[\frac{(x-x_0)^2}{2\sigma_x^2} + \frac{(x-x_0)^2}{2\sigma_y^2} - \frac{\rho\,(x-x_0)\,(y-y_0)}{\sigma_x\sigma_y}\right]\right). \tag{4.22}$$

If the measurement apparatuses used to measure the marginals σ_x and σ_y and the statistical correlation ρ have a resolution of Π_x and Π_y, respectively, then the deconvolved marginals σ'_x and σ'_y and the deconvolved statistical correlation ρ' are given by,

$$\sigma'_x = \sqrt{\sigma_x^2 - \Pi_x^2} \tag{4.23}$$

$$\sigma'_y = \sqrt{\sigma_y^2 - \Pi_y^2} \tag{4.24}$$

$$\rho' = \frac{\rho\sigma_x\sigma_y}{\sqrt{\left(\sigma_x^2 - \Pi_x^2\right)\left(\sigma_y^2 - \Pi_y^2\right)}}. \tag{4.25}$$

For measurements of the heralded widths, the deconvolutions must be modified since these widths depend on the measurements of both the signal and the idler photon. As such, the deconvolved heralded widths $\sigma\prime_{hx}$ and $\sigma\prime_{hy}$ are given in terms of the measured heralded widths σ_{hx} and σ_{hy} by,

$$\sigma\prime_{hx} = \sqrt{\frac{\sigma_{hy}^2 - \Pi_{hy}^2}{\sigma_{hy}^2 - (1-\rho^2)\,\Pi_{\mathrm{y}}^2}\sigma_{hx}^2 - \Pi_x^2} \tag{4.26}$$

$$\sigma\prime_{hy} = \sqrt{\frac{\sigma_{hx}^2 - \Pi_{hx}^2}{\sigma_{hx}^2 - (1-\rho^2)\,\Pi_{\mathrm{x}}^2}\sigma_{hy}^2 - \Pi_y^2}. \tag{4.27}$$

The deconvolved uncertainty in the sum or difference $\Delta(x \pm y)'$ is given in terms of the measured value $\Delta(x \pm y)$ by,

$$\Delta(x \pm y)' = \sqrt{\Delta(x \pm y)^2 - \Pi_x^2 - \Pi_y^2}. \tag{4.28}$$

Table 4.2: **Fit parameters for source joint plots.** Selected properties of the fits to the joint spectrum, joint temporal intensity, and joint time frequency plots seen in Fig. 4.3. Values in parentheses are deconvolved from a Gaussian response function.

Property (Deconvolved)		Joint-spectrum	Joint-temporal intensity	Signal frequency Idler time	Signal time Idler frequency
Signal	Frequency (ω)	2586.9 ± 0.4 ps^{-1}	-	-	-
	Marginal width	10.57 ± 0.04 ps^{-1} (10.56 ± 0.04 ps^{-1})	0.550 ± 0.009 ps (0.537 ± 0.009 ps)	9.43 ± 0.05 ps^{-1} (9.42 ± 0.05 ps^{-1})	0.533 ± 0.003 ps (0.519 ± 0.003 ps)
	Heralded width	1.16 ± 0.04 ps^{-1} (1.02 ± 0.05 ps^{-1})	0.176 ± 0.008 ps (0.066 ± 0.018 ps)	9.4 ± 0.2 ps^{-1} (9.3 ± 0.2 ps^{-1})	0.514 ± 0.017 ps (0.501 ± 0.018 ps)
Idler	Frequency (ω)	2276.9 ± 0.3 ps^{-1}	-	-	-
	Marginal width	9.69 ± 0.03 ps^{-1} (9.69 ± 0.03 ps^{-1})	0.600 ± 0.015 ps (0.587 ± 0.015 ps)	0.589 ± 0.006 ps (0.576 ± 0.006 ps)	8.03 ± 0.05 ps^{-1} (8.02 ± 0.05 ps^{-1})
	Heralded width	1.06 ± 0.04 ps^{-1} (0.94 ± 0.04 ps^{-1})	0.185 ± 0.009 ps (0.070 ± 0.019 ps)	0.588 ± 0.022 ps (0.576 ± 0.022 ps)	7.7 ± 0.6 ps^{-1} (7.7 ± 0.6 ps^{-1})
Statistical Correlation		-0.9939 ± 0.0001 (-0.9951 ± 0.0001)	0.944 ± 0.003 (0.987 ± 0.004)	0.109 ± 0.008 (0.111 ± 0.008)	-0.103 ± 0.008 (-0.106 ± 0.008)

See Table 4.2 for a list of parameters from the joint spectrum, joint temporal intensity, and frequency-time plots in Fig. 4.3. See Table 4.3 for a collection of parameters for plots of the joint temporal intensity in Fig. 4.5. Raw measurements and deconvolved values are presented in both tables.

Table 4.3: **Fit parameters for the nonlocal dispersion cancellation.** Selected properties of the fits to the joint temporal intensity plots seen in Fig. 4.5. Values in parentheses are deconvolved from a Gaussian response function.

Property (Deconvolved)		No dispersion	Positive dispersion on the signal	Negative dispersion on the idler	Opposite dispersion
Signal	Marginal width	0.536 ± 0.004 ps (0.523 ± 0.004 ps)	0.797 ± 0.009 ps (0.788 ± 0.009) ps	0.518 ± 0.004 ps (0.504 ± 0.004) ps	0.764 ± 0.007 ps (0.754 ± 0.007) ps
	Heralded width	0.206 ± 0.010 ps (0.132 ± 0.012 ps)	0.619 ± 0.040 ps (0.599 ± 0.040) ps	0.405 ± 0.020 ps (0.384 ± 0.021) ps	0.230 ± 0.030 ps (0.160 ± 0.030) ps
Idler	Marginal width	0.592 ± 0.006 ps (0.580 ± 0.006) ps	0.585 ± 0.005 ps (0.572 ± 0.005) ps	0.795 ± 0.010 ps (0.786 ± 0.010) ps	0.820 ± 0.010 ps (0.811 ± 0.010) ps
	Heralded width	0.223 ± 0.012 ps (0.143 ± 0.014) ps	0.448 ± 0.013 ps (0.428 ± 0.014) ps	0.613 ± 0.004 ps (0.592 ± 0.004) ps	0.231 ± 0.015 ps (0.160 ± 0.020) ps
Statistical Correlation		0.912 ± 0.003 (0.956 ± 0.003)	0.589 ± 0.009 (0.609 ± 0.009)	0.56 ± 0.01 (0.58 ± 0.01)	0.951 ± 0.002 (0.973 ± 0.002)

4.7 Additional Experimental Results

The four additional measured TBPs are presented in Table 4.4. We find that the first two TBPs approach the value of 1/2 obtained for a Fourier limited two-dimensional Gaussian pulse. The difference between the measured values and the value of 1/2 could be due to a few reasons. Uncompensated dispersion will increase both TBPs. The time-frequency plots do exhibit small correlations in Fig. 4.3, which would also arise from a nonzero spectral phase. In addition, bandwidth filtering will increase the heralded width $\Delta t^{(h)}$ as it depends directly on the marginal spectrum and thus further increase $\Delta\omega^{(m)}\Delta t^{(h)}$. We observe a small amount of spectral clipping from the edge filters in the source which will reduce the spectral bandwidth of the photons. Any bandwidth filtering from the grating compressors would have the same effect. Moreover, since the heralded width depends on the measurements on both the signal and idler side, errors associated with it tend to be larger. This error translates to the deconvolved value, and the measured error on the TBPs involving $\Delta t^{(h)}$.

When observing the other two TBPs, we find that the marginal TBP $\Delta\omega^{(m)}\Delta t^{(m)}$ is much larger than the minimum of 1/2. This is consistent with either a mixed state or a spectrally correlated state. The heralded TBP $\Delta\omega^{(h)}\Delta t^{(h)}$ is smaller than the classically allowed value of 1/2, providing yet another confirmation that the photons exhibit energy-time entanglement.

Table 4.4: **Time-bandwidth products.** The four time-bandwidth products of the signal and idler photons from SPDC are obtained from the marginal and heralded widths of Fig. 4.3(a,d). Values in parentheses are deconvolved with a Gaussian response function.

TBP (Deconvolved)	Signal	Idler
$\Delta\omega^{(m)}\Delta t^{(h)}$	1.64 ± 0.07 (0.62 ± 0.15)	1.64 ± 0.09 (0.62 ± 0.16)
$\Delta\omega^{(h)}\Delta t^{(m)}$	0.63 ± 0.03 (0.55 ± 0.03)	0.64 ± 0.03 (0.55 ± 0.03)
$\Delta\omega^{(m)}\Delta t^{(m)}$	5.16 ± 0.07 (5.03 ± 0.07)	5.3 ± 0.1 (5.2 ± 0.1)
$\Delta\omega^{(h)}\Delta t^{(h)}$	0.20 ± 0.01 (0.07 ± 0.02)	0.20 ± 0.01 (0.07 ± 0.02)

4.8 Conclusion

We have directly measured both the temporal and frequency correlations of an ultrafast biphoton pulse. Optical gating employed here was critical for realizing ultrafast coincidence detection and correspondingly high-resolution temporal measurements. We observe energy-time entanglement via a joint time-bandwidth inequality and demonstrate ultrafast nonlocal dispersion cancellation of the biphotons with direct and independent detection. This work can be extended to quantum interference measurements on ultrafast time scales, and can be combined with temporal imaging to greatly increase the versatility of energy-time entangled photons for quantum information applications.

Chapter 5

Ultrafast Quantum Interferometry with Energy-Time Entangled Photons

Notes and acknowledgements

The contents of this chapter were published on June 13, 2018, as [266]:

J.P.W. MacLean, J.M. Donohue, K.J. Resch. *Ultrafast quantum interferometry with energy-time entangled photons.* Phys. Rev. A **97**, 063826 (2018).

Author Contributions

Kevin Resch and **John Donohue** conceived of the study.

John Donohue built the initial photon source and acquisition software.

Jean-Philippe MacLean and **John Donohue** carried out the experiment and analyzed the data.

Jean-Philippe MacLean wrote the first draft of the manuscript.

All authors contributed to the final version.

5.1 Chapter Overview

Many quantum advantages in metrology and communication arise from interferometric phenomena. Such phenomena can occur on ultrafast time scales, particularly when energy-time entangled photons are employed. These have been relatively unexplored as their observation necessitates time resolution much shorter than conventional photon counters. Integrating nonlinear optical gating with conventional photon counters can overcome this limitation and enable subpicosecond time resolution. Here, using this technique and a Franson interferometer, we demonstrate high-visibility quantum interference with two entangled photons, where the one- and two-photon coherence times are both subpicosecond. We directly observe the spectral and temporal interference patterns, measure a visibility in the two-photon coincidence rate of $(85.3 \pm 0.4)\%$, and report a CHSH-Bell parameter of 2.42 ± 0.02, violating the local-hidden variable bound by 21 standard deviations. The demonstration of energy-time entanglement with ultrafast interferometry provides opportunities for examining and exploiting entanglement in previously inaccessible regimes.

5.2 Context

Interferometry based on entangled quantum states is essential for enhanced metrology and quantum communication. Quantum correlations can enable interferometric measurements with improved sensitivity [267] and resolution [268], and quantum advantages have been found for interferometric applications involving optical coherence tomography [269], precise measurements of optical properties [246, 270], and the detection of gravitational waves [271]. In laser physics, the development of ultrafast light sources has led to innovations in atomic spectroscopy, time-resolved measurements for quantum chemistry, nonlinear optics, X-ray sources, with applications in health sciences and industrial machining [272]. For quantum light, energy-time entangled photons can also be produced with temporal features on ultrafast time scales [273, 274, 275] and the wide availability of pulsed lasers has made this regime accessible for quantum state engineering [157, 167, 74]. However, quantum interferometry with these states is challenging as the interference time scales are below the resolution of standard photon detectors [67, 75]. To overcome detector limitations, optical techniques have been developed to directly observe energy-time entangled quantum states on ultrafast time scales [209, 276] by building effective fast photon counters using ultrafast optical gating in conjunction with standard photon counters [208, 252, 260]. Extending the measurement of quantum interference to subpicosecond time scales will be essential for developing new applications with ultrafast energy-time states of light.

An important class of interferometers that has been used to observe quantum interference effects with energy-time entangled photons was developed by Franson in 1989 [49]. Photon pairs are sent through two unbalanced interferometers creating interference in the coincidence rate but not in the single-photon detection rates. High-visibility interference was observed in such an interferometer using spontaneous parametric downconversion (SPDC) [50, 277]. Franson interferometers with energy-time entangled states have since become important for applications in long-distance quantum key distribution [95], measuring entanglement in high-dimensional [140] and multiphoton states [103, 254], scaling quantum information tasks to larger dimensions [278, 279], and improving molecular spectroscopy [280]. However, when both the single-photon and two-photon coherence times are ultrafast, as is often the case for SPDC photons produced with pulsed lasers, observing quantum interference effects with a Franson interferometer requires new techniques to overcome detector limitations and the original interferometer concept can be adapted to provide delays on shorter time scales.

In this work, we temporally resolve two-photon interference with subpicosecond timing resolution. The detectors are implemented by optically gating the photons in a nonlinear medium via noncollinear sum-frequency generation (SFG) with a short gate pulse [208, 252, 260, 209]. Using this technique and single-photon spectrometers, we measure both the joint temporal and joint spectral features of a spatially separated two-photon state at the output of a Franson interferometer.

5.3 Concept and Theory

We produce energy-time entangled photon pairs with parametric downconversion pumped by a broadband laser pulse. The photons are produced with strong anti-correlations between the signal, ω_s, and idler, ω_i, frequencies leading to a narrow joint uncertainty $\Delta(\omega_s+\omega_i)$ set by the bandwidth of the pump in broadly phasematched materials [281, 209]. For a two-photon state with no spectral phase, the photon pairs will also exhibit strong correlations between the time of arrival of the signal, t_s, and the idler, t_i, leading to smaller joint uncertainty than their individual widths in time, $\Delta(t_s - t_i) < \Delta t_{s,i}$ [209]. A Franson interferometer, shown schematically in Fig. 5.1, separates the photons on each side into a short and long path, with a time delay τ, resulting in four possible combinations of paths. The single-photon detection rates, which vary with the phase in each arm, $\phi_{s,i}$, have a coherence time inversely proportional to the single-photon spectral band-

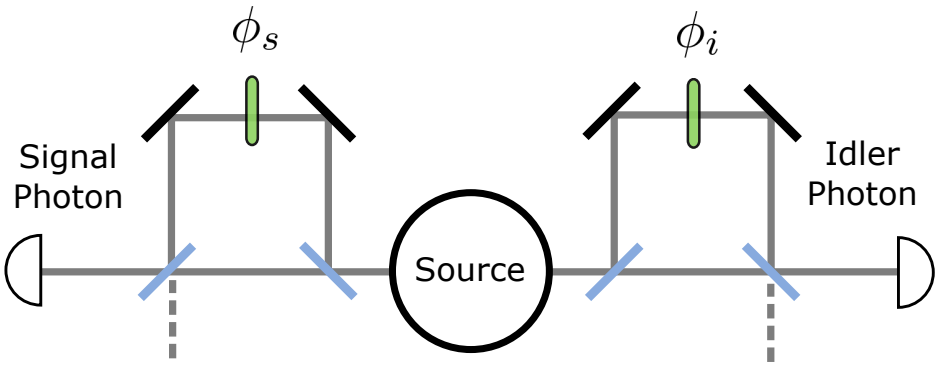

Figure 5.1: **Franson interferometer composed of two unbalanced interferometers.** Quantum interference can be seen by sending each photon of a two-photon energy-time entangled pair through an unbalanced interferometer. Each photon is split into early and late time bins and recombined with a phase applied to one bin. Interference in the coincidence rates may be observed which does not arise from interference in the single rates.

width, $\tau_{c_{s,i}}^{(1)} = 1/\Delta\omega_{s,i}$, whereas the coincidence rate, which varies with $\phi_s + \phi_i$, has a two-photon coherence time inversely proportional to the two-photon spectral bandwidth, $\tau_c^{(2)} = 1/\Delta(\omega_s + \omega_i)$ (see Section 5.3.1). A visual representation of the single-photon and two-photon spectral bandwidths is presented in Fig. 5.2. When the time delay τ is set to be much larger than the single-photon coherence time but less than the two-photon coherence time, $\tau_{c_{s,i}}^{(1)} \ll \tau < \tau_c^{(2)}$, interference in the coincidence rate can be observed without any present in the single detection rates.

The interference in the coincidences results from the indistinguishability between the cases where both of the photons take the short path in the interferometer and where both take the long path. Meanwhile, the cases where they take opposite paths, labeled short-long and long-short, do not exhibit interference, thus limiting the visibility to 50% without temporal resolution. This, however, is the same maximum visibility that can be obtained in coincidence measurements with classically correlated light when zero visibility is observed in the single-photon rates [155]. To observe higher visibility interference with energy-time entangled photons, sufficient time resolution is needed to resolve the arrival times of the early and late photons. This condition is typically met using continuous-wave-pumped downconversion sources whose two-photon coherence times are much longer. They can therefore support interferometer delays in the range of 10 cm to 1 m [94, 282, 256, 283], which can be implemented in free space or fiber, such that the time difference τ

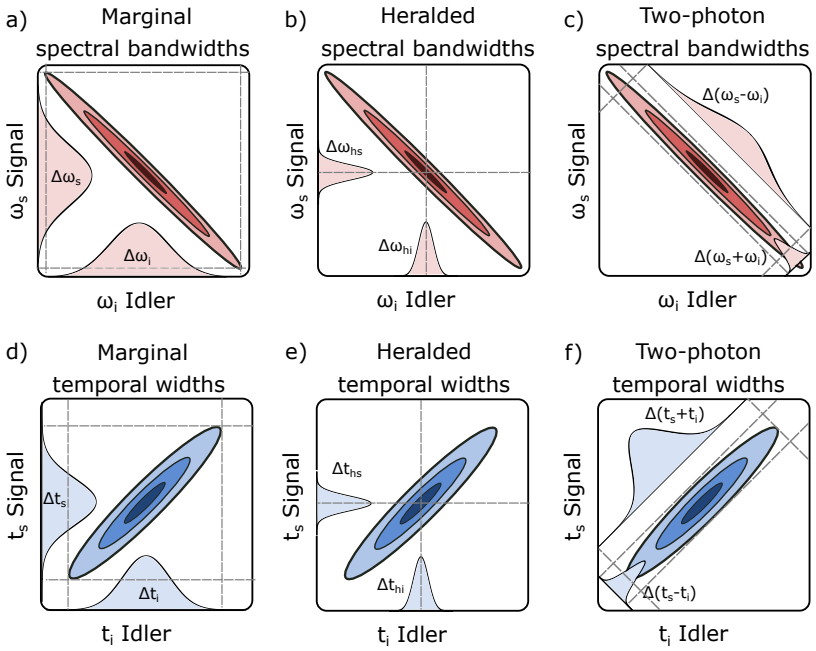

Figure 5.2: **Spectral bandwidths and temporal widths for a frequency anti-correlated two-photon state.** (a) The single-photon spectral bandwidth, $\Delta\omega$, is given by the marginal distribution obtained by projecting the joint spectral intensity onto either the signal or idler axes. The single-photon coherence time, the time scale over which interference in the single-photon rates can occur, is related to the inverse of the single-photon spectral bandwidth, $\tau_c^{(1)} = 1/\Delta\omega$. (b) The heralded spectral bandwidths, $\Delta\omega_h$, are the spectral bandwidths of the signal or idler photon when the frequency of the other is fixed. (c) The two-photon spectral bandwidths for the semi-minor, $\Delta(\omega_s + \omega_i)$, and semi-major axes, $\Delta(\omega_s - \omega_i)$, are obtained by projecting the joint spectral intensity along the corresponding diagonal axes $\omega_s \pm \omega_i$. The two-photon coherence time, the time scale over which interference in the coincidences can occur, is related to the inverse of the two-photon spectral bandwidth, $\tau_c^{(2)} = 1/\Delta(\omega_s + \omega_i)$. (d-f) The marginal temporal widths, Δt, the heralded temporal widths, Δt_h, as well as the two-photon temporal widths, $\Delta(t_s \pm t_i)$ are obtained from the joint temporal intensity in the same way as their spectral analogues.

between early and late photons (30 μs to 3 ns) remains much larger than standard detector resolution.

5.3.1 Franson interferometry with finite correlations

In this section, we first calculate the overall coincident and single-photon detection rates of an energy-time entangled two-photon state after the Franson interferometer. We will show that this leads to two distinct time scales of interference for the single-photon detection rates and the coincidence detection rate. We then describe the need for temporal selection to improve the visibility of the interference in the coincidence rate after the Franson interferometer, and describe the effect of spectral or temporal selection by calculating the joint spectrum and joint temporal intensity for the two-photon state after the Franson interferometer. Finally, we discuss the parameters for optimizing the visibility of the two-photon interference.

Consider the two-mode state with signal ω_s and idler ω_i frequency modes,

$$|\psi\rangle = \int d\omega_s d\omega_i F(\omega_s, \omega_i) a^\dagger_{\omega_s} a^\dagger_{\omega_i} |0\rangle . \tag{5.1}$$

At the source, the joint spectral amplitude $F(\omega_s, \omega_i)$ of a pure two-mode state with no spectral phase can be described in Gaussian form as,

$$\begin{aligned} F_{\text{source}}(\omega_s, \omega_i) = & \frac{1}{\sqrt{2\pi\sigma_{\omega_s}\sigma_{\omega_i}}\left(1-\rho_\omega^2\right)^{1/4}} \\ & \exp\left(-\frac{1}{2\left(1-\rho_\omega^2\right)}\left[\frac{\left(\omega_s-\omega_{s0}\right)^2}{2\sigma_{\omega_s}^2}+\frac{\left(\omega_i-\omega_{i0}\right)^2}{2\sigma_{\omega_i}^2}-\frac{\rho_\omega\left(\omega_s-\omega_{s0}\right)\left(\omega_i-\omega_{i0}\right)}{\sigma_{\omega_s}\sigma_{\omega_i}}\right]\right), \end{aligned} \tag{5.2}$$

where σ_{ω_s} and σ_{ω_i} are the marginal bandwidths of the signal and idler, respectively, and where the correlation parameter $\rho_\omega = \Delta(\omega_s\omega_i)/\Delta\omega_s\Delta\omega_i$ describes the statistical correlations between the frequency of the signal and idler modes, and can be related to the purity of the partial trace, $P = \sqrt{1-\rho_\omega^2}$. For frequency anti-correlated photons, as shown in Fig. 5.5(a), the frequency correlations are negative and $\rho_\omega < 0$.

The Franson interferometer introduces delays τ_s and τ_i between the short and long arms of each unbalanced interferometer with a phase ϕ_s and ϕ_i on the signal and idler sides, respectively. The joint spectral amplitude after the Franson interferometer takes the form,

$$F_{\text{franson}}(\omega_s, \omega_i) = F_{\text{source}}(\omega_s, \omega_i) \times \frac{1}{4}\left(1+e^{i(\omega_s\tau_s+\phi_s)}\right)\left(1+e^{i(\omega_i\tau_i+\phi_i)}\right). \tag{5.3}$$

The overall coincidence rate directly after the interferometer is,

$$
\begin{aligned}
C\left(\phi_s,\phi_i\right) &= \int_{-\infty}^{\infty} d\omega_s d\omega_i \left|F_{\text{franson}}(\omega_s,\omega_i)\right|^2 \\
&\propto 1+\exp\left(\frac{-\tau_s^2\sigma_{\omega_s}^2}{2}\right)\cos\left(\omega_{s0}\tau_s-\phi_s\right)+\exp\left(\frac{-\tau_i^2\sigma_{\omega_i}^2}{2}\right)\cos\left(\omega_{i0}\tau_i-\phi_i\right) \\
&+\frac{1}{2}\exp\left(-\frac{1}{2}(\sigma_{\omega_s}\tau_s-\sigma_{\omega_i}\tau_i)^2-\left(1+\rho_\omega\right)\sigma_{\omega_s}\sigma_{\omega_i}\tau_s\tau_i\right)\cos\left[(\omega_{s0}\tau_s-\phi_s)+(\omega_{i0}\tau_i-\phi_i)\right] \\
&+\frac{1}{2}\exp\left(-\frac{1}{2}(\sigma_{\omega_s}\tau_s-\sigma_{\omega_i}\tau_i)^2-\left(1-\rho_\omega\right)\sigma_{\omega_s}\sigma_{\omega_i}\tau_s\tau_i\right)\cos\left[(\omega_{s0}\tau_s-\phi_s)-(\omega_{i0}\tau_i-\phi_i)\right].
\end{aligned}
\tag{5.4}
$$

For frequency anti-correlated photons, $\rho\to-1$, we expect interference which depends on the phase sum $\phi_s+\phi_i$, whereas for frequency correlated photons $\rho\to1$, the interference depends on the phase difference $\phi_s-\phi_i$. Considering the idealized case of frequency anti-correlations ($\rho\to-1$), assuming the signal and idler photon bandwidths σ_ω are the same, and the interferometer delays τ are equal, Eq. 5.4 simplifies to,

$$
\begin{aligned}
C\left(\phi_s,\phi_i\right) &\propto 1+\exp\left(\frac{-\tau^2\sigma_\omega^2}{2}\right)\cos\left(\omega_{s0}\tau-\phi_s\right)+\exp\left(\frac{-\tau^2\sigma_\omega^2}{2}\right)\cos\left(\omega_{i0}\tau-\phi_i\right) \\
&+\frac{1}{2}\exp\left(-\left(1+\rho_\omega\right)\sigma_\omega^2\tau^2\right)\cos\left[(\omega_{s0}\tau-\phi_s)+(\omega_{i0}\tau-\phi_i)\right].
\end{aligned}
\tag{5.5}
$$

On the other hand, single-photon detection events have interference fringes described by,

$$
S(\phi_j)\propto 1+\exp\left(-\frac{1}{2}\sigma_{\omega_j}^2\tau_j^2\right)\cos\left(\omega_{j0}\tau_j-\phi_j\right). \tag{5.6}
$$

where $j\in\{s,i\}$. Comparing Eq. 5.5 and Eq. 5.6, we find that there are two time scales for interference for the two-photon state from downconversion. The single-photon interference in Eq. 5.6 varies with ϕ_j and has a coherence time that depends on the inverse bandwidth of the photons, $\tau_c^{(1)}=1/\sigma_\omega=1/\Delta\omega$, whereas the two-photon interference in Eq. 5.5 varies with the sum $\phi_s+\phi_i$ and has a coherence time that depends on the two-photon spectral bandwidth, $\tau_c^{(2)}=1/\left(\sqrt{2}\sqrt{1+\rho}\sigma_\omega\right)=1/\Delta(\omega_s+\omega_i)$. The Franson interferometer can thus be used to separate these two time scales by setting the delay $1/\Delta\omega\ll\tau\leq1/\Delta(\omega_s+\omega_i)$ between the single-photon and two-photon coherence times. Thus, with the appropriately chosen delay settings, we find the singles detection rates are constant whereas the coincident detection rate has oscillating fringes which depends on $\phi_s+\phi_i$ with an interference visibility

of $V = \frac{1}{2}\exp\left(-\frac{1}{2}\Delta(\omega_s+\omega_i)^2\tau^2\right)$. The visibility $V \leq \frac{1}{2}$ without temporal selection is limited by the non-interfering background contributions from the short-long and long-short paths of the interferometer. In order to improve the measured visibility, these non-interfering background terms must be temporally filtered.

5.3.2 Franson interferometry with spectral or temporal filtering

We now discuss the spectral and temporal features of the downconverted state after the Franson interferometer. We will show that visibilities in the coincident rates greater than 50% can be achieved with temporal filtering. This is achieved by calculating the joint spectrum and joint temporal intensity. The joint spectrum is obtained from the modulus squared of Eq. 5.3,

$$\left|F_{\text{franson}}\left(\omega_s,\omega_i\right)\right|^2 = \left|F_{\text{source}}\left(\omega_s,\omega_i\right)\right|^2 \times \cos\left(\frac{\omega_{s0}\tau_s+\phi_s}{2}\right)^2 \cos\left(\frac{\omega_{i0}\tau_i+\phi_i}{2}\right)^2. \tag{5.7}$$

It consists of the original source spectrum $|F_{\text{source}}(\omega_s,\omega_i)|^2$, which is intensity modulated. When $\phi_i+\phi_s=0$, the oscillations for the anti-correlated frequencies remain in phase, as in Fig. 5.5(b), whereas when $\phi_s+\phi_i=\pi$, they will be out of phase, as in Fig. 5.5(c).

The joint temporal amplitude is obtained by taking the Fourier transform of the joint spectral amplitude,

$$f_{\text{franson}}\left(t_s,t_i\right) = \int d\omega_i d\omega_s F_{\text{franson}}\left(\omega_i,\omega_s\right) e^{i\omega_i t_i} e^{i\omega_s t_s} \tag{5.8}$$

from which we can obtain the joint temporal intensity,

$$\begin{aligned}\left|f_{\text{franson}}\left(t_s,t_i\right)\right|^2 \propto\ & f_{ss}^2\left(t_s,t_i\right) + f_{ls}^2\left(t_s,t_i\right) + f_{sl}^2\left(t_s,t_i\right) + f_{ll}^2\left(t_s,t_i\right) \\ & + 2\left[f_{ss}\left(t_s,t_i\right) f_{ls}\left(t_s,t_i\right) + f_{sl}\left(t_s,t_i\right) f_{ll}\left(t_s,t_i\right)\right]\cos\left(\omega_{s0}\tau_s-\phi_s\right) \\ & + 2\left[f_{ss}\left(t_s,t_i\right) f_{sl}\left(t_s,t_i\right) + f_{ls}\left(t_s,t_i\right) f_{ll}\left(t_s,t_i\right)\right]\cos\left(\omega_{i0}\tau_i-\phi_i\right) \\ & + 2 f_{sl}\left(t_s,t_i\right) f_{ls}\left(t_s,t_i\right)\cos\left[\left(\omega_{s0}\tau_s-\phi_s\right)-\left(\omega_{i0}\tau_i-\phi_i\right)\right] \\ & + 2 f_{ss}\left(t_s,t_i\right) f_{ll}\left(t_s,t_i\right)\cos\left[\left(\omega_{s0}\tau_s-\phi_s\right)+\left(\omega_{i0}\tau_i-\phi_i\right)\right],\end{aligned} \tag{5.9}$$

where

$$f_{ss}\left(t_s,t_i\right) = \exp\left[-\left(\sigma_{\omega_s}t_s-\sigma_{\omega_i}t_i\right)^2 - 2(1+\rho)\sigma_{\omega_s}\sigma_{\omega_i}t_s t_i\right] \tag{5.10}$$

$$f_{ls}\left(t_s,t_i\right) = \exp\left[-\left(\sigma_{\omega_s}(t_s+\tau_s)-\sigma_{\omega_i}t_i\right)^2 - 2(1+\rho)\sigma_{\omega_s}\sigma_{\omega_i}(t_s+\tau_s)t_i\right] \tag{5.11}$$

$$f_{sl}\left(t_s,t_i\right) = \exp\left[-\left(\sigma_{\omega_s}t_s-\sigma_{\omega_i}(t_i+\tau_i)\right)^2 - 2(1+\rho)\sigma_{\omega_s}\sigma_{\omega_i}t_s(t_i+\tau_i)\right] \tag{5.12}$$

$$f_{ll}\left(t_s,t_i\right) = \exp\left[-\left(\sigma_{\omega_s}(t_s+\tau_s)-\sigma_{\omega_i}(t_i+\tau_i)\right)^2 - 2(1+\rho)\sigma_{\omega_s}\sigma_{\omega_i}(t_s+\tau_s)(t_i+\tau_i)\right] \tag{5.13}$$

are the four terms that represent the different combinations of paths the photons can take in the Franson interferometer, either short-short (f_{ss}), long-short (f_{ls}), short-long (f_{sl}), or long-long (f_{ll}). These are two-dimensional correlated Gaussian functions that are shifted with respect to the origin by the applied delays τ_i and τ_s. Different types of interference can occur between these paths. The first line in Eq. 5.9 contains the non-interference terms, the second and third lines accounts for single-photon interference, while the fourth and fifth lines account for nonlocal two-photon interference, which depends on the overlap between f_{ls} and f_{sl} and between f_{ss} and f_{ll}, respectively. For anti-correlated photons ($\rho \rightarrow$-1), the short-long f_{sl} and long-short f_{ls} terms do not overlap and the fourth line goes to zero since $f_{sl} f_{ls} \rightarrow 0$. The single-photon temporal marginal, on the other hand, is given by,

$$\begin{aligned} |f_{\text{marginal}}(t)|^2 \propto & \exp\left(-2t^2\left(1-{\rho_\omega}^2\right){\sigma_\omega}^2\right) + \exp\left(-2(t+\tau)^2\left(1-{\rho_\omega}^2\right){\sigma_\omega}^2\right) \\ & + 2\exp\left(-2t^2\left(1-{\rho_\omega}^2\right){\sigma_\omega}^2\left(t+\frac{\tau}{2}\right)^2 - \frac{1}{2}{\sigma_\omega}^2{\tau_\omega}^2\right)\cos\left(\tau\omega_0-\phi\right). \end{aligned} \tag{5.14}$$

Comparing Eq. 5.9 and Eq. 5.14, we find, as before, two different timescale for two-photon and single-photon interference. The interference term which varies as $\phi_s + \phi_i$ depends on the overlap between f_{ss} and f_{ll}, whereas the single-photon interference has a coherence time that depends on the inverse bandwidth ($1/\sigma_\omega = 1/\Delta\omega$) of the downconverted light.

In order to calculate the expected coincidence and single-photon rates with temporal selection, we consider the limiting case where we temporally select only the photon arrival times halfway between the short and long paths. This is equivalent to setting $t_s = -\tau_s/2$ and $t_i = -\tau_i/2$ in Eq. 5.9 and Eq. 5.14, which simplify to,

$$\begin{aligned} & \left|f_{\text{franson}}\left(-\frac{\tau_s}{2},-\frac{\tau_i}{2}\right)\right|^2 \propto \\ & 2\exp\left(-\frac{1}{2}\sigma_{\omega_s}^2\tau_s^2 - \frac{1}{2}\sigma_{\omega_i}^2\tau_i^2\right)\left[\cos\left(\omega_{s0}\tau_s-\phi_s\right)+\cos\left(\omega_{i0}\tau_i-\phi_i\right)\right] \\ & + \exp\left(-\frac{1}{2}\left(\sigma_{\omega_s}\tau_s-\sigma_{\omega_i}\tau_i\right)^2 - \left(1+\rho_\omega\right)\sigma_{\omega_s}\sigma_{\omega_i}\tau_s\tau_i\right)\left[1+\cos\left(\omega_{s0}\tau_s+\omega_{i0}\tau_i-\phi_s-\phi_i\right)\right] \end{aligned} \tag{5.15}$$

$$\left|f_{\text{marginal}}\left(-\frac{\tau}{2}\right)\right|^2 \propto \exp\left(-\frac{1}{2}\left(1-{\rho_\omega}^2\right){\sigma_\omega}^2\tau^2\right) + \exp\left(-\frac{1}{2}{\sigma_\omega}^2\tau^2\right)\cos\left(\omega_0\tau-\phi\right) \tag{5.16}$$

The visibility of the two-photon interference term in Eq.5.15 is then maximized under two conditions: the ratio of the delays is proportional to the ratio of the marginal bandwidths, $\sigma_{\omega_s}\tau_s = \sigma_{\omega_i}\tau_i$, and the delays are less than the two-photon coherence time, $\tau_s\tau_i \ll$

$1/\left[2(1+\rho)\sigma_{\omega_s}\sigma_{\omega_i}\right]$. Under these conditions, assuming the photon bandwidths are equal, and substituting the expressions for the single- and two-photon spectral bandwidths, the coincidence rate and single-photon rates of photon detections with temporal selection at $t_i = -\tau_i/2$ and $t_s = -\tau_s/2$ become,

$$C(\phi_s, \phi_i) = \left| f_{\text{franson}}\left(-\frac{\tau_s}{2}, -\frac{\tau_i}{2}\right)\right|^2 \propto \exp\left(-\frac{1}{2}\Delta\left(\omega_s+\omega_i\right)^2\tau^2\right)\left[1+\cos\left(\omega_{s0}\tau_s+\omega_{i0}\tau_i-\phi_s-\phi_i\right)\right] \tag{5.17}$$

$$S(\phi_j) = \left| f_{\text{marginal}}\left(-\frac{\tau}{2}\right)\right|^2 \propto \exp\left(-\frac{1}{2}\left(1-{\rho_\omega}^2\right){\Delta\omega_j}^2\tau^2\right) + \exp\left(-\frac{1}{2}\Delta\omega_j^2\tau^2\right)\cos\left(\omega_0\tau-\phi_j\right) \tag{5.18}$$

As before, single-photon interference is removed by making the delays larger than the single-photon coherence time, $\tau \gg 1/\Delta\omega$. However now, with temporal selection, the non-interfering terms have been filtered and 100% interference visibility can be achieved in the two-photon coincidence rate.

5.4 Experimental Setup

5.4.1 The unbalanced interferometer for ultrafast photons

The experimental implementation of the Franson interferometer presented in Fig. 5.3 was chosen to provide a stable and compact method of creating time bin states with subpicosecond temporal separations. We construct the ultrafast Franson interferometer using birefringent crystals where the long and short paths arise due to the different refractive indices, and hence different optical path lengths, for horizontally and vertically polarized light [96], as seen in Fig. 5.3(b). Two millimeters of α-BBO creates an interferometer with relative delays below one picosecond and does not require any active phase stabilization. In this section, we analyze the transformations applied to the polarization state of the photon by the unbalanced interferometer in Fig. 5.3(b), composed of a birefringent crystal, wave plates, and a polarizing beam splitter.

We denote the eigenstates of the Pauli operators σ_z as $|H\rangle$ and $|V\rangle$, representing the horizontal and vertical polarization states of light. After downconversion, the polarization state of each photon is vertical, $|\psi\rangle_{\text{pol}} = |V\rangle$. The α-barium borate (α-BBO) birefringent crystals at 45 degrees separate the photons on each side into early, $|e\rangle$, and late, $|l\rangle$, time

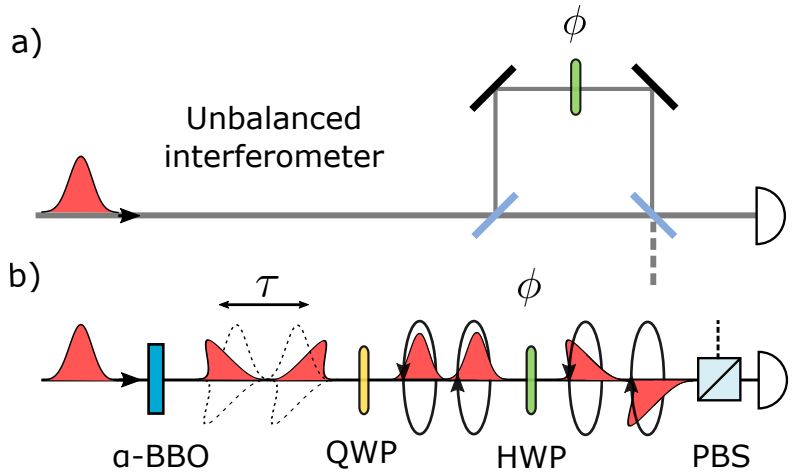

Figure 5.3: **The unbalanced interferometer for ultrafast states.** (a) Each photon is split into early and late time bins and recombined with a phase applied to one bin. (b) The delays and phases are implemented through birefringent material and wave plates, creating a path difference on subpicosecond time scales between the short and long paths. A birefringent crystal (α-BBO) splits a horizontally polarized photon into a diagonal and a delayed anti-diagonal mode. A quarter-wave plate (QWP) converts diagonal and anti-diagonal to left- and right-circularly polarized light. A half-wave plate (HWP) introduces a phase between the circularly polarized photons. Both polarizations are then projected into the horizontal state with a polarizing beam splitter (PBS). See Section 5.4.1 for further details.

bins with a temporal separation of $\tau_s = 0.820$ ps and $\tau_i = 0.910$ ps, for the signal and idler, respectively. The two time bins have orthogonal polarizations, which we denote as diagonal, $|D\rangle = \frac{1}{\sqrt{2}}(|H\rangle + |V\rangle)$ and anti-diagonal, $|A\rangle = \frac{1}{\sqrt{2}}(|H\rangle - |V\rangle)$. As a result, the polarization state is transformed to, $|\psi\rangle_{\text{pol}} \rightarrow \frac{1}{\sqrt{2}}(|D\rangle|e\rangle + |A\rangle|l\rangle)$. The phase difference ϕ between the two time bins can be controlled by manipulating the polarization of the two modes after the α-BBO crystals with two wave plates and a PBS. A quarter-wave plate (QWP) first converts the two orthogonal polarization modes into left-circular, $|L\rangle = \frac{1}{\sqrt{2}}(|H\rangle - i|V\rangle)$, and right-circular polarizations, $|R\rangle = \frac{1}{\sqrt{2}}(|H\rangle + i|V\rangle)$, resulting in the state $\frac{1}{\sqrt{2}}(|L\rangle|e\rangle + |R\rangle|l\rangle)$. A half-wave plate (HWP) at an angle θ, described by the unitary

operator,

$$U_{\mathrm{HWP}}(\theta) = i \begin{pmatrix} \cos 2\theta & \sin 2\theta \\ \sin 2\theta & -\cos 2\theta \end{pmatrix}, \tag{5.19}$$

next applies the following transformations on the left- and right-circular polarizations of light,

$$U_{\mathrm{HWP}}(\theta) |R\rangle = i e^{i2\theta} |L\rangle \tag{5.20}$$

$$U_{\mathrm{HWP}}(\theta) |L\rangle = i e^{-i2\theta} |R\rangle , \tag{5.21}$$

thus modifying the state to $\frac{1}{\sqrt{2}} i \left(e^{i2\theta} |R\rangle |e\rangle + e^{-i2\theta} |L\rangle |l\rangle \right)$. The PBS then erases the polarization information by projecting both circular polarizations into the horizontal mode $|H\rangle$, transforming the state to $\frac{1}{2} i |H\rangle \left(e^{-i2\theta} |e\rangle + e^{i2\theta} |l\rangle \right)$. As a result of these transformations, the photon at the output of the unbalanced interferometer is in a time bin state with a phase difference between the early and late bins that can be set by the angle of the HWP through the parameterization $\phi = 4\theta$.

5.4.2 Experimental setup and details

The experimental setup is shown in Fig. 5.4. Signal-idler photon pairs are produced using SPDC with center wavelengths of 730 nm and 827 nm, respectively. A pair of tunable edge filters in the source control the single-photon spectral bandwidths by making effective bandpass filters of 3.0 nm (s.d.) and 3.5 nm, for the signal and idler respectively. The photon pairs are coupled into fiber, allowing for direct detection, spectral, or temporal measurements in coincidence, with or without the Franson interferometer. Spectral measurements are performed using two grating-based single-photon monochromators with a resolution of approximately 0.1 nm, while temporal measurements are implemented by optically gating the single-photons using SFG with femtosecond laser pulses which have an intensity pulse width of 0.120 ps (s.d.) [209].

Photons from the source were detected at a rate of 626,000 coincidence counts per second with 3.6×10^6 and 3.3×10^6 single-detection events per second for the signal and idler, respectively. The heralded second-order coherence of the source, measured with a Hanbury Brown-Twiss interferometer, was $g^{(2)}(0) = 0.391 \pm 0.004$ for the signal and $g^{(2)}(0) = 0.395 \pm 0.006$ for the idler. In general, double-pair emission will lead to a broad background in the joint spectrum and joint temporal intensity, however, due to the tight

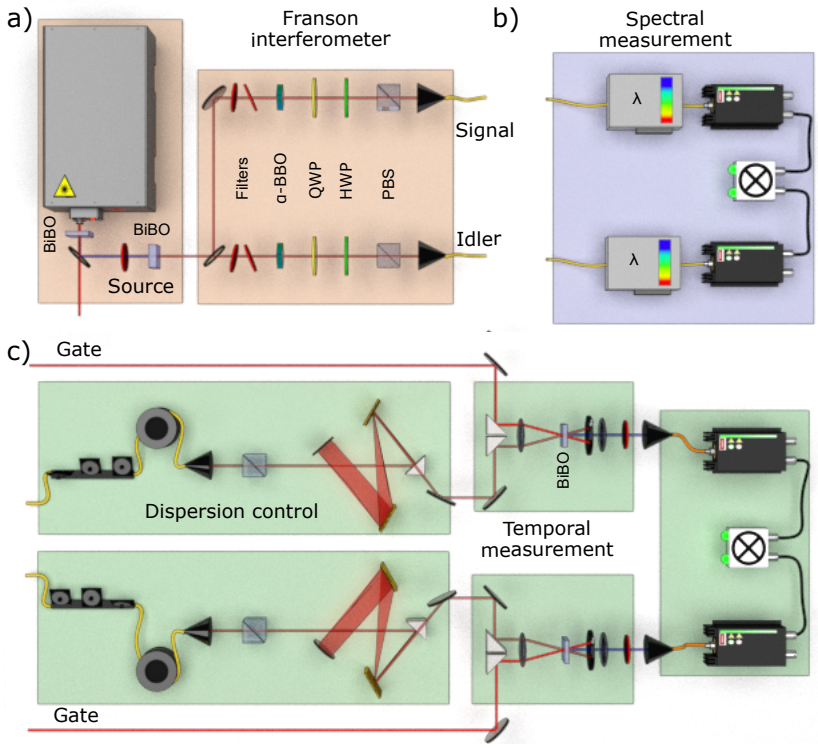

Figure 5.4: **Experimental setup.** (a)A Ti:sapphire laser pulse (775nm, 3.8W average power, 0.120 ps (s.d.) pulse-width), is frequency doubled in 2 mm of β-bismuth borate (BiBO). After spectral filtering with a 0.2 nm FHWM bandpass filter, the second harmonic (387.6 nm, 300 mW average power, approximately 0.940 ps (s.d.) coherence time) pumps a 5 mm BiBO crystal for type-I spontaneous parametric downconversion (SPDC) generating frequency entangled photons centered at 730 nm and 827 nm. The photons are separated by a dichroic mirror and their bandwidth is controlled using tunable edge filters. Each photon passes through an unbalanced interferometer consisting of α-BBO, QWP, HWP, and PBS. We use 2.00 mm and 2.25 mm of α-BBO to create a difference between the short and long paths of $\tau_s = 0.820$ ps and $\tau_i = 0.910$ ps on the signal and idler side, respectively. The output of the Franson interferometer is coupled into single-mode fibers. (b) Spectral measurements are made with single-photon spectrometers. (c) Temporal measurements are performed using ultrafast gating with a strong laser pulse. A pair of grating compressors compensates for the dispersion introduced by the fibers.

temporal filtering on both sides, we estimate that double pairs contribute to less than 1% of the measured up-converted signal. After the up-conversion on each side (without the

Franson interferometer), approximately 44 coincidence counts (12,000 up-converted signal singles and 21,000 up-converted idler singles per second) per second were measured at the peak, from which about 0.8 coincidence counts (400 signal and 2,500 idler singles) per second were background from the second harmonic of the gate pulse.

5.5 Experimental Results

5.5.1 Franson interferometry with fast detectors

Joint spectral and temporal characterization

The joint spectral intensity and joint temporal intensity of the state *before* the Franson interferometer were measured and the data is shown in Figs. 5.5(a) and 5.5(d), respectively. We observe strong anti-correlations between the photon frequencies and strong positive correlations between their arrival times. In Table 5.1, we present the fit parameters for the measured widths of the joint spectral intensity in Fig. 5.5(a) and the joint temporal intensity in Fig. 5.5(d). The marginal widths are obtained by fitting the marginals of Figs. 5.5(a) and 5.5(d) to a one-dimensional Gaussian, while the heralded widths are obtained taking the average of several slices of the data when the frequency or time of one photon is fixed. The statistical correlation, ρ, is obtained by finding the value that best fits a two-dimensional Gaussian with the measured marginals. To account for the finite resolution of the spectrometers and temporal gates, the fit parameters are deconvolved assuming a Gaussian response function, and these values are presented in parentheses alongside the values obtained from the raw measurements in Table 5.1.

Measurements of the spectral widths in these plots allow us to estimate the one- and two-photon coherence times. The deconvolved frequency marginals are found to be $\Delta\omega_s = 10.65$ ps^{-1} and $\Delta\omega_i = 9.57$ ps^{-1}, from which we estimate single-photon coherence times of $\tau_{cs}^{(1)} = 0.094$ ps and $\tau_{ci}^{(1)} = 0.105$ ps for the signal and idler respectively. Gaussian fits to histograms of the spectral semi-minor and semi-major axes yield deconvolved two-photon spectral bandwidths of $\Delta(\omega_s + \omega_i) = 1.531$ ps^{-1} and $\Delta(\omega_s - \omega_i) = 17.81$ ps^{-1}. From the former, we estimate a two-photon coherence time of $\tau_c^{(2)} = 0.653$ ps. The temporal measurements yield deconvolved temporal marginal widths of $\Delta t_s = 0.455$ ps and $\Delta t_i = 0.488$ ps and deconvolved temporal widths of the semi-minor and semi-major axes of $\Delta(t_s + t_i) = 0.895$ ps and $\Delta(t_s - t_i) = 0.091$ ps.

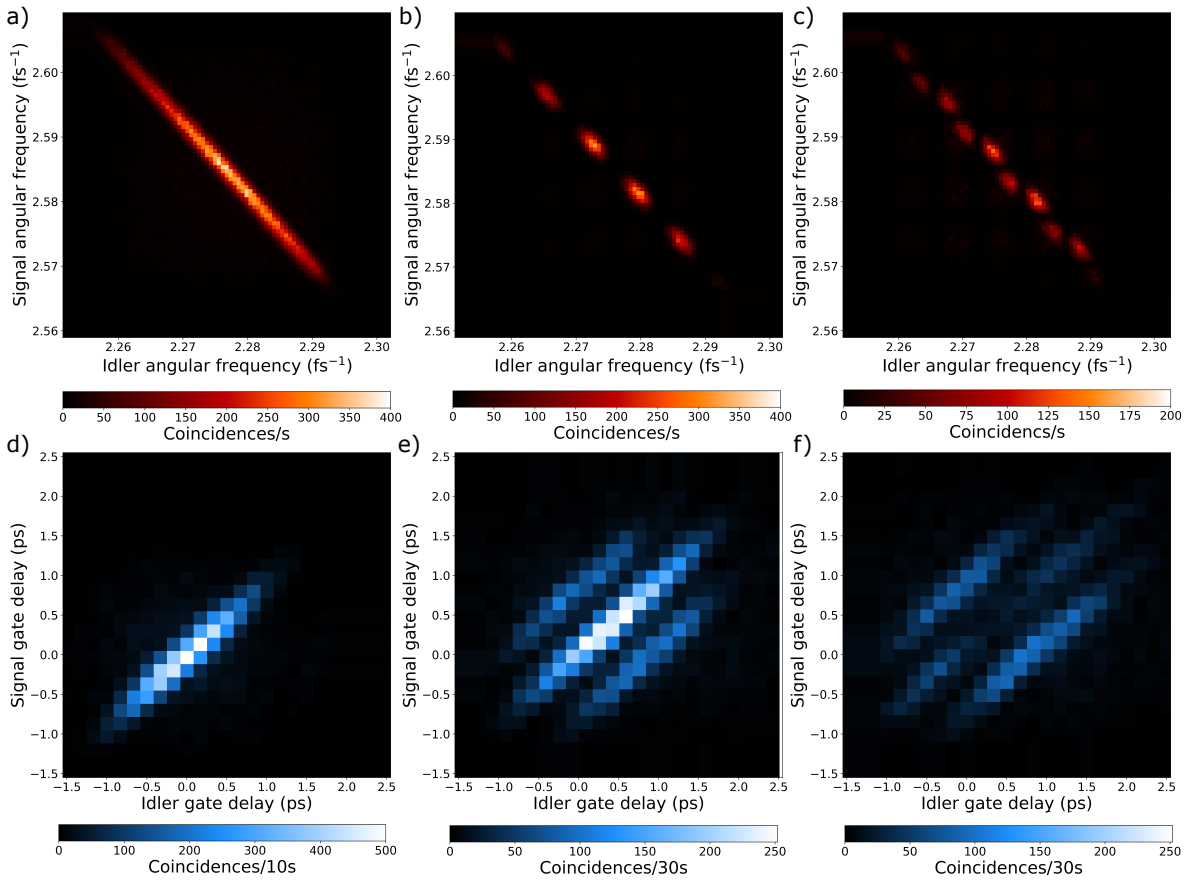

Figure 5.5: **Spectral and temporal characterization of two-photon states.** The joint spectral intensity and joint temporal intensity of the two-photon state shown (a,d) before and (b,c,e,f) after the Franson interferometer. After the interferometer, different fringe patterns are observed in the joint spectrum for (b) constructive and (c) destructive interference. The interferometer shifts the temporal profile in (d) creating four different combinations of paths: short-short, short-long, long-short, and long-long. We observe (e) constructive and (f) destructive interference in the central peak between the cases where the photons both take the short path and both take the long path. These correspond to two-photon states where the signal and idler phases sum to (b,e) $\phi_i + \phi_s = 0$, and (c,f) $\phi_i + \phi_s = \pi$.

The joint spectral intensity and joint temporal intensity of the state *after* the Franson interferometer are shown in Figs. 5.5(b, c, e, f) for two different combinations of phase

Table 5.1: **Fit parameters for source joint plots.** Fit parameters for the joint spectral intensity and the joint temporal intensity as seen in Fig. 5.5(a) and 5.5(d). All measured values are standard deviations and values in parentheses are deconvolved from a Gaussian response function.

Property (Deconvolved)		Joint-spectrum	Joint-temporal intensity
Signal	Frequency (ω_0)	2584.6 ± 0.4 ps^{-1}	-
	Marginal width	10.65 ± 0.04 ps^{-1} (10.63 ± 0.04 ps^{-1})	0.471 ± 0.004 ps (0.455 ± 0.004 ps)
	Heralded width	1.25 ± 0.04 ps^{-1} (1.13 ± 0.05 ps^{-1})	0.171 ± 0.009 ps (0.059 ± 0.022 ps)
Idler	Frequency (ω_0)	2276.7 ± 0.4 ps^{-1}	-
	Marginal width	9.57 ± 0.04 ps^{-1} (9.56 ± 0.04 ps^{-1})	0.502 ± 0.005 ps (0.488 ± 0.005 ps)
	Heralded width	1.13 ± 0.02 ps^{-1} (1.02 ± 0.02 ps^{-1})	0.183 ± 0.010 ps (0.063 ± 0.023 ps)
Statistical Correlation		-0.9929 ± 0.0001 (-0.9942 ± 0.0001)	0.920 ± 0.003 (0.979 ± 0.004)

settings which provide the highest contrast between the constructive and destructive interference in the central peak of the temporal plots. In Fig. 5.5(b), we observe a joint spectral intensity similar to the one found in Fig. 5.5(a) but with a periodic amplitude modulation. The joint spectral intensity in Fig. 5.5(c) is also modulated by two sinusoidal functions, but shifted with respect to the ones in Fig. 5.5(b). These patterns correspond to the expected fringes for unbalanced interferometers applied to both the signal and idler, with phases $\phi_s + \phi_i = 0$ and $\phi_s + \phi_i = \pi$, respectively. In the corresponding temporal plots, we observe constructive interference in Fig. 5.5(e) and destructive interference in Fig. 5.5(f), presenting, respectively, a strong peak and trough in the center of the distribution, while the two side peaks on either side of the central peak exhibit no interference. Through these measurements, we are able to observe the effect of the interferometer in both spectral and temporal domains.

Optically gated Franson interference

We then measure the phase-dependent interference fringes of the Franson interferometer. The signal and idler gate delays are set to 0.455 ps and 0.410 ps, respectively, upconverting

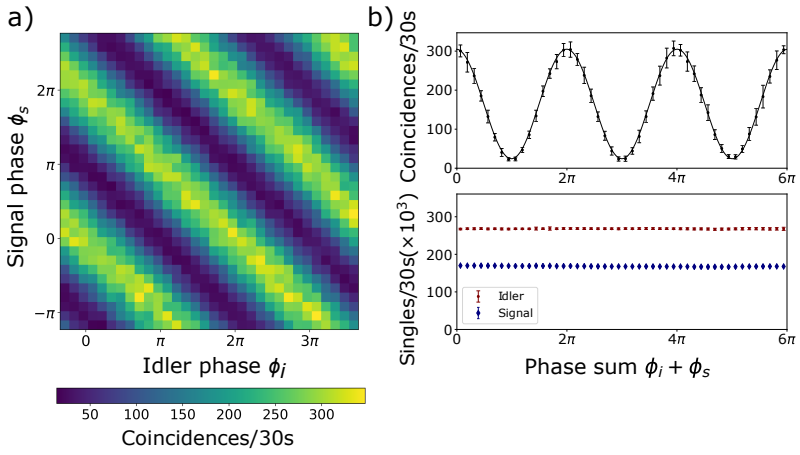

Figure 5.6: **Two-photon interference fringes.** Franson interference between the up-converted signal and idler pair is measured by varying the signal and idler phases while setting the idler gate delay and signal gate delay halfway between the short and long paths of each side of the Franson interferometer. (a) We observe high-visibility interference with fringe oscillations along the diagonal which depend on the sum of the two phases $\phi_s + \phi_i$. (b) Weighted average of the coincidences and weighted average of the singles for the signal and idler pair as viewed as a function of their phase sum. Interference fringes display oscillations of $(85.3 \pm 0.4)\%$ visibility, while the singles detection events show no apparent oscillations.

only the photons in the center of the joint temporal intensity where the highest contrast interference is observed, and corresponding to one pixel in Figs. 5.5(e) and 5.5(f). The measured coincidences as a function of the signal and idler phases, ϕ_s, ϕ_i, are presented in Fig. 5.6. We observe high-visibility interference fringes along one diagonal in Fig. 5.6(a) which corresponds to interference in the correlated phase setting, $\phi_s + \phi_i$, as expected for frequency anti-correlated photons (see Section 5.3.2 for further details). From the same data set, we plot the integrated single and coincidence rates as a function of the phase sum, $\phi_s + \phi_i$, in Fig. 5.6(b). The coincidence rate exhibits fringes with $(85.4 \pm 0.4)\%$ visibility without background subtraction, whereas the single-photon rates exhibit no visible interference. Error bars are obtained from a weighted average of the data points assuming Poissonian noise.

To maximize the visibility of the Franson interference, we found that the interferometer delays need to shift the joint-temporal intensity in Fig. 5.5(d) along its semi-major axis, such that a maximum overlap is obtained between the cases where both photons take the

long path and where both photons take the short path. This can be achieved by matching the ratio of the applied interferometer delays τ to the ratio of the marginal temporal widths Δt, such that $\tau_i/\tau_s = \Delta t_i/\Delta t_s$. The measured ratio was $\Delta t_i/\Delta t_s = 1.07$, differing from unity due to the particular phase-matching conditions which can change the angle of the joint spectral amplitude function [164]. We found that using different lengths of α-BBO crystals, 2.00 mm and 2.25 mm, created the appropriate temporal separations of approximately $\tau_s = 0.820$ ps and $\tau_i = 0.910$ ps, for the signal and idler, respectively, in order to approach this ratio and satisfy the conditions for two-photon interference. We repeated the measurement when both crystal lengths were chosen to be 2.00 mm and observed a reduction of 10% in the visibility.

5.5.2 Bell inequality violation

The measured detector counts for each phase setting ϕ in the unbalanced interferometers can be viewed as one binary outcome of a projective measurement, which we assign the value $(+1)$. The corresponding outcome (-1) could be obtained by placing a second detector to measure the photon events at the second output port of the unbalanced interferometer, however, here the second outcome (-1) is instead obtained by measuring the photon events from the same detector but with an additional π phase shift introduced in the interferometer using the HWPs in Fig. 5.4. Given measurement outcomes ± 1 for two measurement choices labeled a, a' for the signal and b, b' for the idler, we measure the coincidence rates for the four outcomes of each joint projective measurement, denoted $R_{i,j}(a,b), (i,j = \pm 1)$, and evaluate the correlation coefficient [95],

$$E(a,b) = \frac{R_{++}(a,b) + R_{--}(a,b) - R_{+-}(a,b) - R_{-+}(a,b)}{R_{++}(a,b) + R_{--}(a,b) + R_{+-}(a,b) + R_{-+}(a,b)}. \tag{5.22}$$

Assuming a local-hidden variable model, the CHSH inequality [284] provides an upper limit to the combination of four correlation coefficients, which can be written as,

$$S = |E(a,b) + E(a,b') + E(a',b) - E(a',b')| \leq 2. \tag{5.23}$$

Thus, we can look for a violation of the CHSH inequality from 16 combinations of signal-idler phases, 4 outcomes for each of the 4 joint projective measurements in the inequality [95] (see Section 5.5.2). In Table 5.2, we provide a table of raw coincidence counts for a particular combination of two projective measurements in the $x - z$ plane of the Bloch sphere on both the signal and idler sides. We count for 200 seconds for each outcome,

Table 5.2: **Measured coincidence counts for the CHSH-Bell inequality.** The optical gate delays are set to upconvert photons in the center of the joint-temporal intensity. Upconverted coincidence counts are measured over 200 seconds for 16 combinations of signal-idler phases in the Franson interferometer. These correspond to projective measurements performed on the signal and idler sides respectively labeled a, a' and b, b' with binary outcomes (± 1) assigned for each phase setting.

				Signal Phase (ϕ_s)			
				$7\pi/4$	$3\pi/4$	$\pi/4$	$5\pi/4$
				a		a'	
				$(+1)$	(-1)	$(+1)$	(-1)
Idler Phase (ϕ_i)	0	b	$(+1)$	1292	367	1419	336
	π		(-1)	315	1331	329	1394
	$\pi/2$	b'	$(+1)$	1423	294	358	1333
	$3\pi/2$		(-1)	301	1469	1401	335

and obtain from these counts a CHSH-Bell parameter of 2.42 ± 0.02, a violation of the local-hidden variable bound of 2 by 21 standard deviations [284]. This is a consequence of the entanglement in our system and shows the high quality of the interference and the general performance of our measurement device.

The visibility of the Franson interference and Bell violation could be further improved by reducing the second-harmonic generation (SHG) background from the laser in the optical gating. From the measured upconversion rates after the source, we obtain a coincidence rate of about 44 Hz from which about 0.8 Hz can be attributed to the SHG background of the laser. This corresponds to a signal-to-noise ratio (SNR) of 54. After the Franson interferometer, the measured coincidence rate at the peak is reduced by a factor of 4 but the SHG background remains the same, giving a SNR of 13.5. This translates to a reduction in visibility of 13%, which accounts for most of the observed visibility loss. The SHG background source could be reduced by utilizing a type-II process which would allow for additional polarization filtering.

5.6 Conclusion

We have experimentally observed two-photon quantum interference on ultrafast time scales. The optical gating detection mechanism enables the direct measurement of the joint tempo-

ral intensity as well as the observation of quantum interference phenomena and the violation of a CHSH-Bell inequality in a previously inaccessible regime. The Franson interferometer is stable and compact and could thus support future integration on chip. In addition to interferometry, access to both spectral and temporal features will provide new tools for creating and characterizing two-photon states and will be essential for new applications in quantum state engineering, such as shaping ultrafast entangled photon pulses.

Chapter 6

Reconstructing ultrafast energy-time entangled two-photon pulses

Notes and acknowledgments

The contents of this chapter have been submitted for publication and appeared on the arXiv on January 30, 2019, as [285]:

J.P.W. MacLean, S. Schwarz, K.J. Resch. *Reconstructing ultrafast energy-time entangled two-photon pulses.* arXiv: 1901.11116 (2019).

Author Contributions

Kevin Resch and **Jean-Philippe MacLean** conceived of the study.

Jean-Philippe MacLean developed and tested the algorithm and built the initial numerical model for optical gating.

Jean-Philippe MacLean and **Sacha Schwarz** developed the software framework to analyze two-photon states.

Jean-Philippe MacLean and **Sacha Schwarz** carried out the experiment and analyzed the data.

Jean-Philippe MacLean wrote the first draft of the manuscript.

All authors contributed to the final version.

6.1 Chapter Overview

The generation of ultrafast laser pulses and the reconstruction of their electric fields is essential for many applications in modern optics. Quantum optical fields can also be generated on ultrafast time scales, however, the tools and methods available for strong laser pulses are not appropriate for measuring the properties of weak, possibly entangled pulses. Here, we demonstrate a method to reconstruct the joint-spectral amplitude of a two-photon energy-time entangled state from joint measurements of the frequencies and arrival times of the photons, and the correlations between them. Our reconstruction method is based on a modified Gerchberg-Saxton algorithm. Such techniques are essential to measure and control the shape of ultrafast entangled photon pulses.

6.2 Context

The generation, control, and measurement of high-dimensional entangled quantum states of light are important for optical computing and communication [286, 145, 287, 28]. One form of this entanglement, in the energy-time degree of freedom, can exhibit strong correlations in frequency and time [150, 151], nonlocal interference phenomena [49, 50], and dispersion cancellation [245, 255], with applications in high-capacity quantum key distribution [71, 278], enhanced spectroscopy [280], sensing [288], and two-photon absorption [273]. The generation and control of energy-time entanglement has been realized in both bulk crystals and waveguide structures [289, 74, 290, 291, 110], however, it remains an important challenge to reconstruct the quantum state of the photons produced. The performance of any quantum optical technology using time and frequency depends on being able to both shape and measure such photonic states.

In ultrafast optics and laser physics, the ability to measure the amplitude and phase of laser pulses on ultrafast time scales is essential for nonlinear optics and spectroscopy. In this context, the problem of electric field reconstruction has been extensively studied [182]. Optical pulses can be produced on time scales much shorter than any photodetector response time [292], and consequently, the only thing fast enough to measure an ultrafast laser pulse is another ultrafast pulse. Techniques such as FROG [224] and SPIDER [293] make use of nonlinear optical processes to measure and reconstruct ultrafast pulses. However, adapting them to quantum states of light is challenging due to the low power levels of single photons. In addition, the algorithms developed for laser pulses do not account for the possibility that photons can be entangled. New innovations are therefore needed to reconstruct the joint state of entangled ultrafast photon pulses.

Approaches for characterizing the optical modes of photons have been explored using homodyne measurements [294, 45, 295, 296, 297, 298], or two-photon interference effects [299, 300, 301]. The increased interest in time-frequency modes has also led to nonlinear ultrafast approaches for characterization [109, 179, 302]. To measure both the frequency and time intensity correlations of energy-time entangled states, optical methods based on optical gating and frequency resolved measurements have recently been developed. These have been used to observe nonlocal dispersion cancellation [209] and two-photon quantum interferometry [266] on time scales inaccessible to standard photodetectors. For complete characterization, however, the joint spectral phase is also required.

Recovering the phase of a field from intensity measurements in Fourier-related domains is known as a phase-retrieval problem. In 1972, Gerchberg and Saxton provided a practical solution to this problem. They introduced an iterative algorithm, referred to as the Gerchberg-Saxton algorithm (GS), to extract the complete wavefunction of an electron beam, including its phase, from intensity recordings in the image and diffraction planes [216]. Their algorithm can be applied to problems involving electromagnetic waves [236, 223] including optical wavelengths [217].

In this chapter, we implement a technique to recover the phase of ultrafast energy-time entangled two-photon pulses based on intensity measurements of the frequency and the arrival time. Inspired by the conventional phase retrieval problem, we develop an algorithm based on a method of alternate projections [216, 218, 220] that iterates between the frequency and time domains imposing the measured intensity constraints at each iteration. Measurements in frequency are performed with single-photon spectrometers and measurements in time are implemented via optical gating with an ultrafast optical laser pulse.

6.3 Reconstruction of two-photon states of light

A pure energy-time two photon state can be modelled as [151, 74],

$$|\psi\rangle = \int d\omega_s d\omega_i F_{\omega\omega}(\omega_s, \omega_i) a_s^\dagger(\omega_s) a_i^\dagger(\omega_i) |0\rangle , \tag{6.1}$$

corresponding to a superposition of frequency modes for the signal $a_s^\dagger(\omega_s)$ and the idler $a_i^\dagger(\omega_i)$ weighted by the joint spectral amplitude (JSA) function $F_{\omega\omega}(\omega_s, \omega_i)$. The joint spectral amplitude, $F_{\omega\omega}(\omega_s, \omega_i) = |F_{\omega\omega}(\omega_s, \omega_i)| \exp[i\phi(\omega_s, \omega_i)]$, describes the amplitude, $|F_{\omega\omega}(\omega_s, \omega_i)|$, and phase, $\phi(\omega_s, \omega_i)$, of the state. For downconversion, it is related to the

pump properties and the phase matching conditions of the nonlinear material [167]. In this form, the joint-spectral intensity $I(\omega_s, \omega_i) = |F_{\omega\omega}(\omega_s, \omega_i)|^2$ characterizes the frequency correlations and the joint temporal intensity (JTI), $I(t_s, t_i) = |F_{tt}(t_s, t_i)|^2$, obtained from the modulus of the Fourier transform, characterizes the temporal correlations. The intensity time-frequency correlations, $I(\omega_s, t_i) = |F_{\omega t}(\omega_s, t_i)|^2$ and $I(t_s, \omega_i) = |F_{t\omega}(t_s, \omega_i)|^2$, can provide additional information on the spectral phase for entangled states [209].

6.3.1 Phase retrieval algorithm

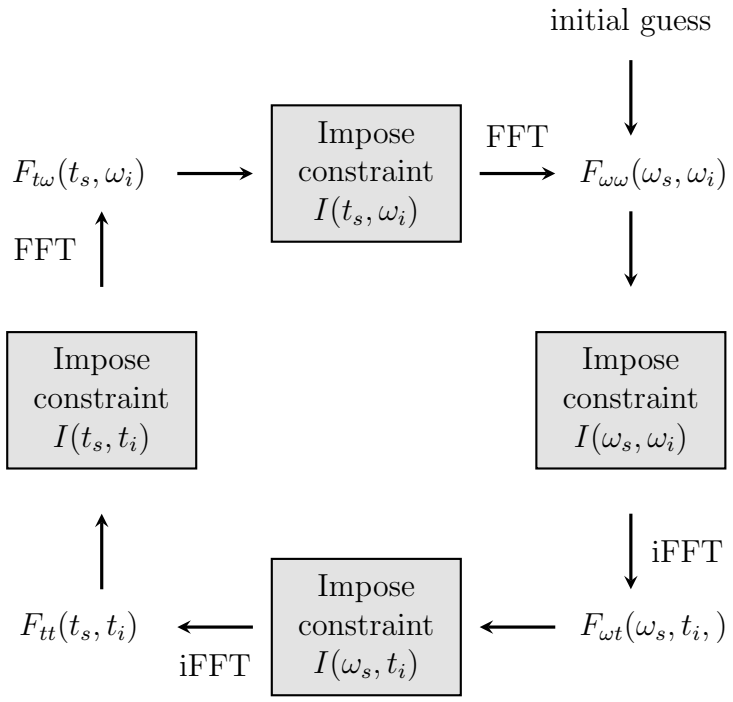

Figure 6.1: **Block diagram of the phase retrieval algorithm.** The algorithm is seeded with an initial guess of the state. At every iteration, the Fast Fourier Transform (FFT) is applied along one dimension of the state after which the magnitude of the state is replaced with the measured data while the phase of the state is preserved. At each iteration the error between the measured and recovered intensities either remains the same or is reduced.

The phase retrieval algorithm is shown in Fig. 6.1. Four time-frequency intensity correlation measurements are performed, $I(\omega_s, \omega_i), I(t_s, \omega_i), I(\omega_s, t_i), I(t_s, t_i)$ [209]. The effect

of the limited instrument resolution for each measured intensity is deconvolved using a Wiener Filter [303]. The algorithm is seeded with an initial guess accompanied with a random phase. In the first iteration, we project the state onto the constraint set that satisfies the measured intensities in frequency. This is achieved by replacing the spectral amplitudes $|F_{\omega\omega}(\omega_s, \omega_i)|$ with the measured spectral amplitudes $\sqrt{I(\omega_s, \omega_i)}$ but keeping the phase,

$$F_{\omega\omega}(\omega_s, \omega_i) \rightarrow \frac{F_{\omega\omega}(\omega_s, \omega_i)}{|F_{\omega\omega}(\omega_s, \omega_i)|}\sqrt{I(\omega_s, \omega_i)}. \tag{6.2}$$

We then apply the Fast Fourier Transform algorithm (FFT) to obtain an estimate of $F_{t\omega}(t_s, \omega_i)$ and again replace the amplitudes $|F_{t\omega}(t_i, \omega_s)|$ with the measured amplitudes $\sqrt{I(t_i, \omega_s)}$. This is repeated two more times, as in Fig. 6.1, completing one iteration of the algorithm.

At each iteration, the error between the measured and the reconstructed JSI (or JTI) is calculated,

$$E_{\omega}^{(k)} = \sqrt{\frac{1}{N^2}\sum_{i,j=1}^{N}\left(I(\omega_i, \omega_j) - \mu\left|F_{\omega\omega}^{(k)}(\omega_i, \omega_j)\right|^2\right)^2} \tag{6.3}$$

$$E_{t}^{(k)} = \sqrt{\frac{1}{N^2}\sum_{i,j=1}^{N}\left(I(t_i, t_j) - \mu\left|F_{tt}^{(k)}(t_i, t_j)\right|^2\right)^2}, \tag{6.4}$$

where $I(\omega_i, \omega_j)$ and $I(t_i, t_j)$ are the measured intensity of the i, jth bin, $|F_{\omega\omega}^{(k)}(\omega_i, \omega_j)|^2$ and $|F_{tt}^{(k)}(t_i, t_j)|^2$ are the reconstructed states at the kth iteration, μ is a real normalization constant that minimizes the error, and N^2 is the total number of data points. If the measured intensities are normalized to one before inserting them into Eq. 6.3 and Eq. 6.4, then the reconstruction error can be thought of as the average percentage error between the measured and recovered trace. An important feature of these types of algorithms is that the measured error will always decrease or remain constant at each iteration, and will not diverge [216, 214]. More sophisticated error models exist which can remove the effects of global or linear phase terms (translations) which should not be included as part of the error in the time-time plots [226].

Phase retrieval algorithms have a well-known ambiguity. If the intensity distribution in the Fourier plane is centrosymmetric, then the complex conjugate of any given solution in the object plane is also a solution [226]. For the energy-time degree of freedom, this implies a time-reversal ambiguity, i.e., it is not possible to distinguish between positive and negative

dispersion from the intensity measurements in frequency and time alone. Measurements of the time-frequency correlations can distinguish between these two cases and break the time-reversal ambiguity. We find a significant improvement of the algorithm's performance when these are included in the constraint set.

6.3.2 Measurements of time-frequency correlations as an indication of dispersion

We illustrate how the measurements of the correlation in the frequency of one photon and time of arrival of the other, as illustrated in Fig. 6.2, provide information on dispersion. A temporal measurement is applied to the signal photon ω_s and a spectral measurement is applied to the idler photon ω_i. The temporal measurement is modelled as a convolution of the input signal photon spectra with the gate pulse,

$$G\left(\omega_g, \tau\right) = \frac{1}{\left(2\pi\sigma_g^2\right)^{\frac{1}{4}}} \exp\left(-\frac{\left(\omega_g - \omega_{g_0}\right)^2}{4\sigma_g^2} + i\tau\left(\omega_g - \omega_{g_0}\right)\right), \tag{6.5}$$

which has centre frequency ω_g, marginal bandwidth σ_g, and delay τ. The up-converted signal photon at frequency $\omega_{u_s} = \omega_s + \omega_g$, is then measured in coincidence with the spectrally filtered idler photon ω_i. The probability of measuring a coincidence is,

$$I\left(\tau_s, \omega_i\right) = \int d\omega_{u_s} \left| \int d\omega_s G\left(\omega_{u_s} - \omega_s, \tau_s\right) \Phi_{\mathrm{SFG}}\left(\omega_s, \omega_{u_s} - \omega_s, \omega_{u_s}\right) \; F_{\omega\omega}\left(\omega_s, \omega_i\right) \right|^2, \tag{6.6}$$

where Φ_{SFG} is the phase matching function of the sum-frequency generation process in the temporal measurement and $F_{\omega\omega}(\omega_s, \omega_i)$ is the joint spectral amplitude. For now, we assume the phase matching is flat, i.e., $\Phi_{\mathrm{SFG}} \approx 1$. This assumption is valid for thin crystals which have a broad phase-matching bandwidth, and does not hold for the crystals used in the previous experiments. The effect of thick crystals on the measurement in time will be considered in Sec. 6.6.

Since the convolution of two Gaussian functions is a Gaussian, we can re-express $I(\tau_s, \omega_i)$ of Eq. 6.6 as a two-dimensional Gaussian (see Appendix B), with the marginal

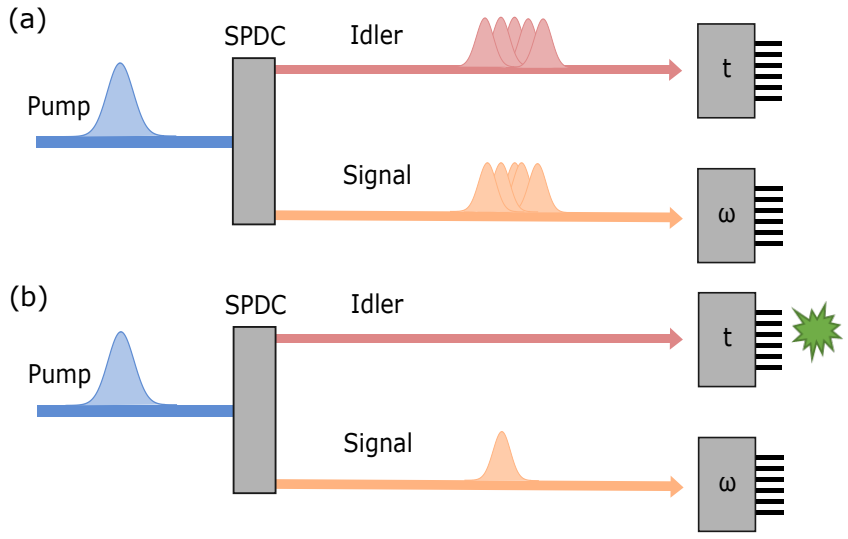

Figure 6.2: **Time-frequency intensity correlation measurements.** The measurements of time and frequency are similar to the two-stage measurement in FROG, but the second-stage frequency measurement is performed on the other photon. (a) For energy-time entangled photons in these experiments, the temporal modes are correlated in time. (b) The first measurement in time projects the second photon into the same temporal mode. The second-stage measurement then resolves the frequency of this mode. By repeating this for different measurements in time, it's possible to build up a nonlocal spectrogram of the first photon.

bandwidth ${\Delta\omega_i}^{(m)}$, marginal pulse width ${\Delta t_s}^{(m)}$, and statistical correlation ρ_f as follows,

$$ {\Delta\omega_i}^{(m)} = \sigma_s \tag{6.7} $$

$$ {\Delta t_s}^{(m)} = \sqrt{\frac{1}{4\sigma_g^2} + \frac{1}{4(1-\rho_\omega^2)\sigma_s^2} + 4{A_s}^2{\sigma_s}^2} \tag{6.8} $$

$$ \rho_f = \frac{-4A_s\rho_\omega\sqrt{1-\rho_\omega^2}\sigma_g{\sigma_s}^2}{\sqrt{(1-\rho_\omega^2)\,{\sigma_s}^2 + {\sigma_g}^2\,(1+16A_s^2\,(1-\rho_\omega^2)\,{\sigma_s}^4)}}. \tag{6.9} $$

We see that the marginal bandwidth of the idler ${\Delta\omega_i}^{(m)}$ in Eq. 6.7 is independent of the chirp A_i on the idler as the spectral measurements are insensitive to spectral phase. In the limit of zero chirp on the signal, $A_s = 0$, the marginal pulse width ${\Delta t_s}^{(m)}$ in Eq. 6.8 is a quadrature sum of the gate pulse width $1/2\sigma_g$ and the coherence length of the signal

$1/(2\sqrt{1-\rho_\omega^2}\sigma_s)$ from Eq. 4.7. The frequency of the idler and time of arrival of the signal are also uncorrelated, $\rho_f = 0$, as can be seen in Eq. 6.9. When $A_s \neq 0$, the signal marginal is stretched by the presence of the extra term $4A_s^2\sigma_s^4$ in Eq. 6.8 and the correlations increase with A_s in Eq. 6.9. Moroever, for frequency anti-correlated photons $\rho_\omega < 0$, positive chirp ($A_s > 0$) leads to positive correlations ($\rho_f > 0$) in time and frequency, and negative chirp ($A_s < 0$) leads to negative correlations ($\rho_f < 0$). The sign of the correlations ρ_f is thus the same as the sign of the chirp parameter A_s.

6.4 Experimental Setup

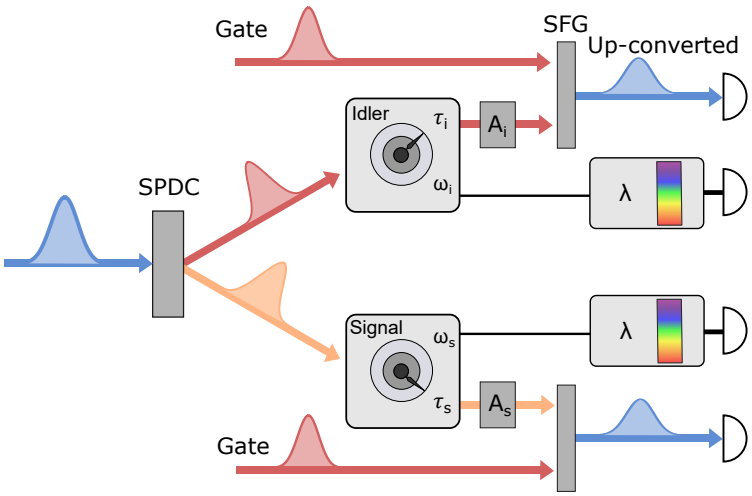

Figure 6.3: **Experimental setup for two-photon state reconstruction.** Energy-time entangled photons are produced through spontaneous parametric downconversion (SPDC). Each photon can be measured in frequency using a scanning monochromoter or in time by optically gating the single photon using sum-frequency generation (SFG) in a nonlinear medium with a strong gate pulse. The delays τ_s and τ_i are between the gate pulse and the photon on the signal and idler side, respectively. The quadratic spectral phases, A_s, on the signal photon and, A_i, on the idler photon, are controlled using a fibre and grating compressor on each side. Measurements in coincidence of all four combinations of the frequency and time of arrival of the photons allow the reconstruction of the joint spectral amplitude function using a phase retrieval algorithm.

The setup is schematically depicted in Fig. 6.3 and described in detail in Refs. [209, 266]. We produce pairs of energy-time entangled photons at 823 nm and 732 nm using spontaneous parametric downconversion. These are coupled in single mode fibres allowing for direct, spectrally resolved, or temporally resolved measurements. Spectral measurement are performed via monochrometers with a resolution of 0.1 nm. Temporal measurements are implemented via optical gating, i.e., via noncollinear sum-frequency generation (SFG) with femtosecond laser pulses in 1 mm of bismuth borate (BiBO) crystal. The electric field of the gate pulse is characterized using an SHG-FROG measurement, as shown in Fig. 6.4. We find an intensity pulse width of 130 fs (s.d.). The instrument resolutions set the filter functions used in the numerical deconvolution of the measured intensities.

6.4.1 Spectral phase calibration using XFROG

The quadratic spectral phase on the photons, $\phi(\omega_s, \omega_i) \approx A_s (\omega_s - \omega_{s0})^2 + A_i (\omega_i - \omega_{i0})^2$, is controlled with a combination of normally dispersive single-mode fibre and adjustable grating compressor for anomalous dispersion [209], where A_s and A_i are the chirp parameters for the signal and idler, respectively. The relative position of the gratings inside the compressor sets the magnitude and sign of the overall dispersion. We calibrate both grating compressors using (cross-correlation FROG) XFROG spectrogram measurements between the strong gate pulse from Fig. 6.4 and a weak laser pulse with the same centre wavelength and path through the fibre-compressor system as the photons on each side. The phase at each relative grating separation is reconstructed using the Principal Component Generalized Projection (PCGP) FROG algorithm [239, 192].

An example measured and reconstructed XFROG spectrogram with corresponding frequency and time marginals is presented in Fig. 6.5. An 822 nm laser pulse (130 fs rms) with a Gaussian spectral profile is separated at a beam splitter into two copies. One copy acting as the signal pulse (30 mW avg. power) is sent through 21.2 m of fibre followed by a grating compressor to compensate for the fibre dispersion. It is subsequently overlapped with the other copy (15mW avg. power), acting as the gate pulse, in 1 mm of BiBO for type-I noncollinear sum-frequency generation. The resulting upconverted light is spectrally resolved on a spectrometer.

The measured background subtracted spectrogram is shown in Fig. 6.5(a). The fork shape observed in the spectrogram is likely the result of self-phase modulation occurring in the fibre. This feature disappears as the signal power is reduced before the fibre. The

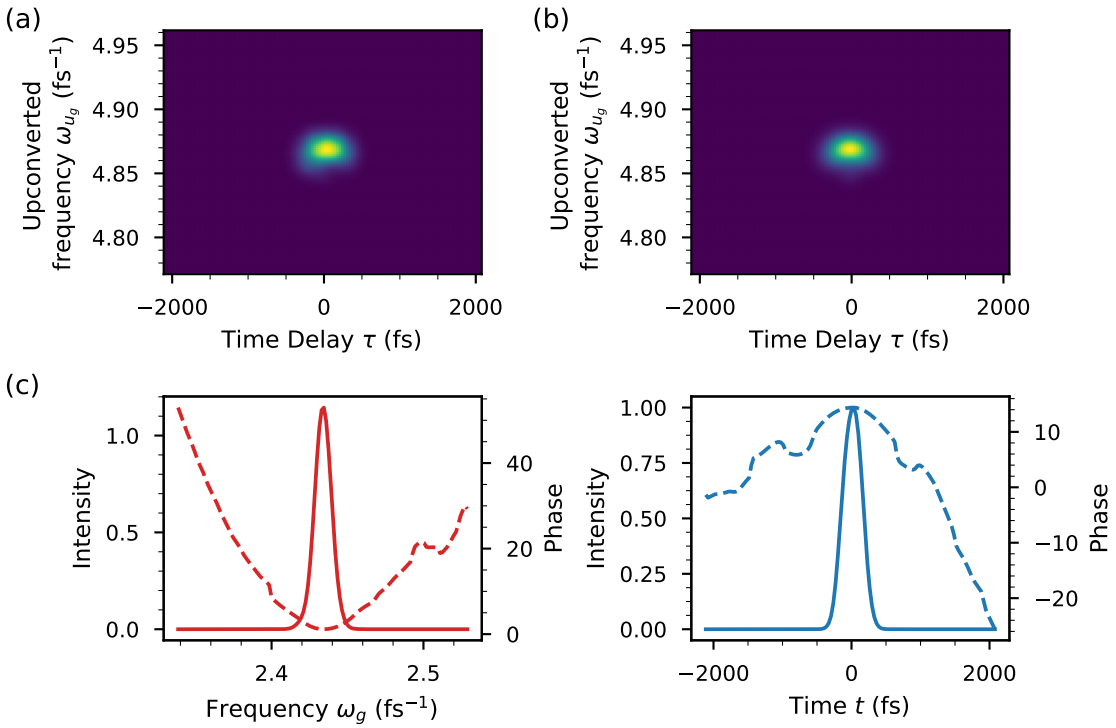

Figure 6.4: **SHG-FROG reconstruction of the gate pulse.** The optical gate pulse used in the experiment is characterized using SHG-FROG. (a) Measured and (b) reconstructed SHG-FROG spectrogram of the optical gate set at 775 nm. (c) Reconstructed electric field intensity (solid) and phase (dashed) in frequency and in time of the gate pulse. We find a gate pulse with a spectral bandwidth of 5.7 ps^{-1}, a quadratic spectral phase of 8,600 fs^2, and a pulse duration of 130 fs.

measured spectrogram is processed using a low-pass filter, corner-suppression method [192], and is binned for the FROG algorithm. The post-processed spectrogram is shown in Fig. 6.5(b). The PCGP algorithm is then run for 500 iterations and the reconstructed spectrogram is shown in Fig. 6.5(c). The measured FROG error between the reconstructed and post-processed spectrograms at each iteration is shown in Fig. 6.6(c). The algorithm converges in approximately in the first 20-50 iterations and stays constant afterwards with a final error of $E_{\mathrm{FROG}} = 0.0104$.

The reconstructed intensity (solid line) and phase (dashed line) of the signal field in

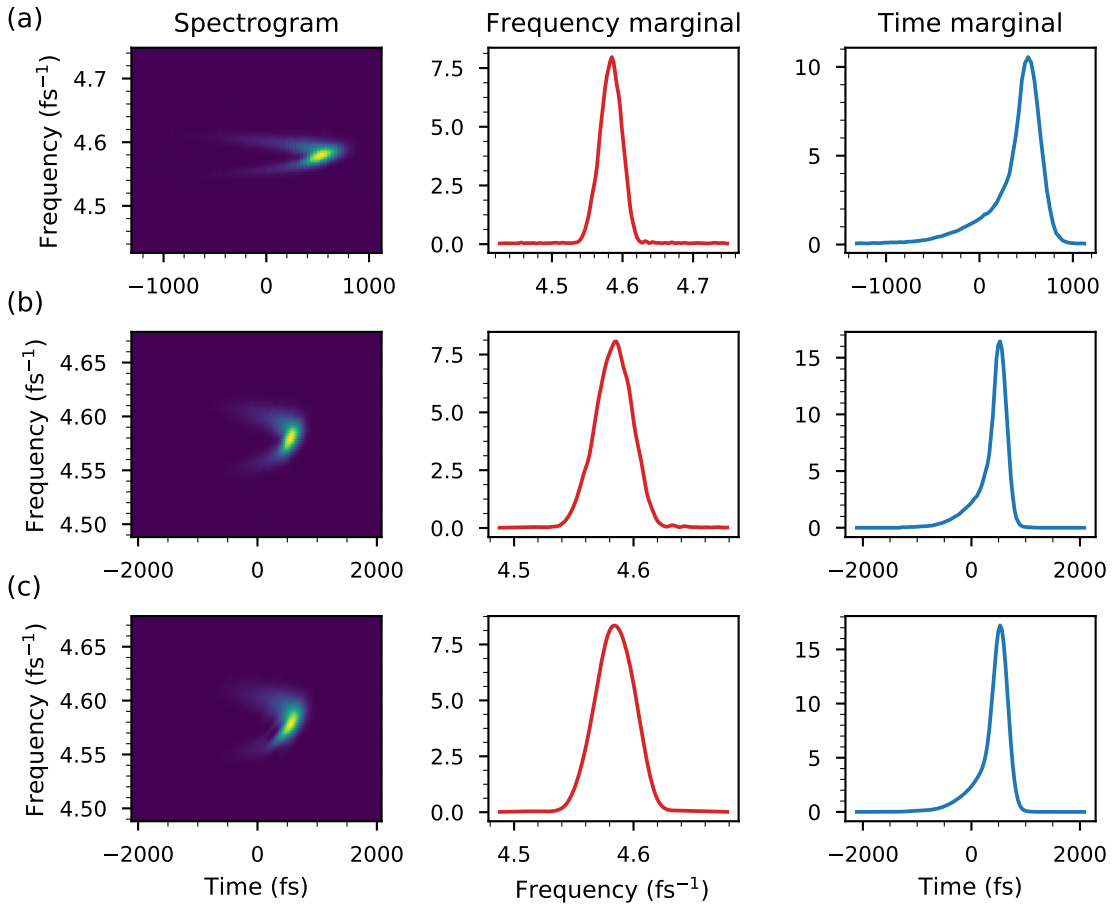

Figure 6.5: **Example measured and reconstructed XFROG spectrograms.** (a) Measured, (b) post-processed and binned, and (c) reconstructed XFROG spectrograms between an unknown signal and a known Gaussian gate pulse using the PCGP FROG algorithm. The signal is sent through a fibre and grating compressor. The marginal in frequency and in time are displayed to the right of each spectrogram. The FROG Error between the (b) post-processed and (c) reconstructed spectrograms is $E_{\mathrm{FROG}} = 0.0104$

.

frequency $E(\omega)$ and in time $E(t)$ are shown in Fig. 6.6(a) and Fig. 6.6(b) respectively. More evidence of self-phase modulation is observed in the jagged peaks on the spectrum in Fig. 6.6(a). The effect of uncompensated third order dispersion is observed in the repeated oscillations trailing the pulse in time. A polynomial fit to the spectral phase in Fig. 6.6(a)

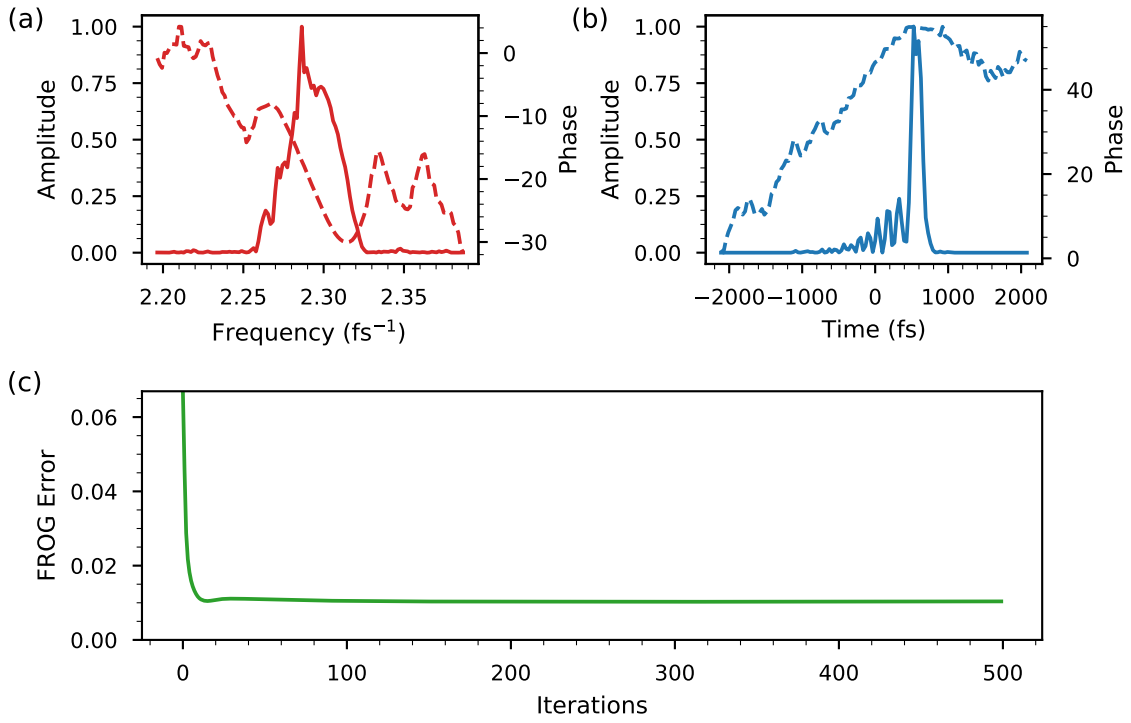

Figure 6.6: **Reconstructed field from measured XFROG spectrogram.** Reconstructed intensity (solid line) and phase (dashed line) in (a) frequency and in (b) time of a pulse for the measured XFROG spectrogram in Fig. 6.5. The spectrum shows evidence of self-phase modulation whereas the oscillations trailing the pulse result from uncompensated third-order dispersion. (c) FROG error at the end of each iteration. The error converges rapidly in the first 20-50 iterations and stays constant afterwards.

confirms this. We find a quadratic spectral phase of $A^{(2)} = 1800$ fs^2 and a cubic spectral phase of $A^{(3)} = 436,000$ fs^3. As a result, the quadratic spectral phase imparted by the fibre is mostly compensated by the grating compressor, but the cubic spectral phase of the fibre and compressor is additive.

We reconstruct the quadratic spectral phase of the weak pulse from the XFROG spectrograms in a similar way for different grating separations in the compressors used on both the signal (732 nm) and idler (823 nm) sides. The results are plotted in Fig. 6.7. We find a quadratic phase that depends linearly on the grating separation of -1360 ± 60 fs^2/mm for the signal [Fig. 6.7(a)] and -2190 ± 70 fs^2/mm [Fig. 6.7(b)] for the idler. The difference

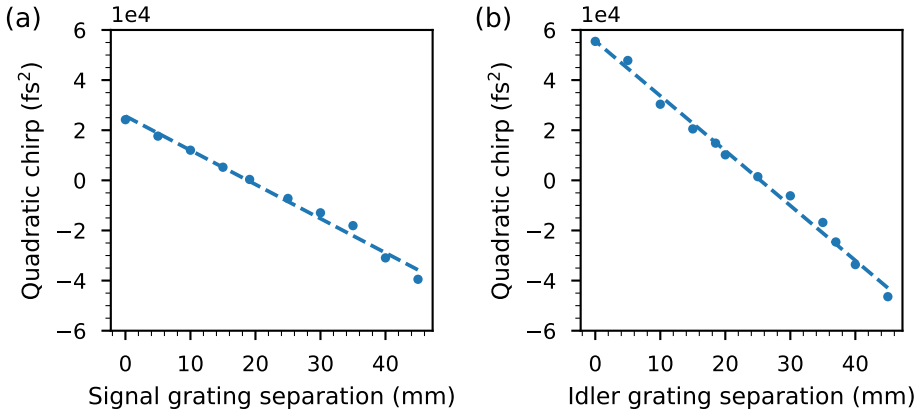

Figure 6.7: **Spectral phase calibration of the grating compressors.** We show the quadratic spectral phase for different relative grating separations of the reconstructed field from XFROG spectrograms on the (a) signal and (b) idler sides. Linear fits to the data have slopes of (-1360 ± 60) fs^2/mm and (-2190 ± 70) fs^2/mm, for the signal and idler respectively.

between the two is attributed to the cubic dependence of dispersion on the wavelength in a grating compressor [196].

6.5 Experimental Results

6.5.1 Time-frequency correlations

We first compare the time-frequency plots with and without dispersion, as shown in Fig. 6.8, to illustrate how these provide additional information on the sign of the chirp. In Fig. 6.8(a) and Fig. 6.8(c), we measure the correlations between the time of arrival of the idler and the frequency of the signal for the cases with no additional dispersion and with 0.022 ps^{-2} of applied positive dispersion to the idler, respectively. We observe negative correlations of $\rho_f = -0.61$ in Fig. 6.8(c) which is contrasted to the observed correlations of $\rho_f = 0.11$ in Fig. 6.8(a). In Fig. 6.8(b) and Fig. 6.8(d), we measure the correlations between the time of arrival of the signal and the idler frequency with no additional dispersion on the signal and with -0.022 ps^{-2} of applied negative dispersion to the signal, respectively. We observe

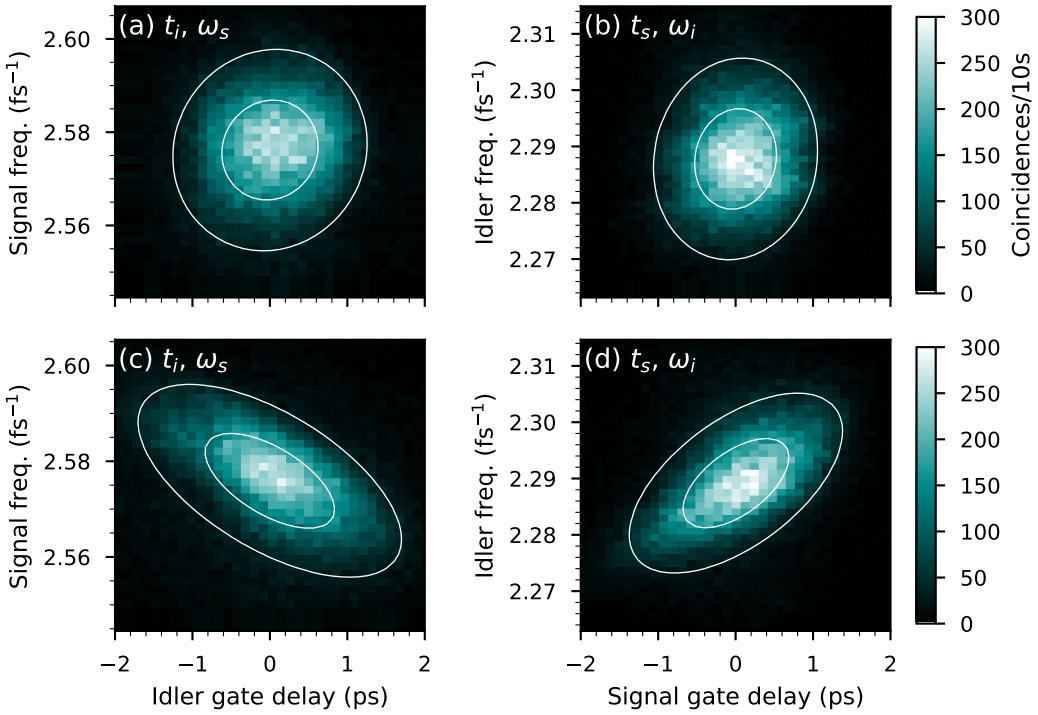

Figure 6.8: **Nonlocal spectrograms as an indication of dispersion.** Measured correlations between the time of arrival of one photon and the frequency of the other for different amounts of applied dispersion. (a,b) We observe very little correlations between the time and frequency axes indicating little to no dispersion applied to the idler and signal, respectively. (c) With negative dispersion of $A_i = -0.022$ ps^{-2} applied to the idler, we observe negative correlations of $\rho_f = -0.61$ between the time and frequency axes, whereas with positive dispersion of $A_s = 0.022$ ps^{-2} applied to the signal, we observe positive correlations of $\rho_f = 0.58$. White lines correspond to 1σ and 2σ contours of Gaussian fits.

positive correlations of $\rho_f = 0.58$ in Fig. 6.8(d) which is again contrasted to the observed correlation of $\rho_f = 0.10$ in Fig. 6.8(b). We thus find that the sign of the correlations depends on the sign of the chirp. The time-frequency plots can distinguish between a positive and a negative spectral phase of the same magnitude, a feature not possible with only the joint spectral intensity and joint temporal intensity.

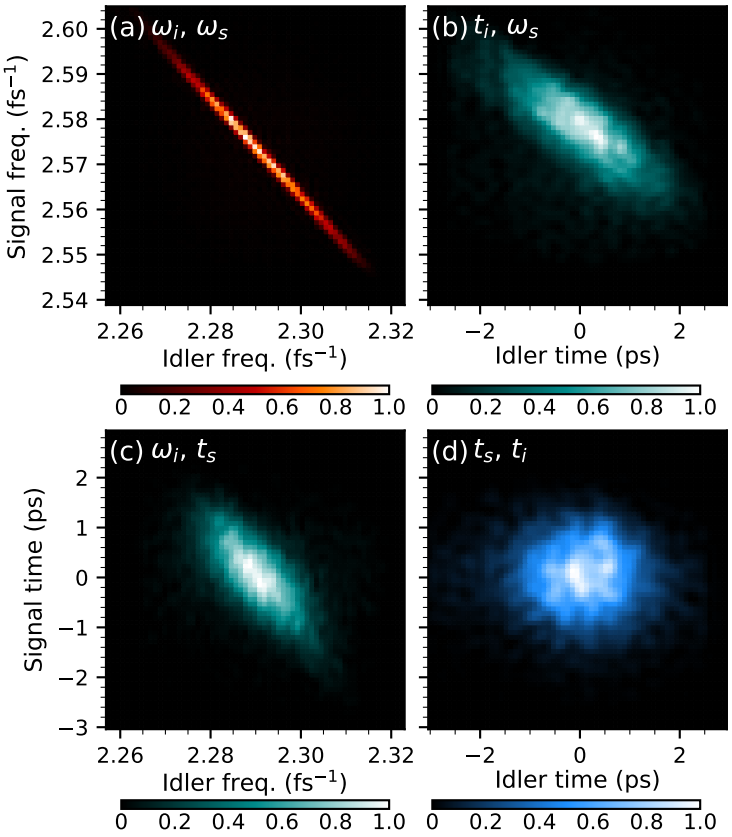

Figure 6.9: **Example deconvolved measured data for two-photon state reconstruction.** Combinations of spectral and temporal measurements are made in coincidence to obtain the (a) joint spectral intensity, (d) joint temporal intensity, and (b,c) correlations between the time and frequency of the photon pair for an SPDC state. We observe strong anti-correlations between the measured quantities in (a), (b), (c) and very little correlations in (d), indicating the presence of negative dispersion on both photons. After post-processing, the measured intensities are used as data constraints for the phase-retrieval algorithm.

6.5.2 Phase reconstructions

We compare the phase retrieval algorithm on measured data for two-photon states with different amounts of dispersion. We set the grating compressors on the signal and idler

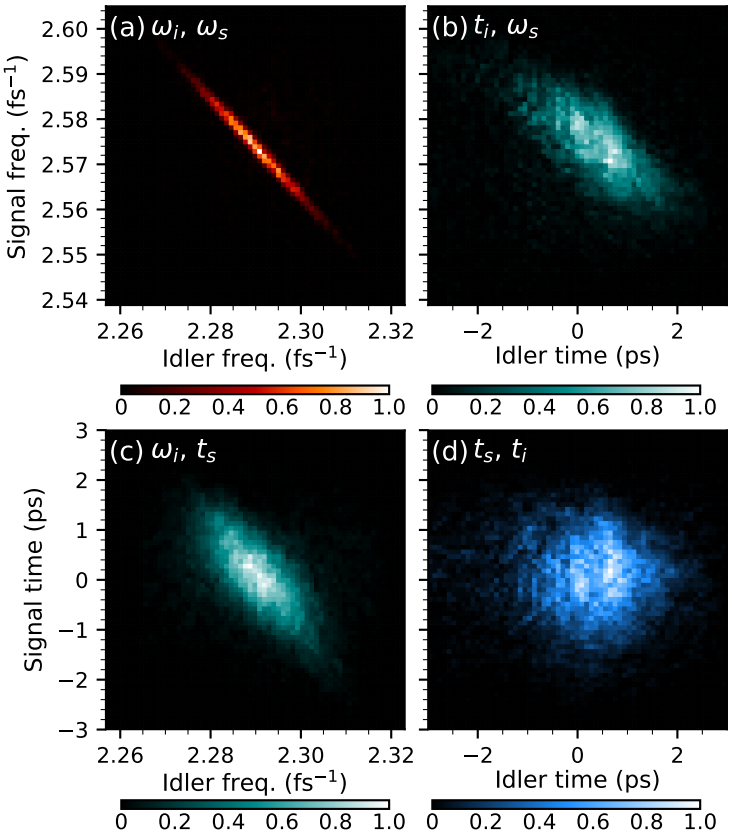

Figure 6.10: **Two-photon state reconstruction.** Reconstructed distributions for the (a) the joint spectral intensity, (d) the joint temporal intensity, as well the (b,c) time-frequency correlations of the measured state in Fig. 6.9 after 1000 iterations of the phase retrieval algorithm. We observe qualitatively similar features and correlations as in Fig. 6.9

side to study four cases: no additional dispersion, with extra positive dispersion applied to the idler, with extra negative dispersion applied to the signal, and with extra negative dispersion applied on both sides. For the case of a two-photon energy-time entangled state with negative dispersion applied to both photons, an example of the four combinations of time and frequency measurements is shown in Fig. 6.9. Background subtraction, a Wiener Filter, and low-pass filters are applied in Fig. 6.9 and prior to the reconstruction [241]. We observe strong anti-correlations in the joint spectral intensity [Fig. 6.9(a)], however, the joint temporal intensity [Fig. 6.9(d)] is uncorrelated due to the presence of dispersion on both photons. The observed shears in both the time-frequency intensity plots [Fig. 6.9(b-c)]

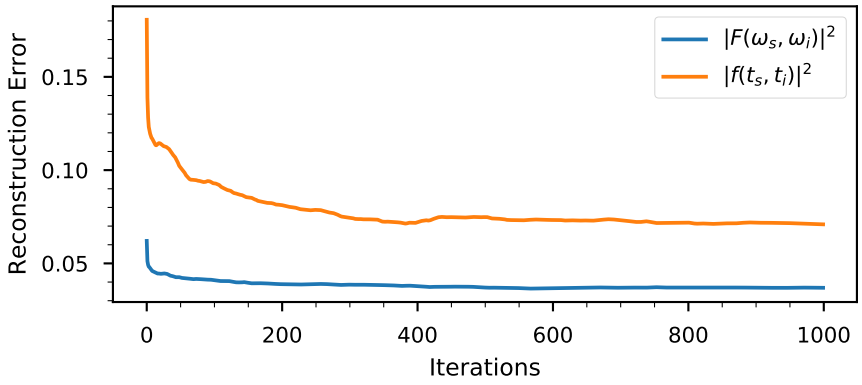

Figure 6.11: **Reconstruction error of the phase retrieval algorithm.** For the example in Fig. 6.10, we calculate at each iteration the error (Eq. 6.3 and Eq. 6.4) between the reconstructed states and the measured intensity in frequency and in time. The error drops rapidly in the first hundred iterations and stabilizes after about 600 iterations.

also illustrate the presence of negative dispersion.

We input these intensity constraints into the phase retrieval algorithm and run the algorithm for 1000 iterations, a number found heuristically after which no reduction in the FROG-trace error is observed. The intensity of the reconstructed wavefunction in frequency and time are shown in Fig. 6.10. The reconstructed intensities are compared to the measured data from Fig. 6.9(a) and Fig. 6.9(d). We find a FROG-trace error between the post-processed and reconstructed spectral intensities after 1000 iterations to be $(3.64 \pm 0.07)\%$ for the joint spectral intensity and $(7.01 \pm 0.35)\%$ for the joint temporal intensity.

Note that the marginal bandwidths of the joint spectral intensity in the reconstruction [Fig. 6.10(a)] are shorter than in the original data [Fig. 6.9(a)]. Numerical simulations suggest this arises as a result of the phase-matching bandwidth in the optical gating. The effect of the phase mismatch on the reconstruction of two-photon states with optical gating is modeled in Sec. 6.6.

Figure 6.12 shows the reconstructed joint spectral phase for the four different cases. Starting with the case where we attempted to minimize the unbalanced dispersion [Fig. 6.12(a)], we observe a relatively flat spectral phase. We then apply $A_s = (0.026 \pm 0.002)$ ps^2 of dispersion on the signal photon [Fig. 6.12(b)], and we observe a positive quadratic variation in the phase along the signal (y) axis, modulo 2π, with little variations along the idler (x) axis.

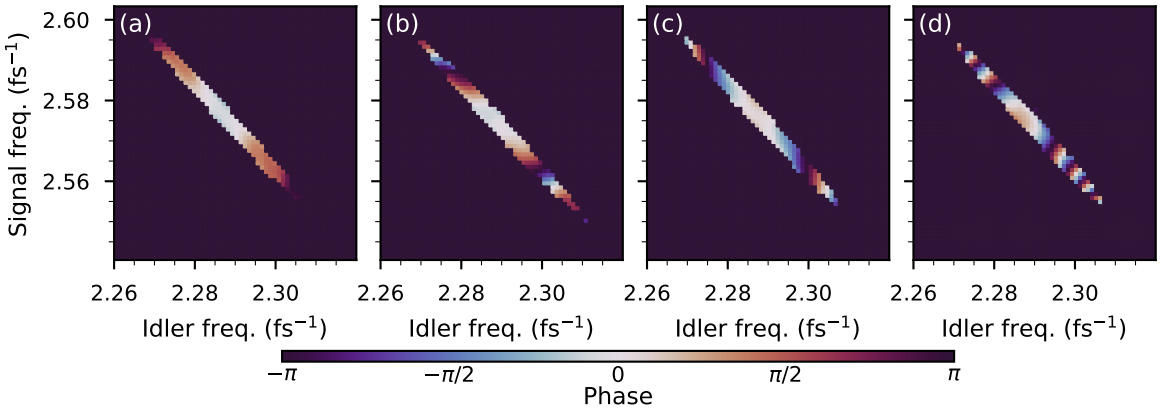

Figure 6.12: **Phase reconstruction of energy-time entangled states.** Reconstructed joint spectral phase for energy-time entangled photon pairs with (a) no added dispersion, (b) positive dispersion on the signal, (c) negative dispersion on the idler, (d) negative dispersion on both the signal and idler. Phase points outside the 2σ contours are removed for clarity. We observe (a) a relatively flat phase variation, (b) a positive quadratic phase variation along the signal axis, (c) a negative quadratic phase variation along the idler axis, (d) and a negative quadratic phase variation along both axes.

When we apply $A_i = (-0.025 \pm 0.002)$ ps^2 of dispersion to the idler photon [Fig. 6.12(c)], we observe a negative quadratic variation in the spectral phase along the idler (x) axis, with again little variations along the signal (y) axis. When we apply $A_s = (-0.036 \pm 0.003)$ ps^2 and $A_i = (-0.043 \pm 0.002)$ ps^2 of dispersion to the signal and idler [Fig. 6.12(d)], we observe a negative quadratic variation along the diagonal x-y axis.

For the three cases where dispersion is applied, we fit the reconstructed quadratic spectral phase in Fig. 6.12(b-d). For each, we unwrap the 2D phase and perform a polynomial fit to the phase distribution. For the reconstruction in Fig. 6.12(b) we obtain a quadratic spectral phase on the signal of $A_s = (0.024 \pm 0.003)$ ps^2 and for the one in Fig. 6.12(c), we obtain a quadratic phase on the idler of $A_i = (-0.026 \pm 0.003)$ ps^2. For the reconstruction in Fig. 6.12(d), we obtain a quadratic phase on the signal and idler of $A_s = (-0.036 \pm 0.004)$ ps^2 and $A_i = (-0.028 \pm 0.003)$ ps^2, respectively. The corresponding uncertainties are obtained from the variance in the fitted spectral phase after performing Monte Carlo simulations assuming Poissonian noise. When dispersion is applied to only one photon, Fig. 6.12(b) and Fig. 6.12(c), the phase obtained using the phase-retrieval algorithm corresponds to the reconstructed phases measured using the XFROG algorithm.

In the last case, Fig. 6.12(d), we find a discrepancy between the two. This, again, is likely due to the effect of the phase mismatch on the temporal measurements and on the subsequent reconstruction of two-photon states, which will be more pronounced for the photons which have much larger bandwidth than for the weak pulse used for the XFROG reconstructions (see Sec. 6.6).

6.6 Effects of phase matching on the measurement of two-photon states

The effect of phase matching on the measurement of photons in time is now considered. In the SFG process used for optical gating, a photon and a strong gate pulse in the near-infrared (NIR) are up-converted to produce a higher energy photon in the ultraviolet. In the presence of phase matching, photons of different frequencies walk off from each other inside the crystal. When the up-converted photon walks off from the signal and the gate, we expect the up-conversion to become partially mode selective and no longer sensitive to all input frequencies [107]. This has the effect of filtering the upconverted frequencies which lie outside the phase matching bandwidth.

We'll consider the effect of phase matching in optical gating on the measurement of two-photon states that are transform-limited and that have dispersion. We construct an analytical model, which is valid only up to first-order dispersion, as well as a numerical model, which is valid for all orders of dispersion. We show that in the presence of phase mismatch, the measured intensity correlations in time and frequency are modified, and no longer related by the Fourier Transform, as required for the phase-retrieval algorithm to work. We propose solutions to reduce this effect.

6.6.1 Analytical model for optical gating with transform limited states

When the photons are energy-time entangled, the effective frequency filtering on one side as a result of the phase mismatch also reduces the measured spectral bandwidth of the photon on the other side. This effect can be observed analytically in the time-frequency correlations using Eq. 6.6. We use an analytical model to observe this for a photon and a gate pulse initially with no dispersion. The frequency of the idler photon is measured in coincidences with the optically gated signal photon. As before, we assume a crystal of length L and first-order phase mismatching such that $\Delta k = \eta_{ug}(\omega_u - \omega_{u0}) + \eta_{gi}(\omega_i - \omega_{i0})$

where the parameter η_{ij} corresponds to the difference in the inverse group velocities between frequency modes i and j. We insert this into the phase mismatch function $\Phi(\omega_i, \omega_g, \omega_{ui})$ in Eq. 6.6, and after performing the integral, we find the time-frequency correlations can be described by a correlated Gaussian function with frequency and time marginals given by,

$$\Delta\omega_i{}^2 = \frac{\left[1 + 4L^2\gamma\left(\eta_{gu}{}^2\sigma_g{}^2 + \eta_{iu}{}^2\left(1-\rho_\omega^2\right)\sigma_i{}^2\right)\right]\sigma_s{}^2}{1 + 4L^2\gamma\left(\eta_{gu}{}^2\sigma_g{}^2 + \eta_{iu}{}^2\sigma_i{}^2\right)} \tag{6.10}$$

$$\Delta t_s^2 = \frac{1}{4\left(1-\rho_\omega^2\right)\sigma_i{}^2} + \frac{\left(1 + 4\eta_{gi}{}^2L^2\gamma\sigma_g{}^2\right)}{4\sigma_g{}^2}. \tag{6.11}$$

We find that both marginals in frequency and in time are modified by imperfect phase matching of the upconversion as characterized by the length of the crystal L and the group velocity mismatch η. The marginal in time in Eq. 6.11 depends on η_{gi}, the group velocity mismatch between the idler and the gate. If the idler and gate have similar wavelengths, this mismatch will be small, and the marginal in time will remain unmodified. However, when energy-time entanglement is present ($\rho_\omega \neq 0$) the marginal in frequency in Eq. 6.10 depends on both η_{gu} and η_{iu}, the group velocity mismatch between the upconverted photon in the ultraviolet and the gate or idler in the infrared. The group velocity mismatch between these frequencies will not be negligible, and this will reduce the measured marginal in frequency. We observe this reduction when comparing the marginal bandwidth in the joint spectrum and time-frequency plots in the experimental data presented in Table 4.2. For the case where the initial state has dispersion, we numerically model the optical gating as detailed below.

6.6.2 Numerical model for optical gating

If the photons are chirped before the optical gating, high and low frequencies components will arrive at different times in the nonlinear medium. In the presence of phase mismatch, these may be upconverted via the gate pulse to frequencies which lie outside the phase matching filter. As a result, for the same frequency bandwidth and spectral phase, the effective measured length of the photon in time will be reduced.

To study this effect, we construct a numerical model of optical gating for a two-photon state. The initial state is a two-photon energy-time entangled state with a joint-spectral amplitude $F_{\omega\omega}(\omega_s, \omega_i)$ for the signal ω_s and idler ω_i frequencies modelled as a two-dimensional correlated Gaussian function, as in Eq. 2.66. The marginal frequency bandwidths and statistical correlations of the state are set to the values measured experimentally. We consider states with and without spectral chirp applied to both the signal

and the idler. We calculate all four combinations of joint measurements in frequency and in time. We model the optical gating as sum-frequency generation process in the low-efficiency regime between the photons on each side and a gate pulse with centre frequency ω_g and a pulse duration of 0.130 ps, leading to upconverted frequencies $\omega_{u_s} = \omega_s + \omega_g$ and $\omega_{u_i} = \omega_i + \omega_g$ on the signal and idler side, respectively. The three intensity measurements involving optical gating are calculated via the following,

$$I\left(\tau_s, \omega_i\right) = \int d\omega_{u_s} \left| \int d\omega_s G\left(\omega_{u_s} - \omega_s, \tau_s\right) \Phi_{\mathrm{SFG}}\left(\omega_s, \omega_{u_s} - \omega_s, \omega_{u_s}\right) \; F_{\omega\omega}\left(\omega_s, \omega_i\right) \right|^2, \quad (6.12)$$

$$I\left(\omega_s, \tau_i\right) = \int d\omega_{u_i} \left| \int d\omega_i G\left(\omega_{u_i} - \omega_i, \tau_i\right) \Phi_{\mathrm{SFG}}\left(\omega_i, \omega_{u_i} - \omega_i, \omega_{u_i}\right) \; F_{\omega\omega}\left(\omega_s, \omega_i\right) \right|^2, \quad (6.13)$$

$$\begin{aligned} I\left(\tau_s, \tau_i\right) = \int d\omega_{u_s} d\omega_{u_i} \Bigg| \int d\omega_s d\omega_i G\left(\omega_{u_s} - \omega_s, \tau_s\right) \Phi_{\mathrm{SFG}}(\omega_s, \omega_{u_s} - \omega_s, \omega_{u_s}) \\ \times \; G\left(\omega_{u_i} - \omega_i, \tau_i\right) \Phi_{\mathrm{SFG}}(\omega_i, \omega_{u_i} - \omega_i, \omega_{u_i}) F_{\omega\omega}(\omega_s, \omega_i) \Bigg|^2, \end{aligned} \quad (6.14)$$

where the gate pulse G is the same on both sides but with delays τ_i and τ_s introduced. The phase matching function is,

$$\Phi_{\mathrm{SFG}}(\omega_j, \omega_{u_j} - \omega_j, \omega_{u_j}) = \exp\left(-i\frac{\Delta k L}{2}\right) \mathrm{sinc}\left(\frac{\Delta \mathrm{kL}}{2}\right), \quad (6.15)$$

with the phase mismatch,

$$\Delta k(\omega_j, \omega_{u_j} - \omega_j, \omega_{u_j}) = \frac{n_e(\omega_j)\omega_j}{c} + \frac{n_e(\omega_{u_j} - \omega_j)(\omega_{u_j} - \omega_j)}{c} + \frac{n_o(\omega_{u_j})\omega_{u_j}}{c}, \quad (6.16)$$

calculated for type-I SFG with 1 mm of BiBO and the experimentally measured wavelengths. For the cases, where phase matching of the upconversion is not included, the phase matching function $\Phi_{\mathrm{SFG}} = 1$ is set to unity, corresponding to an infinitely small crystal.

To evaluate the integrals, first, we note that the integrals over the upconverted frequencies can be performed ahead of time by expanding the absolute values in Eq. 6.6 and

Eq. 6.14. This leads to two transfer functions for optical gating on the signal and idler sides, which are, respectively,

$$T(\omega_s, \omega_s', \tau_s) = \tag{6.17}$$
$$\int d\omega_{u_s} G\left(\omega_{u_s} - \omega_s, \tau_s\right) G^*\left(\omega_{u_s} - \omega_s', \tau_s\right) \Phi_{\mathrm{SFG}}(\omega_s, \omega_{u_s} - \omega_s, \omega_{u_s}) \Phi^*_{\mathrm{SFG}}(\omega_s', \omega_{u_s} - \omega_s', \omega_{u_s}),$$
$$T(\omega_i, \omega_i', \tau_i) = \tag{6.18}$$
$$\int d\omega_{u_i} G\left(\omega_{u_i} - \omega_i, \tau_i\right) G^*\left(\omega_{u_i} - \omega_i', \tau_i\right) \Phi_{\mathrm{SFG}}(\omega_i, \omega_{u_i} - \omega_i, \omega_{u_i}) \Phi^*_{\mathrm{SFG}}(\omega_i', \omega_{u_i} - \omega_i', \omega_{u_i}).$$

Then, the intensity distributions involving optical gating can be obtained by applying the transfer functions in Eq. 6.17 and Eq. 6.18 to the initial state,

$$I(\tau_s, \omega_i) = \int d\omega_s d\omega_s' T(\omega_s, \omega_s', \tau_s) F_{\omega\omega}(\omega_s, \omega_i) F^*_{\omega\omega}(\omega_s', \omega_i) \tag{6.19}$$
$$I(\omega_s, \tau_i) = \int d\omega_i d\omega_i' T(\omega_i, \omega_i', \tau_i) F_{\omega\omega}(\omega_i, \omega_i) F^*_{\omega\omega}(\omega_i', \omega_i) \tag{6.20}$$
$$I(\tau_s, \tau_i) = \int d\omega_s d\omega_s' d\omega_i d\omega_i' T(\omega_s, \omega_s', \tau_s) T(\omega_i, \omega_i', \tau_i) F^*_{\omega\omega}(\omega_s, \omega_i) F_{\omega\omega}(\omega_s', \omega_i') \tag{6.21}$$

To evaluate these expressions numerically, we write each function as a tensor. All integrals are approximated as discrete sums and performed using the numpy einsum routine in python. The transfer functions in Eq. 6.18 and Eq. 6.17 in tensor form are,

$$T_{\omega_s, \omega_s', \tau_s} = \sum_{\omega_{u_s}} G_{\omega_s, \omega_{u_s}, \tau_s} G^*_{\omega_s', \omega_{u_s}, \tau_s} \Phi_{\omega_s, \omega_{u_s}} \Phi^*_{\omega_s', \omega_{u_s}} \tag{6.22}$$
$$T_{\omega_i, \omega_i', \tau_i} = \sum_{\omega_{u_i}} G_{\omega_i, \omega_{u_i}, \tau_i} G^*_{\omega_i', \omega_{u_i}, \tau_i} \Phi_{\omega_i, \omega_{u_i}} \Phi^*_{\omega_i', \omega_{u_i}}, \tag{6.23}$$

and the measured intensities for the different correlation measurements in Eqs. [6.19-6.21] are obtained in a similar way,

$$I_{\tau_s, \omega_i} = \sum_{\omega_s, \omega_s'} T_{\omega_s, \omega_s', \tau_s} F_{\omega_s, \omega_i} F^*_{\omega_s', \omega_i} \tag{6.24}$$
$$I_{\omega_s, \tau_i} = \sum_{\omega_i, \omega_i'} T_{\omega_i, \omega_i', \tau_i} F_{\omega_s, \omega_i} F^*_{\omega_s, \omega_i'} \tag{6.25}$$
$$I_{\tau_s, \tau_i} = \sum_{\omega_s, \omega_s', \omega_i, \omega_i'} T_{\omega_s, \omega_s', \tau_s} T_{\omega_i, \omega_i', \tau_i} F_{\omega_s, \omega_i} F^*_{\omega_s', \omega_i'}. \tag{6.26}$$

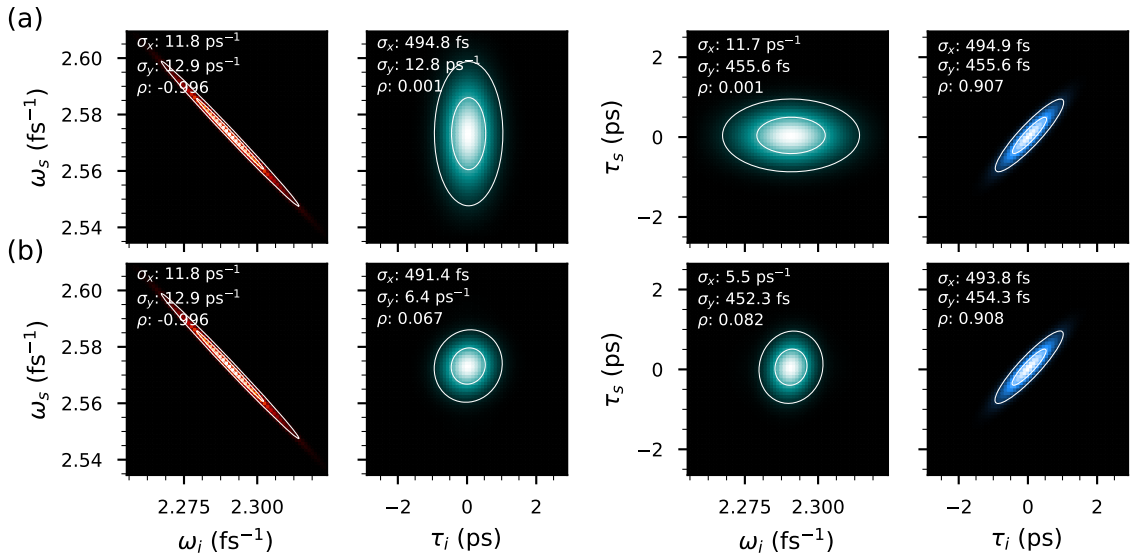

Figure 6.13: **Effect of phase matching on joint time and frequency measurements for a transform-limited two-photon state.** We construct a numerical model of the joint-frequency and time measurements for a two-photon energy-time entangled state similar to the one measured experimentally. We model the optical gating of photons in the low-efficiency regime in 1 mm of BiBO with a 0.130 ps gate pulse (a) without and (b) with phase matching included. In the presence of phase matching, the marginal bandwidths of the time-frequency plots are reduced but the photon marginals in time remain unaffected, as in the analytical model.

We first study the effect of phase matching on the upconversion for the same case as in the analytical model, a two photon transform limited state with no dispersion applied to the signal and idler. The modelled time-frequency measurements are shown in Fig. 6.13. We compare the cases without phase matching in Fig. 6.12(a) and with phase matching in 1 mm of BiBO in Fig. 6.13(b). When the idler photon is optically gated, we find that the frequency bandwidth of the signal, σ_y, is reduced in the time-frequency plots from 12.8 ps^{-1} to 6.4 ps^{-1}. Likewise, when the signal photon is optically gate, we find that the idler photon frequency bandwidth, σ_x, is reduced from 11.7 ps^{-1} to 5.5 ps^{-1}. In both cases, however, and in the joint temporal intensity, the photon marginals in time remain the same. This is the same behaviour predicted using the analytical model in Sec. 6.6.1.

We next study the effect of optical gating two-photon states that have dispersion ap-

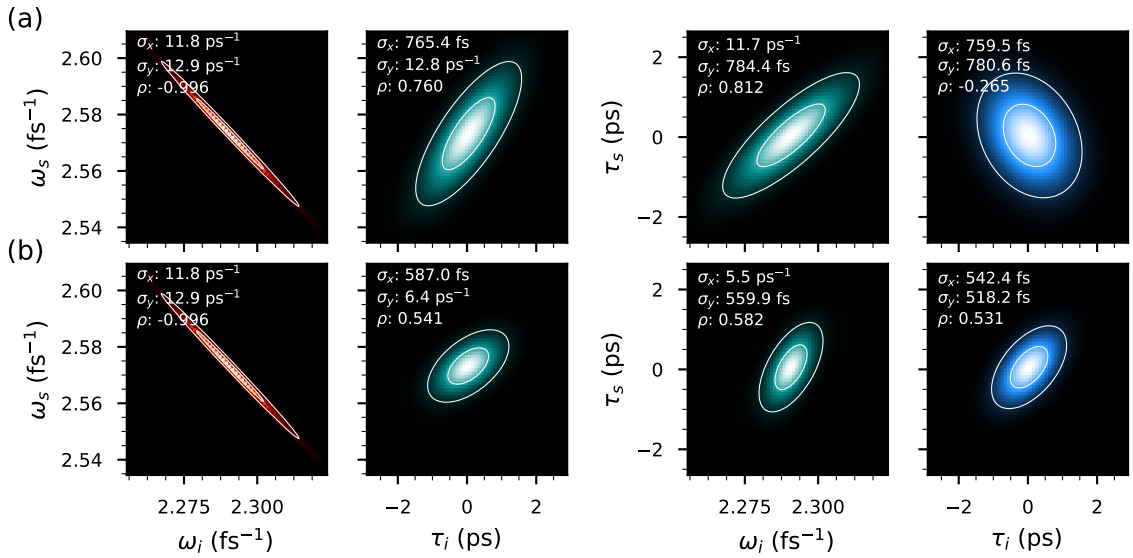

Figure 6.14: **Effect of phase matching on the joint time and frequency measurements for a two-photon state with dispersion.** We begin with an initial energy-time entangled two-photon state with chirp $A_s = A_i$ =0.025ps^2 applied to the signal and idler photons. We use the same numerical model as in Fig. 6.13 for optical gating (a) without and (b) with phase matching included. We find that reduction in the marginal bandwidths of the time-frequency plots is the same as in the previous case where no dispersion was applied. In addition, all marginals in time are reduced by presence of phase matching.

plied to both the signal and idler. We consider the same initial state as before with the addition of the chirp parameters which are set to $A_s = A_i = 0.025$ ps^2. The resulting frequency and time measurements are shown in Fig. 6.14 for the case with and without phase matching included in the upconverison. We find that the reduction in the frequency marginal bandwidths to be the same as in previous case where no dispersion was applied [Fig. 6.13], 12.8 ps^{-1} to 6.4 ps^{-1} and 11.7 ps^{-1} to 5.5 ps^{-1}. However, now, all the marginals in time are significantly reduced when comparing the measurements without [Fig. 6.14(a)] and with phase matching included [Fig. 6.14(b)]. In the time-frequency plots, when only the idler is gated, its marginal σ_x is reduced from 765 fs to 587 fs, and when the signal is gated, its marginal σ_y is reduced from 784 fs to 560 fs. The effect is more pronounced in the joint temporal intensity where the marginals are reduced from 781 fs to 518 fs and from 760 fs to 542 fs for the signal and idler, respectively. The reduction of the marginals in time also has the effect of significantly changing observed statistical correlations, ρ, as

shown when comparing Fig. 6.14(a) and Fig. 6.14(b).

6.6.3 Effect of phase matching on two-photon state reconstruction

We've seen that phase matching in optical gating changes the observed time-frequency correlations as well as the joint-temporal intensity. How will this affect the phase retrieval algorithm? Phase mismatch in the optical gating changes the measured intensity correlations and, therefore, it changes the intensity constraints that are applied in the phase retrieval algorithm. Since the phase mismatch affects the time-frequency intensity measurement and joint temporal intensity measurements differently, the applied constraints will no longer correspond to the modulus of the Fourier transform of a physical state, thereby affecting the reconstruction.

We quantify this effect using the numerical model developed above. We model all the steps in the phase-retrieval process. We numerically create frequency anti-correlated states, with the same centre wavelength and bandwidth as those measured experimentally, but with different amounts of applied spectral phases, given by the chirp parameters A_s and A_i. We calculate the four joint correlations in frequency and time, using different lengths of BiBO for optical gating, apply the numerical deconvolution to each intensity measurement, and insert these as constraints for the phase retrieval algorithm. After reconstruction, we unwrap the 2D spectral phase of the reconstructed joint spectral amplitude function and fit it to a third-order 2D polynomial.

The reconstructed spectral phases are compared to the applied spectral phases in Fig. 6.15 for different lengths of BiBO used in optical gating and for different applied spectral phases. In Fig. 6.15(a) and Fig. 6.15(b), the signal chirp parameter A_s is kept fixed while the idler chirp parameter is varied, whereas in Fig. 6.15(c) and Fig. 6.15(d), the idler chirp parameter A_i is kept fixed while the signal chirp parameter A_s is varied. When the length of the crystal is set to zero ($L = 0$ μm), the reconstructed phase corresponds exactly to the applied phase, and the line at $L = 0$ μm appears at 45 degrees with a slope of one. As the length of the crystal increases, we find that the slope remains fairly constant at 45 degrees, but the offset depends on the configuration. For example, comparing Fig. 6.15(a) and Fig. 6.15(b), we find the values of the reconstructed idler chirp parameter A_i depend on whether the signal chirp parameter has a value of $A_s = 5,000$ fs^2 [Fig. 6.15(a)] or $A_s = 40,000$ fs^2 [Fig. 6.15]. The difference between the reconstructed and applied phase in Fig. 6.15 also becomes larger for longer crystals where the phase matching

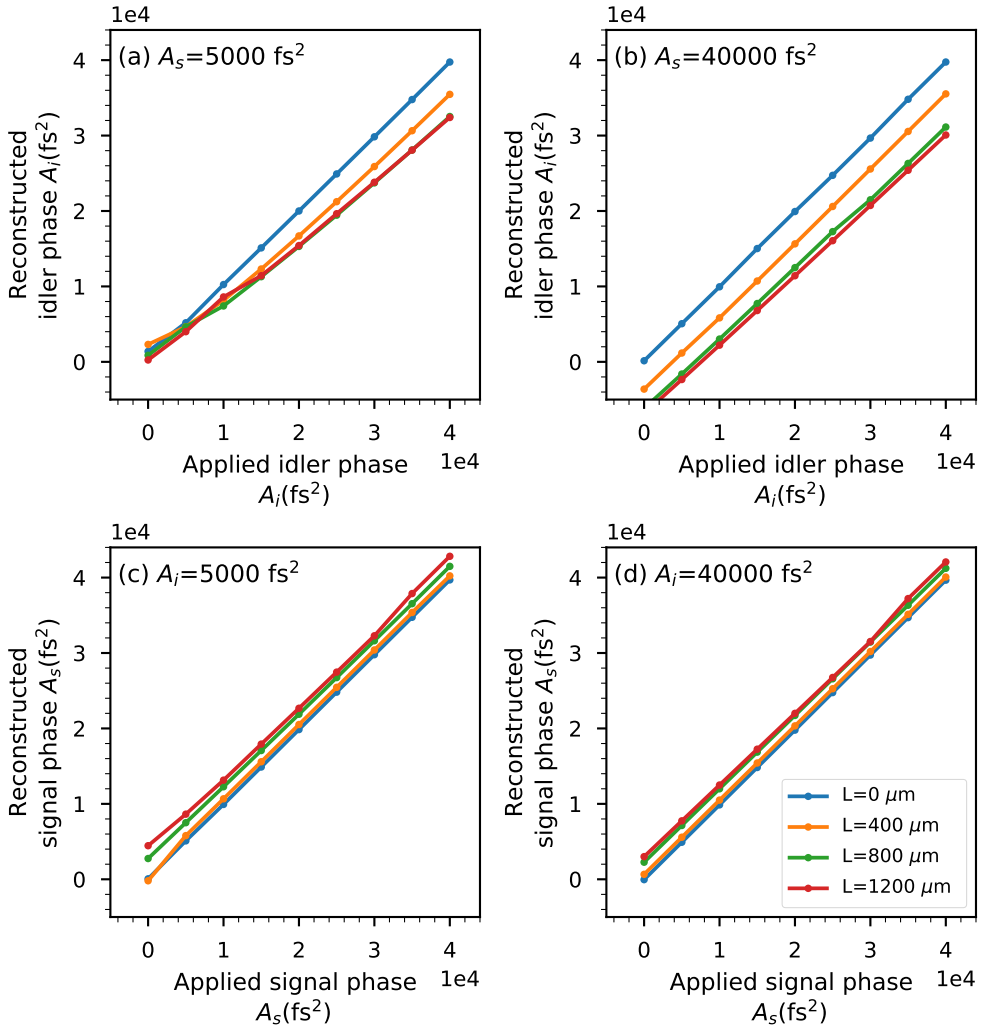

Figure 6.15: **Effect of crystal length on the reconstructed spectral phase.** We model the effect of optical gating with different lengths L of BiBO on the reconstructed phase. The reconstructed phase is compared to the applied phase for four different cases. The signal chirp parameter is fixed to the values of (a) $A_s = 5,000$ fs^2 and (b) $A_s = 40,000$ fs^2 while the idler chirp parameter A_i is varied. The idler chirp parameter is fixed to the values of (c) $A_i = 5,000$ fs^2 and (d) $A_i = 40,000$ fs^2 while the signal chirp parameter A_s is varied. At $L = 0$ μm, the reconstructed phase is the same as the applied phase. As L is increased, phase mismatch becomes more important and this changes the value of the reconstructed phase.

function is more restrictive.

Figure 6.15 thus makes it clear that one solution to reduce the effect of phase matching is to reduce the length of the crystal. This increases the phase-matching bandwidth and reduces its effect on the measurement of photons in time, at the cost of a decrease in conversion efficiency. The requirement for thin crystals for multi-shot experiments turns out to be overly restrictive. It is the phase-matching bandwidth *integrated* over the measurement time that needs to exceed the pulse bandwidth. Since the range of frequencies that are phase-matched depends on the crystal angle, the effective phase-matching bandwidth can be increased by changing the angle of a thick crystal during the measurement period. Techniques have been developed to increase the effective phase-matching bandwidth of otherwise too narrowband crystals by rapidly dithering the crystal angle [304, 305].

6.7 Conclusion

We have demonstrated a method to recover ultrafast two-photon energy-time entangled pulses. Our technique is based on a method of alternate projections that iterates between the frequency and time domains imposing the measured intensity constraints at each iteration. The use of nonlinear phenomena, i.e., optical gating, to measure the timing correlations is an artifact of the time scales at play and is not a fundamental requirement. For sufficiently long pulses, there may exist photodetectors that can measure the temporal intensity directly [70]. For subpicosecond resolution involving optical gating, the effect of phase-matching in the upconversion could be reduced using shorter crystals or angle-dithering [304]. Moreover, extensions of this algorithm to characterize two-photon mixed states may be possible based on techniques used to reconstruct partially coherent light [306, 240], removing assumptions about the purity of the quantum states. Measurement and reconstruction capabilities similar to those available in ultrafast optics will be essential for developing new applications in quantum state engineering and ultrafast shaping of entangled photons, paving the way to characterizing and manipulating high-dimensional quantum states of light.

References

[1] H. Bernien *et al.* Probing many-body dynamics on a 51-atom quantum simulator. *Nature* **551**, 579 (2017). 1

[2] J. Zhang *et al.* Observation of a many-body dynamical phase transition with a 53-qubit quantum simulator. *Nature* **551**, 601 (2017). 1

[3] W. Knight. IBM announces a trailblazing quantum machine. 1

[4] D. Castelvecchi. IBM's quantum cloud computer goes commercial. *Nature News* **543**, 159 (2017). 1

[5] C. Neill *et al.* A blueprint for demonstrating quantum supremacy with superconducting qubits. *Science* **360**, 195 (2018). 1

[6] M. Amy *et al.* Estimating the Cost of Generic Quantum Pre-image Attacks on SHA-2 and SHA-3. In R. Avanzi & H. Heys, editors, Selected Areas in Cryptography – SAC 2016, Lecture Notes in Computer Science, pp. 317–337. Springer International Publishing (2017). ISBN 978-3-319-69453-5. 1

[7] J. Preskill. Quantum Computing in the NISQ era and beyond. *Quantum* **2**, 79 (2018). 2

[8] F. Fillion-Gourdeau, S. MacLean, & R. Laflamme. Algorithm for the solution of the Dirac equation on digital quantum computers. *Phys. Rev. A* **95**, 042343 (2017). 2

[9] D. A. B. Miller. Are optical transistors the logical next step? *Nature Photonics* **4**, 3 (2010). 2

[10] R. G. Beausoleil. Large-scale integrated photonics for high-performance interconnects. *ACM Journal on Emerging Technologies in Computing Systems* **7**, 1 (2011). 2

[11] R. W. Boyd. Nonlinear Optics. Elsevier (2008). ISBN 978-0-08-048596-6. 2, 34, 35, 47, 64, 68, 69

[12] A. Weiner. Ultrafast Optics. John Wiley & Sons (2011). ISBN 978-1-118-21147-2. 2, 66, 70, 72, 76

[13] I. L. Chuang & Y. Yamamoto. Simple quantum computer. *Phys. Rev. A* **52**, 3489 (1995). 2

[14] J. H. Shapiro. Single-photon Kerr nonlinearities do not help quantum computation. *Phys. Rev. A* **73** (2006). 2

[15] M. Bajcsy *et al.* Efficient All-Optical Switching Using Slow Light within a Hollow Fiber. *Phys. Rev. Lett.* **102**, 203902 (2009). 2

[16] H. Tanji-Suzuki *et al.* Vacuum-Induced Transparency. *Science* **333**, 1266 (2011). 2

[17] W. Chen *et al.* All-Optical Switch and Transistor Gated by One Stored Photon. *Science* **341**, 768 (2013). 2

[18] O. Firstenberg *et al.* Attractive photons in a quantum nonlinear medium. *Nature* **502**, 71 (2013). 2

[19] J. D. Thompson *et al.* Symmetry-protected collisions between strongly interacting photons. *Nature* **542**, 206 (2017). 2

[20] Q.-Y. Liang *et al.* Observation of three-photon bound states in a quantum nonlinear medium. *Science* **359**, 783 (2018). 2

[21] E. Knill, R. Laflamme, & G. J. Milburn. A scheme for efficient quantum computation with linear optics. *Nature* **409**, 46 (2001). 2, 58

[22] J. L. O'Brien *et al.* Demonstration of an all-optical quantum controlled-NOT gate. *Nature* **426**, 264 (2003). 2

[23] P. Walther *et al.* Experimental one-way quantum computing. *Nature* **434**, 169 (2005). 2

[24] N. C. Menicucci, S. T. Flammia, & O. Pfister. One-Way Quantum Computing in the Optical Frequency Comb. *Phys. Rev. Lett.* **101**, 130501 (2008). 2

[25] S. Yokoyama *et al.* Ultra-large-scale continuous-variable cluster states multiplexed in the time domain. *Nature Photonics* **7**, 982 (2013). 2

[26] T. Rudolph. Why I am optimistic about the silicon-photonic route to quantum computing. *APL Photonics* **2**, 030901 (2017). 3

[27] X. Qiang *et al.* Large-scale silicon quantum photonics implementing arbitrary two-qubit processing. *Nature Photonics* **12**, 534 (2018). 3

[28] C. Sparrow *et al.* Simulating the vibrational quantum dynamics of molecules using photonics. *Nature* **557**, 660 (2018). 3, 134

[29] J. M. Kovac *et al.* Detection of polarization in the cosmic microwave background using DASI. *Nature* **420**, 772 (2002). 3

[30] SPTpol Collaboration *et al.* Detection of B-Mode Polarization in the Cosmic Microwave Background with Data from the South Pole Telescope. *Phys. Rev. Lett.* **111**, 141301 (2013). 3

[31] D. Bouwmeester *et al.* Experimental quantum teleportation. *Nature* **390**, 575 (1997). 3, 12, 16

[32] C. J. Pugh *et al.* Airborne demonstration of a quantum key distribution receiver payload. *Quantum Sci. Technol.* **2**, 024009 (2017). 3

[33] J. Yin *et al.* Satellite-based entanglement distribution over 1200 kilometers. *Science* **356**, 1140 (2017). 3

[34] A. Aspect, P. Grangier, & G. Roger. Experimental Tests of Realistic Local Theories via Bell's Theorem. *Phys. Rev. Lett.* **47**, 460 (1981). 3, 12

[35] L. K. Shalm *et al.* Strong Loophole-Free Test of Local Realism. *Phys. Rev. Lett.* **115**, 250402 (2015). 3

[36] B. Hensen *et al.* Loophole-free Bell inequality violation using electron spins separated by 1.3 kilometres. *Nature* **526**, 682 (2015). 3

[37] M. Giustina *et al.* Significant-Loophole-Free Test of Bell's Theorem with Entangled Photons. *Phys. Rev. Lett.* **115**, 250401 (2015). 3

[38] M. D. Mazurek *et al.* An experimental test of noncontextuality without unphysical idealizations. *Nat. Commun.* **7**, ncomms11780 (2016). 3

[39] K. Ried *et al.* A quantum advantage for inferring causal structure. *Nat. Phys.* **11**, 414 (2015). 3

[40] J.-P. W. MacLean, K. Ried, R. W. Spekkens, & K. J. Resch. Quantum-coherent mixtures of causal relations. *Nat. Commun.* **8**, 15149 (2017). 3

[41] K. Ried, J.-P. W. MacLean, R. W. Spekkens, & K. J. Resch. Quantum to classical transitions in causal relations. *Phys. Rev. A* **95**, 062102 (2017). 3

[42] S. E. Harris, M. K. Oshman, & R. L. Byer. Observation of Tunable Optical Parametric Fluorescence. *Phys. Rev. Lett.* **18**, 732 (1967). 3

[43] D. Magde & H. Mahr. Study in Ammonium Dihydrogen Phosphate of Spontaneous Parametric Interaction Tunable from 4400 to 16 000 A. *Phys. Rev. Lett.* **18**, 905 (1967). 3

[44] D. C. Burnham & D. L. Weinberg. Observation of Simultaneity in Parametric Production of Optical Photon Pairs. *Phys. Rev. Lett.* **25**, 84 (1970). 3

[45] A. I. Lvovsky *et al.* Quantum State Reconstruction of the Single-Photon Fock State. *Phys. Rev. Lett.* **87**, 050402 (2001). 3, 135

[46] A. Zavatta, S. Viciani, & M. Bellini. Tomographic reconstruction of the single-photon Fock state by high-frequency homodyne detection. *Phys. Rev. A* **70**, 053821 (2004). 3

[47] P. G. Kwiat *et al.* New high-intensity source of polarization-entangled photon pairs. *Phys. Rev. Lett.* **75**, 4337 (1995). 3, 15

[48] A. Mair, A. Vaziri, G. Weihs, & A. Zeilinger. Entanglement of the orbital angular momentum states of photons. *Nature* **412**, 313 (2001). 3

[49] J. D. Franson. Bell inequality for position and time. *Phys. Rev. Lett.* **62**, 2205 (1989). 3, 17, 19, 93, 115, 134

[50] P. G. Kwiat, A. M. Steinberg, & R. Y. Chiao. High-visibility interference in a Bell-inequality experiment for energy and time. *Phys. Rev. A* **47**, R2472 (1993). 3, 19, 27, 94, 115, 134

[51] M. E. Reimer *et al.* Bright single-photon sources in bottom-up tailored nanowires. *Nat. Commun.* **3**, 737 (2012). 4

[52] F. Kaneda *et al.* Time-multiplexed heralded single-photon source. *Optica* **2**, 1010 (2015). 4

[53] J. Nunn *et al.* Enhancing Multiphoton Rates with Quantum Memories. *Phys. Rev. Lett.* **110**, 133601 (2013). 4

[54] A. I. Lvovsky, B. C. Sanders, & W. Tittel. Optical quantum memory. *Nature Photonics* **3**, 706 (2009). 4

[55] C. Liu, Z. Dutton, C. H. Behroozi, & L. V. Hau. Observation of coherent optical information storage in an atomic medium using halted light pulses. *Nature* **409**, 490 (2001). 4

[56] M. Afzelius, C. Simon, H. de Riedmatten, & N. Gisin. Multimode quantum memory based on atomic frequency combs. *Phys. Rev. A* **79** (2009). 4

[57] K. F. Reim *et al.* Towards high-speed optical quantum memories. *Nat Photon* **4**, 218 (2010). 4

[58] D. England *et al.* Storage and Retrieval of THz-Bandwidth Single Photons Using a Room-Temperature Diamond Quantum Memory. *Phys. Rev. Lett.* **114**, 053602 (2015). 4

[59] P. J. Bustard *et al.* Quantum frequency conversion with ultra-broadband tuning in a Raman memory. *Phys. Rev. A* **95**, 053816 (2017). 4

[60] K. A. G. Fisher *et al.* Storage of polarization-entangled THz-bandwidth photons in a diamond quantum memory. *Phys. Rev. A* **96**, 012324 (2017). 4

[61] K. A. G. Fisher *et al.* Frequency and bandwidth conversion of single photons in a room-temperature diamond quantum memory. *Nat. Commun.* **7**, 11200 (2016). 4

[62] D. G. England *et al.* Phonon-Mediated Nonclassical Interference in Diamond. *Phys. Rev. Lett.* **117** (2016). 4

[63] R. Finkelstein *et al.* Fast, noise-free memory for photon synchronization at room temperature. *Science Advances* **4**, eaap8598 (2018). 4

[64] T. Inagaki *et al.* Entanglement distribution over 300 km of fiber. *Opt. Express* **21**, 23241 (2013). 4, 19

[65] A. Boaron *et al.* Secure Quantum Key Distribution over 421 km of Optical Fiber. *Phys. Rev. Lett.* **121**, 190502 (2018). 4

[66] K. Boone *et al.* Entanglement over global distances via quantum repeaters with satellite links. *Phys. Rev. A* **91**, 052325 (2015). 4

[67] R. H. Hadfield. Single-photon detectors for optical quantum information applications. *Nat. Photonics* **3**, 696 (2009). 4, 5, 114

[68] F. Marsili *et al.* Detecting single infrared photons with 93% system efficiency. *Nat. Photonics* **7**, 210 (2013). 4

[69] C. M. Natarajan, M. G. Tanner, & R. H. Hadfield. Superconducting nanowire single-photon detectors: physics and applications. *Supercond. Sci. Technol.* **25**, 063001 (2012). 4

[70] B. A. Korzh *et al.* Demonstrating sub-3 ps temporal resolution in a superconducting nanowire single-photon detector. *arXiv:1804.06839* (2018). 4, 159

[71] J. Nunn *et al.* Large-alphabet time-frequency entangled quantum key distribution by means of time-to-frequency conversion. *Opt. Express* **21**, 15959 (2013). 5, 93, 134

[72] J. M. Lukens *et al.* Orthogonal Spectral Coding of Entangled Photons. *Phys. Rev. Lett.* **112**, 133602 (2014). 5, 93

[73] S. Wengerowsky *et al.* An entanglement-based wavelength-multiplexed quantum communication network. *Nature* **564**, 225 (2018). 5

[74] J. M. Donohue, M. Mastrovich, & K. J. Resch. Spectrally Engineering Photonic Entanglement with a Time Lens. *Phys. Rev. Lett.* **117**, 243602 (2016). 5, 96, 101, 105, 114, 134, 135

[75] M. D. Eisaman, J. Fan, A. Migdall, & S. V. Polyakov. Invited Review Article: Single-photon sources and detectors. *Rev. Sci. Instrum.* **82**, 071101 (2011). 5, 94, 114

[76] E. Muybridge. Horses and Other Animals in Motion: 45 Classic Photographic Sequences. Courier Corporation (1985). ISBN 978-0-486-24911-7. 5

[77] H. E. Edgerton & J. R. K. Jr. Moments of Vision: The Stroboscopic Revolution in Photography. MIT Press (1979). ISBN 978-0-262-05023-4. 5

[78] R. S. Bennink. Optimal collinear Gaussian beams for spontaneous parametric down-conversion. *Phys. Rev. A* **81**, 053805 (2010). 5

[79] X.-s. Ma *et al.* Experimental generation of single photons via active multiplexing. *Phys. Rev. A* **83**, 043814 (2011). 5

[80] G. Harder *et al.* An optimized photon pair source for quantum circuits. *Opt. Express* **21**, 13975 (2013). 5, 96

[81] M. Allgaier *et al.* Highly efficient frequency conversion with bandwidth compression of quantum light. *Nat. Commun.* **8**, 14288 (2017). 5

[82] P. Kumar. Quantum frequency conversion. *Optics letters* **15**, 1476 (1990). 5

[83] D. Kielpinski, J. F. Corney, & H. M. Wiseman. Quantum Optical Waveform Conversion. *Phys. Rev. Lett.* **106**, 130501 (2011). 5

[84] J. Lavoie *et al.* Spectral compression of single photons. *Nat. Photonics* **7**, 363 (2013). 5, 74

[85] R. Loudon. The Quantum Theory of Light. OUP Oxford (2000). ISBN 978-0-19-158978-2. 6, 7, 21

[86] C. Gerry, P. Knight, & P. L. Knight. Introductory Quantum Optics. Cambridge University Press (2005). ISBN 978-0-521-52735-4. 6

[87] K. Resch. Quantum Optics. Course Notes (2016). 6, 21, 34, 47

[88] K. J. Blow, R. Loudon, S. J. Phoenix, & T. J. Shepherd. Continuum fields in quantum optics. *Phys. Rev. A* **42**, 4102 (1990). 7

[89] H. Rubinsztein-Dunlop *et al.* Roadmap on structured light. *J. Opt.* **19**, 013001 (2017). 9

[90] D. F. V. James, P. G. Kwiat, W. J. Munro, & A. G. White. Measurement of qubits. *Phys. Rev. A* **64**, 052312 (2001). 10

[91] A. G. White, D. F. V. James, W. J. Munro, & P. G. Kwiat. Exploring Hilbert space: Accurate characterization of quantum information. *Phys. Rev. A* **65**, 012301 (2001). 10

[92] Y. Wu & W. Y. Zou. Orthogonal frequency division multiplexing: a multi-carrier modulation scheme. *IEEE Transactions on Consumer Electronics* **41**, 392 (1995). 11

[93] S. Kawanishi. Ultrahigh-speed optical time-division-multiplexed transmission technology based on optical signal processing. *IEEE Journal of Quantum Electronics* **34**, 2064 (1998). 11

[94] J. Brendel, N. Gisin, W. Tittel, & H. Zbinden. Pulsed energy-time entangled twin-photon source for quantum communication. *Phys. Rev. Lett.* **82**, 2594 (1999). 11, 19, 116

[95] W. Tittel, J. Brendel, H. Zbinden, & N. Gisin. Violation of Bell inequalities by photons more than 10 km apart. *Phys. Rev. Lett.* **81**, 3563 (1998). 11, 19, 115, 130

[96] J. M. Donohue, M. Agnew, J. Lavoie, & K. J. Resch. Coherent Ultrafast Measurement of Time-Bin Encoded Photons. *Phys. Rev. Lett.* **111**, 153602 (2013). 11, 122

[97] J. Jin *et al.* Demonstration of analyzers for multimode photonic time-bin qubits. *arXiv:1509.07490* (2015). 11

[98] K. Inoue, E. Waks, & Y. Yamamoto. Differential-phase-shift quantum key distribution using coherent light. *Phys. Rev. A* **68**, 022317 (2003). 11

[99] C. Xu, X. Liu, & X. Wei. Differential phase-shift keying for high spectral efficiency optical transmissions. *IEEE Journal of Selected Topics in Quantum Electronics* **10**, 281 (2004). 11

[100] J. M. Donohue, J. Lavoie, & K. J. Resch. Ultrafast Time-Division Demultiplexing of Polarization-Entangled Photons. *Phys. Rev. Lett.* **113**, 163602 (2014). 11, 74

[101] L. Olislager *et al.* Frequency-bin entangled photons. *Phys. Rev. A* **82**, 013804 (2010). 11

[102] C. Reimer *et al.* Integrated frequency comb source of heralded single photons. *Opt. Express* **22**, 6535 (2014). 11

[103] C. Reimer *et al.* Generation of multiphoton entangled quantum states by means of integrated frequency combs. *Science* **351**, 1176 (2016). 11, 115

[104] H.-H. Lu *et al.* Electro-Optic Frequency Beam Splitters and Tritters for High-Fidelity Photonic Quantum Information Processing. *Phys. Rev. Lett.* **120**, 030502 (2018). 12

[105] J. M. Lukens & P. Lougovski. Frequency-encoded photonic qubits for scalable quantum information processing. *Optica* **4**, 8 (2017). 12

[106] P. C. Humphreys *et al.* Linear Optical Quantum Computing in a Single Spatial Mode. *Phys. Rev. Lett.* **111**, 150501 (2013). 12

[107] B. Brecht, D. V. Reddy, C. Silberhorn, & M. G. Raymer. Photon Temporal Modes: A Complete Framework for Quantum Information Science. *Phys. Rev. X* **5**, 041017 (2015). 12, 93, 151

[108] A. Eckstein, B. Brecht, & C. Silberhorn. A quantum pulse gate based on spectrally engineered sum frequency generation. *Opt. Express* **19**, 13770 (2011). 12

[109] V. Ansari *et al.* Temporal-mode measurement tomography of a quantum pulse gate. *Phys. Rev. A* **96**, 063817 (2017). 12, 55, 135

[110] V. Ansari, J. M. Donohue, B. Brecht, & C. Silberhorn. Tailoring nonlinear processes for quantum optics with pulsed temporal-mode encodings. *Optica* **5**, 534 (2018). 12, 134

[111] M. A. Nielsen & I. L. Chuang. Quantum Computation and Quantum Information: 10th Anniversary Edition. Cambridge University Press (2010). ISBN 978-1-139-49548-6. 12, 13, 58

[112] G. Tóth & O. Gühne. Detecting Genuine Multipartite Entanglement with Two Local Measurements. *Phys. Rev. Lett.* **94**, 060501 (2005). 13, 22

[113] M. Żukowski, A. Zeilinger, M. A. Horne, & A. K. Ekert. "Event-ready-detectors" Bell experiment via entanglement swapping. *Phys. Rev. Lett.* **71**, 4287 (1993). 14

[114] D. Gottesman & I. L. Chuang. Demonstrating the viability of universal quantum computation using teleportation and single-qubit operations. *Nature* **402**, 390 (1999). 14

[115] J. Brendel, E. Mohler, & W. Martienssen. Experimental Test of Bell's Inequality for Energy and Time. *EPL* **20**, 575 (1992). 15, 17

[116] P. G. Kwiat *et al.* Ultrabright source of polarization-entangled photons. *Phys. Rev. A* **60**, R773 (1999). 15

[117] S.-Y. Baek & Y.-H. Kim. Spectral properties of entangled photon pairs generated via frequency-degenerate type-I spontaneous parametric down-conversion. *Phys. Rev. A* **77**, 043807 (2008). 15

[118] Y. Nambu *et al.* Generation of polarization-entangled photon pairs in a cascade of two type-I crystals pumped by femtosecond pulses. *Phys. Rev. A* **66**, 033816 (2002). 16

[119] C. H. Bennett, D. P. DiVincenzo, J. A. Smolin, & W. K. Wootters. Mixed-state entanglement and quantum error correction. *Phys. Rev. A* **54**, 3824 (1996). 16

[120] D. Bouwmeester *et al.* Observation of Three-Photon Greenberger-Horne-Zeilinger Entanglement. *Phys. Rev. Lett.* **82**, 1345 (1999). 16

[121] J.-W. Pan *et al.* Experimental test of quantum nonlocality in three-photon Greenberger–Horne–Zeilinger entanglement. *Nature* **403**, 515 (2000). 16

[122] W. P. Grice, R. Erdmann, I. A. Walmsley, & D. Branning. Spectral distinguishability in ultrafast parametric down-conversion. *Phys. Rev. A* **57**, R2289 (1998). 16

[123] G. Di Giuseppe, L. Haiberger, F. De Martini, & A. V. Sergienko. Quantum interference and indistinguishability with femtosecond pulses. *Phys. Rev. A* **56**, R21 (1997). 16

[124] D. Branning, W. P. Grice, R. Erdmann, & I. A. Walmsley. Engineering the Indistinguishability and Entanglement of Two Photons. *Phys. Rev. Lett.* **83**, 955 (1999). 16

[125] Y.-H. Kim, S. P. Kulik, & Y. Shih. High-intensity pulsed source of space-time and polarization double-entangled photon pairs. *Phys. Rev. A* **62**, 011802 (2000). 16

[126] Y.-H. Kim, S. P. Kulik, & Y. Shih. Bell-state preparation using pulsed nondegenerate two-photon entanglement. *Phys. Rev. A* **63**, 060301 (2001). 16

[127] T. Kim, M. Fiorentino, & F. N. C. Wong. Phase-stable source of polarization-entangled photons using a polarization Sagnac interferometer. *Phys. Rev. A* **73**, 012316 (2006). 16

[128] B.-S. Shi & A. Tomita. Generation of a pulsed polarization entangled photon pair using a Sagnac interferometer. *Phys. Rev. A* **69**, 013803 (2004). 16

[129] L. Vermeyden *et al.* Experimental test of environment-assisted invariance. *Phys. Rev. A* **91**, 012120 (2015). 16

[130] X.-C. Yao *et al.* Observation of eight-photon entanglement. *Nature Photonics* **6**, 225 (2012). 16

[131] X.-L. Wang *et al.* Experimental Ten-Photon Entanglement. *Phys. Rev. Lett.* **117**, 210502 (2016). 16

[132] D. R. Hamel *et al.* Direct generation of three-photon polarization entanglement. *Nature Photonics* **8**, 801 (2014). 17

[133] Z. Y. Ou, X. Y. Zou, L. J. Wang, & L. Mandel. Observation of nonlocal interference in separated photon channels. *Phys. Rev. Lett.* **65**, 321 (1990). 17

[134] J. D. Franson. Two-photon interferometry over large distances. *Phys. Rev. A* **44**, 4552 (1991). 17

[135] A. Einstein, B. Podolsky, & N. Rosen. Can Quantum-Mechanical Description of Physical Reality Be Considered Complete? *Phys. Rev.* **47**, 777 (1935). 17

[136] R. Grobe, K. Rzazewski, & J. H. Eberly. Measure of electron-electron correlation in atomic physics. *J. Phys. B: At. Mol. Opt. Phys.* **27**, L503 (1994). 18

[137] C. K. Law, I. A. Walmsley, & J. H. Eberly. Continuous frequency entanglement: effective finite Hilbert space and entropy control. *Phys. Rev. Lett.* **84**, 5304 (2000). 18

[138] A. Eckstein, A. Christ, P. J. Mosley, & C. Silberhorn. Highly Efficient Single-Pass Source of Pulsed Single-Mode Twin Beams of Light. *Phys. Rev. Lett.* **106**, 013603 (2011). 18, 96

[139] M. A. Horne, A. Shimony, & A. Zeilinger. Two-particle interferometry. *Phys. Rev. Lett.* **62**, 2209 (1989). 19

[140] R. T. Thew, A. Acín, H. Zbinden, & N. Gisin. Bell-Type Test of Energy-Time Entangled Qutrits. *Phys. Rev. Lett.* **93**, 010503 (2004). 19, 115

[141] I. Marcikic *et al.* Time-bin entangled qubits for quantum communication created by femtosecond pulses. *Phys. Rev. A* **66**, 062308 (2002). 19, 93

[142] R. T. Thew *et al.* Experimental investigation of the robustness of partially entangled qubits over 11 km. *Phys. Rev. A* **66**, 062304 (2002). 19

[143] I. Marcikic *et al.* Long-distance teleportation of qubits at telecommunication wavelengths. *Nature* **421**, 509 (2003). 19

[144] J. Roslund *et al.* Wavelength-multiplexed quantum networks with ultrafast frequency combs. *Nat. Photon.* **8**, 109 (2013). 19

[145] M. Kues *et al.* On-chip generation of high-dimensional entangled quantum states and their coherent control. *Nature* **546**, 622 (2017). 19, 134

[146] P. Grangier, G. Roger, & A. Aspect. Experimental Evidence for a Photon Anticorrelation Effect on a Beam Splitter: A New Light on Single-Photon Interferences. *EPL* **1**, 173 (1986). 20

[147] R. Hanbury Brown & R. Q. Twiss. A Test of a New Type of Stellar Interferometer on Sirius. *Nature* **178**, 1046 (1956). 22, 103

[148] A. Peres. Separability Criterion for Density Matrices. *Phys. Rev. Lett.* **77**, 1413 (1996). 22

[149] L.-M. Duan, G. Giedke, J. I. Cirac, & P. Zoller. Inseparability Criterion for Continuous Variable Systems. *Phys. Rev. Lett.* **84**, 2722 (2000). 22, 24, 27

[150] P. van Loock & A. Furusawa. Detecting genuine multipartite continuous-variable entanglement. *Phys. Rev. A* **67**, 052315 (2003). 23, 134

[151] L. K. Shalm *et al.* Three-photon energy-time entanglement. *Nat. Phys.* **9**, 19 (2013). 23, 93, 95, 134, 135

[152] J. Bavaresco *et al.* Measurements in two bases are sufficient for certifying high-dimensional entanglement. *Nat. Phys.* **14**, 1032 (2018). 23

[153] R. Bracewell. The Fourier Transform and Its Applications. Electrical engineering series. McGraw Hill (2000). ISBN 978-0-07-303938-1. 24

[154] P. G. Kwiat *et al.* Correlated two-photon interference in a dual-beam Michelson interferometer. *Phys. Rev. A* **41**, 2910 (1990). 27

[155] C. Su & K. Wódkiewicz. Quantum versus stochastic or hidden-variable fluctuations in two-photon interference effects. *Phys. Rev. A* **44**, 6097 (1991). 27, 116

[156] J. D. Franson. Violations of a simple inequality for classical fields. *Phys. Rev. Lett.* **67**, 290 (1991). 27, 29, 59

[157] W. P. Grice, A. B. URen, & I. A. Walmsley. Eliminating frequency and space-time correlations in multiphoton states. *Phys. Rev. A* **64**, 063815 (2001). 44, 50, 51, 96, 114

[158] M. Hillery & L. D. Mlodinow. Quantization of electrodynamics in nonlinear dielectric media. *Phys. Rev. A* **30**, 1860 (1984). 47

[159] D. A. Kleinman. Nonlinear Dielectric Polarization in Optical Media. *Phys. Rev.* **126**, 1977 (1962). 47

[160] J. J. Sakurai & J. Napolitano. Modern Quantum Mechanics. Pearson (2013). ISBN 978-1-292-02410-3. 49

[161] J. M. Donohue. Ultrafast manipulation of single photons using dispersion and sum-frequency generation. Ph.D. thesis (2016). 49, 62, 68

[162] N. Quesada & J. E. Sipe. Time-Ordering Effects in the Generation of Entangled Photons Using Nonlinear Optical Processes. *Phys. Rev. Lett.* **114**, 093903 (2015). 49

[163] J. M. Donohue, M. D. Mazurek, & K. J. Resch. Theory of high-efficiency sum-frequency generation for single-photon waveform conversion. *Phys. Rev. A* **91**, 033809 (2015). 49, 62, 103

[164] W. P. Grice & I. A. Walmsley. Spectral information and distinguishability in type-II down-conversion with a broadband pump. *Phys. Rev. A* **56**, 1627 (1997). 50, 51, 96, 130

[165] A. M. Brańczyk, T. C. Ralph, W. Helwig, & C. Silberhorn. Optimized generation of heralded Fock states using parametric down-conversion. *New J. Phys.* **12**, 063001 (2010). 50

[166] T. Guerreiro *et al.* High efficiency coupling of photon pairs in practice. *Opt. Express* **21**, 27641 (2013). 50

[167] P. J. Mosley *et al.* Heralded Generation of Ultrafast Single Photons in Pure Quantum States. *Phys. Rev. Lett.* **100**, 133601 (2008). 51, 96, 114, 136

[168] V. Giovannetti, L. Maccone, J. H. Shapiro, & F. N. C. Wong. Extended phase-matching conditions for improved entanglement generation. *Phys. Rev. A* **66** (2002). 51

[169] V. Giovannetti, L. Maccone, J. H. Shapiro, & F. N. C. Wong. Generating Entangled Two-Photon States with Coincident Frequencies. *Phys. Rev. Lett.* **88** (2002). 51

[170] M. Avenhaus, A. Eckstein, P. J. Mosley, & C. Silberhorn. Fiber-assisted single-photon spectrograph. *Opt. Lett.* **34**, 2873 (2009). 51, 93

[171] E. Meyer-Scott *et al.* Limits on the heralding efficiencies and spectral purities of spectrally filtered single photons from photon-pair sources. *Phys. Rev. A* **95**, 061803 (2017). 51

[172] Multivariate normal distribution. *Wikipedia* (2018). Page Version ID: 859967185. 53

[173] W. Mauerer, M. Avenhaus, W. Helwig, & C. Silberhorn. How colors influence numbers: Photon statistics of parametric down-conversion. *Phys. Rev. A* **80** (2009). 55

[174] A. Branczyk. Non-classical states of light. Ph.D. thesis, University of Queensland (2010). 55

[175] F. M. Miatto, H. Di Lorenzo Pires, S. M. Barnett, & M. P. van Exter. Spatial Schmidt modes generated in parametric down-conversion. *Eur. Phys. J. D* **66**, 263 (2012). 55

[176] F. M. Miatto, T. Brougham, & A. M. Yao. Cartesian and polar Schmidt bases for down-converted photons. *Eur. Phys. J. D* **66**, 183 (2012). 55

[177] F. M. Miatto. High dimensional spatial entanglement with photon pairs. Ph.D. thesis, University of Strathclyde (2012). 55

[178] A. Dosseva, Ł. Cincio, & A. M. Brańczyk. Shaping the joint spectrum of down-converted photons through optimized custom poling. *Phys. Rev. A* **93**, 013801 (2016). 55

[179] V. Ansari *et al.* Tomography and Purification of the Temporal-Mode Structure of Quantum Light. *Phys. Rev. Lett.* **120**, 213601 (2018). 55, 135

[180] A. Starikov & E. Wolf. Coherent-mode representation of Gaussian Schell-model sources and of their radiation fields. *J. Opt. Soc. Am.* **72**, 923 (1982). 55

[181] A. Christ *et al.* Probing multimode squeezing with correlation functions. *New J. Phys.* **13**, 033027 (2011). 55

[182] I. A. Walmsley & C. Dorrer. Characterization of ultrashort electromagnetic pulses. *Adv. Opt. Photonics* **1**, 308 (2009). 57, 63, 64, 67, 73, 82, 93, 134

[183] M. V. Fedorov, M. A. Efremov, P. A. Volkov, & J. H. Eberly. Short-pulse or strong-field breakup processes: a route to study entangled wave packets. *Journal of Physics B: Atomic, Molecular and Optical Physics* **39**, S467 (2006). 58

[184] L. Mandel & E. Wolf. Optical Coherence and Quantum Optics. Cambridge University Press (1995). ISBN 978-0-521-41711-2. 58, 75, 187

[185] R. J. Glauber. The Quantum Theory of Optical Coherence. *Phys. Rev.* **130**, 2529 (1963). 58

[186] R. J. Glauber. Nobel Lecture: One hundred years of light quanta*. *Rev. Mod. Phys.* **78**, 1267 (2006). 58

[187] P. Zhou, H. Schulz, & P. Kohns. Atomic spectroscopy with ultrashort laser pulses using frequency-resolved optical gating. *Optics Communications* **123**, 501 (1996). 63

[188] A. H. Zewail. Femtochemistry: Atomic-Scale Dynamics of the Chemical Bond. *J. Phys. Chem. A* **104**, 5660 (2000). 63, 93

[189] W. R. Zipfel, R. M. Williams, & W. W. Webb. Nonlinear magic: multiphoton microscopy in the biosciences. *Nat. Biotech.* **21**, 1369 (2003). 63, 93

[190] D. Meshulach & Y. Silberberg. Coherent quantum control of two-photon transitions by a femtosecond laser pulse. *Nature* **396**, 239 (1998). 63

[191] A. M. Weiner. Femtosecond optical pulse shaping and processing. *Progress in Quantum Electronics* **19**, 161 (1995). 63

[192] R. Trebino. Frequency-Resolved Optical Gating: The Measurement of Ultrashort Laser Pulses. Springer Science & Business Media (2012). ISBN 978-1-4615-1181-6. 63, 64, 87, 88, 90, 91, 141, 142

[193] B. E. A. Saleh & M. C. Teich. Fundamentals of Photonics. Wiley (2007). ISBN 978-0-471-35832-9. 68, 69, 70

[194] O. E. Martinez, J. P. Gordon, & R. L. Fork. Negative group-velocity dispersion using refraction. *J. Opt. Soc. Am. A* **1**, 1003 (1984). 68

[195] R. L. Fork, O. E. Martinez, & J. P. Gordon. Negative dispersion using pairs of prisms. *Opt. Lett.* **9**, 150 (1984). 68, 72

[196] E. Treacy. Optical pulse compression with diffraction gratings. *J. Quantum Electron.* **5**, 454 (1969). 68, 70, 103, 107, 145

[197] A. M. Weiner. Femtosecond pulse shaping using spatial light modulators. *Review of Scientific Instruments* **71**, 1929 (2000). 68

[198] M. D. Mazurek *et al.* Dispersion-cancelled biological imaging with quantum-inspired interferometry. *Scientific Reports* **3** (2013). 68

[199] A. K. Gunther. PPLN-based photon pair sources toward biphoton quantum frequency conversion. Ph.D. thesis (2018). 68

[200] S. Akturk, X. Gu, P. Gabolde, & R. Trebino. The general theory of first-order spatio-temporal distortions of Gaussian pulses and beams. *Opt. Express* **13**, 8642 (2005). 68

[201] S. Akturk, X. Gu, M. Kimmel, & R. Trebino. Extremely simple single-prism ultrashort-pulse compressor. *Opt. Express* **14**, 10101 (2006). 68

[202] I. Walmsley, L. Waxer, & C. Dorrer. The role of dispersion in ultrafast optics. *Review of Scientific Instruments* **72**, 1 (2001). 68, 69, 71

[203] N. Photonics. Thin BiBO Crystals (2018). 70

[204] O. Martinez. 3000 times grating compressor with positive group velocity dispersion: Application to fiber compensation in 1.3-1.6 um region. *IEEE Journal of Quantum Electronics* **23**, 59 (1987). 72

[205] R. L. Fork, C. H. B. Cruz, P. C. Becker, & C. V. Shank. Compression of optical pulses to six femtoseconds by using cubic phase compensation. *Opt. Lett.* **12**, 483 (1987). 72

[206] C. H. B. Cruz, P. C. Becker, R. L. Fork, & C. V. Shank. Phase correction of femtosecond optical pulses using a combination of prisms and gratings. *Opt. Lett.* **13**, 123 (1988). 72

[207] M. Hentschel *et al.* Attosecond metrology. *Nature* **414**, 509 (2001). 73

[208] O. Kuzucu, F. N. Wong, S. Kurimura, & S. Tovstonog. Time-resolved single-photon detection by femtosecond upconversion. *Opt. Lett.* **33**, 2257 (2008). 74, 94, 114, 115

[209] J.-P. W. MacLean, J. M. Donohue, & K. J. Resch. Direct Characterization of Ultrafast Energy-Time Entangled Photon Pairs. *Phys. Rev. Lett.* **120**, 053601 (2018). 74, 92, 114, 115, 124, 135, 136, 141

[210] G. Taft *et al.* Measurement of 10-fs laser pulses. *IEEE Journal of Selected Topics in Quantum Electronics* **2**, 575 (1996). 76, 81

[211] F. Salin, P. Georges, G. Roger, & A. Brun. Single-shot measurement of a 52-fs pulse. *Appl. Opt., AO* **26**, 4528 (1987). 76

[212] M. Allgaier *et al.* Streak camera imaging of single photons at telecom wavelength. *Appl. Phys. Lett.* **112**, 031110 (2018). 76

[213] W. Pauli. The General Principles of Wave Mechanics. University of Illinois ar Urbana-Champaign (1950). 82

[214] W. O. Saxton. Computer Techniques for Image Processing in Electron Microscopy. Academic Press (2013). ISBN 978-1-4832-8464-4. 82, 85, 137

[215] H. Stark. Image Recovery: Theory and Application. Elsevier (2013). ISBN 978-0-323-14597-8. 82, 83, 87

[216] R. W. Gerchberg & W. Saxton. A practical algorithm for the determination of the phase from image and diffraction plane pictures. *Optik* **35**, 237 (1972). 82, 85, 135, 137

[217] D. Peri. Optical implementation of a phase retrieval algorithm. *Appl. Opt.* **26**, 1782 (1987). 82, 135

[218] J. R. Fienup. Reconstruction of an object from the modulus of its Fourier transform. *Opt. Lett.* **3**, 27 (1978). 82, 87, 135

[219] J. R. Fienup. Iterative method applied to image reconstruction and to computer-generated holograms. *Opt. Eng* **19**, 297 (1980). 82

[220] J. R. Fienup. Phase retrieval algorithms: a comparison. *Appl. Opt.* **21**, 2758 (1982). 82, 87, 135

[221] R. P. Millane. Phase retrieval in crystallography and optics. *J. Opt. Soc. Am. A* **7**, 394 (1990). 82

[222] H. N. Chapman *et al.* High-resolution ab initio three-dimensional x-ray diffraction microscopy. *J. Opt. Soc. Am. A* **23**, 1179 (2006). 82

[223] Y. Shechtman *et al.* Phase Retrieval with Application to Optical Imaging: A contemporary overview. *IEEE Signal Processing Magazine* **32**, 87 (2015). 82, 87, 135

[224] D. J. Kane & R. Trebino. Single-shot measurement of the intensity and phase of an arbitrary ultrashort pulse by using frequency-resolved optical gating. *Opt. Lett.* **18**, 823 (1993). 82, 90, 134

[225] R. Trebino *et al.* Measuring ultrashort laser pulses in the time-frequency domain using frequency-resolved optical gating. *Rev. Sci. Instrum.* **68**, 3277 (1997). 82, 93

[226] M. Guizar-Sicairos & J. R. Fienup. Understanding the twin-image problem in phase retrieval. *J. Opt. Soc. Am. A* **29**, 2367 (2012). 85, 137

[227] G. Whyte & J. Courtial. Experimental demonstration of holographic three-dimensional light shaping using a Gerchberg–Saxton algorithm. *New J. Phys.* **7**, 117 (2005). 85, 86

[228] M. A. Fiddy & U. Shahid. Legacies of the Gerchberg–Saxton algorithm. *Ultramicroscopy* **134**, 48 (2013). 86

[229] A. Rundquist, A. Efimov, & D. H. Reitze. Pulse shaping with the Gerchberg–Saxton algorithm. *J. Opt. Soc. Am. B* **19**, 2468 (2002). 86

[230] D. S. Moore *et al.* Use of the Gerchberg–Saxton algorithm in optimal coherent anti-Stokes Raman spectroscopy. *Anal Bioanal Chem* **402**, 423 (2012). 86

[231] F. Bouchard *et al.* Quantum cryptography with twisted photons through an outdoor underwater channel. *Opt. Express* **26**, 22563 (2018). 86

[232] B. Heacock *et al.* Sub-micrometer resolution neutron tomography. *arXiv:1808.07476* (2018). 86

[233] E. Serabyn, D. Mawet, & R. Burruss. An image of an exoplanet separated by two diffraction beamwidths from a star. *Nature* **464**, 1018 (2010). 86

[234] E. J. Akutowicz. On the Determination of the Phase of a Fourier Integral, I. *Transactions of the American Mathematical Society* **83**, 179 (1956). 87

[235] E. J. Akutowicz. On the Determination of the Phase of a Fourier Integral, I. *Transactions of the American Mathematical Society* **83**, 179 (1956). 87

[236] J. R. Fienup. Phase retrieval algorithms: a personal tour [Invited]. *Appl. Opt.* **52**, 45 (2013). 87, 135

[237] V. Wong & I. A. Walmsley. Ultrashort-pulse characterization from dynamic spectrograms by iterative phase retrieval. *J. Opt. Soc. Am. B* **14**, 944 (1997). 88

[238] K. W. DeLong & R. Trebino. Improved ultrashort pulse-retrieval algorithm for frequency-resolved optical gating. *J. Opt. Soc. Am. A* **11**, 2429 (1994). 90

[239] D. J. Kane. Recent progress toward real-time measurement of ultrashort laser pulses. *IEEE Journal of Quantum Electronics* **35**, 421 (1999). 90, 141

[240] C. Bourassin-Bouchet & M.-E. Couprie. Partially coherent ultrafast spectrography. *Nat. Commun.* **6**, 6465 (2015). 91, 159

[241] D. N. Fittinghoff, K. W. DeLong, R. Trebino, & C. L. Ladera. Noise sensitivity in frequency-resolved optical-gating measurements of ultrashort pulses. *J. Opt. Soc. Am. B* **12**, 1955 (1995). 91, 148

[242] D. Spangenberg *et al.* Time-domain ptychography. *Phys. Rev. A* **91**, 021803 (2015). 91

[243] S. Ramelow *et al.* Discrete Tunable Color Entanglement. *Phys. Rev. Lett.* **103**, 253601 (2009). 93

[244] Q. Zhang *et al.* Distribution of Time-Energy Entanglement over 100 km fiber using superconducting single-photon detectors. *Opt. Express* **16**, 5776 (2008). 93

[245] J. D. Franson. Nonlocal cancellation of dispersion. *Phys. Rev. A* **45**, 3126 (1992). 93, 94, 134

[246] A. M. Steinberg, P. G. Kwiat, & R. Y. Chiao. Dispersion cancellation in a measurement of the single-photon propagation velocity in glass. *Phys. Rev. Lett.* **68**, 2421 (1992). 93, 114

[247] V. Giovannetti, S. Lloyd, & L. Maccone. Quantum-enhanced positioning and clock synchronization. *Nature* **412**, 417 (2001). 93

[248] S.-W. Bahk *et al.* Generation and characterization of the highest laser intensities (10^{22} W/cm^2). *Opt. Lett.* **29**, 2837 (2004). 93

[249] Z. Chang *et al.* Generation of Coherent Soft X Rays at 2.7 nm Using High Harmonics. *Phys. Rev. Lett.* **79**, 2967 (1997). 93

[250] S. Mancini, V. Giovannetti, D. Vitali, & P. Tombesi. Entangling Macroscopic Oscillators Exploiting Radiation Pressure. *Phys. Rev. Lett.* **88**, 120401 (2002). 93, 95

[251] S. Schwarz, B. Bessire, & A. Stefanov. Experimental violation of a d-dimensional Bell inequality using energy-time entangled photons. *Int. J. Quantum Inform.* **12**, 1560026 (2014). 93

[252] O. Kuzucu, F. N. C. Wong, S. Kurimura, & S. Tovstonog. Joint Temporal Density Measurements for Two-Photon State Characterization. *Phys. Rev. Lett.* **101**, 153602 (2008). 93, 94, 114, 115

[253] Y.-W. Cho, K.-K. Park, J.-C. Lee, & Y.-H. Kim. Engineering Frequency-Time Quantum Correlation of Narrow-Band Biphotons from Cold Atoms. *Phys. Rev. Lett.* **113**, 063602 (2014). 93, 94

[254] S. Agne *et al.* Observation of Genuine Three-Photon Interference. *Phys. Rev. Lett.* **118**, 153602 (2017). 94, 115

[255] T. Wasak, P. Szankowski, W. Wasilewski, & K. Banaszek. Entanglement-based signature of nonlocal dispersion cancellation. *Phys. Rev. A* **82**, 052120 (2010). 94, 107, 134

[256] J. A. Jaramillo-Villegas *et al.* Persistent energy-time entanglement covering multiple resonances of an on-chip biphoton frequency comb. *Optica* **4**, 655 (2017). 94, 116

[257] S.-Y. Baek, Y.-W. Cho, & Y.-H. Kim. Nonlocal Dispersion Cancellation using Entangled Photons. *Opt. Express* **17**, 19241 (2009). 94

[258] K. A. O'Donnell. Observations of Dispersion Cancellation of Entangled Photon Pairs. *Phys. Rev. Lett.* **106**, 063601 (2011). 94

[259] R. Prevedel, K. M. Schreiter, J. Lavoie, & K. J. Resch. Classical analog for dispersion cancellation of entangled photons with local detection. *Phys. Rev. A* **84**, 051803 (2011). 94, 96

[260] M. Allgaier *et al.* Fast time-domain measurements on telecom single photons. *Quantum Sci. Technol.* **2**, 034012 (2017). 94, 114, 115

[261] J. C. Howell, R. S. Bennink, S. J. Bentley, & R. W. Boyd. Realization of the Einstein-Podolsky-Rosen Paradox Using Momentum- and Position-Entangled Photons from Spontaneous Parametric Down Conversion. *Phys. Rev. Lett.* **92**, 210403 (2004). 95

[262] M. Edgar *et al.* Imaging high-dimensional spatial entanglement with a camera. *Nat. Commun.* **3**, 984 (2012). 95

[263] C. Chen *et al.* Efficient generation and characterization of spectrally factorable biphotons. *Opt. Express* **25**, 7300 (2017). 96

[264] B. Brecht & C. Silberhorn. Characterizing entanglement in pulsed parametric down-conversion using chronocyclic Wigner functions. *Phys. Rev. A* **87**, 053810 (2013). 99

[265] A. P. Vandevender & P. G. Kwiat. High efficiency single photon detection via frequency up-conversion. *J. Mod. Opt.* **51**, 1433 (2004). 103

[266] J.-P. W. MacLean, J. M. Donohue, & K. J. Resch. Ultrafast quantum interferometry with energy-time entangled photons. *Phys. Rev. A* **97**, 063826 (2018). 113, 135, 141

[267] S. Slussarenko *et al.* Unconditional violation of the shot-noise limit in photonic quantum metrology. *Nat. Photonics* **11**, 700 (2017). 114

[268] M. W. Mitchell, J. S. Lundeen, & A. M. Steinberg. Super-resolving phase measurements with a multiphoton entangled state. *Nature* **429**, 161 (2004). 114

[269] M. B. Nasr, B. E. A. Saleh, A. V. Sergienko, & M. C. Teich. Demonstration of Dispersion-Canceled Quantum-Optical Coherence Tomography. *Phys. Rev. Lett.* **91**, 083601 (2003). 114

[270] F. Kaiser *et al.* Quantum enhancement of accuracy and precision in optical interferometry. *Light: Science & Applications* **7**, 17163 (2018). 114

[271] J. Aasi *et al.* Enhanced sensitivity of the LIGO gravitational wave detector by using squeezed states of light. *Nat. Photonics* **7**, 613 (2013). 114

[272] S. Backus, C. G. Durfee, M. M. Murnane, & H. C. Kapteyn. High power ultrafast lasers. *Review of Scientific Instruments* **69**, 1207 (1998). 114

[273] B. Dayan, A. Pe'er, A. A. Friesem, & Y. Silberberg. Two Photon Absorption and Coherent Control with Broadband Down-Converted Light. *Phys. Rev. Lett.* **93**, 023005 (2004). 114, 134

[274] M. B. Nasr *et al.* Ultrabroadband Biphotons Generated via Chirped Quasi-Phase-Matched Optical Parametric Down-Conversion. *Phys. Rev. Lett.* **100**, 183601 (2008). 114

[275] S. Sensarn, G. Y. Yin, & S. E. Harris. Generation and Compression of Chirped Biphotons. *Phys. Rev. Lett.* **104**, 253602 (2010). 114

[276] R.-B. Jin, T. Saito, & R. Shimizu. Experimental demonstration of time-frequency duality of biphotons. *arXiv:1801.09044* (2018). 114

[277] A. Pe'er, B. Dayan, A. A. Friesem, & Y. Silberberg. Temporal Shaping of Entangled Photons. *Phys. Rev. Lett.* **94**, 073601 (2005). 115

[278] T. Zhong *et al.* Photon-efficient quantum key distribution using time–energy entanglement with high-dimensional encoding. *New J. Phys.* **17**, 022002 (2015). 115, 134

[279] T. Ikuta & H. Takesue. Four-dimensional entanglement distribution over 100 km. *Scientific Reports* **8**, 817 (2018). 115

[280] M. G. Raymer, A. H. Marcus, J. R. Widom, & D. L. P. Vitullo. Entangled Photon-Pair Two-Dimensional Fluorescence Spectroscopy (EPP-2dfs). *J. Phys. Chem. B* **117**, 15559 (2013). 115, 134

[281] Y. M. Mikhailova, P. A. Volkov, & M. V. Fedorov. Biphoton wave packets in parametric down-conversion: Spectral and temporal structure and degree of entanglement. *Phys. Rev. A* **78**, 062327 (2008). 115

[282] D. Grassani *et al.* Micrometer-scale integrated silicon source of time-energy entangled photons. *Optica* **2**, 88 (2015). 116

[283] M. Peiris, K. Konthasinghe, & A. Muller. Franson Interference Generated by a Two-Level System. *Phys. Rev. Lett.* **118**, 030501 (2017). 116

[284] J. F. Clauser, M. A. Horne, A. Shimony, & R. A. Holt. Proposed Experiment to Test Local Hidden-Variable Theories. *Phys. Rev. Lett.* **23**, 880 (1969). 130, 131

[285] J.-P. W. MacLean, S. Schwarz, & K. J. Resch. Reconstructing ultrafast energy-time entangled two-photon pulses. *arXiv:1901.11116* (2019). 133

[286] B. P. Lanyon *et al.* Simplifying quantum logic using higher-dimensional Hilbert spaces. *Nat. Phys.* **5**, 134 (2009). 134

[287] Y. Cai *et al.* Multimode entanglement in reconfigurable graph states using optical frequency combs. *Nat. Commun.* **8**, 15645 (2017). 134

[288] Z. Zhang, S. Mouradian, F. N. C. Wong, & J. H. Shapiro. Entanglement-Enhanced Sensing in a Lossy and Noisy Environment. *Phys. Rev. Lett.* **114**, 110506 (2015). 134

[289] D. Kang, A. Pang, Y. Zhao, & A. S. Helmy. Two-photon quantum state engineering in nonlinear photonic nanowires. *J. Opt. Soc. Am. B* **31**, 1581 (2014). 134

[290] J. M. Donohue *et al.* Quantum-Limited Time-Frequency Estimation through Mode-Selective Photon Measurement. *Phys. Rev. Lett.* **121**, 090501 (2018). 134

[291] F. Arzani, C. Fabre, & N. Treps. Versatile engineering of multimode squeezed states by optimizing the pump spectral profile in spontaneous parametric down-conversion. *Phys. Rev. A* **97**, 033808 (2018). 134

[292] U. Keller. Recent developments in compact ultrafast lasers. *Nature* **424**, 831 (2003). 134

[293] C. Iaconis & I. A. Walmsley. Spectral phase interferometry for direct electric-field reconstruction of ultrashort optical pulses. *Opt. Lett.* **23**, 792 (1998). 134

[294] A. I. Lvovsky & M. G. Raymer. Continuous-variable optical quantum-state tomography. *Rev. Mod. Phys.* **81**, 299 (2009). 135

[295] T. Aichele, A. I. Lvovsky, & S. Schiller. Optical mode characterization of single photons prepared by means of conditional measurements on a biphoton state. *Eur. Phys. J. D* **18**, 237 (2002). 135

[296] C. Polycarpou *et al.* Adaptive Detection of Arbitrarily Shaped Ultrashort Quantum Light States. *Phys. Rev. Lett.* **109**, 053602 (2012). 135

[297] O. Morin, C. Fabre, & J. Laurat. Experimentally Accessing the Optimal Temporal Mode of Traveling Quantum Light States. *Phys. Rev. Lett.* **111**, 213602 (2013). 135

[298] Z. Qin *et al.* Complete temporal characterization of a single photon. *Light: Science & Applications* **4**, e298 (2015). 135

[299] P. Chen *et al.* Measuring the Biphoton Temporal Wave Function with Polarization-Dependent and Time-Resolved Two-Photon Interference. *Phys. Rev. Lett.* **114**, 010401 (2015). 135

[300] N. Tischler *et al.* Measurement and Shaping of Biphoton Spectral Wave Functions. *Physical Review Letters* **115**, 193602 (2015). 135

[301] J. Tiedau *et al.* Quantum state and mode profile tomography by the overlap. *New J. Phys.* **20**, 033003 (2018). 135

[302] A. O. C. Davis, V. Thiel, M. Karpiński, & B. J. Smith. Measuring the Single-Photon Temporal-Spectral Wave Function. *Phys. Rev. Lett.* **121**, 083602 (2018). 135

[303] W. H. Press, S. A. Teukolsky, W. T. Vetterling, & B. P. Flannery. Numerical Recipes 3rd Edition: The Art of Scientific Computing. Cambridge University Press (2007). ISBN 978-0-521-88068-8. 137

[304] P. O'Shea, M. Kimmel, X. Gu, & R. Trebino. Increased-bandwidth in ultrashort-pulse measurement using an angle-dithered nonlinear-optical crystal. *Opt. Express* **7**, 342 (2000). 159

[305] S. Akturk *et al.* Measuring several-cycle 1.5-um pulses using frequency-resolved optical gating. *Opt. Express* **11**, 3461 (2003). 159

[306] P. Thibault & A. Menzel. Reconstructing state mixtures from diffraction measurements. *Nature* **494**, 68 (2013). 159

APPENDICES

Appendix A

List of publications during PhD

[10]**J.P.W. MacLean**, S. Schwarz, and K. J. Resch. *Reconstructing ultrafast energy-time entangled pulses.* arXiv: 1901.11116 (2019).

[9] **J.P.W. MacLean**, J.M. Donohue, K.J. Resch. *Ultrafast quantum interferometry with energy-time entangled photons.* Phys. Rev. A **97**, 063826 (2018).

[8] **J.P.W. MacLean**, J.M. Donohue, K.J. Resch. *Direct characterization of ultrafast energy-time entangled photon pairs.* Phys. Rev. Lett. **120**, 053601 (2018).

[7] B. Heacock, D. Sarenac, D.G. Cory, M.G. Huber, **J.P.W. MacLean**, H. Miao, H. Wen, and D.A. Pushin. *Sub-micrometer resolution neutron tomography.* arXiv: 1808.07476 (2018).

[6] **J.P.W. MacLean***, K. Ried*, R.W. Spekkens, K.J. Resch. *Quantum-coherent mixtures of causal relations.* Nature Communications **8**, 15149 (2017).

[5] K. Ried*, **J.P.W. MacLean***, R.W. Spekkens, K.J. Resch. *Quantum to classical transitions in causal relations.* Phys. Rev. A **95**, 062102 (2017).

[4] K. A. G. Fisher, D. G. England, **J.P.W. MacLean**, P. J. Bustard, K. Heshami, K. J. Resch, and B. J. Sussman. *Storage of Polarization-Entangled THz-Bandwidth Photons in a Diamond Quantum Memory.* Phys. Rev. A **96**, 012324 (2017).

[3] D.G. England, K.A.G. Fisher, **J.P.W. MacLean**, P.J. Bustard, K. Heshami, K.J. Resch, and B.J. Sussman. *Phonon-mediated nonclassical interference in diamond.* Phys. Rev. Lett. **117**, 073603 (2016).

[2] K.A.G. Fisher, D.G. England, **J.P.W. MacLean**, P.J. Bustard, K.J. Resch, and B.J. Sussman. *Frequency and bandwidth conversion of single photons in a room-temperature diamond quantum memory.* Nature Communications **7**, 11200 (2016).

[1] D.G. England, K.A.G. Fisher, **J.P.W. MacLean**, P.J. Bustard, R. Lausten, K.J. Resch, and B.J. Sussman. *Storage and Retrieval of THz-Bandwidth Single Photons Using a Room-Temperature Diamond Quantum Memory.* Phys. Rev. Lett. **114**, 053602 (2015).

* These authors contributed equally.

Appendix B

Correlated Gaussian functions

Correlated two-dimensional gaussian functions often come up in this thesis as they are very useful for obtaining intuition on the properties of entangled two-photon states of light. This appendix provides a useful model for describing two-dimensional Gaussian functions and a list of some of its properties [184].

Two-dimensional correlated gaussian function

$$F(x,y) = \frac{1}{\sqrt{2\pi\sigma_x\sigma_y}\left(1-\rho^2\right)^{1/4}} \times \exp\left(-\frac{1}{2\left(1-\rho^2\right)}\left[\frac{\left(x-x_0\right)^2}{2\sigma_x^2} + \frac{\left(y-y_0\right)^2}{2\sigma_y^2} - \frac{\rho\left(x-x_0\right)\left(y-y_0\right)}{\sigma_x\sigma_y}\right]\right) \tag{B.1}$$

Normalization

$$\int dxdy|F(x,y)|^2 = 1 \tag{B.2}$$

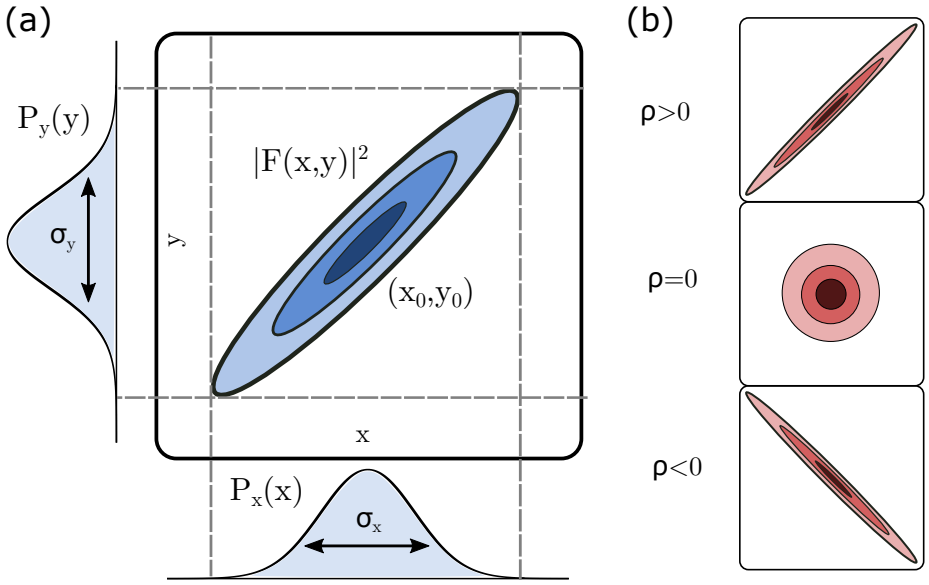

Figure B.1: **Two-dimensional correlated Gaussian function**(a) A two-dimensional correlated Gaussian function with mean (x_0, y_0), standard deviation σ_x and σ_y, statistical correlation ρ, and marginal distribution $F_x(x)$ and $F_y(y)$. The sign of ρ determines whether the variables x and y are positively correlated ($\rho > 0$), uncorrelated ($\rho = 0$), or negatively correlated ($\rho < 0$).

Mean

$$\langle x \rangle = \int dxdy\ x|F(x,y)|^2 = x_0 \tag{B.3}$$

$$\langle y \rangle = \int dxdy\ y|F(x,y)|^2 = y_0 \tag{B.4}$$

Standard deviation

$$\Delta x \equiv \sqrt{\langle x^2\rangle - \langle x\rangle^2} = \sqrt{\int dxdy\ x^2|F(x,y)|^2 - \left(\int dxdy\ x|F(x,y)|^2\right)^2} = \sigma_x \tag{B.5}$$

$$\Delta y \equiv \sqrt{\langle y^2\rangle - \langle y\rangle^2} = \sqrt{\int dxdy\ y^2|F(x,y)|^2 - \left(\int dxdy\ y|F(x,y)|^2\right)^2} = \sigma_y \tag{B.6}$$

$$\Delta(x \pm y) = \sqrt{\langle (x \pm y)^2\rangle - \langle x \pm y\rangle^2} = \sqrt{\sigma_x^2 \pm 2\rho\sigma_x\sigma_y + \sigma_y^2}, \tag{B.7}$$

Satistical correlation

$$\frac{\langle (x-x_0)(y-y_0)\rangle}{\sigma_x\sigma_y} = \frac{1}{\sigma_x\sigma_y}\int dxdy(x-x_0)(y-y_0)|F(x,y)|^2 = \rho \tag{B.8}$$

Marginal distribution

$$F_y(y) = \int dx|F(x,y)|^2 = \frac{1}{\sqrt{2\pi}\sigma_x}\exp\left[\frac{(y-y_0)^2}{2\sigma_y^2}\right] \tag{B.9}$$

$$F_x(x) = \int dy|F(x,y)|^2 = \frac{1}{\sqrt{2\pi}\sigma_y}\exp\left[\frac{(x-x_0)^2}{2\sigma_x^2}\right] \tag{B.10}$$

Conditional moments

$$\langle x\rangle_y = \int dx\ xF(x|y) = \frac{1}{F_y(y)}\int dx\ x|F(x,y)|^2 = x_0 + \frac{(y-y_0)\rho\sigma_x}{\sigma_y} \tag{B.11}$$

$$\langle y\rangle_x = \int dy\ yF(y|x) = \frac{1}{F_x(x)}\int dy\ y|F(x,y)|^2 = y_0 + \frac{(x-x_0)\rho\sigma_y}{\sigma_x} \tag{B.12}$$

Fourier transform

$$
\begin{aligned}
f(k_x, k_y) &= \frac{1}{\sqrt{2\pi}} \int dx dy F(x, y) e^{-ik_x x - ik_y y} \\
&= \sqrt{2\pi\sigma_x\sigma_y}(1-\rho^2)^{1/4} \exp\left[-\sigma_x k_x^2 - \sigma_y k_y^2 - 2k_x k_y \rho\sigma_x\sigma_y - i(k_y y_0 + k_x x_0)\right]
\end{aligned}
\tag{B.13}
$$

which can be recast into a gaussian function of the form Eq. B.1, with,

$$\sigma_{k_x} = \sqrt{\frac{1}{4(1-\rho^2)\sigma_x^2}} \tag{B.14}$$

$$\sigma_{k_y} = \sqrt{\frac{1}{4(1-\rho^2)\sigma_y^2}} \tag{B.15}$$

$$\rho_k = -\rho \tag{B.16}$$